Activity and Stability of RuOx Based Electrocatalysts for the Oxygen Evolution Reaction

Paoli, Elisa Antares

Publication date:
2014

Document Version
Publisher's PDF, also known as Version of record

Activity and Stability of RuO_x Based Electrocatalysts for the Oxygen Evolution Reaction

A Ph.D. thesis by

Elisa Antares Paoli

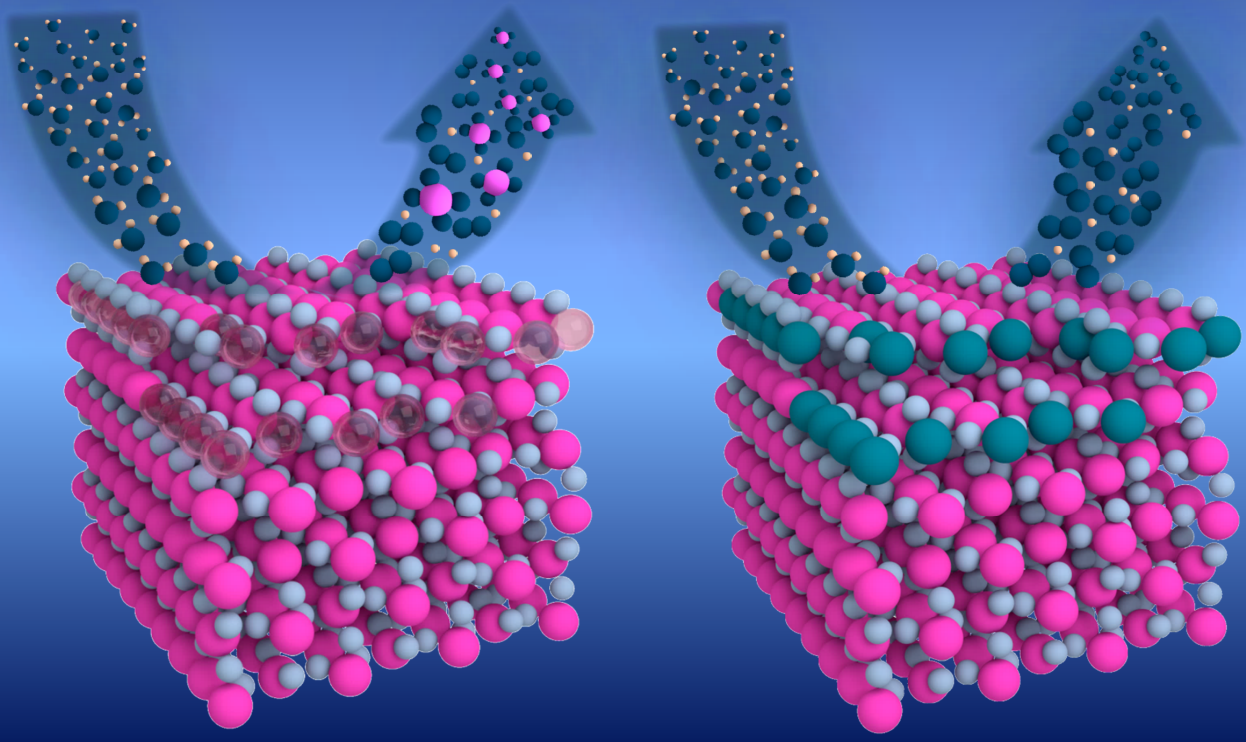

November 2014

Department of Physics
Technical University of Denmark

Activity and Stability of RuO_x Based Electrocatalysts for the Oxygen Evolution Reaction

Ph.D. dissertation by

Elisa Antares Paoli

Supervisor: Professor Ib Chorkendorff
Co-supervisor: Assistant Professor Ifan E. L. Stephens

November 2014

Center for Individual Nanoparticle Functionality
Department of Physics
Technical University of Denmark

Front image
Left: illustration of the oxygen evolution reaction and ruthenium dioxide corrosion on a rough RuO_2 (110) surface. Right: illustration of the oxygen evolution reaction on the same surface, where the undecoordinated sites are decorated with iridium oxide.

Preface

This work was accomplished at Technical University of Denmark, Department of Physics, at the Center for Individual Nanoparticle Functionalities (CINF) under the supervision of Prof. Ib Chorkendorff and Assistant professor Ifan E. L. Stephens. CINF is funded by the Danish Research Foundation and my PhD project has been funded by the UNIK initiative CAtalysis for Sustainable Energy (CASE) which are both greatly acknowledged. The project was carried out between December 2011 and December 2014.

I would like to thank my supervisors for giving me the possibility of working in such a great and inspiring environment. I thank you both for your support, guidance and many ideas that motivated me throughout my project.

I express many thanks to all my colleagues at CINF, CAMD and CEN. In particular, I would like to thank all the persons that I have collaborated with: Patricia Hernandez-Fernandez for her help at the beginning of my PhD; Federico Masini for the preparation of the nanoparticles; Christian Schlaup for the electrochemical scanning tunneling microscopy images; Mauro Malizia for the gas chromatograph measurements; Björn Wickman for the help with the Electrochemical Quartz Crystal Microbalance (EQCM); Paolo Malacrida for the X-ray Photoelectron Spectroscopy (XPS) measurements; Davide Deiana for the Transmission Electron Microsocpy (TEM) images; Katarzyna A. Janik for her help with Glancing Angle - X-ray Diffraction (GA-XRD) and Scanning Electron Microscopy (SEM); and Jan Rossmeisl for the inspirational calculations and ideas. A special thank to Robert Jensen that helped me solving several problems and even more frustrations related to the sputter chamber. Thank you for trying to teach me vacuum science and for our trip to AJA international. I am very grateful to Brian P. Knudsen for setting up the Inductively Coupled Plasma Mass Spectrometry (ICP-MS) and for answering to my many and countless questions. I had the pleasure to work and share the office with Arnau Verdaguer-Casadevall, from whom I have learned so much. I am sorry for my interminable and endless monologues that you had to deal with every

day in the office. A special thank to Mathilde Raad Lilledal, who I have worked with at the beginning of my project and shared with so many frustrations; but most importantly thank you for your friendship.

Finally I would like to thank all my friends that made my period here in Denmark enjoyable and entartaining, especially Ana Sofia Varela, Tobias Johansson, Arnau Verdaguer-Casadeall, Brian Knudsen, Elisa Biasin, Falco Hüser, Ivano Castelli, Fabio Dionigi, Federico Masini, Marta Majkut, Simone Latini, Mauro Malizia, Anders Nierhoff and Jesper Hjølund Thrane. A special thank to my best friend Francesca, regardless the distance, you are always a true friend.

I am most grateful to Rasmus, who was an excellent colleague and even better boyfriend. Thank you for all the clever suggestions and discussions about oxygen evolution, thin films, sputtering, etc., thank you for proof reading my thesis and translating my abstract. But mostly, thank your for your patience, your support and your calming attitude. I would not have achieved as much, without your endless help.

Finally, I would like to thank my family, who supported me all the time even if I decided to move far away.

Kongens Lyngby, 28^{th} November 2014
Elisa Antares Paoli

Abstract

The focus of this Ph.D. thesis is on the electrocatalytic oxygen evolution reaction (OER) in acidic media for Proton Exchange Membrane (PEM) Electrolyser applications. This technology is an attractive alternative for storage of renewable energy, such as from solar and wind power, in small scale delocalised hydrogen refueling stations. The sluggish kinetics of OER and the high costs of the materials represent some of the biggest technological challenges for PEM electrolysers. The current technology relies on Pt group based materials and in particular ruthenium and iridium are the most active and stable OER catalysts. To contain costs and precious metals supply, the mass activity should be maximised. However, in order to define the properties of a catalyst, knowing the distinction between geometric and electronic effects is fundamental.

It is not trivial to determine the intrinsic catalytic activity on oxides and studies on well-defined surfaces are required. Notably, industrial applications demand maximised surface-to-bulk ratio, hence fabrication of catalysts in nanoparticulate form. In this perspective, this project aimed at investigating well-defined mass-selected ruthenium and ruthenium dioxide nanoparticles (NPs) in the technological relevant size range of $2-9$ nm. The objectives were to estimate the intrinsic catalytic activity of ruthenium and to identify any particle size effects. The results show that activity and stability are strongly influenced by the surface pre-treatment. Furthermore, these RuO_2 NPs exhibit over an order of magnitude improvement in activity and turnover frequency in comparison to the current state-of-the-art, and a tentative maximum at around $3-5$ nm.

Although high activity is essential for an efficient catalyst, stability should be also considered, in particular under the harsh acidic and oxidizing conditions of a PEM electrolyser. Standardised protocols for assessing the stability have not been established for the oxygen evolution reaction. Hence, this thesis focuses on providing guidelines for quantifying the corrosion rate of an OER catalyst. By coupling Electrochemical Quartz Crystal Microbalance (EQCM) measurements with Inductively Coupled Plasma - Mass Spectrometry (ICP-MS) analyses of

the electrolyte, we emphasize the importance of monitoring the mass loss.

Finally, the thesis focuses on improving the stability of ruthenium dioxide under OER conditions, by sub-monolayer addition of iridium oxide. The approach was inspired by theoretical calculations, which suggested that iridium would impede Ru corrosion by migrating to the undercoordinated sites at the surface, such as step and kink sites, which are the most prone to corrosion. Preliminary results show that an improvement of stability can be obtained, slightly decreasing the activity as well. Unfortunately, a drastic enhancement, as hoped, was not detected. Instead the results serve as a starting point from which the strategy and method for stability improvements can be further developed.

Dank Resumé

Forskningen i denne Ph.D afhandling omhandler den elektrokatalytiske reaktion ilt udvikling (OER) i syre, for Proton Exchange Membrane Electrolyser (PEMEC) systemer. Denne teknologi giver mulighed for at lagre bæredygtig energi, såsom fra sol og vindenergi, i små delokaliserede brintopfyldningsstationer. To af de største teknologiske udfordringer for PEMEC elektrolyse systemer er langsom kinetik for OER kombineret med brug af dyre materialer som katalysatorer for reaktionen. Den nuværende teknologi er baseret på ædle metaller og især ruthenium og iridium er de mest aktive og stabile katalysatorer for OER. For at holde udgifter og materialebrug nede bør aktiviteten normaliseret til masse derfor maksimeres. Samtidig, for at definere egenskaberne for en katalysator, er det essentielt at kunne kende forskel på geometriske og elektroniske effekter.

Det er ikke trivielt at bestemme den intrinsiske katalytiske aktivitet for oxider og studier af veldefinerede overflader er nødvendige. Det bør også noteres at for industrielle systemer skal overfladearealet per gram materiale maksimeres og fabrikation af katalysatorer som nanopartikler er derfor yderst relevant. Af denne grund har et fokus i projektet været at undersøge veldefinerede og massefiltrerede Ru og RuO_2 nanopartikler i det teknologiske relevante størrelsesregime $2 - 9$ nm. Målet har været at estimere den intrinsiske katalytiske aktivitet for ruthenium og identificere effekter af partikelstørrelse. Resultaterne viser at aktivitet og stabilitet er stærkt påvirkede af hvordan overfladen er behandlet før test. Endvidere viser disse RuO_2 nanopartikler en størrelsesorden højere aktivitet og "turnover frequency" sammenlignet med nuværende "state-of-the-art" materialer og et forsigtigt maksimum omkring $3 - 5$ nm er identificeret.

Selvom høj aktivitet er essentiel for en effektiv katalysator, bør stabilitet også tages i betragtning og især under de stærkt oxiderende og sure betingelser i en PEM elektrolysecelle. Standardiserede protokoller for vurdering af stabilitet er ikke veletableret for forskningen indenfor OER. Derfor er det et fokus for dette projekt at formulere retningslinjer for kvantificering af korrosion og stabilitet af OER katalysatorer. Ved at kombinere målinger på Electrochemi-

cal Quartz Crystal Microbalances (EQCM) med Inductively Coupled Plasma – Mass Spectrometry (ICP-MS) analyser af elektrolytten bliver det vist at det er yderst vigtigt at måle massetab direkte.

Endelig har der været fokus på at forbedre stabiliteten af RuO_2 under OER betingelser, ved at tilføje submonolag af IrO_2. Denne strategi er inspireret af kvantemekaniske beregninger på et modelsystem, der indikerer at iridium kan forhindre Ru korrosion ved at segregere til underkoordinerede overfladepositioner, såsom "steps" og "kinks", der er mest tilbøjelige til at korrodere. Foreløbige resultater viser at en forbedring kan opnås, med et lille fald i aktivitet. Desværre var forbedringen ikke så drastisk som forventet. Resultaterne er derfor primært brugbare som en basis fra hvilken strategien og metoden yderligere kan udvikles.

List of publications

Appended Publications

Paper I

Oxygen Evolution on Well-defined Mass-Selected Ru and RuO_2 Nanoparticles
Elisa A. Paoli, Federico Masini, Rasmus Frydendal, Davide Deiana, Christian Schlaup, Thomas W. Hansen, Sebastian Horch, Ifan E.L. Stephens, Ib Chorkendorff
Chemical Science, 2014, *DOI* : 10.1039/*C*4*SC*02685*C*

Paper II

Benchmarking the Stability of Oxygen Evolution Reaction Catalysts: The Importance of Monitoring Mass Losses
Rasmus Frydendal, Elisa A. Paoli, Brian P. Knudsen, Björn Wickman, Paolo Malacrida, Ifan E.L. Stephens, Ib Chorkendorff
ChemElectroChem, 2014, *DOI* : 10.1002/*celc*.201402262

Other publications

Paper III

Surface Stabilisation of a Manganese Oxide Catalyst for Oxygen Evolution in Acidic Media
Rasmus Frydendal, Elisa A. Paoli, Ifan E.L. Stephens, Ib Chorkendorff, Jan Rossmeisl
In preparation

Paper IV

Enhancing Activity for the Oxygen Evolution Reaction: the Beneficial Interaction of Au with Mn and Co Oxides
Rasmus Frydendal, Michael Busch, Niels Halck-Brendtsen, Elisa A. Paoli, Peter Krtil, Ib Chorkendorff, Jan Rossmeisl
ChemCatChem, 2014, *DOI* : 10.1002/*cctc*.201402756

Paper V

Enabling direct H_2O_2 production through rational electrocatalyst design
Samira Siahrostami, Arnau Verdaguer-Casadevall, Mohammadreza Karamad, Davide Deiana, Paolo Malacrida, Björn Wickman, Maria Escudero-Escribano, Elisa A. Paoli, Rasmus Frydendal, Thomas W. Hansen, Ib Chorkendorff, Ifan E.L. Stephens, Jan Rossmeisl
Nature Materials, **12**, 2013, 1137-1143

Contents

Chapter 1

Introduction

1.1 The Energy Challenge

The net growth in world population is at the moment estimated at 2.37 per second, considering birth and death rates [1]. The population has already passed 7 billions and is projected to grow much further, approaching 10 billions in the next decades [2]. Moreover, the number of people with access to modern living standards is increasing as well. Ludwig Boltzman stated "Available energy is the main object at stake in the struggle for existence and the evolution of the world" [3]. Population growth and high quality life demands have immense effects on our society. It defines our energy consumption, water usage, food consumption, pollution, CO_2 emission, health, etc. All these issues are interrelated, but they can be solved, by facing the most critical "struggle": the energy challenge [4–7]. With cheap energy, water can be cleaned, fertilizers can be produced and products can be transported around the world, far from the production site. Moreover, energy production has the biggest impact on CO_2 emission and pollution of the planet.

At the moment we completely rely on fossil fuels, which are the main energy source, accounting for the 87% of the total world consumption [8]. The availability of oil is very much under debate with a production peak estimated around now and 2040. However, it is undoubtedly true that oil is a finite resource, and extracting oil has became more and more difficult with higher energy and costs investments needed [9]. Even though natural gas and coal reserves will be usable for a longer time, the limited availability, uneven distribution on Earth [8] and environmental concerns [10] regarding the fossil fuels have lead to urgent calls

for replacements.

The global energy demand in 2014 is assessed around 17 terawatt [8] and its projection for 2050 is to reach 30 TW. Therefore, in order for any technology to substitute fossil fuels and have a large impact on the global energy scenario, it will need to be scaled to the terawatt-level [4, 7]. A new technology will have to assure low-cost, abundant and clean energy and finally provide energy independence.

The sun with its 120000 TW of electromagnetic radiation reaching the Earth every moment could sustain the global energy demand. Nathan Lewis calculated that by covering 0.16% of the total land area (around the size of United Kingdom) with a solar cell technology having 10% efficiency, the energy production would be 20 TW [11].

Recently, many countries have developed new policies to favor renewable energy, which account only for the 2% of the global primary energy. In particular, wind and solar power are considered as the attractive technologies. Denmark provides a very interesting case in this scenario. The country is known for being one of the most environmentally friendly in the world [12], with their wind mills and wind farms widely distributed on the country and offshore, people going around by bike, and high taxes for vehicles. In 2013 the percentage of primary energy coming from renewable energy was high compared to most countries, around 20% of the total primary energy [8]. Furthermore, the Danish government has recently set very ambitious goals for the coming years. In March 2012, a new Energy Agreement was approved with a wide consensus [13]. At the core of the energy policy is increasing the use of renewable energy sources, with a long-term goal of complete energy independence by 2050. All energy supply, including transport and industry, will have to come from renewable energy and fossil fuels will have to be phased out. A series of short-term milestones was also defined with the first achievement to be reached by 2020: a 40% reduction of green-house gas emission, 50% of the electricity from wind power and 35% of total energy consumption from renewable sources.

However, in the renewable energy scenario, sustained by wind and solar, a major drawback must be considered: renewable sources have a variable output. If we consider the wind power production and the energy demand in Denmark in January 2014, we obtain the situation depicted in Figure 1.1. In this plot the wind power variability over 14 days is illustrated. Notably, the wind power fluctuates over almost one order of magnitude difference, from less than 500 MW to more than 4000 MW. On the other hand, the energy demand varies between 3000 MW and $\sim$ 5500 MW every day. Interestingly, there are periods where the wind power is higher than the demand, e.g. days 3, 10 and 11. The Danish Energy Agreement envisages a much larger implementation of wind farms, so that wind power contribution to electricity could pass from the current 20% to 50%. Hence, by doubling the wind power production in the figure, for most days the energy production would overcome the demand. However, in some cases wind power would still not be enough, e.g. days 5, 6 and 9. Furthermore,

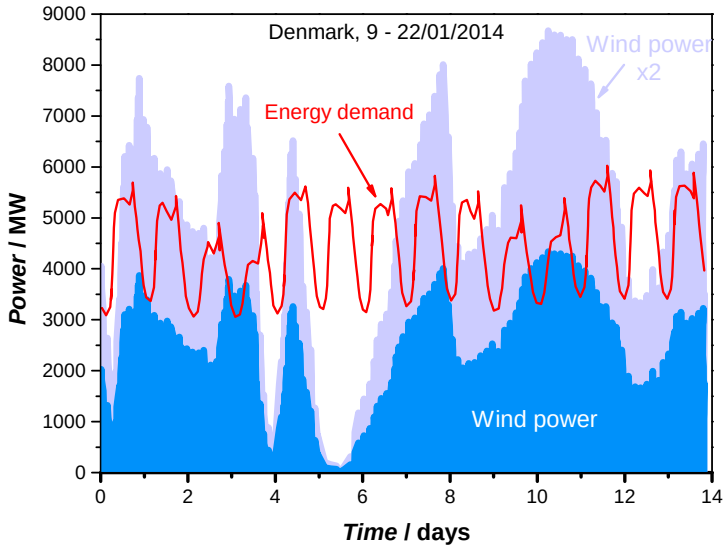

Figure 1.1: Wind variability (blue region) and electric energy demand (red line) in Denmark in two weeks in January 2014. By assuming to double the implementations of wind farms, the wind power would correspond to the light blue region. Graph adapted from EMD International [14].

the high variability imposes high stress in the electric grid for maintaining its stability.

It is clear that in order to expand the usage of renewable energy, it would be extremely advantageous to store the excess of energy [10]. Unfortunately, the current technology is not advanced enough for large quantity storage and are not competitive yet. Batteries are an attractive option, however their energy density is very poor in comparison to fossil fuels. Another and more promising process in this direction is the use of clean electricity to drive chemical reactions, hence storing the energy as chemicals [15].

Water electrolysis to produce hydrogen is a very attainable prospect. Electrolytic hydrogen possesses several advantages as energy carrier: it is simple, clean, it can be stored in gaseous and liquid form for long periods without degrading, and it can be generated locally using wind and solar power. It also provides high flexibility: it can be used to store energy, it can directly be fed into a fuel cell to generate power, it can be used in syngas or to upgrade biofuel [16]. Furthermore, water electrolysis can be employed to reduce CO_2 and produce synthetic hydrocarbon fuels, e.g. methane and methanol, which are more easily handled than hydrogen (methanol is liquid at room temperature) and could be integrated in the existing grids with lower technological barriers [16, 17].

From this point water electrolysis for storage of energy will be the focus of this thesis.

1.2 Electrolysers: Proton Exchange Membrane *vs.* Alkaline

Water electrolysis consists of splitting water into gaseous hydrogen and oxygen, passing electricity between two electrodes. The chemical reaction is

$$2H_2O \rightarrow 2H_2(g) + O_2(g) \tag{1.1}$$

and it is endothermic, hence, energy is required to drive it. The only reactant is water and the energy input, while the products are clean hydrogen and oxygen. The purity of these gases is very high, compared to other hydrogen production processes, i.e. burn of fossil fuels and steam reforming.

Water is not very conductive, hence electrolyte is required to sustain the passage of current between the cathode and the anode electrodes. There are two kinds of electrolysers, that are commercially available at present: proton exchange membrane (PEM) electrolysers and traditional alkaline electrolysers. The former works in acidic environment, while the latter in basic. An electrolyser consists of a series of electrochemical cells, with the primary components being the electrodes and the electrolyte. Schematics of an electrochemical cell for the two technologies are represented in figure 1.2.

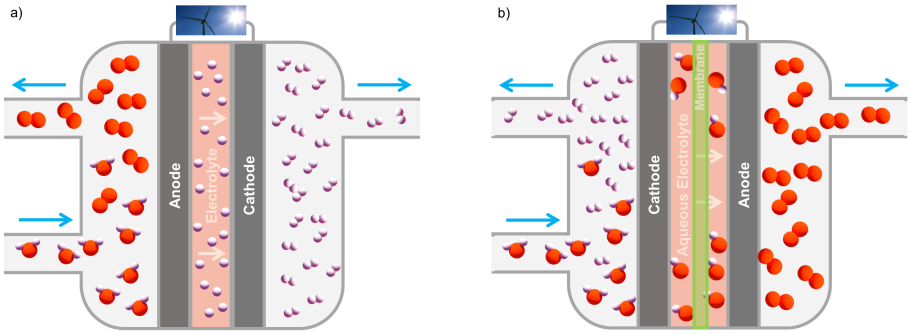

Figure 1.2: Sketches of an electrochemical cell in a) a PEM electrolyser and b) a traditional alkaline electrolyser.

In this field, it is worth mentioning the alkaline polymer electrolyte (APE) electrolysers, which use anion exchange membrane [18]. This technology is still at a research stage and several technological challenges must be overcome in order for APE electrolysers to compete with PEM electrolysers. In particular,

to achieve similar performances, the conductivity and the alkali stability of the anion exchange membranes will need to be significantly improved [18]. Although this kind of electolysers has the distinct advantage of allowing the usage of non precious metal catalysts, the required loading at the cathode is dramatically higher than the corresponding values in acid [19]. Finally, Solid Oxide (SO) Electrolysers represent another type, however their technology is at an early stage. The main parameters of the electrolyser technologies are summarised in table 1.1. APE electrolyser and SO electrolyser will not be described any further in this thesis [16].

Electrolyser	Electrolyte	Temp. (^oC)	Catalyst
Traditional electrolyser	KOH or NaOH	$50-100$	Ni-based
PEM electrolyser	Humidified polymer membrane	$20-100$	Pt/Ir
APE electrolyser	Alkaline polymer membrane for OH^- or Cl^-	$50-100$	Ni based
SO electrolyser	Ceramic	$500-1000$	Ni-cerment

Table 1.1: Comparison between different electrolyser technologies, adapted from [16] and [18].

The first commercial electrolysers were based on the traditional alkaline electrolyser technology and they now represent the most mature technology. Traditional alkaline electrolysers are reliable and robust, with a lifetime up to 15 years and with an efficiency that varies between $45-82\%$ [20]. They represent the current standard for large scale electrolysis. The electrolyte is either concentrated potassium hydroxide or concentrated sodium hydroxide, which means the environment is highly corrosive. The electrodes are typically nickel coated steel [21, 22].

On the other hand, the first electrolyser using a polymer membrane as electrolyte was commercialised in 1978. The main drawbacks of PEM electrolysers are short lifetime and high costs, mainly due to the price of the membrane (Nafion®) and the use of precious metals for the electrodes (Pt and Ir [23]). PEM electrolysers have distinct advantages compared to traditional alkaline electrolysers [16, 22, 24], which make them attractive, in particular for small-scale delocalised storage of renewable energy, e.g future hydrogen refueling stations [22]. First of all, PEM electrolysers can operate at higher current densities than traditional alkaline electrolysers, $1-2$ A/cm^2 compared to $0.3-0.5$ A/cm^2. Figure 1.3 shows the operating range for traditional alkaline electrolysers and PEM electrolysers, using commercially available references [24]. Secondly, the energy losses at the cathode of PEM electrolysers, where protons are used to produce hydrogen, are minimised and are very close to the thermodynamic value. Furthermore, high efficiency can be reached with tiny amounts of catalysts [25].

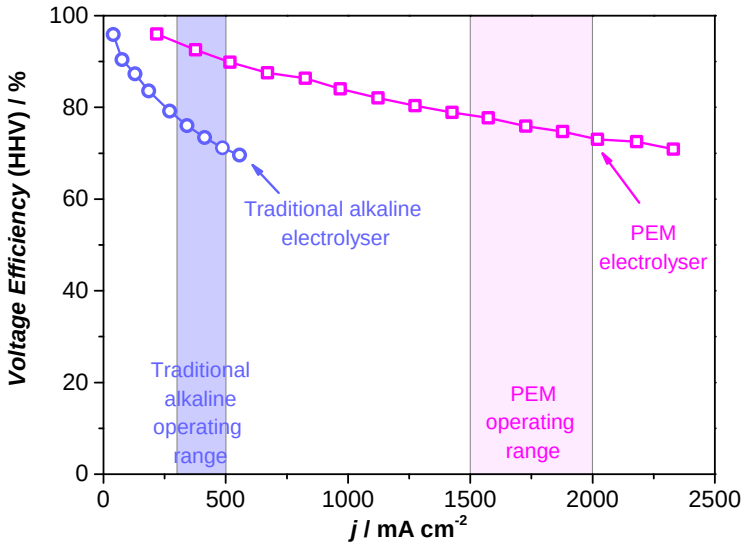

Figure 1.3: Voltage efficiency referred to the higher heating value (HHV) for PEM and traditional alkaline electrolysers. The operating range for both kind is highlighted and a reference for a real PEM electrolyser produced by Proton Energy System and for traditional alkaline electrolyser by QuantumSphere, Inc. are shown. Data adapted from [24].

Therefore, the majority of the energy losses are only due to the anode side. Another great advantage of PEM electrolysers is related to the membrane working both as electrolyte and as gas separator, which permits to feed only water to the elctrolyser. Moreover, it is solid, highly conductive, and allows for very fast response to power fluctuations. This means that PEM electrolysers can work under variable feeding regimes, which is of paramount importance when they are combined with an intermittent renewable source. It also allows very fast start up, in opposition to traditional electrolysers [16,24]. The produced hydrogen is extremely pure, which means it does not require further purification steps and it can be directly used for other applications, like being send to a fuel cell. Hydrogen produced by traditional alkaline elctrolyser is less pure [22,24]. PEM electrolysers can also operate under differential pressures, which means that hydrogen can be produced at higher pressure than oxygen, avoiding to work with highly pressurized oxygen. Conversely, traditional alkaline electrolyser requires balanced pressure operations and highly pressurised oxygen. Finally, PEM electrolysers can be potenitially be utilised as regenerative fuel cells: cells that can operate in electrolyser mode when energy needs to be stored and in fuel cell mode when electricity is required.

Despite all these benefits, significant advances are required in order to make PEM electrolysers cost competitive and to increase the efficiency. Minimising the energy losses at the electrodes, at the oxygen evolution reaction which exhibits sluggish kinetics, and improving their lifetime are among the most challenging technological issues. The only active catalysts with a sufficient stability belong to the noble metal group, e.g. platinum, iridium and ruthenium, which have scarce and inelastic production [7]. Recently, great performances have been achieved using platinum iridium nanostructured materials with unprecedented low precious metal loading of 0.30 $mg/cm^2_{Pt\ group}$ at the anode [26].

At the beginning of this chapter it was pointed out that, in order to have significant impact on the global energy demand, any technology will ultimately need to be scaled to the terawatt level. If we consider to distribute PEM electrolysers based on the current technology, [1] we estimate that half a year and 10 years of platinum and iridium annual production, respectively, would be required per terawatt of hydrogen storage capacity.[2] These estimations clearly show some of the limitations for the widespread market of electrolysers. However, if the noble metal loading would be decreased significantly, at least one order of magnitude [27], and the lifetime improved, PEM electrolysers could be eventually scaled up.

1.3 Thesis Outline

The main focus of this thesis is on PEM electrolyser technology and is related to one of its biggest technological challenge: the catalyst for the anode reaction. The goal is double: 1) investigating the intrinsic catalytic activity of the most active material, ruthenium oxide; 2) improving and quantifying its stability in acid environment.

The thesis is hence structured as follow.

In the next chapter (chapter 2) a general overview on water splitting and, in particular, the oxygen evolution reaction is illustrated. Theoretical background and main technological issues are examined.

In chapter 3, the experimental set-ups and analytical techniques employed throughout this thesis to prepare, characterise and test the catalysts are presented.

Chapter 4 is dedicated to ruthenium nanoparticles as catalysts for OER. Particular attention is given to mass-selected nanoparticles, in the attempt to

[1] 0.30 $mg/cm^2_{Pt\ group}$ of Pt-Ir nanostructured thin film at the anode [26] and 0.05 $mg/cm^2_{Pt\ group}$ of Pt at the cathode [25].

[2] Pt and Ir annual productions are $2 \cdot 10^8$ g and $9 \cdot 10^6$ g, respectively [7]. The power stored at the equilibrium potential at 80^oC (1.18 V) and for a 65% efficiency is 1.65 W/cm^2. The total precious metal per TW of hydrogen storage capacity is $2.1 \cdot 10^8$ g; from which the required Pt and Ir amounts are $1 \cdot 10^8$ g and $9 \cdot 10^7$ g, respectively. In turn, this gives half a year of Pt annual production and 10 years of Ir annual production.

evaluate the intrinsic catalytic activity of ruthenium oxide. As-deposited and thermally oxidised nanoparticles activity and stability are compared.

Chapter 5 provides guidelines for investigating the stability of an electrocatalysts, focusing on the importance of combining electrochemical analyses with mass monitoring techniques. In particular, Inductively Coupled Plasma - Mass Spectrometry together with Electrochemical Quartz Crystal Microbalance is used to investigate the stability of ruthenium dioxide thin film.

In chapter 6 a new strategy for improving the stability of an active but unstable oxygen evolution catalyst with a more stable material is offered. Ruthenium and iridium dioxide are used as a case study.

Chapter 7 is dedicated to general conclusions and outlook.

Papers and manuscripts written during this PhD project and relevant for the illustrated topic are attached at the end of this thesis, after the bibliography.

Chapter 2

Electrocatalysis and The Oxygen Evolution Reaction

"*Electrocatalysis*, i.e. the optimisation of electrode processes by a careful choice of electrode materials, is the ultimate goal of electrochemistry" (Sergio Trasatti) [28].

Indeed, in electrocatalysis one studies the effects of the electrode material properties on the mechanism and rate of an electrochemical reaction occurring at the electrode/ electrolyte interface. Cautious design of suitable materials is developed towards improving the efficiency of the total reaction by utilising active and selective catalysts with maximised lifetime, while reducing the system investment and operational costs. In industrial applications high surface area is typically required in order to maximise the mass activity and minimise the catalyst loading, hence the costs. However, in order to understand the activity/ structure relationship and judge the eligibility of a material, it is important to distinguish between electronic and surface area effects, which is often not-trivial. Therefore, fundamental research must begin from well-defined surfaces and then advance to porous nanostructures materials.

Several requirements must be kept in mind during the material development stage. High electrical conductivity is needed for minimising Ohmic losses. Gaseous hydrogen and oxygen are formed via water electrolysis, hence gas bubbles detachment must be favored in order to avoid blocking of active sites. This can be achieved either by improving the wettability of the material, or by designing nanostructures with optimised pore sizes. Finally, the electrode should be made of cheap and abundant materials, in addition to being safe and not

polluting.

In this chapter an overview of the electrocatalytic water splitting reaction is presented and particular attention is given to the main catalytic challenges [22, 29–31].

2.1 Water Electrolysis

The overall reaction for splitting of water, occuring at the three-phases interface liquid-solid-gas, is given by:

$$\mathrm{H_2O(l)} \longrightarrow \mathrm{H_2(g)} + \frac{1}{2}\mathrm{O_2(g)} \tag{2.1}$$

The reaction can be divided into two half reactions, each occurring at one electrode:
the hydrogen evolution reaction (HER) at the cathode

$$2\mathrm{H^+} + 2\mathrm{e^-} \longrightarrow \mathrm{H_2} \tag{2.2}$$

and the oxygen evolution reaction (OER) at the anode

$$\mathrm{H_2O} \longrightarrow \frac{1}{2}\mathrm{O_2} + 2\mathrm{H^+} + 2\mathrm{e^-} \tag{2.3}$$

2.1.1 Thermodynamics

The energy required to split 1 mole of water at standard conditions (298 K and 101 kPa) corresponds to the enthalpy of formation of 1 mole of liquid water, $\Delta H^o_{f,\mathrm{H_2O(l)}}$. For reaction 2.1, $\Delta H^o_{f,\mathrm{H_2O(l)}}$ is 286 kJ/mol and the change in standard Gibbs free energy, ΔG^o, is 237.2 kJ/mol, which indicates that to split water a considerable amount of energy is required.
The Gibbs free energy can be related to the potential, U, at equilibrium through the Nernst equation:

$$U^o = -\frac{\Delta G^o_f}{z\,F} + \frac{RT}{zF}\,ln\left(\frac{a_{H_2}\,a^{1/2}_{O_2}}{a_{H_2O}}\right) \tag{2.4}$$

where z is the number of electrons involved in the reaction (2), F is the Faraday constant, R is the gas constant, T is the temperature expressed in Kelvin, and a denotes the activity of the products and reactants. By assuming all the activities are equal to 1, the second term is zero, and the reversible cell voltage at standard conditions is found to be 1.23 V. However, the cell voltage, at which an electrolytic cell operates, is higher than 1.23 V, due to several energy losses.

Indeed, the cell voltage is given by

$$U_{\mathrm{cell}} = U^0 + \Delta U_\Omega + \eta_{\mathrm{HER}} + \eta_{\mathrm{OER}} \tag{2.5}$$

where η_{HER} and η_{OER} are the overpotential of the cathodic and anodic half-reactions, respectively. The overpotential denotes the extra voltage required to run the reaction. ΔU_{Ω} is the Ohmic drop, related to conduction issues of each component (electrode, membrane) and at the interaction between the components. The operating cell voltage, U_{cell}, for a real PEM electrolyser is illustrated in figure 2.1. The figure graphically shows the different contributions to the to-

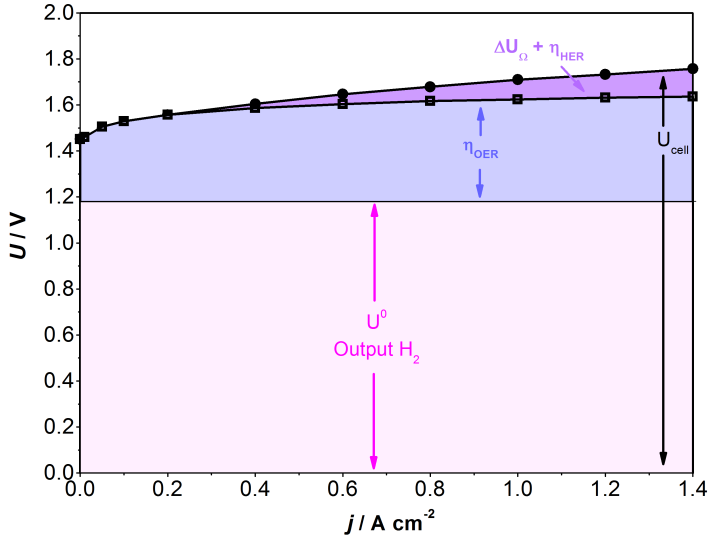

Figure 2.1: Cell voltage of a PEM elctrolyser. The actual energy stored as hydrogen is highlighted in pink, while the blue and violet regions indicate the energy losses. The main contribution to these losses is given by the sluggish kinetics at the anode (light blue area), while lower contribtution is given by the overpotential at the cathode and the Ohmic drop. η_{HER} is shown for completeness but it is almost zero. Figure adapted from [26].

tal potential. The energy stored as hydrogen (the pink region) represents the main component. However, high energy losses occur and the biggest contribution is given by the overpotentials for the oxygen evolution reaction, η_{OER} (light blue region), while Ohmic losses and η_{HER} contributes marginally (violet region). In particular, η_{HER} could be neglected, since in PEM electrolysers it almost approaches zero [25].

2.1.2 Ohmic Loss

As mentioned in the previous section, conductivity issues contribute to diminish the efficiency of the electrolytic cell, although as minor contribution.

Ohmic losses are mainly related to the design of the cell. However the electrode materials must be highly conductive in order to keep as low as possible further Ohmic losses. In a PEM electrolyser, conversely from alkaline electrolysers that requires highly concentrated electrolyte, thanks to the more compact design and to the high conductivity of the membrane, these losses account for less than 120 mV [26].

2.1.3 Hydrogen Evolution Reaction, HER

The Hydrogen Evolution Reaction, HER, is a two electron transfer process, i.e. one intermediate is involved. The general accepted mechanisms [32] in acid on metal surfaces involves a first common step, known as the Volmer reaction, where hydrogen is adsorbed on a free active site, $*$, [33]:

$$H^+ + * + e^- \longrightarrow H^* \tag{2.6}$$

The Volmer step can be followed either by the Tafel reaction [34], where two adsorbed hydrogen species react with the adsorbed H^* to form molecular hydrogen (reaction 2.7); or by the Heyrovsky reaction [35], where a proton and an electron react to molecular hydrogen (reaction 2.8).

$$2H^* \longrightarrow H_2 + 2* \qquad \text{(Tafel)} \tag{2.7}$$

$$H^* + H^+ + e^- \longrightarrow H_2 + * \qquad \text{(Heyrovsky)} \tag{2.8}$$

The equilibrium potential, $U^0_{H_2/H^+}$, for HER is 0 V. The kinetics for the hydrogen evolution reaction (HER) on platinum based electrodes in PEM electrolysers are so fast, that the overpotential is close to zero and almost negligible [25].

Although its simplicity, hydrogen evolution reaction is a widely studied reaction and the activity of several electrode materials have been reported. An overview of the best catalysts for HER in acid and in alkaline are shown in figure 2.2 and figure 2.3, respectively. Pt and Pt alloys catalysts exhibit the best performance with overpotentials very close to the thermodynamic limit. It is important to note that, even though non-noble metals can be used in alkaline, the kinetics in acid are much faster. Furthermore, in acid it is possible to achieve high performances in real electrolysers with very low loading [19]. Neyerlin *et al.* reported overpotenitals lower than < 3 mV for Pt electrodes with a loading of 0.05 mg_{Pt}/cm^2, in a membrane electrode assembly (MEA) cell [25]. Most strikingly, it exhibits an overpotential of 0.05 V at 1 A/cm^2.

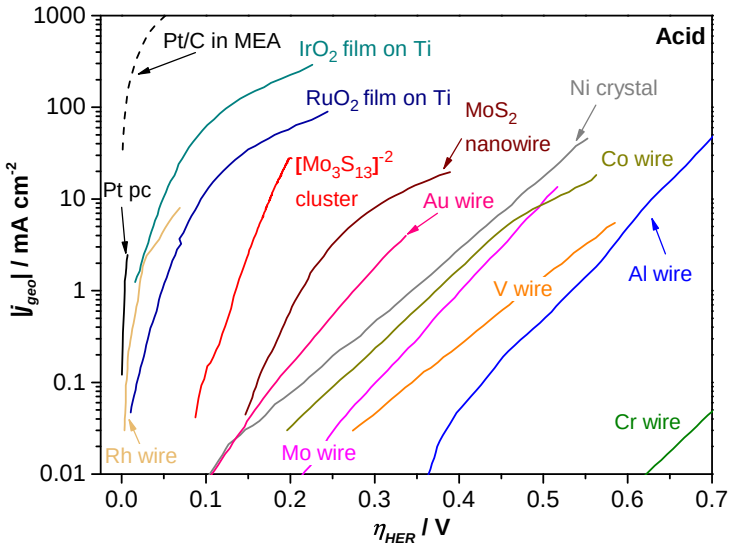

Figure 2.2: Overview of the state-of-the-art for HER in acid solution. Pt pc taken from [19]; Pt/C in MEA from [25]; IrO_2 and RuO_2 films on Ti from [36]; Rh wire, Mo wire and Au wire from [37]; $[Mo_3S_{13}]^{2-}$ clusters from [38]; MoS_2 nanowire from [39]; Ni crystal from [40]; Co wire, Cr wire and V wire from [41]; Al wire from [42].

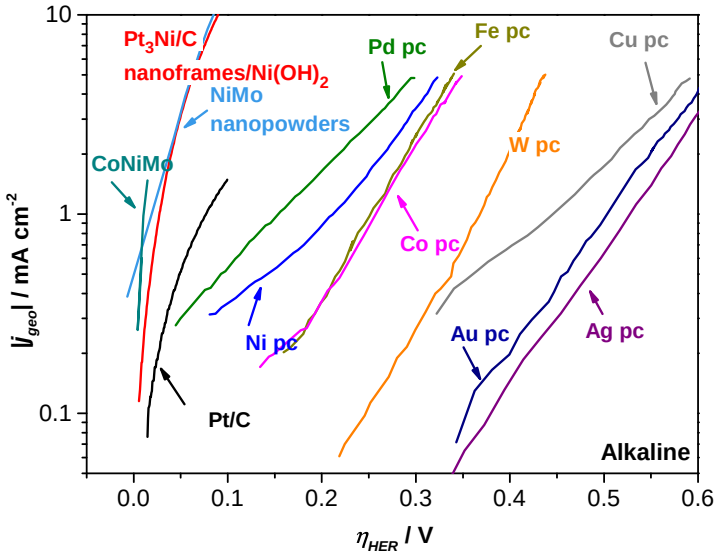

Figure 2.3: Overview of the state-of-the-art for HER in alkaline solution. Pd pc, Ni pc, Fe pc, Co pc, W pc, Au pc, Ag pc and Cu pc taken from [43]; Pt/C and Pt_3Ni/C nanoframes/ $Ni(OH)_2$ from [44]; NiMo nanopowders from [45]; CoNiMo from [46].

2.1.4 Oxygen Evolution Reaction, OER

Both in traditional alkaline and PEM electrolysers, the oxygen evolution reaction exhibits significant energy losses, due to its sluggish kinetics. Understanding the reaction mechanism and decreasing the overpotentials are one of the main focuses of fundamental research for water splitting.

The oxygen evolution reaction is a 4 electron transfer process. Rossmeisl, Nørskov and coworkers proposed the following mechanism, which is widely accepted in the literature. It considers 4 steps with three intermediates involved and a proton and electron transfer per step [31, 32, 47, 48].
The first step involves the dissociation of a water molecule:

$$H_2O + * \longrightarrow HO^* + H^+ + e^- \tag{2.9}$$

The adsorbed HO^* intermediate is then further oxidized:

$$HO^* \longrightarrow O^* + H^+ + e^- \tag{2.10}$$

And a third intermediate is formed when a second water molecule interacts with O^*:

$$O^* \longrightarrow HOO^* + H^+ + e^- \tag{2.11}$$

Finally, molecular gaseous oxygen is formed

$$HOO^* \longrightarrow O_2 + H^+ + e^- + * \tag{2.12}$$

The equilibrium potential for water oxidation, U_{H_2O/O_2}, is 1.23 V. However, the reaction only occurs at potential higher than the thermodynamic value. At these potentials all the metals are covered with a thin oxide layer, hence the catalysts considered for OER are usually oxides [49, 50].

Recent theoretical works in Nørskov and Rossmeisl groups have been devoted to correlate the overpotential of well known catalysts with the electrode material properties [48, 51]. Density functional theory (DFT) has been used to describe the thermochemistry of the reaction. Chemisorption Gibbs free energies for each intermediate has been calculated and related to the electrode potential. Free energy diagrams of OER on several metal and metal oxides were constructed. The free energy diagrams contains valuable information about the reaction: the potential determining step (PDS); and the theoretical minimum overpotential. PSD represents the step with the maximum change of chemisorption Gibbs free energy of two subsequent intermediates, not to be confused with the rate determining step (RDS), which, instead, represents the step with the highest kinetic barrier. In the diagrams the kinetic activation barriers are not considered, however they are likely to follow the ground state energies, via a Brønsted-Evans-Polanyi relation [52, 53].

The free energy diagram for RuO_2 (110) rutile oxide is shown in figure 2.4. At zero potential, all the steps are uphill in energy (ΔG) where the third step,

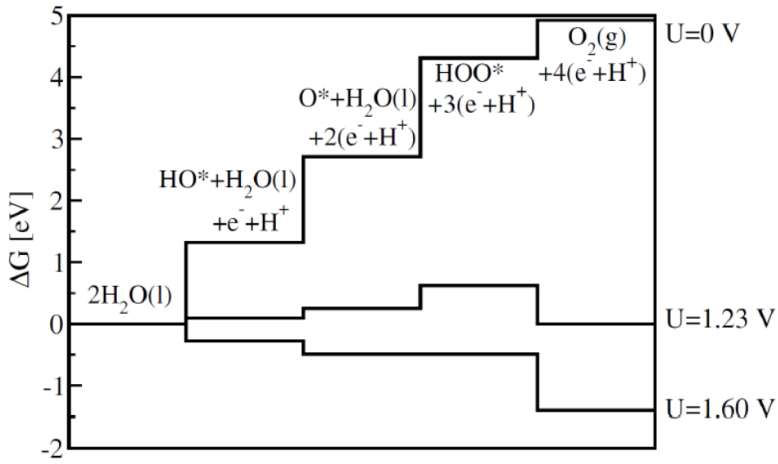

Figure 2.4: Free energy diagram of O* covered RuO_2 (110) at three different potentials (U = 0, 1.23 and 1.6 V). An extra voltage of 0.37 V is needed for all the steps to be downhill in energy. Plot taken from [48].

i.e. the formation of the superoxide HOO*, is the one with the highest energy change. When the potential is increased to the thermodynamic equilibrium potential, 1.23 V, only the last step is downhill and the reaction does not occur. Finally, if a sufficient potential (η = 0.37 V) is applied all the steps become downhill in energy and the oxygen evolution reaction takes place. Same study on IrO_2 (110) rutile oxide showed a slightly higher overpotential of 0.56 V, and the same potential determining step [48].

Although RuO_2 is the best catalysts for OER, the overpotential is still significant. In order to minimise the voltage drop, the ΔG associated with the formation of the superoxide intermediates should be reduced and ideally each step should possess an energy difference of 1.23 eV (since one electron and one proton are transferred per step) [32, 54]. Unfortunately, it is not possible to tune the energy difference of each intermediates separately, because they scale with each other. Indeed, a linear relationship has been found for the adsorption energies of the intermediates (figure 2.5) [48, 51, 54]. Koper and Man reported that the binding energies of HO* and O* are related to each other with a constant difference of 3.2 eV, which is independent from the surface, suggesting an universal scaling relationship between the intermediates. The constant is 0.74 eV higher than the desired 2.46 eV, which in turn gives an inherent minimum overpotential of 0.37 V. This represents a huge challenge for improving the performance of OER catalysts and indicates that it is not possible to minimise the overpotential beyond a certain limit. The same overpotential was found for

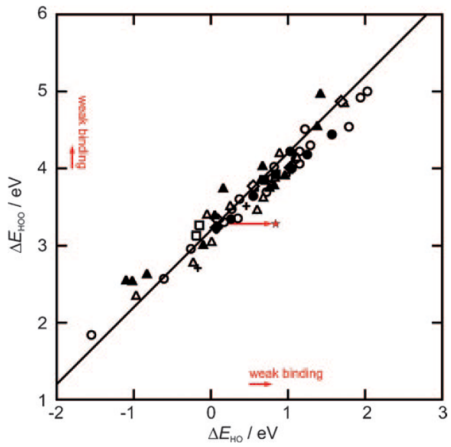

Figure 2.5: Scaling relations between the adsorption energy of HOO* and HO* for perovskites, spinels, anatase and rutile structures with different O* coverage (clean surface and high coverage). The red star denotes an ideal catalyst where the energy difference for all the steps is 1.23 eV. Plot taken from [54].

RuO_2 which explains its superior activity compared to other oxides.

Since the HOO* binding can be expressed as a function of O* and HO* binding energies, the difference in standard Gibbs free energy between O* and HO* can be used as descriptor for the reaction and a volcano shaped plot can be obtained (figure 2.6) [54]. Volcano plots are an elegant way to describe the activity towards a catalytic reaction and graphically represents the Sabatier principle, which defines the optimal interaction between catalyst and reaction intermediate: not too strong nor too weak [55]. The plot displays a volcano-shape with a maximum where the optimal conditions are fulfilled. In order to build such a graph, it is important to find a suitable descriptor for the reaction. Using the difference in binding energy for two intermediates allows to identify trends and better understand the reaction. If the difference $\Delta G^0_{O^*} - \Delta G^0_{HO^*}$ is high, right side of the volcano, the catalyst binds too weakly the intermediates and the reaction is limited by the oxidation of HO*. On the other hand, if the difference is low, left side of the volcano, the catalyst binds the intermediates too strongly and the reaction is limited by the formation of HOO*, i.e. breaking the bond at the surface. Rutile RuO_2 is at the top of the volcano, slightly shifted to the left side, suggesting, as expected, that the bindings to the intermediates is almost optimal, but a bit too strong. Rutile IrO_2 is also on the left side of the volcano but at higher overpotentials.

The theoretical volcano plot agrees well with old experimental results by Trasatti, where the experimental overpotentials of several oxides were correlated

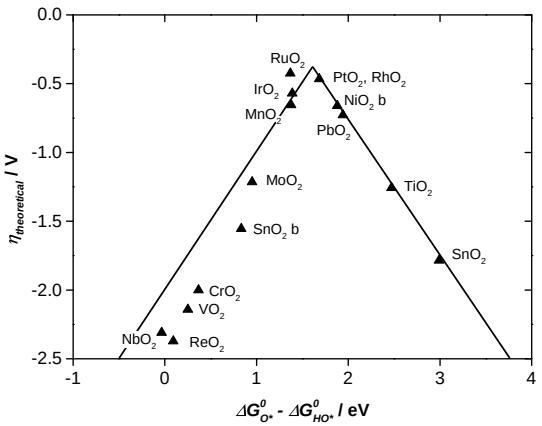

Figure 2.6: Volcano plot where theoretical overpotential are plotted versus the difference in standard free energy for HO* and O* for several rutile oxides. Adapted from [54].

to the enthalpy change of the transition from lower to higher oxide in the bulk [49]. These results are consistent with other experimental studies on metal surfaces [56–58]. The general trend was as follows: Ru> Ir> Pd> Rh> Pt> Au> Nb.

Both theory and experiments indicate ruthenium and iridium oxides as superior catalysts and, because of that and of their excellent conductivity as oxides, they have been the most investigated metals in the last decades. Ruthenium oxides have been studied by several groups in the attempt to identify the reasons behind its greater activity [49] and to relate them to the surface structure. Unfortunately, the surface morphology and crystal structure can vary tremendously with the preparation method and conditions, which in turn can affect the activity [58–65].

To better understand the correlation between activity and crystallographic texture, studies on well-defined surfaces as single crystals are desirable [66]. On the other hand, single crystals undergo significant changes because of surface reconstruction upon OER conditions, altering the well-defined structure and making their study very challenging. A few investigations are available [67,68], although the surface structure and composition have not been characterised with surface science tools. Recently, an interesting study on epitaxially grown single crystalline thin films was proposed by Shao-Horn and coworkers in alkaline media [68]. By comparing the activity of rutile RuO_2 (110) and (100), they observed an activity enhancement for the (100) surface, with one order of magnitude improvement compared to RuO_2 rutile nanoparticles, investigated by the same group [64]. The greater performance was attributed to higher atomic

density on the more accessible (100) facet, in comparison to the closer (110). The same behavior was observed for IrO_2, suggesting an orientation dependent trend in the OER activity. Nevertheless, since single crystals exhibited higher Tafel slopes than polycrystalline samples [50, 67], Katsounaros *et al.* suggested that the activity of polycrystalline samples cannot be solely considered as an average of each single crystal orientations [27, 66].

Another important effect on the activity of ruthenium oxide seems to arise from the oxidation procedure. Although oxide layers are always formed upon reaction conditions due to the anodic potentials, an oxidation pre-treatment has a dramatic influence on the activity [58, 62, 63, 65, 69]. Anodically grown oxides from metallic precursors exhibit much higher activity than thermally prepared oxides, but much lower stability [58, 65, 70, 71]. However, the reason for the loss in activity and improvement in stability is not yet understood. Recently, Danilovic *et al.* investigated in detail anodically grown and thermally oxidised sputtered thin films for several noble metals (Os, Ru, Ir, Pt, Au), suggesting that there is a fundamental link between activity and stability, which is controlled by the nobility of the metal and the defects surface density [58].

Although RuO_2 and IrO_2 are the best catalysts, both materials are expensive and scarce. They are by-products of Pt mining, which means that their production is governed by the platinum demand. Hence, strategies to decrease the amount of noble metals need to be addressed. The primary approach would be to maximise the surface-to-bulk ratio, by adopting catalysts in nanoparticulate forms. In this perspective, the effect of particle size on the oxygen evolution activity is a very interesting phenomenon. However, unlike the oxygen reduction reaction where several studies on well-defined and size-selected particles have been developed [72–74], similar systematic research is very limited for OER [27, 66]. A few studies on particle size dependency were carried out in the Krtil group on chemically prepared RuO_2 nanoparticles [75, 76]. By varying the calcination temperature, the size could be changed between 15 and 45 nm. Interestingly, the experimental results indicated that OER current density increases as the particle size decreases. Nevertheless, studies on well-defined size-selected particles are missing. Furthermore, it is of greater technological relevance to investigate particles with a diameter range smaller than 10 nm, where the surface area is maximised and the size effect enhanced [72, 77, 78].

Alternatively, the amount of precious metal can be reduced by combining it with a more abundant and less expensive metal. Recently, a family of dealloyed metal oxide hybrid core@shell nanoparticles has been proposed by Strasser and coworkers as a novel strategy for more efficient and cheaper oxygen evolution [79]. The concept is to design a core@shell architecture ($IrNi@IrO_x$) where the noble metal content is limited to a thin shell, whereas the core consists of an alloy of the precious metal and a non noble metal. A 3-fold and a 10-fold improvement in mass activity was observed, compared to rutile RuO_2 NPs and rutile IrO_2 NPs, respectively [64].

Similarly, studying a variety of alloy combination could help identifying new

improved catalysts. This approach has been used successfully with Pt for the oxygen reduction reaction [80]. Forgie *et al.* performed a systematic study on ruthenium based bimetallic nanoparticles. RuCo nanoparticles were found to be the best combination with an enhanced Ru mass activity [81]. Comparable results were obtained by Krtil and coworkers on $Ru_{0.8}Co_{0.2}O_x$ nanoparticles and, in a less pronounced fashion, on $Ru_{1-x}Ni_xO_{y-2}$ NPs [75, 76]. Based on these experimental findings [75, 76, 81–83], Rossmeisl and coworkers recently explained the improved activity with a different reaction path [84]. The incorporate heterovalent cation (Co, Ni) modifies the active sites architecture which is now considered in three dimensions. The proposed mechanism suggests that an oxygen atom next to Ni or Co can act as a proton donor/ acceptor, which in turn can diminish the step for HOO^* formation. This strategy allows to break the scaling realtions described previously. Indeed, DFT calculations based on this alternative path suggest lower theoretical overpotentials of 0.3 and 0.1 V for Ni and Co modified RuO_2, respectively. Although the dissolution of Ni and Co in acid solution must be verified, the approach could help in rational design of active sites, where the overpotential can be lowered beyond the scaling relation.

The best performing catalysts in acid and in alkaline are reviewed in the Tafel plots current density vs. overpotential plots, illustrated in figures 2.7 and 2.8.

In acid (figure 2.7) the choice for the catalyst is limited to Pt-group based materials, which are the only catalysts displaying acceptable stability under the harsh and oxidising conditions. Ruthenium based catalysts are the most active, but also unstable. The activities of ruthenium and iridium from a metallic precursor and as rutile oxides are displayed, showing that the anodically grown oxides are more active than the thermally grown. Furthermore, a comparison between bulk and nanoparticles catalysts for Ru, Ir and Pt suggests that the activity trend is mantained when the catalyst form is changed [85]. Bimetallic RuCo and RuIr NPs from the combinatorial study by Forgie *et al.* are also shown [81]; however the improved activity is not appreciable unless the precious metal mass activity is used for comparison. Finally, rutile RuO_2 and IrO_2 NPs present much lower activity than the other catalysts, which is partly due to the fact that an estimate of the real surface area (indicated by #) was used instead of the geometric area. Interestingly, the activity of an anode catalyst used in a PEM electrolyser at 80^oC is comparable to the catalysts tested in half-cell setups. Pt-Ir represents the state-of-the-art for PEM electrolysers and the catalyst illustrated in the plot is the one with the lowest loading reported so far (0.3 $mg/cm^2_{\text{Pt group}}$) [26].

In alkaline media (figure 2.7), on the other hand, the choice of the anode material is much wider and it extends to non noble metals. Indeed, Ni based catalysts represents the state-of-the-art for alkaline elctrolysers. Fe-Ni-Co mixed oxide, recently reported by Berlinguette and coworkers, seems to exhibit the best OER performances [90]. Notably, it has been found that the incorporation of iron on nickel significantly enhances the catalysis [88, 89]. Perovskites

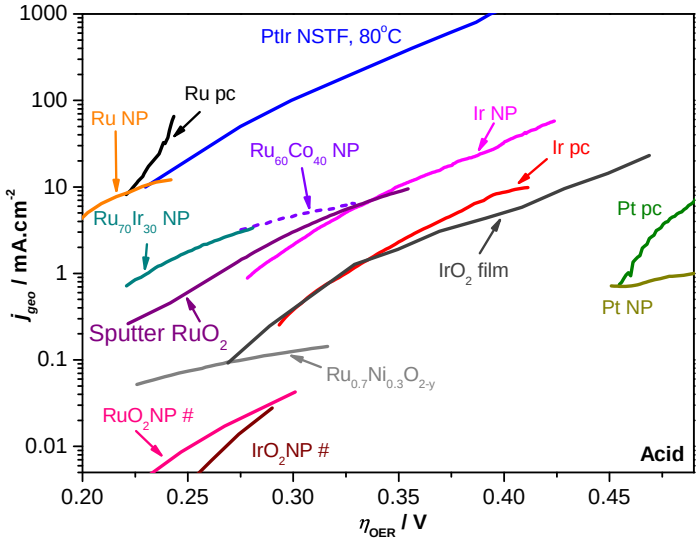

Figure 2.7: Overview of the state-of-the-art for the OER in acid. Ru pc, Ir pc, Pt pc, Ru nanoparticles (NP), Ir NP, Pt NP are taken from [85]; PtIr Nanostructured Thin Film (NSTF) from [26]; $Ru_{60}Co_{40}$ NP and $Ru_{70}Ir_{30}$ NP from [81]; IrO_2 film from [86]; sputter RuO_2 from [87]; $Ru_{0.7}Ni_{0.3}O_{2-y}$ from [76]; RuO_2 NP and IrO_2 NP from [64]. The # indicates that the catalyst was normalised with an estimation of the surface area and not the geometric area.

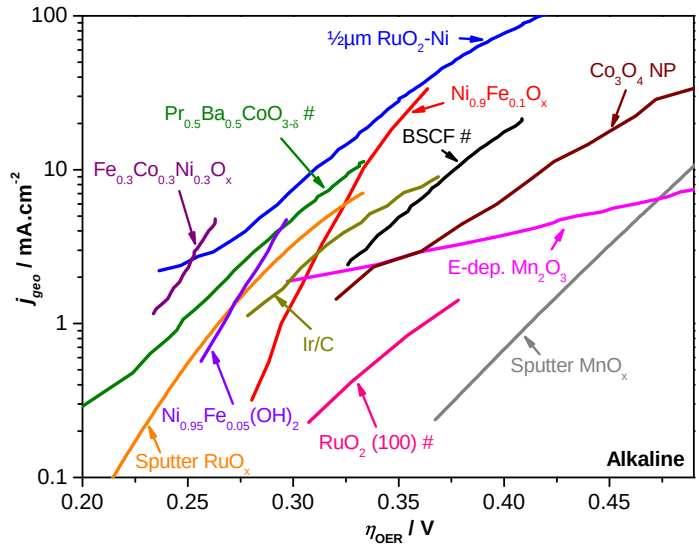

Figure 2.8: Overview of the state-of-the-art for the OER in alkaline. $Ni_{0.9}Fe_{0.1}O_x$ is taken from [88]; $Ni_{0.95}Fe_{0.05}(OH)_2$ from [89]; $Fe_{0.3}Co_{0.3}Ni_{0.3}O_x$ from [90]; $Ba_{0.5}Sr_{0.5}Co_{0.8}Fe_{0.2}O_{3-\delta}$ (BSCF) from [91]; $Pr_{0.5}Ba_{0.5}CoO_{3-\delta}$ from [92]; Ir/C and Electrodeposited Mn_2O_3 from [93]; Co_3O_4 NP from [94]; 1/2 μm RuO_2-Ni from [95]. The # indicates that the catalyst was normalised with an estimation of the surface area and not the geometric area.

and double perovskites prepared in Shao-Horn group are very interesting catalysts and they proved great OER activity, in particular the best reported are $Ba_{0.5}Sr_{0.5}Co_{0.8}Fe_{0.2}O_{3-\delta}$ (BSCF) and $Pr_{0.5}Ba_{0.5}CoO_{3-\delta}$ (an estimate of the surface area was used) [91, 92]. Manganese is often reported as a promising electrocatalyst, because of its use in nature by photosystem II [31]. It is not as active as the other catalysts, however it is very cheap and abundant and recent findings of enhanced activity with Au made it an attractive material [96, 97]. Finally, also in alkaline ruthenium and iridium exhibit great activity, although the current densities are not as high as in acid.

In these plots the geometric area is used to normalise the current. Only in few rare cases, denoted with the symbol #, an estimation of the surface area was employed. All the materials have been prepared with a variety of methods, and the roughness can differ tremendously with the preparation conditions. It is important to highlight the difficulties related to properly evaluate the catalytic activity and compare various materials. Differently from the Oxygen Reduction Reaction (the OER counterpart in a fuel cell), where widely accepted parameters are used to compare the catalytic performance, for OER no common protocol exists. For ORR, the current density at a specific potential (0.9 V vs. RHE) is used to compare the activity and the CO-stripping reaction is employed to evaluate the electrochemically active surface area (ECSA), which allows a good estimation of the surface area [98, 99]. In OER the most common parameters are either the geometric area normalised current at 10 mA/cm^2 [100], a relevant value for combining the electrocatalysts with a photoabsorber, or the current normalised with the precious metal mass at 1.48 V (vs. RHE) [64,81]. Recently, the mass activity at 10 A/g has been proposed as the activity parameter with the least inaccuracies [27]. For catalysts based on precious metals, the most relevant parameter is the mass activity. Indeed, in the case of expensive materials, the aim is to maximise the mass activity so to minise the required amount of precious metal. An overview of the state-of-the-art for OER in acid, expressed in mass activity is shown in figure 2.9. All the reported catalysts exhibit similar activity, with $Ru_{60}Co_{40}$ nanoparticles the most active one.

The mass activity is not an intrinsic parameter and does not allow a fair comparison among catalysts with different particle sizes or molecular mass. However, it possesses some advantages in comparison to other parameters. The geometric area does not take into consideration the loading of the catalysts, which is crucial when dealing with expensive and rare metals. Furthermore, evaluating precisely the surface area or the roughness by electrochemistry is extremely challenging, CO-stripping cannot be used with oxides because CO does not adsorb on the surface. Brunauer-Emmett-Teller analysis (BET) could be a valid alternative to electrochemical measurements, however, it can only be used with high surface area materials and the surface area does not necessarily coincide with the electrochemically active area. Finally, Turnover Frequency, TOF, could be an elegant way of expressing the intrinsic activity, however evaluating the number of active sites accurately is also not trivial.

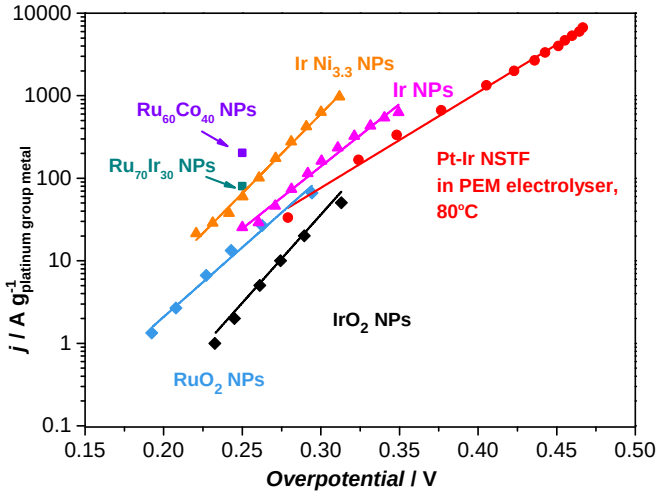

Figure 2.9: Overview of the state-of-the-art for the Oxygen Evolution Reaction in acidic solution, expressed as precious metal mass activity. Data taken from [81] for $Ru_{60}Co_{40}$ NPs and $Ru_{70}Ir_{40}$; [79] for Ir Nanoaprticles (NPs) and $IrNi_{3.3}$; from [26] for Pt-Ir NanoSctructured Thin Films (NSTF); and from [64] for RuO_2 and IrO_2 NPs.

In this scenario the call for OER benchmarks is stringent [64,66,68,100] and investigations on well-defined surfaces with a defined surface area could help elucidating the oxygen evolution reaction. Furthermore, improvements on the anode material, in particular for PEM electrolysers, e.g. lower precious metal loading and better stability, could remarkably ease the widespread implementation of electrolysers [27,101].

2.1.5 Stability

In industrial electrocatalysis the main concern is related to minimise the power consumption, while maximising the energy efficiency. In turn, high current densities and as low as possible potential are desired. To achieve that the potential drop, ΔU, must be minimised [22]. Besides Ohmic losses and overpotentials, another parameter is of paramount importance for industrial applications, that is the stability of the material under the oxidising and acidic conditions. In other words, it is important to follow the potential drift due to modification of the electrode over time, $\Delta U(t)$, induced by processes like electrode degradation or surface modifications [22,29]. We have established that ruthenium oxide has the lowest overpotential and highest activity for OER. However, industry prefers iridium, which is less active. The reason is convincingly shown in figure 2.10. A PEM electrolysis endurance test carried out at 1.8 A/cm^2 over 500 hours at

50°C highlights the instability of ruthenium dioxide under operating conditions: the cell potential drifts dramatically over time, passing from 2.0 V to almost 3.5 V. On the other hand, iridium dioxide exhibits good stability performance, maintaining the cell potential basically constant. In industrial markets compro-

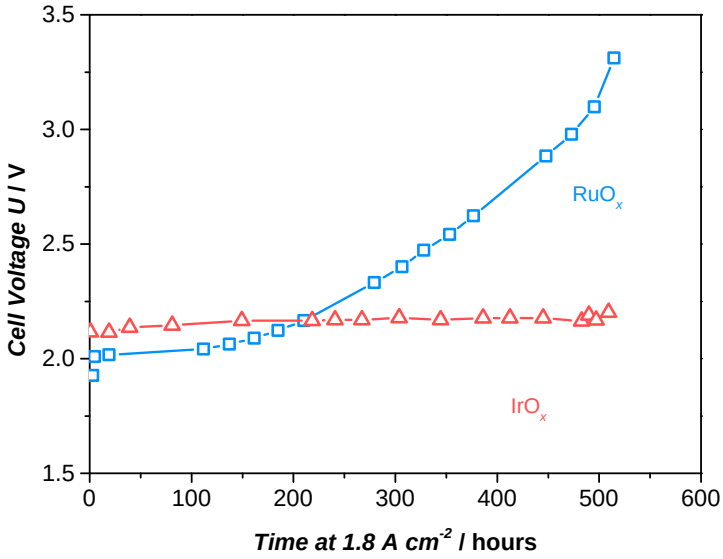

Figure 2.10: PEM electrolysis durability test for ruthenium and iridium oxides at 1.8 A/cm^2 and 50°C. Plot adapted from [102].

mises between different aspects, e.g. activity, stability and price, must be made and stability is often preferred over activity.

On the other hand, fundamental research focuses mainly on improving the catalysis, studying relationships between material structure and activity, whereas stability issues are often neglected or considered secondarily. However, in order to maximise the electrolysers durability, the degradation mechanisms, which the catalysts undergo, must be investigated; standardized protocols for short-and long-term tests must be developed; and strategies to improve the stability must be addressed.

2.1.5.1 Degradation Mechanisms

A reaction mechanism was proposed based on studies with various ruthenium catalysts, which suggested that at OER potentials ruthenium can be oxidised to the valence state (VIII), forming unstable ruthenate species which dissolve into the solution [70]. The formation of RuO_4 species was observed by in situ reflectance spectroscopy and rotating ring disk electrode measurements [103,

104]. Furthermore, the onset for the ruthenium corrosion was found to coincide with the onset for the oxygen evolution reaction, at around 1.4 V (vs. RHE), and to be consistent with the Pourbaix potential vs. pH diagram [105].

The dissolution rate is significantly affected by the type of oxide: anodically grown oxides are far more unstable than the corresponding thermally grown oxides [62, 63, 106, 107]. According to Trasatti, in anodically grown oxides the metal cation is surrounded by aqueous solvatants which are similar to the solution environment. On the other hand, in thermally grown oxides, in order for the metal to dissolve, he proposed that protons should penetrate into the lattice, which does not easily occur in highly conductive oxides as ruthenium and iridium [107]. The general rule about anodically grown oxides being more active but less stable proposed by Trasatti agrees closely with the recent systematic study carried out in Markovic and Stamenkovic group [58]. Anodically (EC-oxides) and thermally grown (TC-oxides) noble metal oxide sputtered films were investigated electrochemically and stability was evaluated with Inductively Coupled Plasma - Mass Spectrometry (ICP-MS) [58]. The activity and stability results for a series of EC- and TC- oxide are shown in figure 2.11 a), together with schematics of the structure, figure 2.11 b).

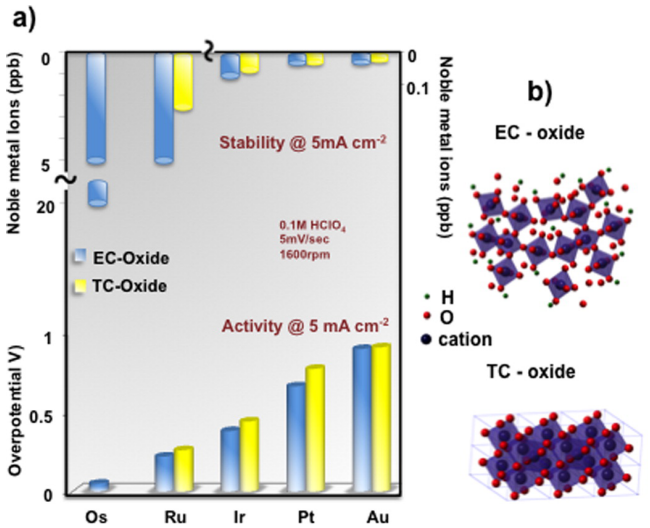

Figure 2.11: a) Stability and activity trend for a series of anodically grown (EC-Oxide) and thermally grown oxides (TC-oxides) based on precious metal. The activity at the bottom is expressed as overpotential at 5 mA/cm^2, evaluated using a rotating ring disk electrode set-up from the first cyclic voltammetry in N_2 saturated 0.1 $HClO_4$ at 5 mV/s and 1600 rpm. The stability is expressed as the concentration of metal (ppb) in solution, evaluated with ICP-MS. b) Schematic representation of the EC-oxides and TC-oxides. Figure taken from [58].

They proposed an explanation, based on differences in surface density of defects, which is considerably higher for anodically grown oxides, as shown by the more disordered EC-oxide structure in figure 2.11 b). This is in agreement with theoretical studies on metallic surfaces, that identify the defects sites as the most prone to corrosion [47,108,109]. The dissolution process can be defined as the removal of an atom from the surface and it is related to the energy change for making a new surface structure. If an atom is removed from a facet, e.g. in a (110) structure, a vacancy with a very high surface energy will be formed. However, when an atom is removed from an undercoordinated site, like a kink or a step, the new surface will be identical to the one before. This situtation is depicted in figure 2.12. Therefore, dissolution of undercoordinated sites is much more favorable than from a facet [108].

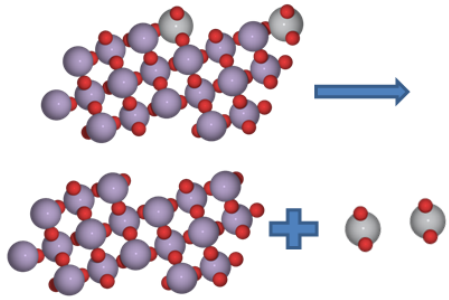

Figure 2.12: Side view of a stepped surface representing the dissolution of two undercoordinated sites, denoted in grey. Figure taken from [109].

Interestingly, Markovic and coworkers observed that for both TC-oxides and EC-oxides the trend in activity is opposite to the trend in stability. Based on these findings and on similar observations on single crystals in alkaline media [110], they suggested the existence of a functional link between activity and stability. This link is not only related to the coordination of surface atoms but also to the nobility of the metal and the ease in passing from a stable state (with valency IV) to an unstable one (> IV). Moreover, they emphasize the fact that this link is a predominant parameter and, due to continuous surface changes under OER, it is impossible to predict the reactivity based on the binding energies towards the intermediates. However, it is important to bear in mind that the activity trend shown in figure 2.11 a) is based on the total current and does not take into account the corrosion contribution. For instance, osmium is considered in the paper as the most active catalyst, with a significant lower overpotential, even better than ruthenium. On the other hand, it is extremely unstable and it exhibits a Faradaic efficiency of 5%. In other words, the majority of the current is due to corrosion and not to oxygen evolution, which makes estimating the overpotential for OER difficult. Should the overpotentials be based only on the

OER current, the activity trend suggested could be significantly different and osmium would likely not be the most active. Furthermore, the stability of the different catalysts is compared at the same current density (5 mA/cm^2), which means that it is evaluated at different potentials. It is, hence, challenging to define a trend in stability, especially in the case of ruthenium and gold, for which the corrosion is highly dependent on the applied potential [57]. Another aspect that makes the functional link controversial is the behaviour of gold, which exhibits poor activity but at the same time high stability. Although the use of ppb instead of corrosion rate make the comparison with literature difficult, these findings seem to be in contrast to the results obtained by Mayrhofer and coworkers [111]. In their comprehensive study on gold stability under potentiodynamic and potentiostatic operations using an on-line ICP-MS, they observed that gold is not active for OER, but it is also unstable. Finally, the annealing conditions which the TC-oxides undergo are not very well defined, making it challenging to replicate the results and compare them with other studies.

Iridium corrosion mechanism, as for ruthenium, has been investigated in the last decades. It seems to involve the formation of high valency species (> IV) [58, 112], whose surface formation was confirmed by ambient pressure XPS measurements on iridium oxide nanoparticles [113]. The higher onset potential for the process, around 2.0 V (vs. RHE), gives rise to the better stability of iridium [105].

Notably, Cherevko *et al.* reported that the degradation process for anodically grown oxides of ruthenium and iridium polycrystalline samples is enhanced by opposite operation conditions [57]. By on-line monitoring the mass loss via ICP-MS on several noble metals (Pt, Ru, Ir, Au, Rh, Pd), they elegantly investigated the dissolution under OER during transient and static experiments. Ruthenium and iridium corrosion rate under potentiostatic operation are shown in figure 2.13.

Ruthenium, similarly to gold, behaves differently from the other nobles metals and it is not affected by potential cycling rather by a "steady-state dissolution", with a maximum dissolution rate above 1.3 V (vs. RHE), in agreement with the Pourbaix diagram [105]. On the other hand, most of the noble metals corrode under transient conditions, favored by formation and reduction of a passivation layer. In particular, it is important to emphasize that iridium do corrode under OER conditions, although the corrosion rate is more than an order of magnitude lower than ruthenium.

Furthermore, by comparing the corrosion rates with the Tafel slopes of the noble metals, they observed the linear trend shown in figure 2.14. Interestingly, ruthenium and gold, which are the most unstable metals, possess the lowest Tafel slopes, whereas Pd and Pt, the most stable ones, exhibit the highest slopes. Iridium and rhodium showed intermediates performances. Based on these results and on previous studies with isotope labelling and differential electrochemical mass spectrometry (DEMS), two dissimilar reaction paths have been suggested: a "solution route" for metals with high Tafel slopes (Pt and Pd) and an "oxide

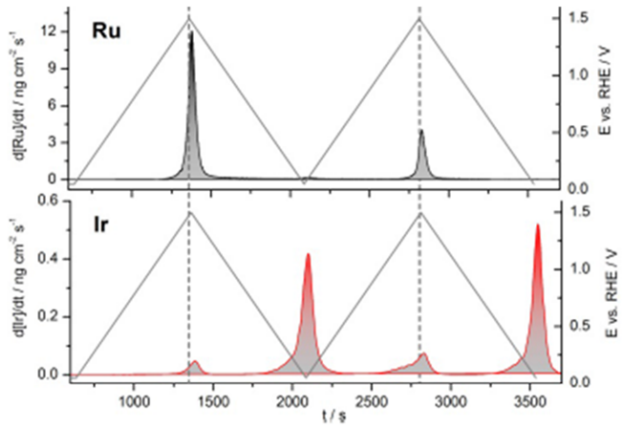

Figure 2.13: Dissolution concentration of ruthenium and iridium polycrystalline metals during two consecutive cyclic voltammograms between 0.05 and 1.5 V (vs. RHE) in 0.5 M H_2SO_4 at 2 mV/s. Figure taken from [57].

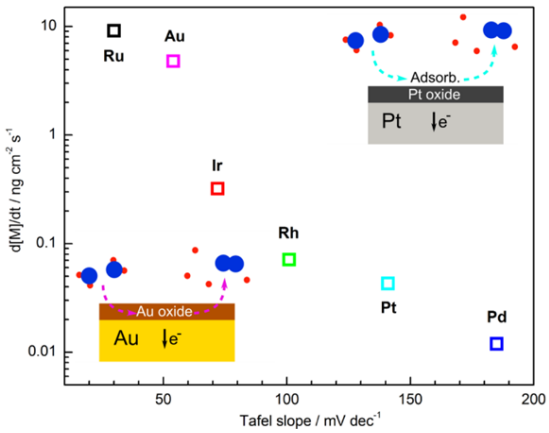

Figure 2.14: Dissolution rate at 5 mA/cm^2 compared with the Tafel slope, evaluated from the Ohmic corrected current-potential curve. Inserted schematics of the proposed "solution route" (right top) and "oxide route" (left bottom) paths. Figure taken from [57].

route" for low Tafel slopes (Ru and Au). In the former pathway oxygen is evolved from the electrolyte, from water interaction with the electrode [114]; in the latter, the oxygen is partially or fully evolved from the oxide formed on the catalyst, favoring its corrosion [115,116]. Finally, on iridium it seems that both

paths take place [117].

Moreover, ruthenium and iridium in nanoparticulate form in the particle size range of $2-6$ nm with anodically grown surface oxide exhibit higher instability in relation to extended surfaces with the same pre-treatment [85]. Reier *et al.* compared the activity and stability of bulk surfaces of Ru, Ir, and Pt, with commercial carbon supported nanoaprticles. The cyclic voltammetry of ruthenium nanoparticles showed a peak at high potentials indicating the complete dissolution of the particles into the electrolyte after the first cycle, which was confirmed by ICP-OES [85].

2.1.5.2 Strategies for Stabilising RuO_x

The strategy of combining different materials has often been adopted in the attempt of obtaining synergetic effects or transferring advantageous properties from a material to another [118].

In the 50s Beer discovered transition metal oxides exhibiting favorable electrocatalytic properties and exceptional stability, the so called dimensionally stable anodes, DSA® [119]. DSA® consists of thermally decomposed oxides from suitable precursor of an inert metal, such as titanium or tantalum, mixed with an activated transition metal, mainly IrO_x and RuO_x, and deposited on an inert substrate, typically titanium. Their success is mainly due to the extraordinary conductivity, similar to metals, and to their versatility, which allowed their widespread use as anodes from the chloro-alkali industry to several other electrochemical processes, e.g water splitting and electrowinning [28]. The chemical and electrochemical stability is definitely improved compared to the corresponding metal, however, the main advantage is given by titanium, which easily form an inert oxide mechanically blocking further corrosion [119]. It is worth emphasizing that outstanding performances were achieved in the chloro-alkali industry. The process could operate at overpotentials near the thermodynamic equilibrium, which are lower for the simple chlorine evolution reaction compared to the more complex oxygen evolution reaction [28].

After the DSA® success, several combinations of inert metals and activated metal oxides have been tested in order to find the optimal catalyst composition [27]. In particular, ruthenium-iridium mixed oxides have been investigated for decades with the aim of improving ruthenium oxide durability, while maintaining its activity [112,118,120–126]. Indeed, it was found that small additions of iridium in sputtered $Ru_xIr_{1-x}O_2$ films induce drastic and promising improvements in stability, paid for with an increase in onset for OER and in Tafel slopes [118]. After this finding several preparation methods have been tested in order to modify texture, morphology, and composition: sputter deposition, hydrothermal decomposition, Adam's fusion and many other variants. It was found that depending on the method and the reacting parameters, the Ru-Ir oxides mixtures exhibit different activity and, in particular, a different extent of surface enrichment of iridium and homogeneity of the phases [58,120,121,124,125]. For

instance, sputtered deposited film exhibited much lower iridium surface enrichment than mixed oxides prepared by chemical synthesis [120, 121]. Moreover, by chemical synthesis depending on the precursor either atomic mixing or segregation can be favored, which in turn can drastically affect the performance of the catalysts [124].

Although the several investigations, it is difficult to quantify precisely the stability improvement of Ru-Ir mixed oxides, since most studies focused on the activity, without evaluating the durability. When the stability is reported, either it is based on short-term electrochemical tests or the method is not well defined. Furthermore, the nature of the stabilising effect is still not understood and different theories are reported. Some proposed it is due to electronic effects [118], while others explain it with the surface enrichment of the more stable component, iridium oxide [122, 124].

In the attempt to explain the stabilising effect of iridium, theoretical calculations by Density Functional Theory (DFT) were performed by Isabela Man in Rossmeisl group and the results are reported in her PhD thesis [47]. She performed calculations on Ru-Ir mixed oxides, where she focused on the segregation and migration energies of the two components at the surface. DFT calculations were performed on a flat rutile (110) surface, which is illustrated in figure 2.15. Two adsorption sites can be distinguished: the Coordinately Unsaturated Sites, cus, and the bridge sites.

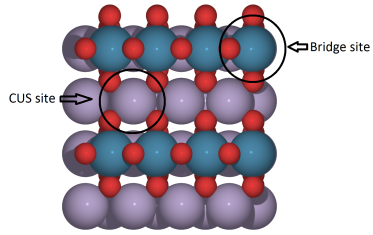

Figure 2.15: Top view of a rutile (110) surface, indicating the cus and bridge sites. Figure taken from [109].

Computations on a flat surface showed that no matter where the iridium oxide is initially placed, it tends to segregate to the surface and at the surface to migrate to the cus sites. On the contrary, RuO_2 prefers to move into the bulk. In turn, this may explain the surface enrichment of iridium experimentally observed [118, 120, 122, 124].

By performing the same calculations on a surface with kink sites, it was found that when Ir is placed on a cus site in the terrace, either it directly diffuse to the the undercoordinated bridge site, or it moves to the undercoordinated cus first and to the undercoordinated bridge afterwards. The strong migration of iridium to the kink sites can also be explained with oxygen affinity. A cus site

in the flat surface has one undercoordinated oxygen, while the kink sites have two. Since iridium has a stronger affinity towards oxygen, it prefers to move to the undercoordinated kink sites.

Subsequently, the dissolution potential of surface modified ruthenium oxide (host material), where iridium behaves like a guest material, was considered. A change in dissolution potential, dependent on the position of Ru and Ir atoms at the surface, was estimated. The standard dissolution potentials, U_{diss}, for ruthenium and iridium oxides were used as references.
Iridium oxide corrosion was described as

$$IrO_2 + 2H_2O \rightleftharpoons IrO_4^{2-} + 4H^+ + 2e^- \tag{2.13}$$

with a standard dissolution potential of 2.06 V [105].
Ruthenium oxide corrosion was instead:

$$RuO_2 + 3H_2O \rightleftharpoons H_2RuO_4 + 4H^+ + 4e^- \tag{2.14}$$

with a standard dissolution potential of 1.38 V [105]. The initial structure was considered with Ir and Ru at the terrace and at the kink site, respectively. In this configuration the dissolution potential is even lower than the standard U_{diss} for RuO_2. However, as described above, Ir prefers to migrate to the kink site. In this configuration, where Ir terminates the ruthenium oxide surface, the dissolution potential is higher, resulting in a more stable structure.

Finally, by evaluating the binding energies towards the intermediates of Ru at different Ir concentration and position in the unit cell, it was found that the energies do not change in a significant fashion. This suggests that the neighbor presence of iridium does not affect the electronic properties of ruthenium and viceversa. Therefore, DFT calculations seem to suggest that the nature of the stabilising effect of iridium oxide in ruthenium-iridium mixed oxides and DSA® is not due to electronic or synergetic effects. Man proposed that it is rather due to the termination of undercoordinated sites (kink, steps) with a more stable material.

A similar conclusion was recently proposed by Danilovic *et al.* [122], although on surfaces with a higher concentration of iridium oxide. Using a surface segregation process they designed a stable Ru-Ir alloy. They found that the best trade-off between stability and activity in the bulk composition is given by $Ru_{0.5}Ir_{0.5}$ which exhibited a 4-fold stability improvements compared to conventional Ru-Ir oxide, while maintaining the same activity [118]. The stabilisation effect was explained as a surface Ir skeleton that protects the underlaying less noble ruthenium atoms. Furthermore, more significant stability improvement were achieved for more ordered structure with lower defects surface density, in accordance with the functional link between activity and stability previously reported by the same authors [58].

Although this explanation seems to agree with Man's calcualtions [47], the preparation of bulk ruthenium iridium oxide does not allow a precise control of

the surface composition due to the surface enrichment of iridium. Indeed the bulk composition of Ru-Ir oxide reported by Danilovic *et al.* was different from the surface composition [122]. In some cases, the range in surface composition is limited and cannot be easily tuned, as reported by Sunde and coworkers [124]. On the other hand, by investigating sub-monolayer additions of iridium oxide on a ruthenium dioxide surface, the surface composition can be tuned and termination concept proposed by Man could be elucidated experimentally.

Other binary and ternary combinations of metals exhibited attractive improvements as well. The beneficial effect of titanium both as substrate and mixed in the outer layer with ruthenium oxides was shown by Jovanovic *et al.* [127]. Interestingly, also the addition of tantalum to ruthenium and to ruthenium iridium oxide significantly blocked the potential drift over time [128]. The opposite effect was obtained with tin, whose addition improved the OER activity while decreasing the stability [129–132].

2.1.5.3 Techniques for Evaluating the Catalyst Stability

Although the catalyst stability has lately gained some attention [57,58,100,110, 111,115,122], standardized procedures for assessing the short- and long- term durability and for simulating real operating conditions are rather missing. So far, the most common methods for determining the stability have been based on chronoamperometry (at constant potential) and chronopotentiometry (at constant current density) measurements for several hours. However, in order to establish the catalyst lifetime, long-term tests of several thousands hours would be needed. Furthermore, it is not entirely clear if potentiostatic analyses can give definite insights for practical uses.

A variety of in situ and ex situ techniques are available for monitoring changes in activity and in physical and chemical states [133]. Among in situ techniques, electrochemical techniques are the most employed [100]. A very simple method with a good time resolution is the use of a ring electrode together with the main electrode to follow a second reaction, involving the species produced during OER [58,104]. However, more valuable information can be obtained by coupling electrochemical measurements with other techniques: electrochemical quartz crystal microbalance (EQCM) allows to follow mass changes at the electrode and to estimate the corrosion rate [134]; electrochemical scanning tunneling microscopy (EC-STM) can image the surface and structure of the catalyst under reaction conditions [135,136]. Furthermore, by using scanning flow cell in combination with Inductively Coupled Plasma Mass Spectrometer (ICP-MS), on-line elemental analysis can be performed [57,111]. Alternatively, the evolved gas can be monitored with a mass spectrometer (DEMS) and by isotope labelling insights into the degradation mechanism can be revealed [114–116]. Latest advances in spectroscopic techniques, in particular for Raman, Fourier Transform IR spectroscopy and ambient pressure XPS, allow their use for in situ monitoring of the reaction products [137,138] and of changes at the elec-

trode surface [113, 139]. Among ex situ techniques, the most widely used are microscopic techniques, e.g. High Resolution Transmission Electron Microscopy (HR-TEM) and Scanning Electron Microscopy (SEM), which can detect the effects of degradation processes up to the atomic level (TEM) [140]. Notably, SEM and TEM can be adopted using the identical location techniques, IL-TEM and IL-SEM, which allow for acquiring images before and after a stability test of the same location [141].
Contrary to ORR, where standardized protocols, i.e. advanced stability tests AST [142], have been optimised, common procedures to define the stability of OER catalysts have not been established yet.

2.2 Conclusion

In summary, efficient water splitting is severely limited by the sluggish kinetics of the oxygen evolution reaction catalysis. The harsh oxidising conditions and the acidic pH set stringent requirements on the choice of the OER electrode, which is restricted to the Pt group metal oxides for PEM-EC. Through theoretical and experimental trends, RuO_2 was found to be the most active catalyst for the reaction. However, defining accurately the intrinsic catalytic activity of oxides is extremely challenging and the need of more systematic studies on well-defined catalysts is addressed. Furthermore, under operating conditions RuO_2 is not stable enough for industrial applications, which requires a lifetime of several years, and advances in this direction must be developed. Interestingly, for the oxygen evolution reaction, in contrast to other electrocatalytic processes, no standardised protocols have been established and the stability has often been overlooked.

An investigation of the intrinsic activity of well-defined ruthenium oxide catalysts, together with guidelines for monitoring the catalyst corrosion under OER and a strategy to improve the durability of ruthenium, is addressed in the following chapters.

Chapter 3

Experimental Methods

The aim of this chapter is to illustrate the several techniques that have been used during this project to prepare, characterise and test the activity and stability of the catalysts.

3.1 Sample Preparation

3.1.1 Mass-Selected Nanoparticles

Mass-selected ruthenium nanoparticles were prepared by Federico Masini, using an UHV compatible system (Cluster Source), which is connected to two other independent UHV chambers through gate valves (Preparation Chamber and Analysis Chamber).

A photograph of the equipment and its schematic are shown in figure 3.1.

3.1.1.1 Preparation Chamber

The preparation chamber is used to prepare and clean the sample. A loadlock facilitates the loading of samples. There is the possibility of degassing, sputter cleaning and heating the sample. Furthermore, the deposition of the nanoparticles is carried out in this chamber. A Quartz Crystal Microbalance (QCM) for measuring the deposition rate is also located in this chamber.

Prior to any deposition, the substrate was heated up to 550 K for 8 hours, in order to eliminate any water residue.

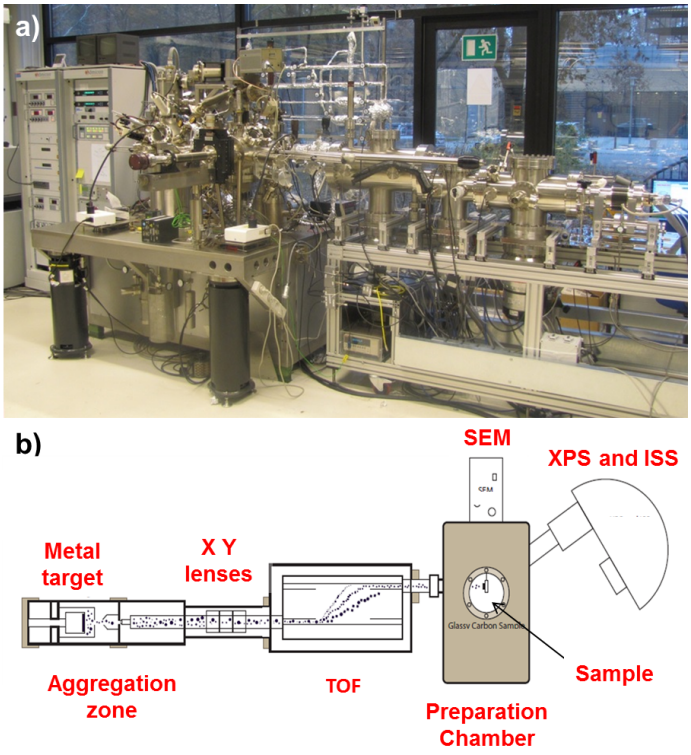

Figure 3.1: a) Picture and b) schematic of the cluster source set-up.

3.1.1.2 Cluster Source

The cluster source was purchased by Birmingham Instruments. The nanoparticles are formed in a magnetron sputter gas aggregation source, which is combined with a mass filter. The base pressure is in the order of 10^{-10} mbar. The process was first described by Haberland in 1992 [143].

Metallic atoms, in this case ruthenium, are sputtered away by argon bombardment, forming a dense vapor in front of the sputter head. The working pressure at which the sputtering occurs ($0.1 - 1$ mbar) is much higher than traditional sputter deposition methods, which works at pressures $1 - 2$ order of magnitude lower. The sputter head, consisting of a ruthenium target and a magnetron chimney, is located in a compartment that is cooled down with liquid nitrogen (aggregation or condensation zone). Cooled argon and helium atoms can facilitate the condensation of the metallic atoms thorugh collision. Dimers start to form and start to agglomerate into clusters. The cluster growth can occur through two processes: a) ad-atom or b) cluster-cluster growth [144].

The prevalence of one process over the other can affect the shape and morphology of the nanoparticles and it can be tuned by changing the metal vapor pressure or the noble gas pressure. Another critical parameter is the residence time: the longer the time the bigger the particles. Therefore, the particles need to be sweeped away by the noble gas from the condensation area and directed through a conical skimmer. After this point, the pressure decreases drastically due to heavy differential pumping and the cluster do not grow further. Since the particles collides with ionized Ar, $30-80\%$ of them are charged [143], which allow a separation based on their mass-to-charge ratio, m/z.

Very detailed investigation on how different factors affect the morphology and the mass distribution of ruthenium nanoparticles has been carried out in our group and optimal conditions for this material have been identified. [145–148]

Time-of-Flight Mass Filter

The Lateral Time-of-Flight (TOF) filter is used to separate the particles depending on their mass-to-charge ratio, m/z. It is based on high voltage pulses, which induce a lateral displacement of the particles beam. This system has very important advantages, in comparison to other mass selection techniques, e.g. magnetic sector mass selector and quadrupole mass selector:

- The ability to select mass over a broad range (from few amu, 30 amu, to 10^{17} amu);
- Reasonable mass resolution over the broad mass range;
- High transmission of the beam and therefore limited waste of the desired material.

Figure 3.2a) shows a scheme of the set-up inside indicating the path which the nanoparticles follow. As explained by Von Issendorff and Palmer in [149], the ion beam is focused and directed into the filter at the left bottom. Here a voltage pulse displaces the beam upwards perpendicularly from its original direction (acceleration pulse). All ions gain the same momentum, so the ones with same mass travel with the same velocity. After a certain delay time, τ_D, another voltage pulse, identical to the acceleration pulse, deflects the beam (deceleration pulse), which moves with its original direction towards the upper right corner of the filter and pass through an exit aperture.

The time between the two pulses determines the mass that passes through the selector. Since ions of the same mass gain and lose the same upward velocity, their relative velocity is not altered and the convergence/divergence of the beam is conserved. A focused beam is essential in order to obtain reasonable mass resolution, since the exit slith cuts out certain masses from the lateral distribution. Indeed, the mass resolution is given by:

$$R = \frac{m}{\Delta m} = \frac{x}{\Delta x} \tag{3.1}$$

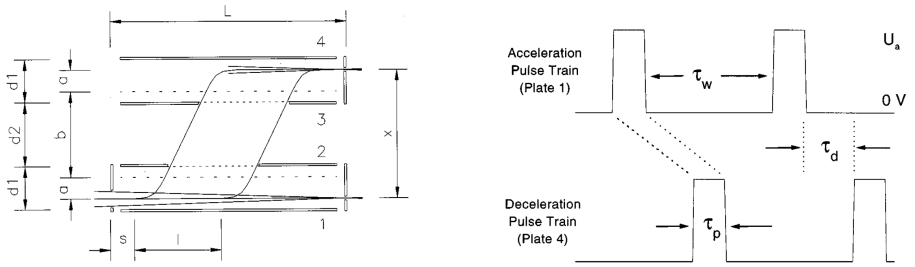

Figure 3.2: (a) Schematic of lateral TOF. L denotes the total length of the filter; a the beam displacement during the acceleration pulse; b the length of the field free region; $d1$ and $d2$ the separation between the plates; s the length of the ion beam that get lost and cannot be used; l the length of the ion beam package displacement; and x the total displacement. (b) Schematic of the pulse timing, representing a train of pulses that are displaced in time. τ_p represents the pulse length; τ_W the delay time before a subsequent pulse is applied; and τ_D the delay between an acceleration and a deceleration pulse. Both figures taken from [149].

where m is the ion mass, Δm is the width of the mass range, x is the lateral displacement and Δx is the full width half maximum (FWHM) of the convolution of the slith opening and the ion beam profile. After the first acceleration pulse is sent, the region at the entrance gets filled by the beam and another acceleration pulse can be applied, after a delay time, τ_W. This results in high overall transmission, where 60% of the cluster beam or more is used.

After the ion beam exits the TOF filter, it is directed onto the support through Einzel lenses. These lenses allow to control the breadth and the position of the beam, which in turn control the coverage of the particles on the substrate.

Particle Deposition

Beside being able to select specific masses, another important advantage of this technique is the possibility of evaluating the particle deposition rate, hence knowing the amount of catalyst deposited on the substrate. This parameter is of paramount importance for evaluating the specific mass activity of the catalyst.

In this system, the deposition can be monitored in two ways:

1. using a Quartz Crystal Microbalance, QCM, located in the preparation chamber where the deposition of the particles is carried out;

2. From the deposition current.

The deposition rate can directly be measured with a QCM, which consists of a resonator and whose frequency changes when mass is deposited onto it. The

relation between resonance and mass is given by the Sauerbrey equation [150]:

$$\Delta f = -\frac{2f_0^2}{A\sqrt{\rho_q \mu_q}}\Delta m \tag{3.2}$$

where Δf is the frequency change (Hz); f_0^2 is the frequency (Hz) of the resonator; A is the active area of the piezoelectric (cm^2); ρ_q is the density of the quartz (2.648 g/cm^3); μ_q is the shear modulus of the quartz ($2.947 \cdot 10^{11}$ $g/cm \cdot s^{-2}$); and Δm is the mass change (g).

The QCM housing is mounted on a mask that is positioned in front of the sample holder. The mask has four apertures of different diameters that can be positioned in front of the sample, as shown in figure 3.3. Both mask and sample holder can be moved linearly, so that the right aperture can be set in front of either the QCM or the sample. Furthermore, they both are floating and grounded through an ammeter. The ammeter has also the possibility of being biased up to ±48 V, which is essential during the deposition of the nanoparticles. The particles are deposited through a soft landing that is achieved by applying a bias to the sample holder [151]. It has been seen that deposition at higher voltages induces deformation of the particles. [152]

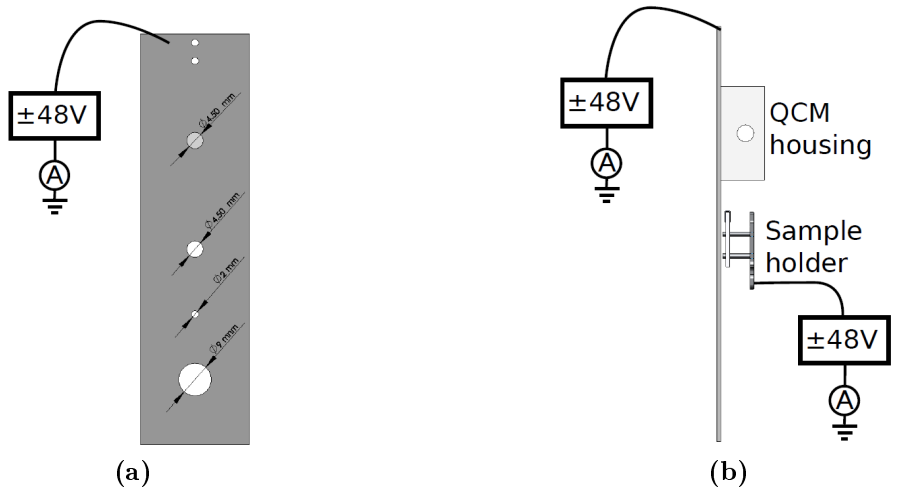

Figure 3.3: (a) Sketch of the front-view of the mask, where the holes with three different diameters are shown. (b) Sketch of the side-view of the mask, illustrating the QCM housing and the sample holder which are mounted in line. Both sketches are taken from [147].

The deposition current, I_{dep}, can also be used to obtain the mass deposited onto the substrate. It is measured with an ammeter, and in combination with

the mass selection gives the total deposited mass, M_{total}. By assuming only single charge ions, the total mass is given by:

$$M_{total} = I_{dep}\, m_p\, t \tag{3.3}$$

where m_p is the filtered single particle mass and t is the deposition time, required to reach the desired coverage.

Before starting the actual deposition, the mass filter is set to scan over a range of masses and a mass spectrum from the deposition current, similar to figure 3.4, is obtained. When the desired mass is found, the right settings are applied and the deposition can be carried out.

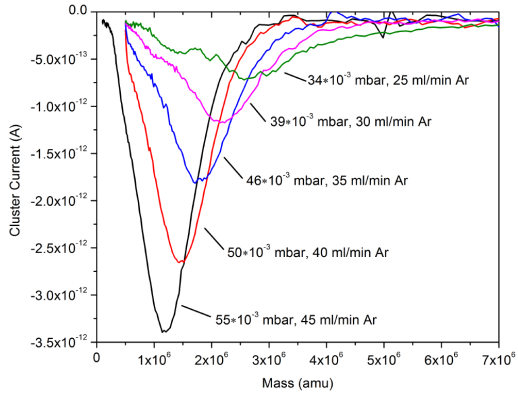

Figure 3.4: Deposition current versus mass curves. Figure taken from [147].

The observation of these current vs. mass curves are extremely important to ensure high quality deposition, where only single mass particles are selected. Instability of the plasma and passage of double and triple mass particles (with a double or triple charge) can drastically affect the mass selection of the particles and the coverage of the sample. Hence, their evolution is followed until they exhibit a stable smooth shape [153].

The ruthenium nanoparticles were deposited onto either a Glassy Carbon or a gold disk for electrochemical measurements or a Si_3N_4 TEM grid for acquiring high resolution images and for size distribution.

3.1.1.3 Analysis Chamber

The analysis chamber is an Omicron Multiscan Lab, equipped with the following tools:

- X-Ray Photoelectron Spectroscopy, XPS

- Ion Scattering Spectroscopy, ISS
- Auger Electron Spectroscopy, AES
- Scaning Electron Microscopy, SEM
- Scanning Tunneling Microscopy, STM

In this investigation, only the results obtained with XPS are shown. XPS was used to analyse the oxidation state of ruthenium before and after thermal oxidation.

3.1.2 Thin Films

Thin films of ruthenium oxide, iridium oxide and surface-modified ruthenium oxides were prepared by sputter and reactive sputter deposition in a UHV compatible system. The sputter chamber was purchased from AJA international in the Fall of 2011. A picture of the sputter chamber is shown in figure 3.5. At the beginning of this PhD project a great deal of efforts was devoted to customize the sputter chamber and define the best deposition conditions for each material.

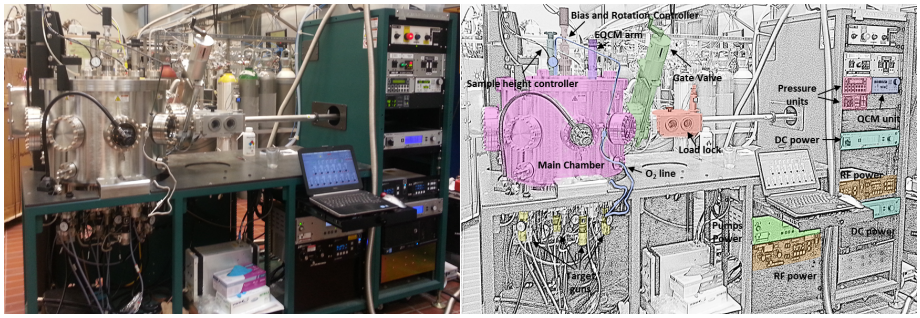

Figure 3.5: Sputter chamber image and correspondent schematic.

A basic handbook about thin film deposition can be found in [154]. Sputter deposition is a widely used and versatile technique to produce thin films, which belongs to the physical vapor deposition category, together with Chemical Vapor Deposition (CVD) and Pulsed Laser Deposition (PLD). Compared to these techniques, sputter deposition has some advantages, e.g. 1) easy control on the composition of the compound; 2) control on the growth of the film and its microstructure, through the ion energy and the particle irradiation; 3) flexibility of working at low temperature.

Sputter deposition consists of bombarding a surface (target) with highly energetic ions, resulting in the ejection of atoms, i.e. sputtering of the material. When the incoming particle hits the surface, the interaction between ion and

surface generates several processes that can occur simultaneously. Figure 3.6 shows the different interaction effects.

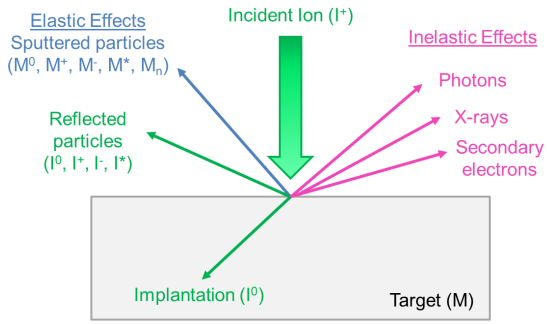

Figure 3.6: Schematic representation of all the simultaneous process occurring when an ion interact with the target surface. The superscript ^{0}, $^+$, $^-$ and * refer to neutral, positive, negative, energetic metastable particles, respectively. The subscript n denotes the number of particles in an ejected cluster. Figure adapted from [155].

The incident atoms can be neutralised and reflected. This process is the base of Ion Scattering Spectroscopy. Inelastic scattering and electronic excitation can also occur, producing X-rays, photons and secondary electrons. Photons and X-rays are relevant for chemical analysis of the plasma, by optical emission spectroscopy. Secondary electrons are used in magnetron sputtering system to enhance the plasma and improve the deposition rate. Finally, the relevant process for sputtering is due to elastic effects. The primary species are neutral particles, mainly single atom, while negative ions become relevant in special cases, e.g. with oxides. Negative ions are accelerated towards the anode (substrate), therefore, they can produce heating, resputtering and etching, damaging the film [155].

During the collision between the ion and the target, a momentum transfer occurs, which ultimately, if the energy is higher than the binding energy, U_s, results in the ejection of an atom or a molecule from the surface. The atoms can be ejected far from the collision event. Indeed, ions can penetrate into the the target and displace temporarily or permanently the lattice atoms, generating a collisions cascade. For instance, the collision event is often compared to the break in a game of atomic billiards. A cartoon illustrating the sputtering process is shown in figure 3.7.

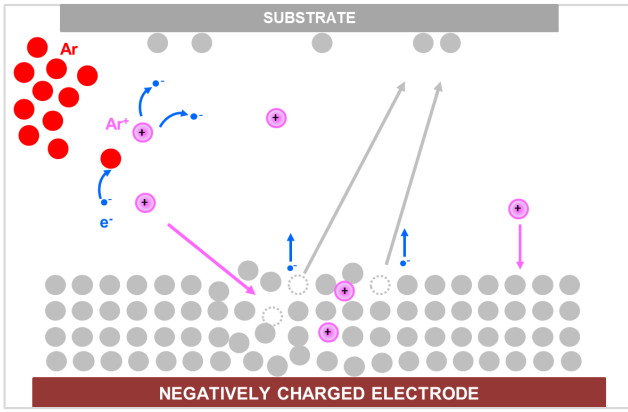

Figure 3.7: Cartoon illustrating the sputtering process. Argon ions are accelerated toward the target where they displace atoms in the lattice. The sputtered atoms are then accelerated towards the substrate and deposited.

Magnetron Sputtering [154]

Ion sources in sputter deposition devices are based on glow discharge processes. In a vacuum chamber, containing two counter electrodes and filled with gas, e.g. Ar, a sufficiently high voltage is applied and the gas is broken down, forming ions. When a discharge occurs, the generated electrons move towards the anode, leaving a cloud of ions around the cathode and behaving like a virtual anode. Between this region (negative glow) and the cathode a voltage drop takes place ("cathode fall") and the length of this drop is called cathode sheath, L, which is a very important parameter in the design of the sputtering systems. In this configuration the trajectory of the electrons is determined by the cathode and anode discharge. In order to ensure sufficient ions formation, the pressure must be high (few Pa). To improve the probability of ionisation, most sputtering devices are now based on magnetron sputtering, where the plasma is created by a magnetically enhanced glow discharge. These devices basically consists of a dc diode, where magnetic field can trap secondary electrons emitted from the target. The magnetic field is around 100 Gauss, so it affects only the trajectories of the electrons and not of the ions. The trapped electrons increase the ionisation and a much higher current for less target voltage is obtained (for 1/6 of the voltage, 50 times greater current is obtained). With this configuration, the substrate is weakly connected to the discharge and the ion bombardment on the substrate is very little. In turn, this gives much higher deposition rate and usually low temperature at the substrate, in comparison with the standard sputtering system.

DC and RF Sputtering

Sputtering can be performed with two power sources: direct current (DC) or radio frequency (RF). The first mode is the most used. It allows high deposition rates, but it can only be used with conductive materials. In contrast to DC, alternate current mode can be employed, which is controlled by a radio frequency power generator. Since this process does not rely on the conductivity of the target, its greatest advantage is that it can be adopted with non-conductive materials. Typically the sputtering rates are dramatically lower than DC, hence RF method is ususally avoided.

DC power source was used for preparing all the thin film shown in this thesis.

Sputtering Yield and Deposition Rate

The number of ejected atoms per incoming ion is called sputter yield, Y, and is given by

$$S = \frac{3\alpha}{4\pi^2} \frac{4m_i m_t}{(m_i + m_t)^2} \frac{E}{U_s} \tag{3.4}$$

where E is the energy of the incident ions, and α is a constant that depends on the relative masses of the ions, m_i, and the target, m_t. The sputtering yields increases linearly with the ion energy up to a maximum, where implantation becomes the predominant effect. Intuitively, it is inversely proportional to the binding energy, U_s. The stronger the bond between atoms, the less likely is the ionisation.

Sputtering yield, in turn, defines another important parameter, the sputtering rate, R:

$$R \propto S\, I \tag{3.5}$$

where I is the current of ions to the target. This means that the deposition rate depends mainly on the power applied to the target and the material. Sputtering rate is a crucial parameter for defining the right film composition and thickness. In some cases, in particular when compounds are formed, it is important to tune it properly. Several parameters can be therefore optimised:

- Target-to-substrate distance: R increases as the distance decreases.
- Power: doubling the power generally doubles the rate; however, it is important to check the material properties which can generate critical issues, e.g. thermal conductivity, melting point, mechanical strength.
- Sputter gas pressure: lowering the gas pressure will increase the mean free path, which in turn will improve the deposition rate. Too low pressure will however lead to very low amount of argon ions, shutting the plasma off.

Reactive Sputtering

One of the most pronounced advantages of the sputtering technique is its versatility. If a reactive gas, e.g. oxygen, nitrogen, etc., is let into the chamber, this can react with the sputtered material (metal) and form a compound. This opens up for preparation of several different film compositions. However, the reactive gas drastically influences the sputtering parameters making the process complex. It is important in reactive sputtering to analyse how the reactive gas affects the sputter deposition [154] [156] [157].

As soon as the reactive gas, e.g. oxygen, enters the chamber, it reacts with the sputtered material, and simultaneously it reacts with the target surface. The oxygen, starts to chemisorb on the target, poisoning it and changing its behavior. Indeed, a new compound, with different binding energy and sputtering yield, starts to form.

When the oxygen flow is low, this process is slow, the oxygen partial pressure is low and the deposition rate is kept high. The deposition is still in metal mode. If the reactive gas flow is increased, the oxygen pressure increases and consequently the deposition rate diminishes. This is called compound or poisoned mode and the sputtered material is basically the pure compound. The transition is generally described by four steps as the reactive gas flow is changed (as shown in figure 3.8). At the beginning (step 1), the consumption of oxy-

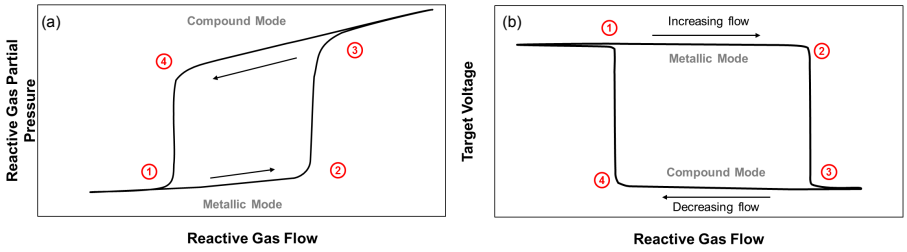

Figure 3.8: (a) Reactive gas partial pressure and (b) target voltage versus reactive gas flow hysteresis curves. The four different steps in the transition from metal to compound mode are highlighted. These curves represent the typical behavior of oxides reactive deposition. Figure adapted from [156].

gen at the substrate and from the sputtered material, the pumping, and the gathering at the target limit any significant change at the target surface and it still behaves like a metal. The partial pressure remains constant. By increasing the oxygen flow, its partial pressure slightly increases, while the voltage remains constant. At this point the gas is covering the target surface, and the deposition rate starts to decrease (the deposition rate of a metal is typically higher than the compound). When step 2 is reached, any small change in the oxygen flow causes an abrupt increase in the partial pressure and a drastic decrease in the

voltage (step 3), which is due to complete poisoning of the target. To clean the surface, the oxygen must be lowered all the way to point 4, where the target again behaves as a metal.

In order to deposit the right compound and not a mixture with the metal, it is preferable to work in the poisoned region. In the case of oxides, which are generally semiconductors, forming an oxide layer on the target can drastically affect the conductivity, up to some cases where RF must be used. In the case of ruthenium and iridium, both oxides are very conductive, so it was possible to carry out the deposition in the compound mode with high rate.

Thin Film Preparation

Thin films of ruthenium and iridium dioxide were prepared by reactive sputtering. Prior to the actual deposition, deposition rate and hysteresis curve, such as the one illustrated in figure 3.8 for ruthenium, were defined.

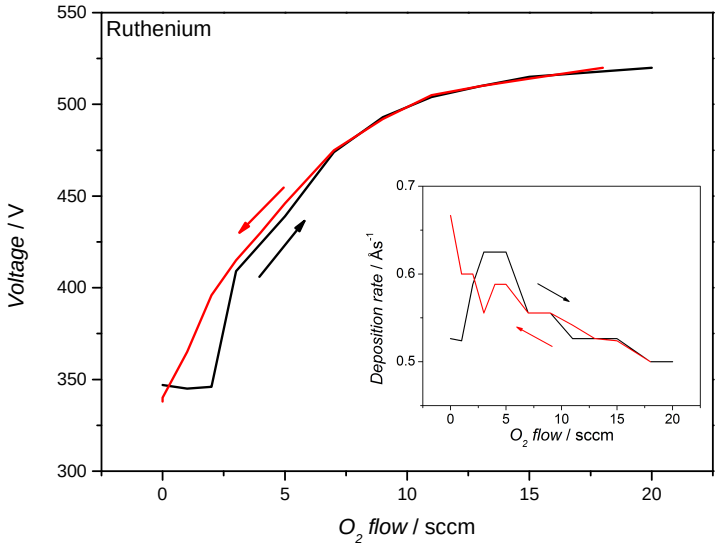

Figure 3.9: Experimental target voltage versus oxygen flow hysteresis curve for ruthenium. In the insert the deposition rate is shown.

The deposition rate was measured with an in-chamber quartz crystal microbalance (QCM), similar to the one in the cluster source. The QCM is mounted at the end of an arm that can be moved to the center of the sputter chamber, in the same position of the sample holder. Unfortunately, it is not possible to monitor the rate during the deposition. The deposition rate was taken after letting the plasma equilibrate for few minutes.

It is possible to ascertain the stability of the plasma by looking at the current and the potential of the target. As soon as oxygen reacts with the target, those parameters change until they reach a stable value. The voltage was used to verify the quality of the actual deposition.

Equipment Details. The sputter chamber used in this project is an A310 magnetron system, purchased from AJA international, inc., equipped with 6 guns and 2 DC power and 2 RF power sources. The substrate holder can be heated up to 800^oC and RF biased.

3.2 Sample Characterisation

3.2.1 X-Ray Photoelectron Spectroscopy

X-Ray Photoelectron Spectroscopy, XPS, is a very powerful technique, frequently used in surface science. It gives information on the elemental composition of a material, the chemical state of the elements and insights into the surface structure. XPS was used throughout this work to investigate the surface composition of the catalysts and the oxidation state of the elements.

The method relies on the photoelectric effect: when a material is irradiated with sufficiently energetic photons, it emits electrons (figure 3.10). In XPS a

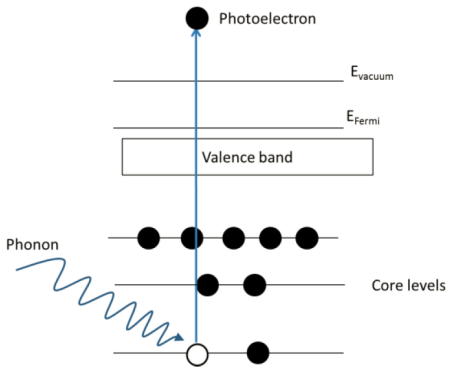

Figure 3.10: Schematic of the photoelectronic effect in XPS. Sufficiently energetic X-rays can induce the emission of an electron from the core levels. Figure taken from [158].

monochromatic X-Ray source, with energy $h\nu$, is used to irradiate the sample. The absorbed photons can then excite electrons from the core level, overcoming the binding energy ($E_{binding}$). If the workfunction is surmounted, the electrons

can escape with a kinetic energy, $E_{kinetic}$, given by:

$$E_{kinetic} = h\nu - E_{binding} - \phi_a \tag{3.6}$$

where ϕ_a is the workfunction of the analyser.

The kinetic energy distribution is usually measured with an hemispherical analyzer. An XPS spectrum is obtained by measuring the intensity of emitted electrons, $N(E)$, as a function of kinetic energy, which can be converted into binding energy. The binding energy is characteristic of the element and it depends on the chemical environment of the electrons, so it is also characteristic of the oxidation state of that element.

The most used X-ray sources are Mg $K\alpha$ ($h\nu = 1253,6eV$) and Al $K\alpha$ ($h\nu = 1486,3eV$) radiation. X-rays can penetrate deep into the sample, whereas the emitted photoelectrons cannot travel long distances in the solid. Figure 3.11 represents the inelastic mean free path of an electron, i.e. the distance that an electron can travel through a solid without inelastic scattering, as a function of kinetic energy. The kinetic energy of the photoelectrons is in the range of $0 - 1000$ eV, which means that their mean free path is only few nanometers. Therefore, the region that is probed with XPS is only the surface, up to few nanometers.

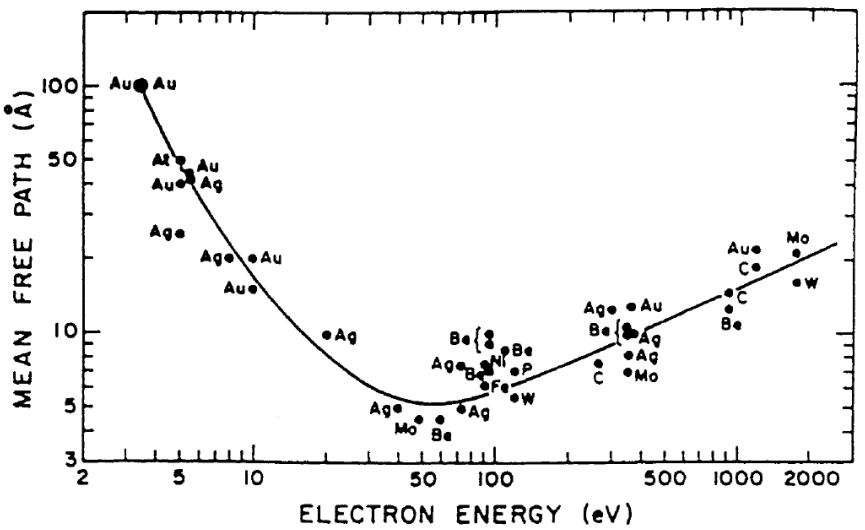

Figure 3.11: Universal curve, showing the mean free path of an electron as a function of its kinetic energy. Figure taken from [159].

Equipment Details. In this study, two different XPS systems have been used:

- Omicron Multiscan Lab in the Cluster Source. This system was used to analyse mass-selected nanoparticles. It uses a Al $K\alpha$ radiation and all the measurements were performed by Federico Masini
- Sigma Probe, Thermo Fischer. This system was used to investigate thin films. It uses Al $K\alpha$ radiation. It has the possibility of doing angle resolved measurement. The measurements were carried out by Paolo Malacrida.

Angle Resolved - XPS

The surface sensitivity of XPS can be improved by changing the angle between the normal to the surface and the analyser. When the analyser is tilted, the distance that the electrons can travel through is still defined by the mean free path, but now the depth is given by $l\,cos(\theta)$ (figure 3.12). By changing the angle

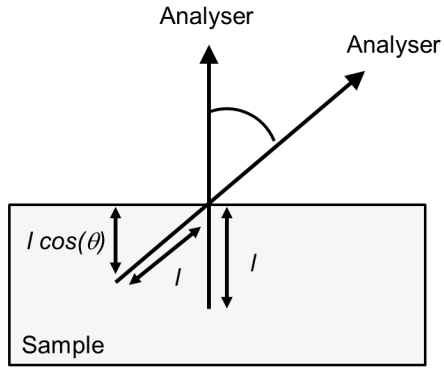

Figure 3.12: Sketch showing how the electron escaping path changes depending on the angle formed between the analyser and the normal to the surface. l is defined by the mean free path and it does not change when the analyser is tilted, hence the depth from which electrons can escape is given by $l\,cos(\theta)$.

θ, depth profile spectra can be obtained, so the change in elemental composition and oxidation state in the top most layer as a function of depth can be probed.

Only the Sigma probe system has the possibility of doing angle-resolved measurement.

XPS and fitting

XPS fitting has been performed by Paolo Malacrida and Federico Masini, using Gaussian-Lorentzian functions, mixed with exponential tail, using a dedicated software.

Carbon

In the case of mass selected nanoparticles, because of the very low coverage, an intense signal coming from the glassy carbon support is present. Unfortunately, C1s Binding Energy (B.E.) coincides with the B.E. of Ru $3d_{3/2}$, making it complicated to distinguish the two signals. However, it was possible to deconvolute the combined signal of Ru and C with the characteristic spectroscopic signature of RuO_2 of the low and high binding energy oxide peaks (see next section) and three species for the carbon. When carbon is oxidised, oxidised species, e.g. C═C, C═O, C—O, can be formed and different peaks need to be considered in order to achieve a better fit [160].

In the case of thin film, where the substrate was fully covered, only the signal from adventitious carbon is observed.

Ruthenium

Ruthenium 3d core level region has been fitted with a pair of doublets, defined as low and high binding energy oxide. The interpretation of these peaks is still bringing disagreement in literature, however the presence of a main and a satellite peak for ruthenium dioxide, and also for iridium dioxide, is well-established. In the ′80s Kötz and Stucki investigated ruthenium and iridium oxide quite extensively and they attributed the satellite peak to the presence at the surface of RuO_3 [70,112]. After the stability of RuO_3 was ruled out [161,162], this interpretation was criticized by Cox *et al.* and the satellite peak was then explained as a metallic character of RuO_2 [163]. The main peak was ascribed to fully screened core-holes, while the satellite to unscreened core-holes. A more recent interpretation [164] was based on first principle calculations of the binding energy shifts in the core level region and it attributed the satellite peak to the only surface cus atoms. However, the most accredited interpretation was given by Over *et al.* [165], using High Resolution Core Level Spectroscopy (HRCLS). They attributes the satellite to energy loss due to a plasmon excitation.

The binding energies for ruthenium $3d_{5/2}$ level and iridium $4f_{7/2}$ as metal and dioxide are shown in table 3.1.

Element	B.E. (eV) Metal, M	B.E. (eV) MO_2
Ru $3d_{5/2}$	280.2	280.9
Ir $4f_{7/2}$	60.8	61.8

Table 3.1: XPS binding energies for ruthenium and iridium in the metal state and as dioxide.

3.2.2 X-Ray Diffraction

X-Ray Diffraction, XRD, is a bulk technique, which is used to identify the crystallographic structure of a material; the size, shape and internal stress of small crystalline regions; the spacing between rows of atoms; and the orientation of grain.

A sample is irradiated with X-rays, which are elastically scattered (diffracted) by the atoms in a periodic lattice. A schematic can be seeen in figure 3.13. If the scattered X-rays are in phase, they give constructive interference, and they add up.

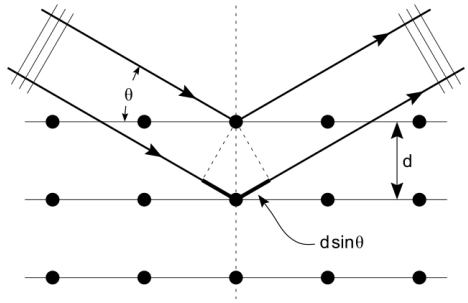

Figure 3.13: Schematic of X-Ray scattering from crystal planes. d denotes the distance between the crystal planes and θ the incident angle. Constructive interference occurs when Bragg's law is fulfilled.

The distance between lattice planes, d, is derived by the Bragg equation:

$$n\lambda = 2dsin(\theta) \tag{3.7}$$

where n is the order of reflection and is an integer, λ is the wavelength of the incident X-rays, and θ is the angle between the incoming X-rays and the normal vector to the crystal planes.

In the parafocusing geometry of standard XRD, the incident beam and the detector are maintained at the same angle, so a diffractogram is obtained as a function of the angle 2θ.

The region that is probed with this techique is deep and, indeed, XRD is not surface sensitive. However, the geometry can be changed so that XRD can become more surface sensitive and the probed region can, in some cases, be limited to few nanometers. This can be achieved with Glancing-Angle XRD [166].

Glancing Angle - XRD

Glancing Angle (or Grazing Incident) - XRD is an ideal technique for investigating thin films and nanoparticles or whenever the signal from the surface should

be maximized.

In this geometry, the incident angle, ϕ, is kept constant, while the detector arm is scanned. Typically, ϕ is set to small angles ($0.5° - 3°$), but above the critical angle (angle at which total reflection occurs). By reducing the incident angle, it is possible to reduce the penetration of the X-rays into the sample, hence limiting the region from where the information are gathered.

In standard XRD the penetration depth, z, changes during the sweep and is given by $z = sin(\theta)/2\mu$, where μ is the linear absorption coefficient and it depends on the material. In GA-XRD, z does not depends on 2θ, but it is defined by the incident angle, ϕ, which means the information are gathered from the same region [167].

Equipment Details. Most diffractogramms shown in this thesis were taken in GA-XRD mode, using a PAN Analytical X'Pert PRO Diffractometer, with X-ray wavelength of 1.54 Å for the $Cu_{K\alpha}$ line. The alignment of the sample was performed each time prior the XRD measurement with reflectometry and at an incident angle of $\phi = 0.5^o$. In one case in situ standard XRD was used to record XRD patterns at different annealing temperatures.

3.2.3 Scanning Electron Microscopy

Scanning electron microscopy, SEM, is used to investigate the morphology of a material with a resolution down to the nanoscale. It employs a focused beam of highly energetic electrons (primary electrons). Their kinetic energy is between 200 eV - 30 keV. The interaction between the primary electrons and the sample induces several signals, as it can be seen in figure 3.14: secondary electrons, backscattered electrons, X-rays, and Auger electrons.

The interaction volume depends on the energy of the primary electrons and it can affect the resolution of the image. SEM images are acquired from the secondary electrons, which escapes from near the surface and gives the best resolution. They are used to inspect the morphology and topography of the specimen. Alternatively, the back scattered electrons can be probed. They escape from a deeper region and show images with different contrast depending on the atomic number of the element, therefore on the elemental composition of the material (compositional contrast). X-rays come from deepest in the sample and can be used for chemical composition analysis (EDS).

Equipment Details. The images presented in this thesis were obtained using a Helios EBS3 microscope at the Center for Electron Nanoscopy, DTU.

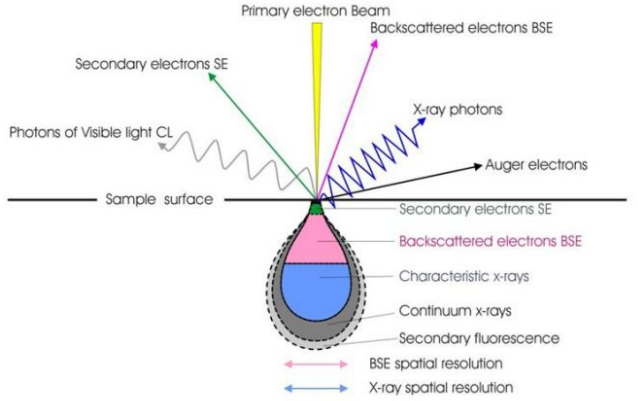

Figure 3.14: Interaction volume between the beam and the sample, producing several different signals, which are used for acquiring diverse information of the sample. Depending on the energy of the electrons, the interaction volume depth can change considerably, affecting the resolution of the image.

3.2.4 Transmission Electron Microscopy and Scanning Transmission Electron Microscopy

Transmission electron microscopy was operated by Davide Deiana to acquire images of ruthenium nanoparticles.

TEM is a microscopy technique based on the transmission of highly energetic electrons through a sample and relies on the wave nature of the electrons. An electron beam, with energies up to 300 keV, is accelerated towards the specimen and is collimated through magnetic lenses. The transmitted electrons are then collected either by a fluorescent screen or a CCD camera. The obtained image represents a 2D projection of a 3D morphology and differences in contrast, i.e. the difference in intensity between two adjacent areas, can be imaged. The interaction of the electron beam with the specimen can induce changes either on the amplitude (amplitude contrast) or on the phase (phase contrast) of the electron wave. The conditions in the microscope can be modified so that one phenomenon is predominant.

- Amplitude contrast arises from differences in mass and/or in thickness or from inhomogeneity of the specimen

    1. Mass-thickness contrast is predominant in amorphous material and it is given by incoherent inelastic scattering (Rutherford scattering). The cross section of Rutherford scattering is thickness and atomic number dependent. Thicker areas or with higher Z, scatter electrons

more strongly.

2. Diffraction contrast is predominant in crystalline and oriented material and it is given by coherent elastic scattering. The contrast is given by diffraction of the electrons at special (Bragg) angles.

- Phase contrast arises from the interference of diffracted beams and it can be used to image the atomic structure of the specimen. It is represented as intensity contrast, usually with "fringes". Its interpretation is complicated because phase contrast depends on many factors, e.g. focus of the beam, astigmatism of the lenses, variations in thickness, scattering factors and orientation of the material.

In a Scanning TEM the working principle is different from TEM and the Z-contrast can be significantly enhanced. Figure 3.15 shows the different working

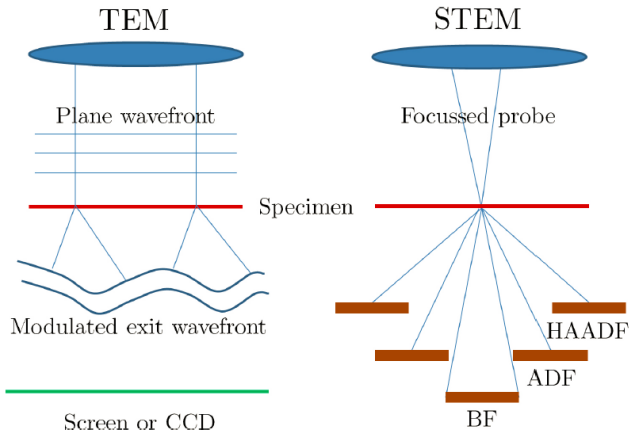

Figure 3.15: TEM and STEM working principle schematics, taken from [168]. While in TEM the beam is parallel and the transmitted electrons escape as a modulated wavefront, in STEM the beam is focused and the escaping electrons are scattered at different angles.

principle of TEM and STEM. In TEM, the incident beam is a coherent parallel beam and the transmitted electrons escape as a modulated wavefront. In STEM, the entering beam is instead focused and the scattered beam can be collected at different angles. Two different kinds of detectors can be employed: dark field (DF) and bright field (BF) detector. The first images mass contrast, while the latter images thickness contrast. High Angles Angular Dark Field collects the electrons that are inelastically scattered at angles higher that 50 mrad off-axis.

Equipment Details. All the TEM and STEM images were obtained by Davide Deiana at Center for Electron Nanoscopy (CEN), DTU. HR-TEM and STEM images were acquired using a FEI Titan Analytical $80-300$ electron microscope equipped with a CEOS Cescor probe spherical aberration corrector. The analyses were carried out using the same settings and microscope conditions: acceleration voltage of 300 kV, HAADF detector settings for STEM mode and same dwell time. The nanoparticles were deposited on Si_3N_4 TEM grids, which can handle an oxidation treatment at high temperature.

3.3 Catalytic Activity

The catalytic activity of mass selected nanoparticles and in some cases of thin films was measured in a rotating ring disk electrode (RRDE) assembly, provided by Pine Instruments Corporation. Cyclic voltammetry was employed as electroanalytical technique.

3.3.1 Electrochemical Set-up

The electrochemical cell, shown in figure 3.16, is a three-compartment glass cell, equipped with:

- Working electrode (WE): RRDE, with a platinum ring and interchangeable disk;
- Reference electrode (RE): $Hg/HgSO_4$ electrode, connected to the cell through a Luggin capillary. Before each measurement its potential was measured with respect to the reversible hydrogen electrode (RHE), by bubbling 1 bar hydrogen and using the platinum ring as working electrode. The shift was typically $729-731$ mV;
- Counter electrode (CE): carbon rod;
- Bubbler: prior each experiment, the electrolyte was purged with an inert gas, either nitrogen or argon.

All electrochemical measurements were carried out at room temperature in acid, using 0.05 M H_2SO_4 (Merck suprapur 96 %, prepared by dilution with 18 MΩ Millipore water). Sulfuric acid was used in place of perchloric acid because of the chemical instability of perchlorate ions in the presence of iridium [85]. At potentials below 1 V (vs. RHE), iridium can catalyse the reduction of perchlorate to chloride ions [169–171]. It has been reported that chloride ions interact strongly with metallic surfaces [172,173]. In order to avoid any possible undesired reaction and contamination of the surface, sulfuric acid was preferred for all the measurements.

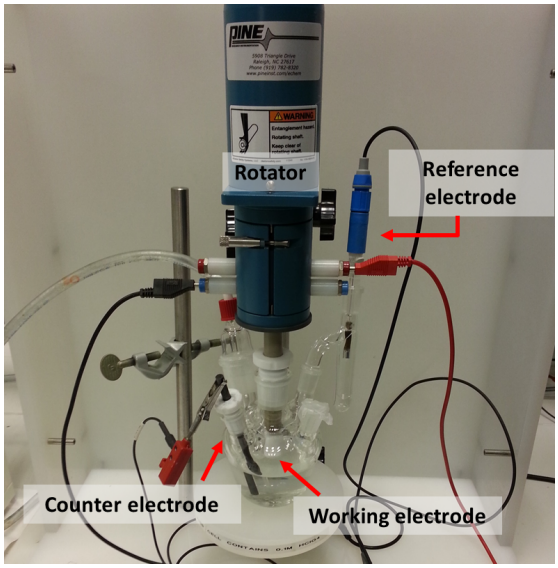

Figure 3.16: Picture of the electrochemical cell, with the working, the reference and the counter electrodes highlighted.

Data were acquired using a Bio-Logic Instruments VMP2 multichannel potentiostat/galvanostat, with EIS analyser, and Bio-Logic EC-Lab software. All potentials are shown using the RHE scale and are Ohmic corrected.

Ohmic Losses. The Ohmic drop was measured using electrochemical impedance spectroscopy (EIS) over the range 1 to 200000 Hz at a DC potential of 10 mV, and evaluated from the fitted high frequency intercept. An example of a Nyquist plot with the fitting is shown in Figure 3.17.

When only the disk current was monitored, the Ohmic drop was compensated at 85% using the EC-Lab Manual IR compensation method (MIR). This technique cannot be used in bipotentiostat mode, when ring and disk are monitored together (see section 3.4.2). In order to be able to compare the stability of the catalysts, the upper limit potential must be the same; it is essential to compensate with the right Ohmic loss.

Capacitance correction. All the Cyclic voltammograms, after being compendsated for Ohmic losses, were corrected for the capacitance, by averaging the anodic (forward) and the cathodic (backward) sweep [91], as shown in figure 3.18.

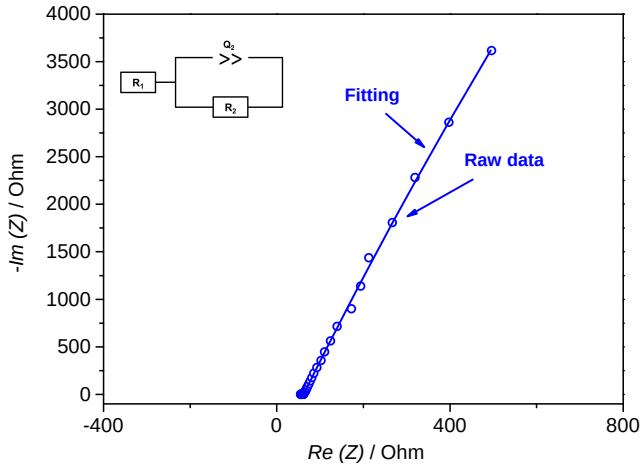

Figure 3.17: Nyquist plot for a Ruthenium dioxide thin film in 0.05 M H_2SO_4 at open circuit potential measured with impedance spectroscopy. Frequency range 1 Hz - 200 kHz. The symbols represent the data and the line is the fitting, using the Randless circuit shown in the in the upper left corner.

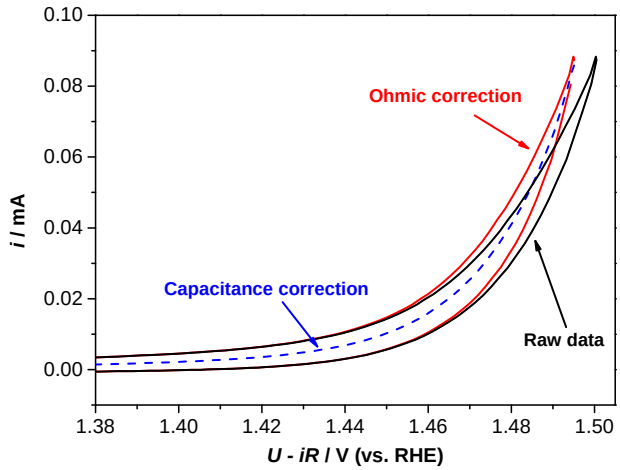

Figure 3.18: Ohmic and capacitance correction. The raw cyclic voltammogram is first corrected for Ohmic drop, which is measured by EIS, and then capacitance corrected by averaging the positive and negative scan.

3.3.2 Cyclic Voltammetry

Cyclic voltammetry is the most frequently used technique in electrochemistry, especially when dealing with a new system. It gives qualitative information on the surface properties and on the processes occurring at the electrode/ electrolyte interface. The technique consists on cycling linearly the potential at a constant rate (scan rate $\nu = dU/dt$), while the current response is monitored. The resulting plot, current i (mA) versus potential U (V), is called cyclic voltammogram (CV). An oxidation process gives positive current, whereas reduction gives a negative current. All these processes are surface sensitive, so the CV can be considered as fingerprints of the surface. For this reason, cyclic voltammetry is a fast and easy way to investigate surfaces.

For example, in the case of metallic ruthenium, the electrochemical formation of an oxide can be followed. Figure 3.19 shows a series of cyclic voltammograms on electrodeposited ruthenium on a glassy carbon (figure 3.19 b)), where the anodic potential (upper limit) is increased after each cycle. The electrodeposition was carried out following the procedure reported in literature by Hadzi-Jordanov *et al.* on a Pt surface and the results were compared [174].

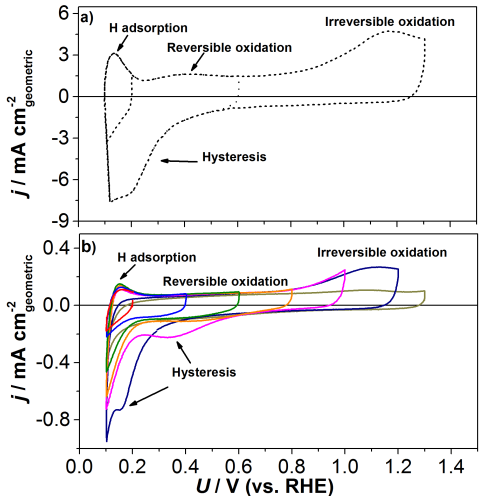

Figure 3.19: a) Pt-ruthenized catalyst adapted from [174]. b) Electrodeposited ruthenium on glassy carbon prepared in our laboratory. The electrodeposition was carried out as described in [174]. The CVs were recorded at a scan rate of 13 mV/s, while the upper limit potential was increased after each cycle.

Hadzi-Jordanov *et al.* designated the following features [174], as the potential was raised:

- $0.05 - 0.3$ V_{RHE}: H adsorption and desorption;

- $0.3 - 0.9$ V_{RHE}: initial surface oxidation (reversible);
- $0.9 - 1.3$ V_{RHE}: broader oxidation region (irreversible);
- above 1.3 V_{RHE}: oxygen evolution;
- $0.9 - 0.3$ V_{RHE} (cathodic sweep): reduction of the surface oxide formed during the anodic sweep.

The reduction peaks in the cathodic scan shifts towards lower potential, when the upper limit potential is above 0.9 V_{RHE}. The hysteresis indicates that the surface oxidation process is irreversible. This is strengthened by the disappearance of the H adsorption peak, which is usually absent on oxidized surfaces.

On thermally grown oxides, those features are absent and the typical CVs are featureless. However, information about the surface area can be gathered from the double layer capacitance and used to compare the roughness of catalysts of the same material.

By providing thermodynamic and kinetic information, cyclic voltammetry is also used to investigate electrochemical reactions, such as the oxygen evolution reaction. CV can be used to evaluate the catalytic activity of a catalyst. The activity can be expressed either as the overpotential at a specific current density (typically 5 or 10 mA/cm^2 [58, 100]) or as current density at a specific overpotential. In the case of precious metals, in particular in the form of nanoparticles, it is interesting to compare the mass activity, i.e. the current normalised with the precious metal mass, at 1.48 V vs. RHE (0.25 V overpotential) [64, 79, 81].

3.4 Stability under reaction conditions

A combination of several techniques was employed in order to evaluate the catalysts lifetime.

3.4.1 Electrochemical Quartz Crystal Microbalance

In an Electrochemical Quartz Crystal Microbalance (EQCM), a QCM is connected to an electrode so that it can be used as working electrode, while the mass change is monitored. The great advantage of an EQCM is the possibility of simultaneously investigate the surface properties of a catalyst and the mass alteration in real time. A QCM, as described in section 3.1.1.2, consists of a oscillating quartz crystal, whose resonance frequency changes when a mass change occurs (loss or gain). It is based on the piezoelectric effect, which is the ability of generating an electric charge when a material is subjected to a mechanical stress (from the Greek word *piezein*, to press). The generated frequency change, due to change in thickness, is expressed by the Sauerbrey equation 3.2 [150].

EQCM is typically used to study thin film deposition, thin film dissolution (e.g. anodic dissolution), change in the surface morphology, and mass variation

due to chemical processes [87, 134, 175]. It is important to highlight that with an EQCM the frequency change, Δf, is directly measured, not the mass change, Δm. Δf is influenced by some properties which must be considered in order to avoid misinterpretations [175]:

- **Viscosity.** When the QCM is immersed in the electrolyte, the interaction with the liquid makes the frequency change complicated. Δf is indeed influenced by the viscosity of the liquid, which is in turn affected by the temperature. The influence of the viscosity is expressed by:

$$\Delta f = -f_0 \sqrt{\frac{\eta_l \rho_l}{\pi \rho_q \mu_q}} \tag{3.8}$$

  where η_l is the viscosity of the liquid and ρ_l is the density of the liquid [176]. If water and quartz are used, Δf at 20^oC would be 710 Hz, and if the temperature increases of 10 degrees the frequency would change from 1000 μPa s to 797 μPa s. Hence, temperature should be kept constant during the experiments.

- **High mass loading.** Significant decrease in frequency, due to high mass loading, affects drastically the sensitivity. Accurate measurements are achieved when the frequency change does not exceed the 2%. This corresponds to a change in mass of 2.4 mg, which in the case of ruthenium dioxide would correspond to 2.5 μg.

- **Surface roughness of QCM electrode.** If the QCM electrode is too rough, liquid molecules can be trapped in the electrode and the mass change can be misread. For instance, during oxidation of a gold electrode in alkaline and in neutral media, it was observed that Δf was significantly larger than what expected [177]. This was explained as water molecules trapped in the cavities and it was found that the 80% of the total frequency change could be accounted as roughness effect.

- **Surface stress.** One side of the QCM electrode is in contact with the liquid while the back side is in contact with air. This leads to an hydrostatic pressure which may affect the frequency. Nevertheless, since the hydrostatic pressure does not change during the experiment, it is not a very important factor. Strain effect coming from thick films can also have a certain influence on the frequency, and its effect can be difficult to predict.

- **Interfacial slippage.** In some cases the first layer of solvent is tightly bounded to the surface of the electrode and it does not slip during the shear movement. This means that sometimes an equilibration time must be accounted for.

- **Non-uniform mass distribution.** A uniform mass distribution is required in order to get good radial sensitivity through the electrode. This

is valid, when the roughness factor is lower than the acoustic wavelength of the resonator, which is usually the case.

- **Bubbles**. When working with gas evolution, bubble formation can be a problem.

Equipment Details. The EQCM used in this thesis is a QCM200 model purchased by Stanford Research System, illustrated in figure 3.20. The QCM

Figure 3.20: Image of the QCM200 model set-up, showing the shaft where the crystals are mounted and the control box that measure the frequency change. The control box is connected to the computer so the frequency change can be displayed together with the electrochemical measurement in the EC-Lab program.

crystal is an AT-cut crystal, with a nominal resonance of 5 MHz, covered with a gold film and a titanium layer is used to improve the adhesion. Pictures of a QCM crystal before and after catalyst deposition is shown in figure 3.21. The geometrical area of the top electrode is 1.37 cm^2, while the quartz is only 0.38 cm^2. This means that only the 28% of the electrochemically active surface area is sensitive to QCM measurement.

The minimum detectable frequency variation corresponds to a few ng cm^{-2} and is limited by the noise level, which is typically below 1 Hz. Time resolution, τ, is related to the equilibration between the instrument and the mass change, typically in the order of milliseconds, and it is expressed by

$$\tau = \frac{Q}{\pi f_0} \tag{3.9}$$

Calibration. The mass changes reported in this thesis were evaluated from the Sauerbrey equation (equation 3.2), using $C_f = 56.6 \pm 2.8$ Hz cm^2 μg^{-1}.

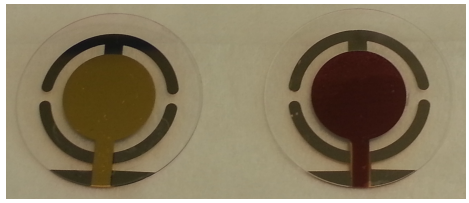

Figure 3.21: QCM crystal of Au/Ti, purchased by Stanford Research System: on the right a bare crystal and on the left with sputter deposited RuO_2 thin film.

The constant C_f was calibrated by electrodeposition of silver onto a gold quartz crystal [178]. The measurements were repeated six times.

Electrochemical cell The electrochemical cell used for EQCM measurements is shown in figure 3.22. It is a three compartment cell, with the EQCM holder as working electrode, a $Hg/HgSO_4$ electrode as RE and a graphite rod as CE. The EQCM holder as a double output, one that is connected to the potentiostat/galvanostat and one connected to the QCM device. Inert gas was bubbled during the experiments, to assure mixing of the electrolyte.

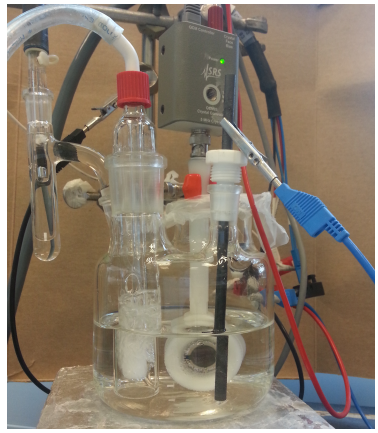

Figure 3.22: Picture of the electrochemical cell used for running stability measurement of thin films. The working electrode is mounted on the big white shaft which has two connections: one, connected to the QCM device, for the frequency monitor and one, linked to the galvanostat/potentiostat, for the electrochemical measurement. $Hg/HgSO_4$ electrode is used as reference electrode and is in contact with the solution through the Luggin capillary. A carbon rod is used as counter electrode and either nitrogen or argon are degassed through a bubbler.

Example: Electrodeposited Ruthenium. EQCM is a good technique for investigating thin film dissolution, e.g. anodic corrosion, and oxide growth. For instance, by considering the case of electrodeposited ruthenium and the series of CVs illustrated in figure 3.19, the same features can be identified in term of mass change.

Figure 3.23 shows a cyclic voltammogram, recorded at 20 mV/s between 0.05 and 1.2 V (vs. RHE), together with the mass change.

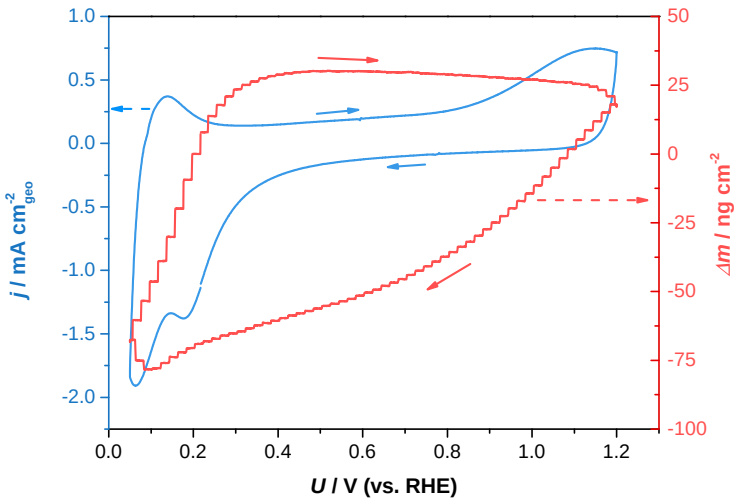

Figure 3.23: Electrodeposited Ru cyclic voltammetry and mass change, in N_2 degassed 0.1 M $HClO_4$. Scan rate 20 mV/s.

- Anodic sweep: at low potential there is an increase of mass, due to surface oxidation; after this gain, the mass remains more or less constant.
- Cathodic sweep: a significant mass loss (almost comparable to the mass gained in the anodic scan) takes place, likely due to hydration molecules desorption and reduction of the oxide.

Similar results can be obtained by considering the whole series of CVs, performed with increasing anodic potential, and by averaging the mass change over 10 scans for each region. Figure 3.24 shows the averaged mass variation versus the upper limit potential. When the potential is scanned up to 1.2 V (vs. RHE), the net mass variation is almost zero and constant, which can be ascribed to hydrogen desorption and to reversible surface oxidation. At higher potential, though, there is a net increase in mass due to the irreversible nature of the oxide. At potentials above the standard dissolution potential of ruthenium (1.38 V vs. RHE [105]) and the onset for oxygen evolution, a net mass loss occurs, due to ruthenium corrosion and oxygen detaching from the surface.

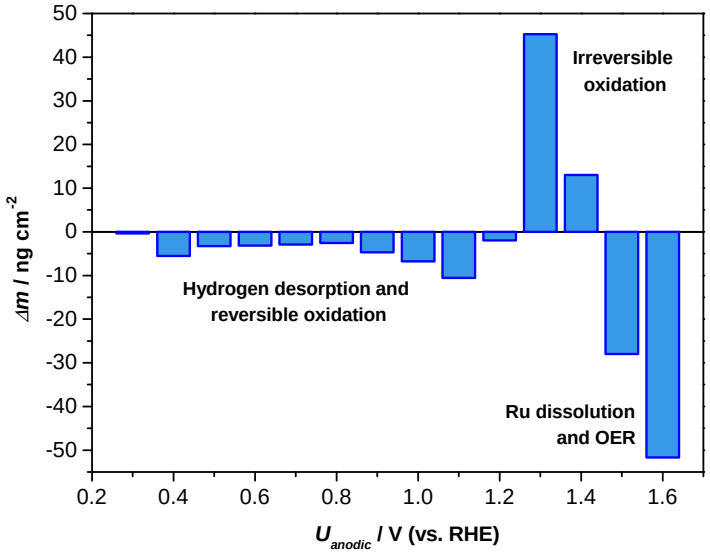

Figure 3.24: Mass change, averaged per cycle, of electrodeposited ruthenium on EQCM crystal versus the upper limit potential (anodic potential) of the cyclic voltammetry. All the CVs were recorded in N_2 saturated 0.1 M $HClO_4$ at 20 mV/s with a cathodic limit of 0.05 V vs. RHE.

3.4.2 Bipotentiostat Measurements

When EQCM could not be used, measurements on the ring electrode of the products generated at the disk electrode (e.g. oxygen, or corroded species) in the RRDE assembly were performed. When possible, they were carried out in combination with analysis of the electrolyte by ICP-MS. RRDE is a hydrodynamic method: due to the movement (rotation) of the electrode with respect to the electrolyte, a convective mass transport of the reactants is generated. The main advantages of this technique is that steady-state currents and mass flows are reached quickly.

An independent ring electrode is located around the disk electrode and an insulating gap (typically made of Teflon) separates the two parts. The products at the disk reach the ring by radial flow, where they are collected. The ring does not affect the disk current and it can also be used alone as an electrode, e.g. in the calibration of the reference electrode. A bi-potentiostat needs to be used, in order to separately adapt the ring and the disk potentials.

Figure 3.25 represents a schematic drawing of the RRDE set-up and a typical collection experiment. The oxygen evolved at the disk can be collected at the ring and reduced back to water. In this way it is possible to evaluate how much

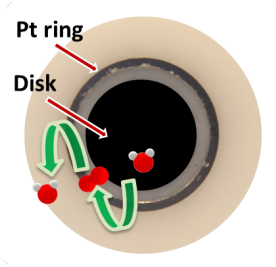

Figure 3.25: Image of the RRDE assembly and example of a collection experiment. In the figure oxygen evolution on the disk and oxygen reduction on the ring are shown as example. Alternatively, the generated RuO_4 species at the disk can be detected and reduced at the ring.

of the disk current is due to oxygen evolution and how much is instead due to catalyst corrosion. In the case of ruthenium, another approach is also available: the corroded species can be collected and reduced at the ring [104]. In this thesis, the measurements were carried out by scanning the potential at the disk, while the ring was held at a fixed potential:

- 0.4 V (vs. RHE) for oxygen reduction
- 1.1 V (vs. RHE) for reduction of the corrosion products

In order to correlate precisely i_R with i_D, it is important to evaluate accurately the collection efficiency, N. The collection efficiency represents how much of the disk products can be collected at the ring and it is expressed by:

$$N = \frac{-i_R}{i_D} \tag{3.10}$$

N depends on the geometry of the disk and the ring (the inner and outer radius of the disk and the inner and outer radius of the ring); while it is independent on the species concentration, the species diffusion and the rotation speed. It can be calculated experimentally, with a known system. The RRDE used in this thesis was calibrated with a ferrocyanide redox couple in a 0.1 M KOH solution [99]. With this configuration, the collection efficiency was estimated to be 0.20 ± 0.01, evaluated from three different measurements.

3.4.3 Gas Chromatography

In the case of ruthenium nanoparticles the faradaic efficiency of oxygen evolution was measured with a Gas Chromatograph. Calibration and actual measurements were conducted with Mauro Malizia.

Gas chromatography is an analytical technique, used to measure the concentration of volatile species in gas phase. A small gas volume of the sample is injected into the gas chromatograph, mixed with an inert carrier gas (helium or argon), which represents the mobile phase. The mobile phase then passes through a column (stationary phase), where the components interact differently with the walls. Depending on how strong they interact, the time requested to pass through the column (retention time) will be different. The retention time is typical of the species and can be changed by modifying the temperature in the column or the flux of the carrier gas. After passing through the column, the species are analysed with a detector and a spectrum intensity versus time is recorded (chromatograph). Depending on the kind of species, the typical detectors are:

- Thermal Conductivity Detector (TCD): used to analyse organic and inorganic species; it is based on changing the thermal conductivity of the carrier when passing to another component.

- Flame Ionisation Detector (FID): employed to analyse organic compounds; it is based on burning the components with an hydrogen flame.

The area of the peaks in the chromatograph is proportional to the concentration of that species in the gas phase of the sample. In order to evaluate quantitatively the concentration, it is necessary to calibrate the instrument with a known concentration of the same species.

Calibration The electrochemical cell was a sealed H-cell with a Pt wire as working electrode, a $Hg/HgSO_4$ as reference electrode and another Pt wire as counter electrode. The working electrode and the counter electrode compartments were separated through a ceramic frit. The cell was purged with helium, until complete removal of the air in the solution, verified with the gas chromatograph. Afterwards, the system was switched to circulation loop and a chronoamperometry test of one hour was started. A sample was injected into the headspace every ten minutes. To evaluate oxygen concentration, 100% Faradaic efficiency on platinum was assumed. Measuring the oxygen concentration accurately is very difficult, especially when working with small currents, since tiny leaks can introduce high amount of air (therefore O_2) into the system. However, at the same time nitrogen would be introduced and detected in the system. By integrating the area due to nitrogen, it is possible to estimate the contribution of the leak to the oxygen peak. The calibration curve is shown in figure 3.26.

Equipment details. The gas chromatograph is a Hewlett Packard 5890 Series II, equipped with a TCD and FID detecors. The column is produced by Restek. TCD was used as detector for O_2 and N_2.

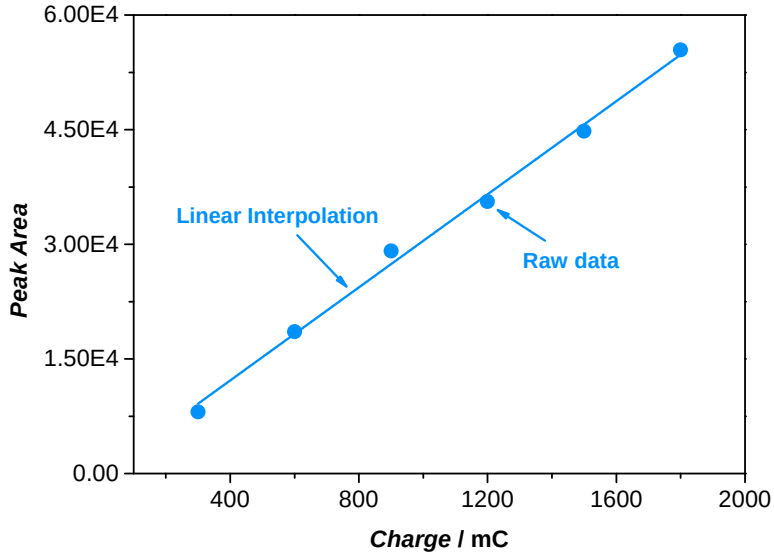

Figure 3.26: Calibration curve for oxygen on a platinum wire. A correction due to leak is applied, by measuring the variation of nitrogen concentration and correlating it to the oxygen concentration. The dots represents the raw data taken every ten minutes and the line denotes the linear fitting with a R^2 of 0.999.

3.4.4 Inductively Coupled Plasma - Mass Spectrometry

Inductively Coupled Plasma - Mass Spectrometer (ICP-MS) is a widely used technique for elemental analysis, employed in a variety of areas. In comparison to other elemental analysis techniques, e.g. atomic absorption spectroscopy, optical emission spectroscopy and inductively coupled plasma - atomic emission spectroscopy, ICP-MS has some distinct advantages. It is a fast multielemental method, which can measure most of the elements in the periodic table down to ultra trace level. In figure 3.27, the periodic table with the instrumental detection limit is shown. The elements detected in this thesis are mainly ruthenium and iridium, both having an extremely low instrumental detection limit, below 0.1 ppb. In ICP-MS, the sample is introduced as aerosol droplets in an Argon plasma in the ICP torch section. While traveling through the plasma the sample get desolvatated, atomised, and, finally it gets ionised. The ions are then sent to the quadrupole MS, which scans all the ions, filtering them depending on their mass-to-charge ratio, m/z. After passing through the MS, the ions hit a dynode of an electron multiplier, which generates a cascade of electrons until the generated signal becomes measurable. By initially calibrating the instrument with standard solutions of known concentration (calibration curve), it is possible to

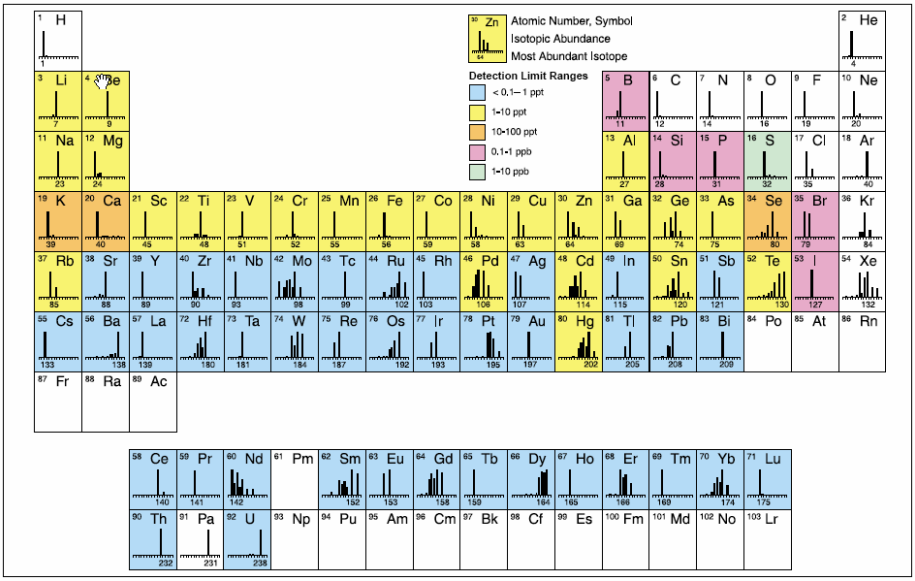

Figure 3.27: Periodic table with the instrumental detection limit and isotopes, taken from [179]. Different colors represent different detection limits, while the elements left white are not detectable with ICP-MS.

evaluate the concentration of the elements. The components of an ICP-MS are summarised as follows:

- **Sample introduction system.** It consists of a nebulizer, used to convert the liquid sample into an aerosol; and a spray chamber to introduce small droplets into the system, while discarding the big droplets.

- **ICP torch adn RF-coil.** It generates the Argon plasma which is used as ion source. The ICP torch consists of concentric quartz tubes, which, at the end, is surrounded by a RF-coil. The plasma is produced by passing Argon through the tubes and by applying a spark. The temperature rises up to 6000^{o}C. In this section, the sample is introduced as droplets, which is then dried and ionised by the plasma.

- **Interface.** This part is essential in order to link two different areas of ICP: the ICP-torch, which is at a very high temperature and high pressure ($1-2$ Torr); and the mass spectrometer, which works in high vacuum (less than 10^{-5} Torr) and room temperature. The interface consists of two inverted funnel-like parts which are called cones: sampler cone and skimmer cone.

- **Vacuum system.** The ion optics, the mass spectrometer and the detector works under high vacuum, so that the ions do not collide with other molecules in the path from the interface to the detector. Vacuum is achieved with a combination of turbo-molecular pump and mechanical roughing pump.

- **Ion Optics.** They are used to guide the ions into the quadrupole mass spectrometer and to separate the positively charged ions from the negatively charged, the neutrals and the photons. The focused beam exiting the cones passes through a quadrupole which deflects the ions, while the neutral particles and the photons keep going straight.

- **Collision/Reaction cell.** Ions formed by the interaction of the argon gas with the matrix of the sample, e.g. oxygen, nitrogen, water, etc., can create interference if their m/z ratio is similar to the one of the analyte. The collision/ reaction cell is used to eliminate these interferences. It can operate in collision or in reaction mode.
  The first mode is used when the interference is physically bigger than the analyte ions: the ions flow is forced to pass though a cloud of inert gas, where the bigger particles collide more often and loose their kinetic energy. An energy barrier at the end of the cell allows only the ions that retained most energy (the smaller) to pass. This mode is referred to as Kinetic Energy Discrimination (KED). This mode reduces the signal from the background, but at the same time it reduces the intensity from the analyte.
  The reaction cell mode takes advantage of the different chemistry of the ions: interferences react exothermically with an active gas, e.g. ammonia; while the analytes react endothermically. In this mode the ions flow is forced to pass through a cloud of an active gas. The interference react with it, forming neutral species, which are then ejected from the cell.
  In this thesis, KED mode was used.

- **Mass spectrometer.** It separates the ions depending on their mass-to-charge, m/z, ratio. The ICP-MS system used in this thesis is equipped with a quadrupole mass spectrometer. It consists of four rods and, by applying different voltages and radio frequency through rods of opposite sides, only a specific m/z can travel through the rods and reach the detector. The electronic is rapidly changed, so that the proper m/z range is scanned.

- **Detector.** When the ions exit from the mass spectrometer, they hit the sensitive surface of the detector, a dynode, which generates electrons that hit other dynodes, forming an amplified signal, which can be detected. Each ion generates a pulse and the number of pulses can be correlated to the concentration of the element through the calibration curve.

- **Data handling and system controller.** The signal from the detector is converted into more useful information, which can be semi- quantitative, quantitative, or isotope ratio, depending on the kind of analysis that has been carried on.

Equipment details. The ICP-MS used in this thesis is from Thermo Fisher Scientific, model iCAP-QC ICP-MS. Quantitative analyses in KED mode were carried out. Each time, a calibration curve with diluted solutions of the analytes (0.1, 1 and 10 μg/L) made from standards with 1000 μg_{metal}/L, was built.

3.4.5 Electrochemical - Scanning Tunneling Microscopy

In case of ruthenium nanoparticles, to directly observe the corrosion under reaction condition, it was possible to use an in situ scanning tunneling microscope (EC-STM).

Scanning tunneling microscopy is used to image surfaces in real time and in real space with atomic resolution.
It is based on two effects:

- **Quantum tunneling effect**: valid only in quantum mechanism, a particle can tunnel through a barrier.
- **Piezoelectric effect**: the ability of certain materials to deform when a potential is applied.

The vertical and lateral motions of the tip of the microscope can be accurately controlled thanks to these two effects. A conductive tip is brought close to the surface up to few tenths of nanometers, and a potential difference, U_t, in the orders of few hundreds millivolts is applied. At this distance, electrons can tunnel through the vacuum between tip and surface, generating a current, i_t. The current is proportional to U_t and to the local density of states at the Fermi level, while it exponentially decays with the distance, d.
STM can be operated in two modes:

- **constant current mode**: the height of the tip is adjusted in order to maintain constant the current, i_t.
- **constant height mode**: it is the opposite approach, the height is maintain fixed and the current changes consequently.

Generally, the first mode is preferred. Therefore, precise control on the tip movements is requested and achieved by using a piezoelectric tube scanner. The tube scanner is divided in four piezoelectric sections as shown in figure 3.28: lateral motion is controlled by applying a potential difference between opposite section, while z movement is guided with the potential difference between the inner and the outer sections. The tip is then scanned across the surface line by

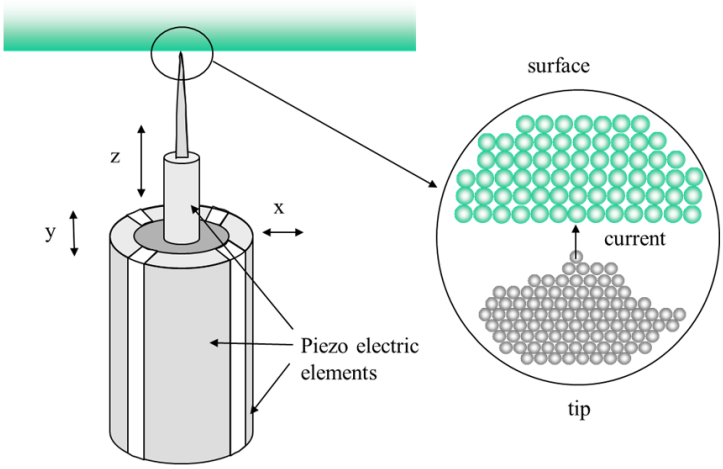

Figure 3.28: EC-STM image of the tip and the piezoelectric tube scanner. In the enlargement, interaction between the tip and the surface is illustrated.

line and a three dimensional images is obtained. It is important to highlight that STM images the density of state of the Fermi level of the surface and not the atoms. STM is indeed not useful if information on the composition are required. Furthermore, STM, in order to achieve atomic resolution, requires well-defined and flat surfaces.

With an electrochemical STM it is possible to acquire images in situ in the electrolyte under reaction conditions, while the potential at the working electrode (the imaged surface) can be changed. All the EC-STM images, presented in this thesis, were taken by Christian Schlaup.

Equipment details. The EC-STM measurement were carried out in a custom-made set-up, based on the set-up described in [180]. The tunneling tips were prepared by electrochemical etching of a 0.24 mm Pt/Ir (90/10) wire and subsequently coated with hot-glue. The EC-STM measurements were carried out in constant current mode, in Ar (Scientific quality 6.0) saturated 0.05 M H_2SO_4. The reference electrode was a Pt wire, used as a pseudo Pt/PtO pseudo reference electrode. Its calibration against RHE potential was performed using the position the butterfly peaks of the order/disorder transition of sulfate on Au(111) [181].

Chapter 4

Mass-Selected Ru and RuO_x Nanoparticles

As mentioned in the introduction, the acidic and oxidising conditions of PEM electrolysers limit the choice of the catalysts to noble metals, which are characterised by low annual production and inelastic supply [7]. Therefore, one possible strategy towards the widespread usage of these devices is to significantly improve the mass activity of precious metals. To do that the catalysts need to be in nanoparticulate form.

In the overview about OER, in section 2.1.4, it was pointed out that systematic studies of the oxygen evolution reaction on well-defined nanoparticles are rather absent. The aim of this chapter is to provide a fundamental investigation on well-defined mass-selected ruthenium oxide nanoparticles. Mass-selected nanoparticles, prepared by a physical method, provide an important advantage over other preparation techniques, which is an accurate evaluation of the loading, allowing in turn a precise estimation of the mass activity. The size investigated here varies from 2 to 10 nm, a range in which the surface area is maximised. Although Macounová *et al.* focused on RuO_2 nanoparticles bigger than 15 nm [76], smaller size particles are of greater technological relevance and the effect of size is expected to be more pronounced [72, 77].

The focus will be primarily on the effect of the pre-treatment on the activity and stability and the effect of size. In particular, the question to what extent the mass activity of ruthenium can be maximized will be addressed.

4.1 Commercial Nanoparticles

Before studying in-house mass-selected nanoparticles, commercial Ru nanoparticles were investigated as a reference. Commercial ETEK Ru NPs, supported on carbon, Vulcan XC72, with a metal loading of 20 wt%, were annealed in a tube furnace with pure oxygen. The conditions for the oxidation were found using XRD and in situ annealing of the catalyst. The sample was mounted in a dedicated furnace in the XRD set-up, through which the oxygen could flow and the evolved gas could be monitored on-line with a mass spectrometer. The catalyst was heated up to 400^oC with intervals of 100^oC. When the set temperature was reached, an XRD pattern was recorded.

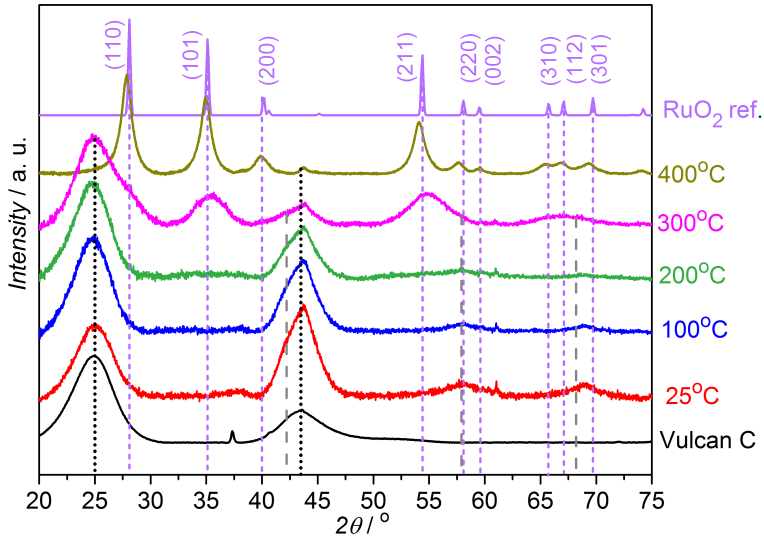

Figure 4.1: XRD patterns at different temperatures of commercial Ru NPs on Carbon Vulcan XC75. The annealing in 1 mbar O_2 was carried out in situ with a dedicated stage in the XRD set-up. After the set temperature was reached, the diffractogram was recorded. Simultaneously the evolved gas was monitored with a mass spectrometer. Reference pattern for rutile RuO_2, taken from [182], is shown and the pattern for the substrate was recorded using the same settings.

Figure 4.1 shows the diffractograms at different temperatures between room temperature and 400^oC. To make the interpretation of the peaks easy, a rutile RuO_2 reference pattern is shown [182] and a diffractogram of the carbon support was also recorded with the same settings. Even though the pattern at room temperature is dominated by the broad peaks of the support at 25^o and 43.5^o, it is possible to identify the peaks of metallic Ru at 57.9^o and 68.2^o and the shoulder at 42.2^o. The ruthenium peaks are very broad, indicating that the

particles are very small. As the temperature increases the ruthenium peaks slowly disappear and the peaks due to the rutile phase of RuO_2 start to emerge. In particular, at 300^oC broad peaks of the oxide appear, and at 400^oC more and sharper peaks become evident. By using the Scherrer equation, it is possible to estimate the mean size of the crystallite, τ, and the relative change with the temperature:

$$\tau = \frac{K\,\lambda}{\beta\,cos(\theta)} \tag{4.1}$$

where K is a a shape factor, λ is the X-ray wavelength, β is the full width at half maximum peak (FWHM), and θ is the Bragg angle [183]. It was found that the crystallite size after oxidation at 400^oC is three times bigger than the initial size, before annealing. At the same time, the peaks of the carbon disappear and have completely vanished in the pattern at 400^oC, suggesting that above 300^oC in the presence of oxygen the carbon burns into CO_2. This phenomenon was confirmed by the gas behavior monitored with a mass spectrometer. Above 300^oC, the oxygen signal drastically went down with a simultaneous peak of the CO_2 signal, confirming the oxidation of the substrate. The burning of the carbon most likely favor sintering of the particles, which are now unsupported.

The oxidation treatment was therefore carried out at 400^oC in a tube furnace with 1 bar O_2 for 1 min. These conditions were enough to fully oxidize the particles, forming the rutile phase.

The nanoparticles were then deposited on a glassy carbon disk for the electrochemical measurement by preparing a catalyst ink. The catalyst ink was obtained by mixing the oxidized RuO_2 NPs (2.6 mg) in the following order with milliQ water (7.1 mL), isopropanol (2.22 mL), 1 wt% Nafion solution (37 μL) and a 2% solution of polyvinylpyrrolidone (PVP) in ethanol (14.8 μL). Before and after adding the Nafion, the solution was horn-sonicated for a few seconds; finally, PVP was added to improve the dispersion and the solution was horn-sonicated for 2 minutes [184]. 10 μL of ink was drop-casted onto a previously polished glassy carbon disk and left to dry overnight. These are the optimised conditions to obtain a well-dispersed ink with a final loading of 10 $\mu g/cm^2$.

The OER activity of the ink in N_2 saturated 0.05 M H_2SO_4 is plotted in figure 4.2, together with the current state-of-the-art for RuO_2 nanoparticles, prepared by a chemical synthesis [64]. The activity of different samples prepared from the same ink batch and from different freshly made solutions is shown. The batch is indicated with a number, while the sample with a letter. The reproducibility between different batches of ink is poor and even within the same bacth there are scattered data (Ink-01a and b). Most strikingly, the first batch (ink-01) exhibited great activity, almost one order of magnitude higher than the ruthenium dioxide nanoparticles reported by Lee *et al.* [64]. On the other hand, the next bacthes showed much lower activity, two orders of magnitude lower than Ink-01.

We speculate that this is related to the poor control over the preparation

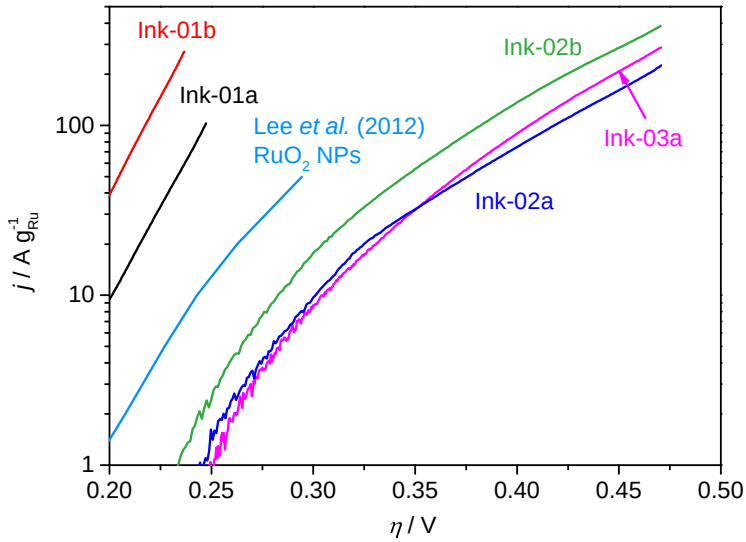

Figure 4.2: OER activity of three different batches of commercial RuO_2 ink in N_2 saturated electrolyte. RuO_2 NPs prepared through synthetic route from [64], representing the state-of-the-art for ruthenium oxide nanoparticles in acid, is shown for comparison.

of the catalyst, from the oxidation procedure, during which most or all support gets burned, to possible impurities addition during the ink preparation, and to the presence of different components that can mask the catalytic activity, e.g. Nafion. Furthermore, the absence of the carbon support made it difficult to get electrical contact, and when the contact was made the Ohmic resistance was high. Post-oxidation addition of carbon by impregnation helped the contact partially, but the ink was not well-dispersed.

This brief investigation of the catalytic activity of commercial nanoparticles points out some of the issues related to working with commercial nanoparticles and chemical synthesis. Low control on the parameters (size, shape, morphology, etc.) and influence of external components (precursors, solvents, etc.) [29,59] can often complicate the distinction between surface area and electronic effect and do not allow an accurate evaluation of the intrinsic catalytic activity. Although chemical routes are required to prepare high surface area catalysts, in order to better understand the electronic properties of ruthenium oxide, fundamental investigations on well-defined surfaces should be considered [66]. With this approach evaluating more precisely the actual catalytic activity and relate it to the size, shape and morphology of the catalyst should be possible.

4.2 Preparation of Mass-Selected Nanoparticles

Ruthenium nanoparticles were prepared by Federico Masini, using a magnetron sputter gas aggregation source (Birmingham Instruments Inc.), combined with a Lateral Time-of-Flight (TOF) mass filter, as described in chapter 3. This technique has distinct advantages compared to chemical synthesis and ink preparation. First of all, it allows for production of well-defined and mono-dispersed nanoparticles with high control over critical parameters, e.g. particle size, electrode coverage and density. Secondly, it does not introduce inherent artefacts, which might come from chemical synthesis and surfactants. The particle mass was varied between $0.035 \cdot 10^6$ to $4 \cdot 10^6$ u, which would correspond to a range in diameter of 2 to 10 nm, if the particles were spherical. From previous studies on as-deposited ruthenium nanoparticles produced with the cluster source in our laboratory, it is known that small ruthenium particles present a more regular shape, while larger particles are irregular and corrugated [147, 148]. However, for simplicity in this thesis the equivalent diameter is preferred over the particle mass unit. Figure 4.3 shows TEM image of as-deposited particles with an equivalent diameter of 4, 7 and 10 nm, respectively.

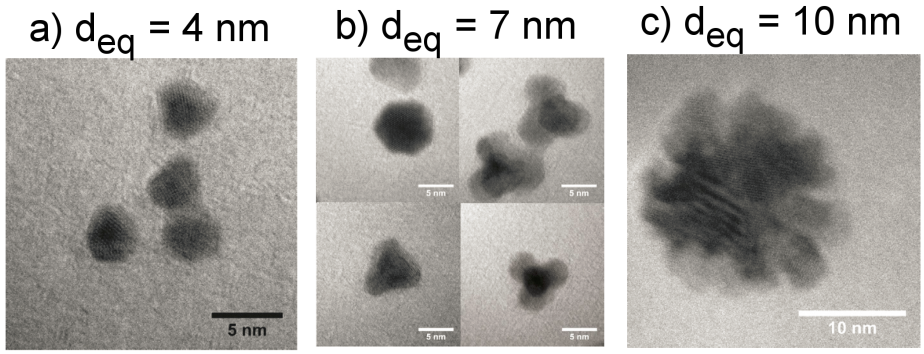

Figure 4.3: HR-TEM images, acquired at CEN, DTU, of Ru NPs prepared in our laboratories. Images taken from reference [148].

The nanoparticles were deposited onto either glassy carbon disks or gold polycrystalline samples to perform electrochemical measurements and surface characterisation, such as XPS, GA-XRD and SEM. In order to do high resolution TEM and STEM, Si_3N_4 TEM grids with a membrane thickness of 20 nm were employed.

The mass loading, used to calculate the electrocatalytic mass activity, was directly evaluated from the deposition current. Furthermore, in order to have a second independent measurement of the mass, the Ru signal from XPS was used. Indeed, the carbon corrected Ru 3d signal, X_{Ru}, is related to the projected coverage of the nanoparticles on the substrate.

4.2.1 Calculation of the Mass Loading from XPS

The total mass of ruthenium, M_{XPS}, can be estimated, by assuming spherical particles and is given by:

$$M_{\mathrm{XPS}} = \left(\frac{A_{\mathrm{XPS}}}{4\pi \left(\frac{d}{2}\right)^2} \right) \cdot m_p \cdot 1.66 \cdot 10^{-18} \cdot 10^{12} \tag{4.2}$$

where m_p is the particle mass, d is the diameter and A_{XPS} is the surface area which is calculated as

$$A_{\mathrm{XPS}} = 4\pi \cdot X_{Ru} \cdot r_{dep}^2 \tag{4.3}$$

with r_{dep}^2 the radius of the area, where the particles are deposited on, and X_{Ru} the Ru signal from the XPS spectrum.
The Ru signal fraction must be corrected for the carbon signal:

$$X_{Ru} = \frac{I_{Ru3d}}{I_{Ru3d} + I'_{C1s}} \tag{4.4}$$

I_{Ru3d} is the integration of the pair of doublets ($3d_{3/2}$ and $3d_{5/2}$) normalised to the Scofield cross section sensitivity factor, S_{Ru}:

$$I_{Ru3d} = \frac{I_{Ru3d_{3/2}} + I_{Ru3d_{5/2}}}{S_{Ru}} \tag{4.5}$$

I'_{C1s} is the corrected integration of the carbon signal:

$$I'_{C1s} = I_{C1s} \left(1 - \frac{\pi(r_{electrode}^2 - r_{dep}^2)}{\pi \cdot r_{electrode}^2} \right) - I_{Ru3d} exp \left(-\frac{d}{\lambda \cdot cos(\alpha_{detector})} \right) \tag{4.6}$$

where $r_{electrode}^2$ is the radius of the electrode (substrate), r_{dep}^2 is again the radius of the deposited area, λ is the mean free path and $\alpha_{detector}$ is the angle between the detector and the normal to the surface of the sample. In this way it was possible to evaluate and compare the total mass from XPS with the value from the deposition current. Figure 4.4 shows the comparison between the two techniques for different particle sizes. Each color represents a different size (3, 5, 7 and 9 nm). For small particles, up to 7 nm, there is a good correlation between the two measurements. Unfortunately, this is not the case for the largest particles. The mass evaluation from XPS is based on the assumption of spherical particles, which is not valid for large particles. This could explain some of the scatter in the data that will be showed later in the chapter.

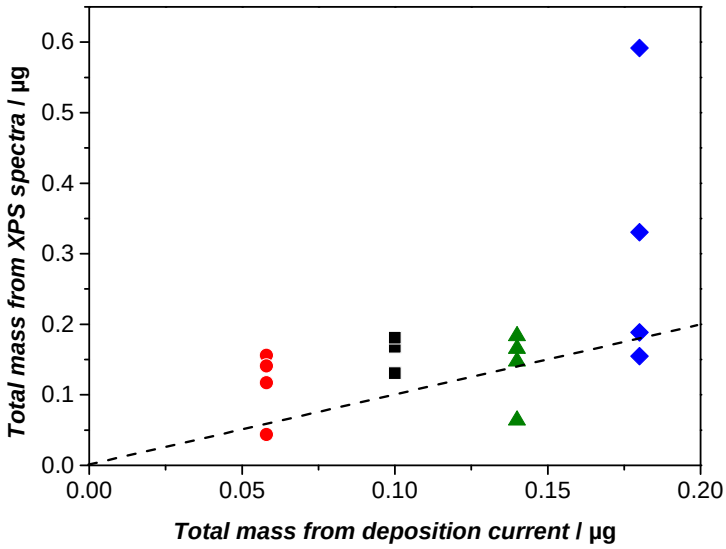

Figure 4.4: Comparison between the total mass evaluated from XPS ruthenium signal and from the deposition current. The dashed line represent the theoretical linear correlation (1 : 1) between the two methods. Each color and symbol represents a different particle size: 3 nm (red cirlce), 5 nm (black square), 7 nm (green triangle), and 9 nm (blue rhombus).

4.3 As-Deposited Ruthenium Nanoparticles

Anodically grown ruthenium oxides are known to be more active but less stable than thermally grown oxides [50, 62, 63, 65, 71]. Furthermore, Strasser and coworkers recently observed that anodically grown oxides of ruthenium nanoparticles, in the range of $4 - 6$ nm, are even more unstable than extended surfaces [85]. In order to confirm those results and to evaluate the activity and corrosion rate, as-deposited ruthenium nanoparticles (Ru NPs) were investigated and characterised. XPS of as-deposited 9 nm nanoparticles on glassy carbon shows the presence of two pairs of doublets of Ru 3d level, indicating the presence of both metallic and oxidised ruthenium (figure 4.5).

The electrochemical activity and stability of 9 nm Ru NPs were measured in a RRDE set-up in N_2 saturated 0.05 M H_2SO_4. The capacitance and Ohmic corrected CV is shown in figure 4.6.

As expected, the stability of these particles is extremely poor. The RuO_4 formation, the reduction of which was followed on the Pt ring, accounts for the 15% of the total anodic current. A similar result was obtained on commercial Ru/C nanoparticles [85] and on polycrystalline samples [58]. From the ring charge it is also possible to estimate the corrosion rate, as mass loss. By assum-

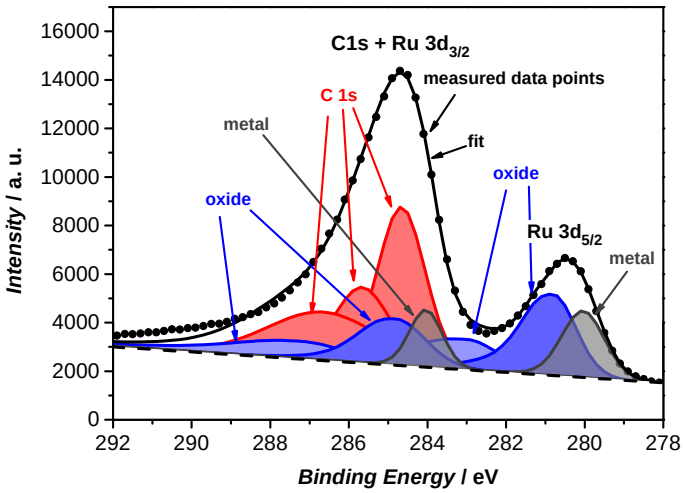

Figure 4.5: XPS spectrum of the Ru 3d core level of as-deposited 9 nm Ru NPs. XPS performed by Federico Masini in the Omicron system.

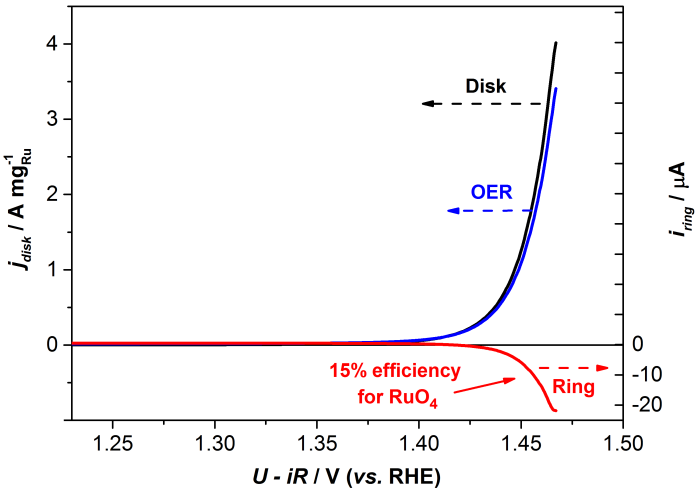

Figure 4.6: RRDE measurement of as-deposited 9 nm Ru NPs in N_2 saturated electrolyte at 1600 rpm. The black line represents the total current measured at the disk, the blue one the current corresponding to OER, evaluated through the ring current in red. During the CV, the ring potential was held at 1.1 V to reduce the produced RuO_4.

ing that the reduction of RuO_4 is a one electron process [104], the number of dissolved Ru atoms, n_{Ru}, and the corresponding mass, M_{Ru}, are, respectively:

$$n_{Ru} = \frac{Q_{ring}}{e^-} \tag{4.7}$$

$$M_{Ru} = \frac{n_{Ru}\, MW_{Ru}}{N_A} \tag{4.8}$$

From which the mass loss percentage, M_{loss}, is

$$M_{loss}\% = \frac{M_{Ru}}{M_{dep}} = 37\,\% \tag{4.9}$$

Although they are very unstable, it is worth noticing that the mass activity of our particles extrapolated at 0.25 overpotential is 2.52 A/mg_{Ru}, which is one order of magnitude higher than the state-of-the-art for Ru nanoparticles in acid [81] and two orders of magnitude than RuO_2 NPs [64].

Another way of expressing the high instability is by performing a chronoamperometric test (CA) at 1.5 V (vs. RHE), shown in figure 4.7. In less than 10 minutes, the current approaches the substrate background current, indicating that the catalyst has completely dissolved into the solution. A 100% dissolution was confirmed by ex situ analysis of the electrolyte with ICP-MS.

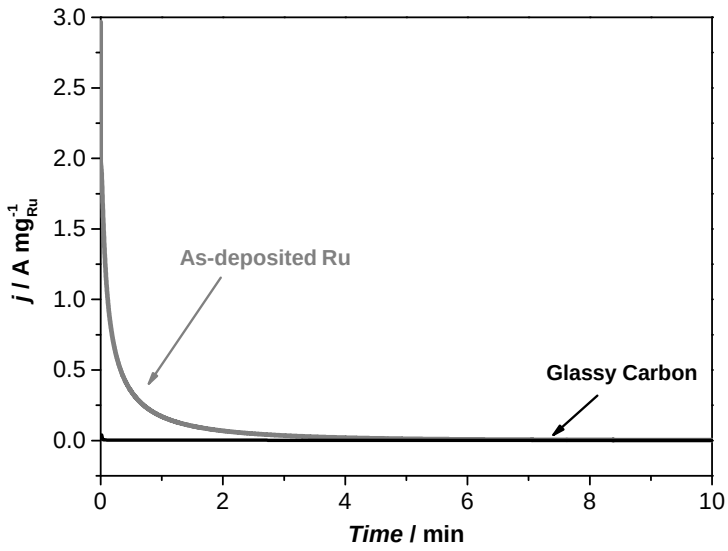

Figure 4.7: Chronoamperometry of 9 nm Ru NPs at 1.5 V (vs. RHE) in N_2 saturated 0.05M H_2SO_4 at 1600 rpm

Based on the ICP-MS data and the Chronoamperometry test, it is possible to roughly estimate the corrosion rate. ICP-MS sample was taken after 20 minutes of CA, but the current reaches the background (the current due to the glassy carbon) in ~ 5 minutes. Therefore, if we assume that it takes 5 minutes to dissolve the total mass of the catalyst ($M_{dep} = 0.18\ \mu$g) that is deposited onto an electrode with a geometric area of $A_{geo} = 0.196$ cm^2 and a projected coverage of $\delta = 15\%$, the estimated corrosion rate is:

$$\frac{dRu}{dt} = \frac{M_{dep}}{A_{geo} \cdot \delta \cdot t} = \frac{180\,nm}{0.196 \cdot 0.15\,cm^2 \cdot 300\,s} = 20\,ng\,cm^{-2}\,s^{-1} \qquad (4.10)$$

which is higher than the corrosion rate reported recently by Cherevko *et al.* for extended surface [57]. At 1.5 V they observed a corrosion rate for Ru of 12 ng cm^{-2} s^{-1}. The difference can be likely explained by the distinct form of the catalysts, in agreement with the observation by Reier *et al.* on Ru nanoparticles and bulk: NPs corrode much faster than extended surfaces [85].

Hence, this kind of catalyst cannot be considered for applications in a real electrolysers, unless the stability is greatly improved. A first strategy would be to pre-treat the particles in order to fully oxidise them or to form a sufficiently thick oxide layer. In this attempt, two different pre-oxidation treatments were adopted:

1. Oxygen plasma in UHV chamber
2. Thermal treatment in oxygen flow at atmospheric pressure

4.4 Oxidation Treatment 1 - Oxygen Plasma

After deposition and XPS characterisation, Ru NPs were moved to another UHV compatible system, the sputter chamber, through exposure to air, for the oxidation treatment. In the sputter chamber, it is possible to create a plasma of oxygen by RF biasing the substrate holder, which can be used to oxidise the catalyst. To avoid to ruining the sample, mild conditions were chosen: RF power of 30 W, base pressure of 20 mTorr, and 20 sccm of O_2 flow for 2 min. The temperature was varied for the plasma treatment between room temperature and 200^oC.

In order to verify the oxidation of the surface of the nanoparticles after the O_2-plasma treatment and to compare it with the as-prepared NPs, XPS was performed on two samples, where the oxidation was carried out at room temperature.

Figures 4.8 a) and b) show XPS spectra after oxidation of 4 nm and 7 nm RuO_x NPs, respectively. In both spectra, a metallic component is still present after the oxidation treatment. For the big particles, 7 nm, the metallic contribution is higher than for the small particles which are almost completely oxidised, at least at the surface. This might be simply related to different size

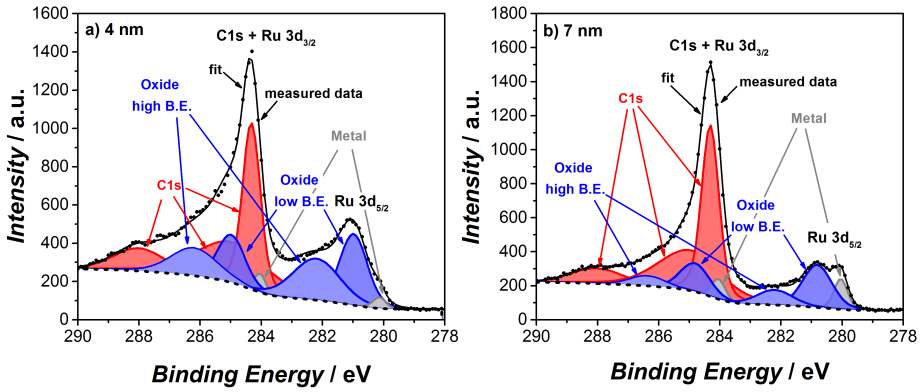

Figure 4.8: XPS spectra of the Ru 3d core level of plasma treated a) 4 nm and b) 7 nm RuO_x NPs. XPS performed by Paolo Malacrida in the ThetaProbe XPS.

and shape of the particles. In the attempt to further oxidise Ru, the substrate was heated up to 200^oC during the oxidation.

The mass activity of the plasma treated RuO_x NPs at 0.25 V overpotential as a function of the particle size (equivalent diameter and cubic root of the single particle mass) is plotted in figure 4.9. The activity of the as-deposited Ru NPs is also shown for comparison. The temperature of the substrate was varied for a number of samples and the influence of the temperature was investigated. The mass activity was evaluated by first correcting the current for Ohmic drop and capacitance and then normalising it with the ruthenium mass loading, which was measured from the neutralisation current in the cluster source. This value was preferred over the XPS estimations, because it is not based on the spherical particles assumption. The overpotential of 0.25 V was chosen in order to make an easy comparison with literature [64, 81, 85].

The not heated particles exhibit the highest activity, although lower than the as-deposited NPs, with a peak at around 5 nm. The heated samples show much lower activity without a clear particle size effect. Furthermore, it seems that heating the sample up to 60^oC or 200^oC does not influence significantly the activity.

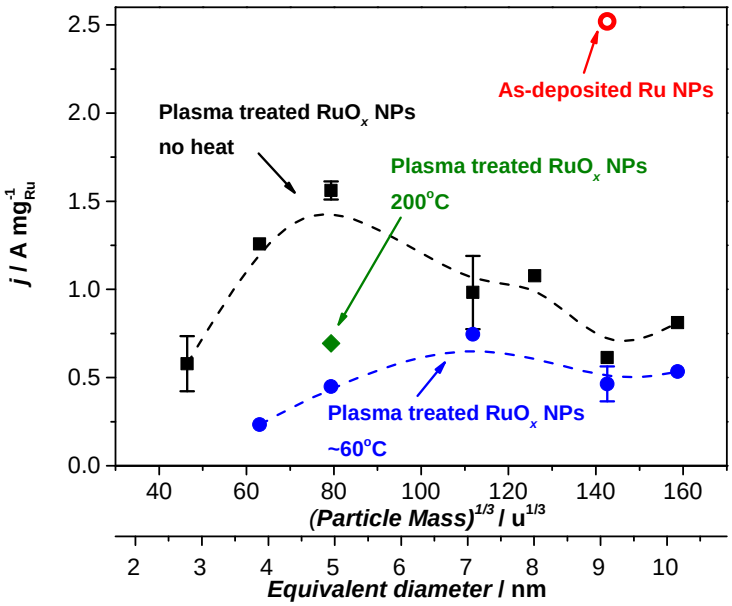

Figure 4.9: OER mass activities at 0.25 V overpotential for different particle size of O_2-plasma treated glassy carbon supported RuO_x NPs. The values are taken from the first Ohmic and capacitance corrected CV, performed at 20 mV/s, 1600 rpm in N_2 saturated 0.05 M H_2SO_4. When reported, the errors bars are based on two or three independent measurements. Not all the measurements were repeated.

RRDE measurement were performed for evaluating the catalytic stability of these particles (figure 4.10). If we compare the plasma treated with the as-deposited particles (figure 4.10 and figure 4.6), a few differences can be distinguished. The activity is ~ 5 times lower and the corrosion is reduced. The RuO_4 Faradaic efficiency is around 15% for the as-deposited particles, while for the plasma treated it is $\sim 8\%$. If we calculate the Ru mass loss percentage, by integrating the ring current in the first cycle, we obtain 18%, which is almost half of the mass loss for the as-deposited Ru NPs. Although the stability is somewhat improved compared to the as-deposited particles, the durability of the plasma treated NPs is still not sufficient and better endurance needs to be achieved.

Figure 4.11 shows the thermodynamically most stable species as a function of atomic oxygen partial pressure and temperature. In the conditions of the sputter chamber, the formation of RuO_4 is thermodynamically favored over the formation of RuO_2. RuO_4 is an unstable and volatile compound [162]. If the evaporation of ruthenium is favored during the oxidation process, the

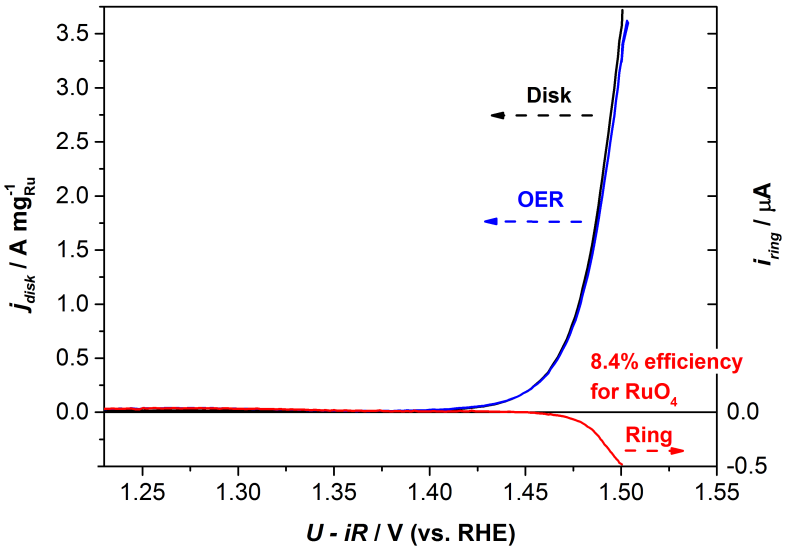

Figure 4.10: RRDE measurement of O_2-plasma treated at room temperature 8 nm RuO_x NPs in N_2 saturated electrolyte at 1600 rpm. The black line represent the disk current, the red line the ring current and the blue line the current corresponding to oxygen evolution. The ring was held at 1.1 V to reduce the collected RuO_4.

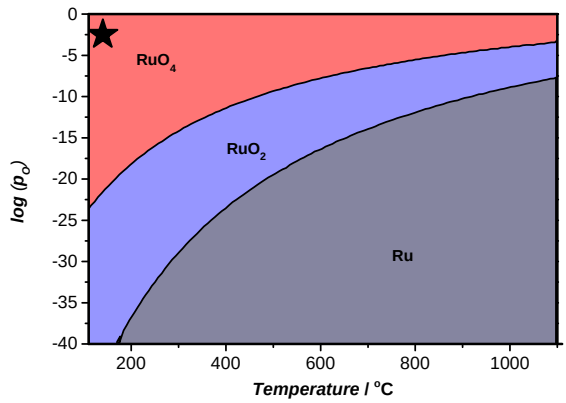

Figure 4.11: Partial pressure of atomic oxygen versus temperature, showing the thermodynamically most stable species of Ru. The star denotes the region of the deposition conditions.

total mass of the particles is not known with precision anymore. This means that is not possible to obtain rigorous conclusions about the particle size effect. Nevertheless, these findings mean that the mass activity of the plasma treated NPs is to some extends underestimated. Because the oxidation in UHV might introduce significant changes in the nanoparticles through evaporation of Ru as RuO_4, misleading the conclusions, further characterisation and investigation on the stability were not carried out.

4.5 Oxidation Treatment 2 - Thermal oxidation

Differently from the oxygen plasma treatment, oxidation with oxygen flow at atmospheric pressure does not favor the formation of RuO_4 thermodynamically, as it is shown in figure 4.12.

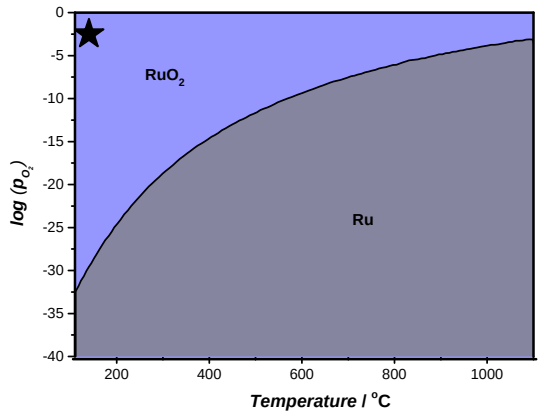

Figure 4.12: Partial pressure of molecular oxygen versus temperature showing the thermodynamic most stable species of Ru. The symbol denotes the region of the annealing conditions.

Therefore, a thermal treatment after deposition, was carried out in a tube furnace. The particles were heated at 400^oC for 1 min in 1 bar O_2, with a ramp time of 20^o C/min, i.e. similar conditions to the commercial Ru/C nanoparticles.

4.5.1 Characterisation of the Nanoparticles

In order to verify the effectiveness of the oxidation treatment and to extensively characterise the structure and morphology of the particles, several techniques have been employed: XPS and GA-XRD to verify the composition of surface and bulk; SEM, HR-TEM and STEM to investigate shape and morphology.

Figure 4.13 shows the XPS spectrum of thermally oxidised 9 nm RuO_2 NPs. It can be seen that the peak due to the metallic component is absent in this spectrum, which exhibits only the characteristic pair of doublets due to RuO_2 [165], in opposition to as-deposited (see XPS in figure 4.5) and plasma treated (see XPS in figure 4.8 b)) nanoparticles of similar size. This suggests that the surface is completely oxidised and the oxide layer should be at least 1.5 nm thick.

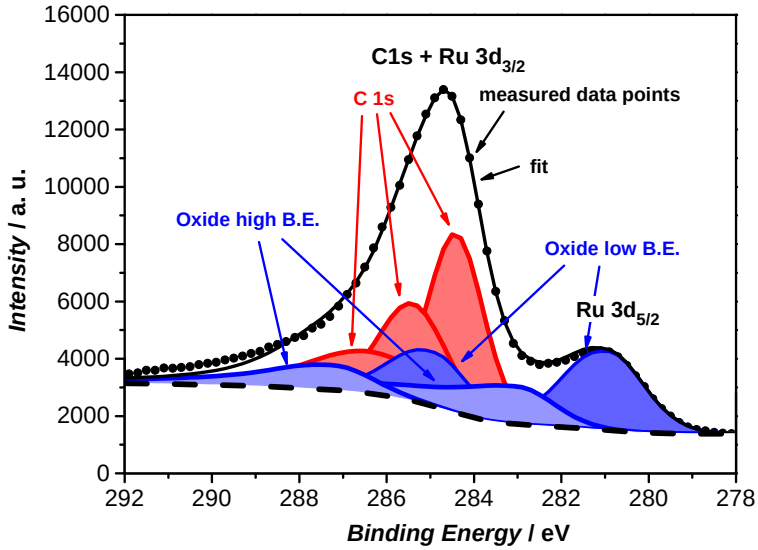

Figure 4.13: XPS spectrum of the Ru 3d core-level of thermally annealed 9 nm NPs. XPS performed by Federico Masini in the Ohmicron system.

By increasing the electrode coverage of the deposited nanoparticles up to more than 100% (mass loading of 20 $\mu g/cm^2$), it was possible to perform GA-XRD and gather information about the bulk composition. Figure 4.14 shows the XRD diffractograms of as-deposited and thermally oxidized 9 nm RuO_2 NPs on a gold disk with reference patterns of metallic Ru, rutile RuO_2 and Au. The loading was not enough to completely cover the signal coming from the substrate, even using glancing angle geometry, and the main peaks are indeed due to the gold. However, it is possible to identify the main peaks of the metal and of the rutile structure. In the diffractogram for as-deposited NPs, the main peak of metallic Ru is visible as a shoulder to the more intense Au peak. In the thermally oxidised pattern, on the contrary, this peak vanishes, while other three peaks, due to RuO_2, appear. A few other peaks due to the oxide are also visible, but less pronounced. This data confirms what was observed by XPS and indicates that also the bulk is oxidised.

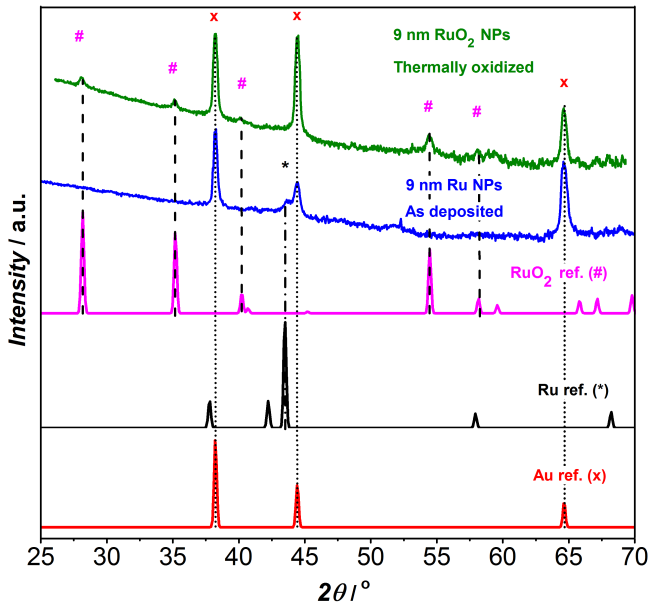

Figure 4.14: GA-XRD of as-deposited and thermally oxidised 9 nm NPs deposited on a gold disk. Au [185], Ru [186] and RuO_2 [182] reference patterns are also shown.

A further confirmation of the formation of RuO_2 was given by High Resolution TEM and Fast Fourier Transform (FFT) on thermally annealed nanoparticles deposited on a Si_3N_4 TEM grid (4.15).

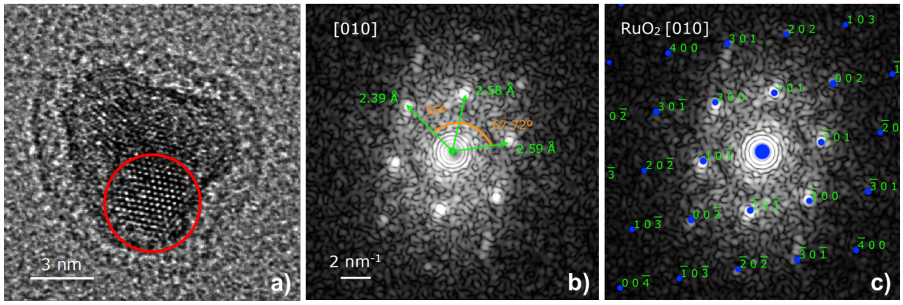

Figure 4.15: a) HR-TEM micrograph of 7 nm RuO_2 NPs. The red circle highlights an area with high atomic resolution. b) FFT of the atomically resolved part of the particle. c) FFT overlapped with a simulated diffraction pattern of RuO_2 along the (010) zone axis. Data acquired and elaborated by Davide Deiana.

A HR-TEM micrograph of a 7 nm particle is shown in figure 4.15 a). In the picture, a red circle highlights a high atomic resolution area. The Fast Fourier Transform of this region is shown in figure 4.15 b) and the values could be matched only with ruthenium dioxide. Finally, a simulation of the diffraction pattern for RuO_2 along the (010) zone axis is overlapped with the FFT in figure 4.15 c), exhibiting a good superimposition, within the error $(5 - 10\%)$.

The morphology of the particles can be observed in figure 4.16, which represents HAADF-STEM images of four different particle size, 3, 5, 7 and 9 nm. Thermally oxidised particles have very similar shape to the as-deposited ones (see figure 4.3). Small particles, indeed, show a much more regular and spherical shape, whereas larger particles, like 9 nm particles, exhibit rough and corrugated morphology [148]. The projected particles area distribution was calculated from

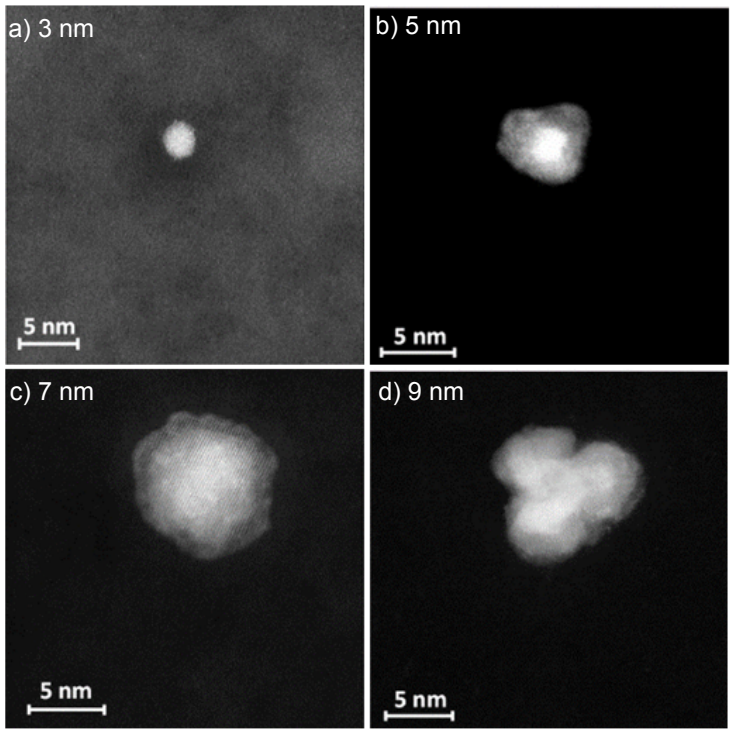

Figure 4.16: HAADF-STEM of thermally oxidised RuO_2 NPs on Si_3N_4 TEM grid for particle size of a) 3, b) 5, c) 7, and d) 9 nm. STEM images acquired by Davide Deiana.

STEM images and it is shown in figure 4.17.

The great advantage of the cluster source is the time of flight mass filter used to select a specific single particle mass. As it is illustrated from the figure,

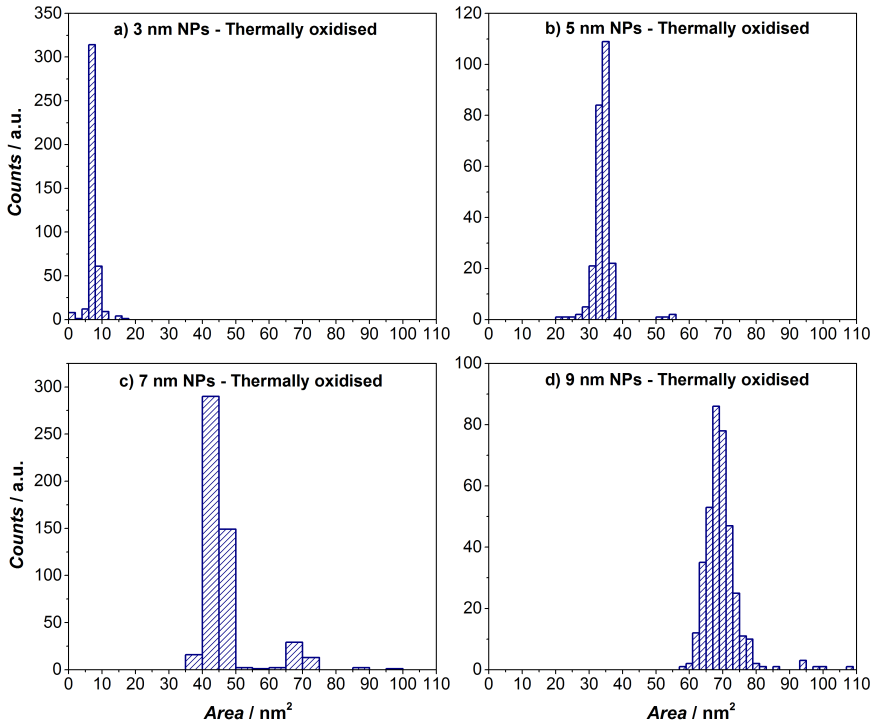

Figure 4.17: Projected particles area distribution of thermally oxidised RuO_2 NPs for four different particle sizes: a) 3, b) 5, c) 7, and d) 9 nm.

the deposited particles have a very narrow dispersion (mono-dispersed), which allows the investigation of a specific size, hence the effect of the particle size. Figure 4.17 c), representing the area distribution of 7 nm RuO_2 particles, shows a small fraction ($\sim$ 4%) of particle with a higher mass. This undesired mass arises from multiple of the targeted mass, that possesses a charge e equals to n (with n an integer). Typically they come from double or triple mass. However, at our laboratory Masini *et al.* have developed a general diagnostic strategy to circumvent this issue and improve the quality of the deposition [153]. The method is based on following over time the changes in the deposition current vs. mass curves (see figure 3.4 in section 3.1.1.2), measured with TOF, which is related to the quality of the deposition. Variation of the shape of the curve may indicate the presence of undesired mass or a low quality deposition, which in turn may introduce unwanted masses and morphologies in the sample. Only the samples with the highest deposition quality were used for electrochemical measurement, i.e. where the feature of the curve remains constant over the

deposition.

Finally, SEM was used to verify any sintering process after the annealing (figure 4.18). The difference in particle density between fig. 4.18 a) and b) is likely due to imaging of different areas on the electrode, where the particles are randomly distributed. However, the overall projected coverage is always set to the same value.

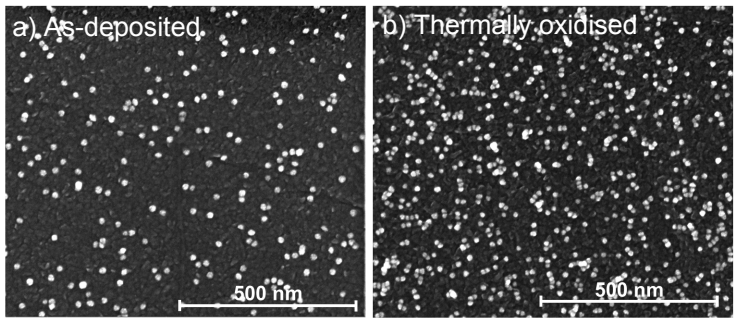

Figure 4.18: SEM micrographs of the same sample 9 nm NPs a) as-deposited and b) thermally oxidised on glassy carbon. Magnification 125000x; accelerating voltage 5.00 kV; secondary electron detector.

4.5.2 Electrocatalytic Activity

The effect of the oxidation treatment and the full oxidation of the particles was observed in the electrochemical behavior as well. The cyclic voltammetry of a thermally oxidised sample compared to a as- prepared Ru sample of the same particle size is plotted in figure 4.19.

RuO_2 NPs, in agreement with previous report by Stucki *et al.* and Vukovic [65, 71], exhibit much lower activity than the not-oxidised particles. The electrochemical activity was measured in a RRDE set-up in N_2 saturated 0.05 M H_2SO_4.

The OER mass activity of RuO_2 NPs as a function of particle size is shown in figure 4.20. Both equivalent diameter and cubic root of the single particle mass is used. The cubic root of the particle mass is proportional to the size of the particles. The mass loading was directly evaluated from the neutralisation deposition current in the cluster source. The mass activity was evaluated at 0.25 V overpotential from the Ohmic and capacitance corrected cyclic voltammogram.

There is some scatter in the data, which we associate with uncertainties in the total mass deposition. A lot of efforts was made in the attempt to improve the scatter, and independent methods to evaluate the mass were employed (see

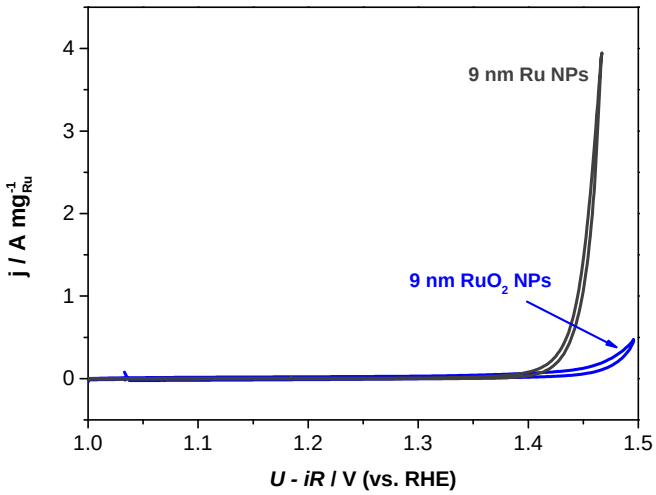

Figure 4.19: Ohmic drop corrected cyclic voltammograms of 9 nm Ru and RuO_2 NPs, deposited on a glassy carbon, recorded at 20 mV/s and 1600 rpm.

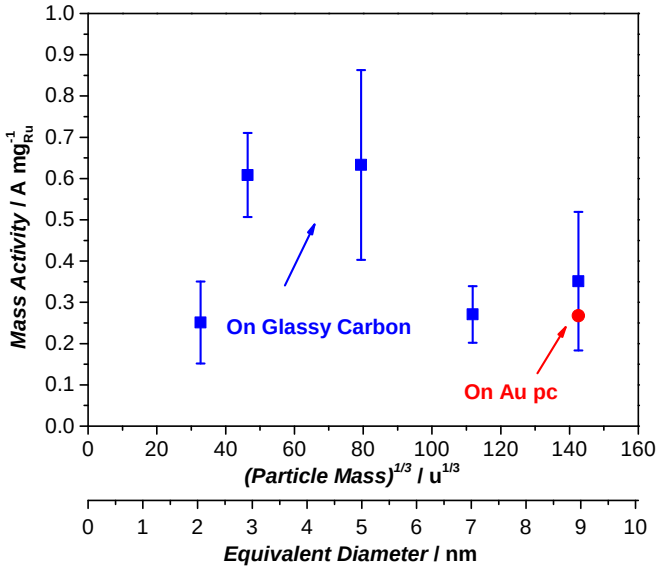

Figure 4.20: OER mass activity of different particle size of RuO_2 NPs on glassy carbon versus equivalent diameter and cubic root of single particle mass at 0.25V overpotential. OER mass activity on Au electrode is also plotted. Error bars are standard deviation based on three independent measurements.

section 4.2). However, we tentatively describe an effect of the particle size on the OER activity and we identify a maximum at around $3-5$ nm.

In figure 4.20 the mass activity of 9 nm RuO_2 on gold polycrystalline electrode is also plotted, exhibiting similar performance of the glassy carbon supported catalyst. This finding confirms that the superior activity of the nanoparticles is not due to carbon corrosion, but to the intrinsic catalytic activity of ruthenium. Furthermore, it may indicate that ruthenium dioxide activity, differently from other OER catalysts, e.g. manganese, nickel and cobalt oxides, is not affected by the presence of gold [96, 97, 187].

It is challenging to evaluate the specific activity, since it is complicated to assess the catalytically active surface area. However, should the particles be spherical, it could be estimated from the single particle mass and the coverage. STEM images showed that larger particles are not spherical, hence the assumption is valid only for smaller particles, up to 7 RuO_2 nm. The specific activity is shown in figure 4.21. In the plot, 9 nm particles were also included for reference.

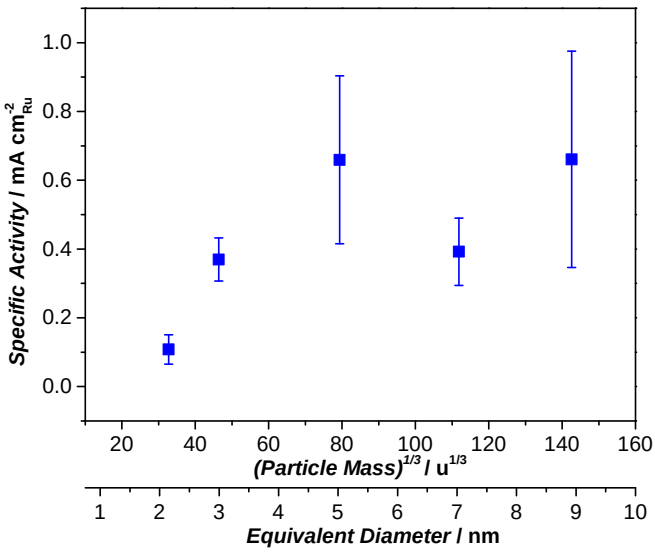

Figure 4.21: OER specific activity of different particle size of RuO_2 NPs on glassy carbon versus equivalent diameter and cubic root of single particle mass at 0.25V overpotential. Error bars are standard deviation based on three independent measurements.

Smaller particles exhibit decreasing specific activity. This trend is analogous to what was observed and predicted for the oxygen reduction reaction (ORR) on platinum nanoparticles [72, 78, 188], which suggests that, like ORR, the terraces

are the active sites for OER. The amount of terrace site would be maximized for a specific size and smaller particles would display lower specific activity, due to the decreased amount of the active sites.

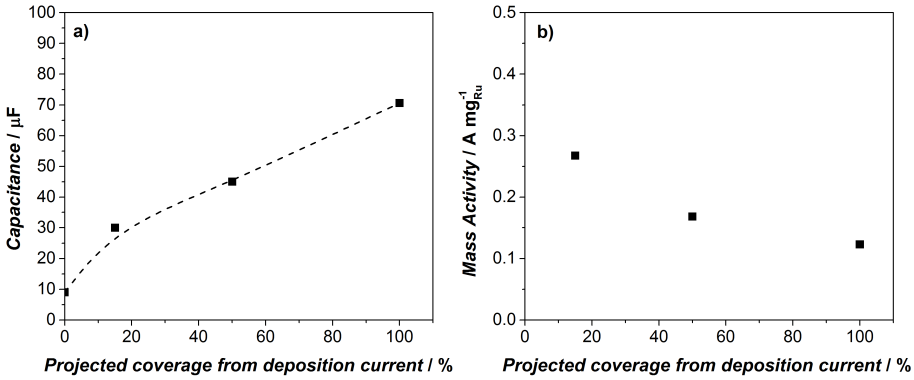

Figure 4.22: a) Capacitance vs. projected coverage evaluated from the neutralisation current during the cluster deposition for 9 nm RuO_2 NPs deposited on Au(111) gold disk. The capacitance was measured with electrochemical impedance spectroscopy. b) Mass activity at 0.25 V overpotential versus the projected coverage.

To establish the electrocatalytic properties of RuO_2 NPs, various coverage of 9 nm particles on the substrate was investigated. An indication of change in coverage can be obtained from the capacitance. Since it was observed that the glassy carbon capacitance changes irregularly when heated in oxygen and varying the substrate does not affect the activity, Au(111) was used instead. Figure 4.22 a) shows the capacitance versus the projected coverage for a few distinct coverage. The capacitance increases as the coverage increases, and, as expected, at higher coverage the increase is less pronounced, due to particle agglomeration.

Interestingly, if we plot the mass activity of the same particles versus the coverage (figure 4.22 b), it looks like the activity increases for low coverage, in contrast to what observed by Arenz and coworkers on size-selected Pt nanoparticles for ORR [73]. However, the difference is comparable to the error bar calculated on glassy carbon supported nanoparticles at 15% coverage. Hence, more experiments are required in order to give a rigorous answer. Furthermore, it would be much more interesting to investigate the effect of the coverage on small and spherical nanoparticles, e.g. 2 or 3 nm.

4.5.3 Stability

While the activity was recorded on the disk electrode by cycling the potential between 1.0 V and 1.5 V (vs. RHE), the Pt ring electrode was held at

the potential at which the corrosion products can be detected. However, ring measurements for the thermally oxidised NPs exhibited negligible currents, indicating that the disk current can be entirely accounted for oxygen evolution or that the corrosion is below the detection limit of this technique.

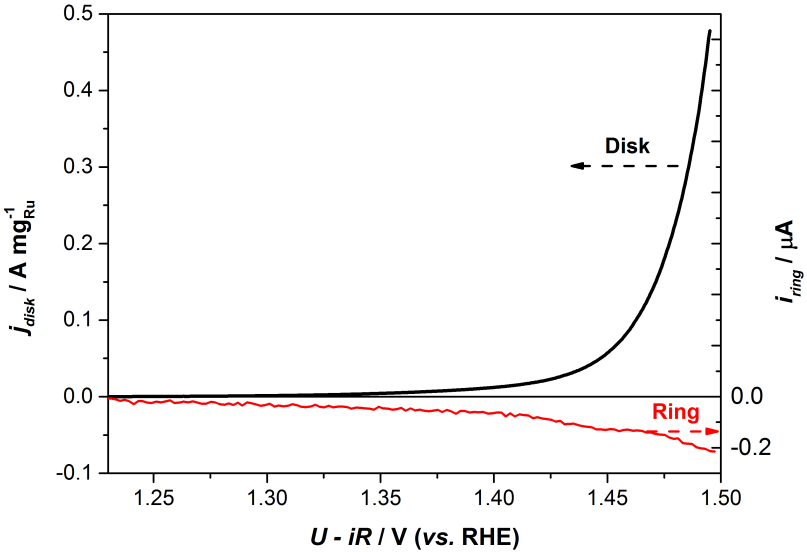

Figure 4.23: RRDE measurement of 9 nm RuO_2 NPs in N_2 saturated electrolyte at 1600 rpm. The black line represents the disk current, while the red one is the current at the ring. The ring was held at 1.1 V to reduce the collected RuO_4.

Figure 4.23 shows the RRDE measurement, where the ring current approaches zero. Because the ring current is close to the noise level, it is difficult to calculate the Faradaic efficiency for RuO_4 dissolution. However, it is estimated to be $\sim 1\%$. This behavior is very different from the as-deposited particles. The thermal treatment in oxygen improved the stability of the catalyst. Oxygen Reduction Reaction at the ring confirmed that all the disk current can be accounted only for oxygen evolution, exhibiting a Faradaic efficiency close to 100% (figure 4.24).

As pointed out by McCrory *et al.*, ORR at the ring is not always simple and it is affected by bubble formation and fast local oxygen saturation [100]. Hence, to reinforce the conclusion that the disk current can be ascribed to oxygen evolution, the evolved oxygen was measured with a gas chromatograph. A different set-up and a sealed cell had to be used, in order to get a leak-tight system. A chronoamperometry measurement of one hour at 1.6 V (vs. RHE) was performed on a 9 nm RuO_2 sample, deposited on a gold foil, in helium saturated 0.05 M H_2SO_4. Every ten minutes a sample of the gas in the

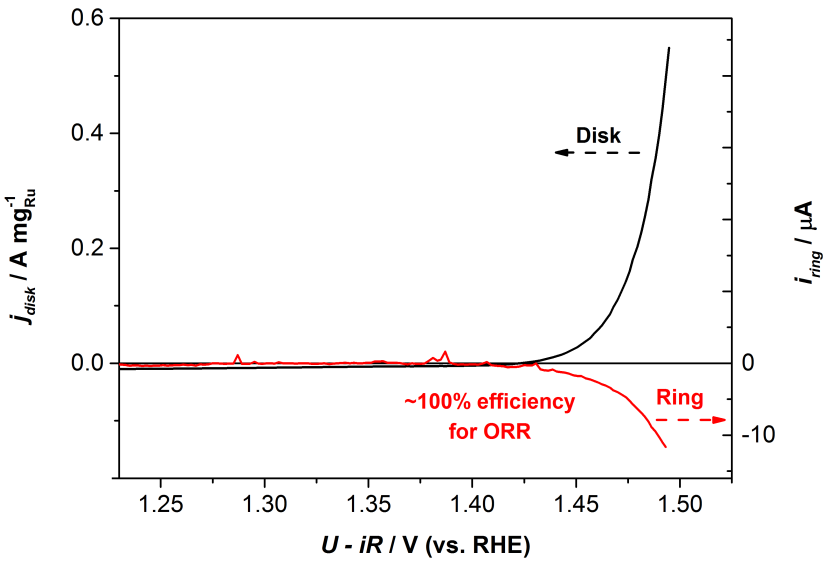

Figure 4.24: RRDE measurement of 5 nm RuO_2 NPs in N_2 saturated electrolyte at 1600 rpm. The black line represents the disk current, while the red one is the current on the ring. The ring was held at 0.4 V (vs. RHE) to reduce the oxygen evolved at the disk.

headspace was injected in the gas chromatograph and the composition of the sample was analysed. In figure 4.25 a) the oxygen concentration detected from the Gas Chromatograph is compared with the theoretical values extrapolated by integration of the chronoamperometric current. During the experiment, the concentration of nitrogen was also monitored, in order to verify the presence of leaks. Furthermore, the relation between nitrogen and oxygen was monitored without running the reaction. The measured data were then corrected, based on the concentration of N_2, which remains almost negligible for the entire duration of the experiment. The test was repeated twice. The measured efficiencies are higher than the theoretical values (figure 4.25 b) and the difference becomes more important with time, which could be related to the increase in oxygen pressure.

The durability of thermally oxidised particles is undoubtedly improved compared to the freshly prepared samples, which have a lifetime of less than 10 minutes at 1.5 V. Figure 4.26 shows a chronoamperometry test of 15 hours at 1.5 V (vs. RHE) in N_2 saturated electrolyte at 1600 rpm of 9 nm RuO_2 NPs.

At the beginning of the test there is a drastic decrease in activity, which might be due to several effects: a) loss in active sites induced by rearrangement of the surface, b) ruthenium dissolution, c) loss of surface area due to agglomer-

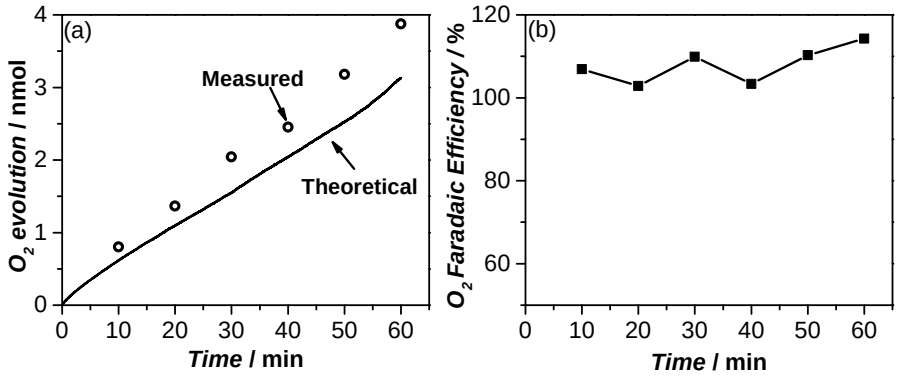

Figure 4.25: (a) Oxygen concentration measured with the gas chromatograph (dots) compared with the theoretical values estimated from the current (solid line). (b) O_2 Faradaic efficiency as a function of time.

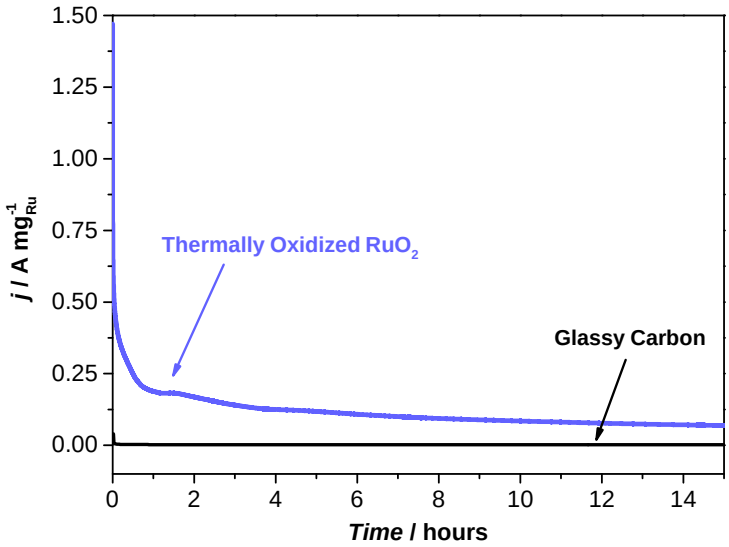

Figure 4.26: Chronoamperometry test of 9 nm RuO_2 NPs at 1.5 V (vs. RHE) for 15 hours in N_2 saturated 0.05 M H_2SO_4 at 1600 rpm.

ation, or d) blocking of the sites due to contamination. ICP-MS analyses of the electrolyte after 15 hours test showed that almost 30% of ruthenium dissolved into the solution. SEM image of the 9 nm RuO_2 after electrochemistry (figure 4.27) revealed the presence of small agglomerates of particles which were not

observed neither in the as-deposited nor in the thermally annealed sample (see figure 4.18). This observation indicates that after few hours of chronoamperometry test, the particles start to migrate. Similar phenomenon was observed by Arenz and coworkers on size-selected Pt nanoparticles upon electrochemical cycles [189]. Since the loss in activity is so sudden and significant, the best

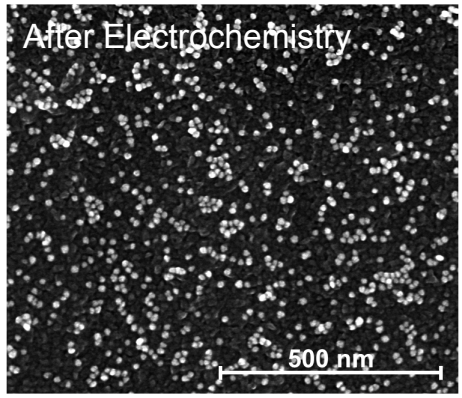

Figure 4.27: SEM micrograph of a 9 nm thermally oxidised particles on a glassy carbon after 4 hours of chronoamperometry at 1.5 V. Magnification 125000x; acceleration voltage 5.00 kV; secondary electron detector.

explanation seems more likely a combination of the above mentioned processes.

The loss in activity after one hour is shown versus the particle size in figure 4.28, where the initial mass activity at 1.5 V is displayed together with the activity after one hour chronoamperometry. The activity loss is almost one order of magnitude. The trend in activity as a function of size after one hour stability test seems to follow the initial behavior, where a more clear maximum can be identified at around 5 nm. Interestingly, the error bars are drastically reduced after 1 hour. This may indicate that the initial uncertainty could arise from the oxidation treatment.

Heitbaum *et al.* [116] using isotope labeling of the electrolyte and the oxide, suggested that the lattice oxygen atoms in Ru and RuO_2 films are involved in the OER mechanism, hence the evolution of oxygen occurs via the oxide. They observed similar results both for Ru and RuO_2, alluding to a similar mechanism. However, it is still not clear why thermally oxidised nanoparticles are more stable than the as-deposited one. What happens under reaction conditions? Can we directly observe differences in the dissolution mechanism?

In the attempt to answer to these questions, EC-STM was used to examine the particles under OER conditions. Unfortunately, acquiring images of nanoparticles with atomic resolution in EC-STM is extremely challenging and we were not successful. Nevertheless, we were able to directly observe very dis-

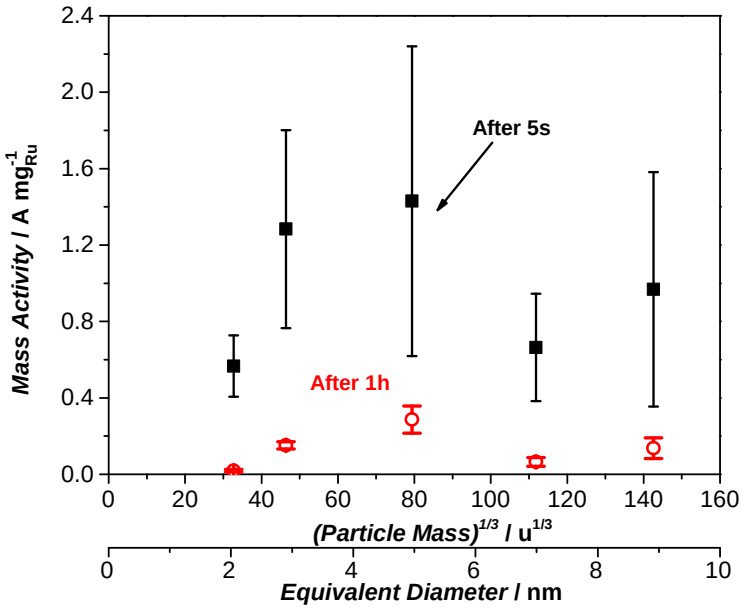

Figure 4.28: OER mass activity at 1.5 V (vs. RHE) for different particle size of RuO_2 at the beginning and after 1 hour CA. The initial value was taken after 5 seconds to avoid the initial charging current.

tinct behavior of thermally annealed and as-deposited particles under reaction conditions.

Figure 4.29 shows potentiodynamic images of as-deposited and thermally oxidised NPs in solution. As mentioned above, it is problematic to acquire images of nanoparticles in EC-STM, therefore small particles of 3 nm were preferred and a coverage of 1% of a monolayer was used. This was to minimize the height of the particles, hence cover the movement of the tip in the z-direction. The potential was slowly increased from 1.3 V, prior OER on Ru and Ru dissolution onset, to 1.5 V (vs. RHE) and then sweeped back to 1.3 V. As the potential is raised, the as-deposited nanoparticles disappear from view (figure 4.29 a), indicating that they undergo heavy corrosion as soon as the potential is above the dissolution potential (1.38 V vs. RHE [105,116]). On the contrary, the thermally oxidised NPs (figure 4.29 b) do not exhibit appreciable corrosion in this potential range. The aspect and the shape of the nanoparticles is significantly influenced by the shape of the tunneling tip. However, the tip convolution does not affect the overall observations.

The presented microscopic observations are in close agreement with the electrochemical tests (RRDE and chronoamperometry) and literature [57], and

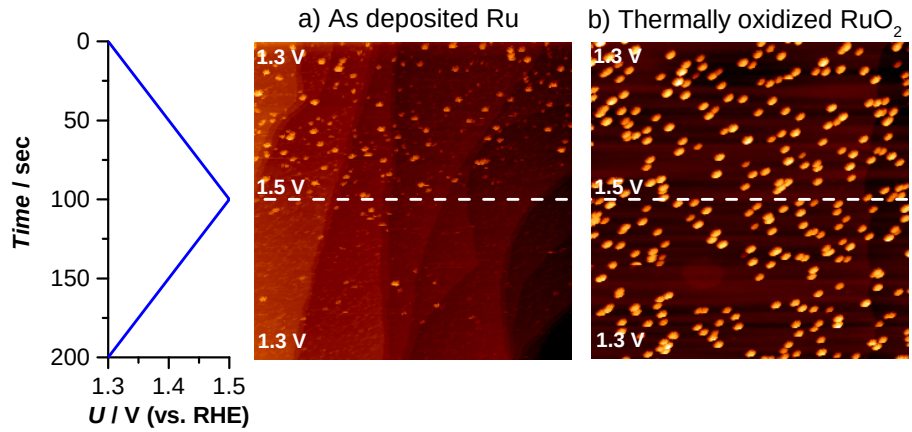

Figure 4.29: Potentiodynamic STM images of Ru dissolution in Argon saturated 0.05 M H_2SO_4. The potential is scanned between 1.3 and 1.5 V (vs. RHE) at slow scan rate of 2 mV/s, as schematised on the left. a) 1% of a monolayer of as-deposited 3 nm Ru NPs; $(520nm)^2$; $U_B = -299$ mV; $I_T = 1$ nA. b) 1% of a monolayer of thermally oxidised 3 nm RuO_2 NPs; $(516nm)^2$; $U_B = -245$ mV; $I_T = 1$ nA.

clearly show that the formation of the oxide improve the stability of ruthenium.

4.6 Discussion

By comparing the catalytic mass activity with the current state-of-the-art in acid media, it turns out that the nanoparticles presented in this work possess at least an order of magnitude higher activity (figure 4.30). More specifically, 3 and 5 nm RuO_2 NPs show 45-fold improvement compared to RuO_2 NPs, prepared by chemical synthesis [64]; a 30-fold enhancement compared to Pt-Ir nanostructured thin films in a real electrolyser at 80^oC [26]; and a 9-fold increase relative to $IrNi_{3.3}$ core-shell particles, prepared by a chemical route [79].

If this performance could be replicated at higher overpotentials, relevant for real electrolysers and other technologies limited by OER, the precious metal loading could be decreased of at least one order of magnitude. More strikingly, in the introduction we have hypothetically estimated the amount of Pt and Ir required for PEM electrolysers based on Pt-Ir to be scaled to the terawatt level. It was found that half a year of Pt and 10 years of iridium annual production would be needed per terawatt of hydrogen storage capacity. If we assume to substitute Pt-Ir with these nanoparticles, we can do a similar estimation. In particular, the annual ruthenium production ($2.5 \cdot 10^7$ g) is one order of magnitude higher than the Ir one ($9 \cdot 10^6$ g) [7], and there is a 30-fold improvement

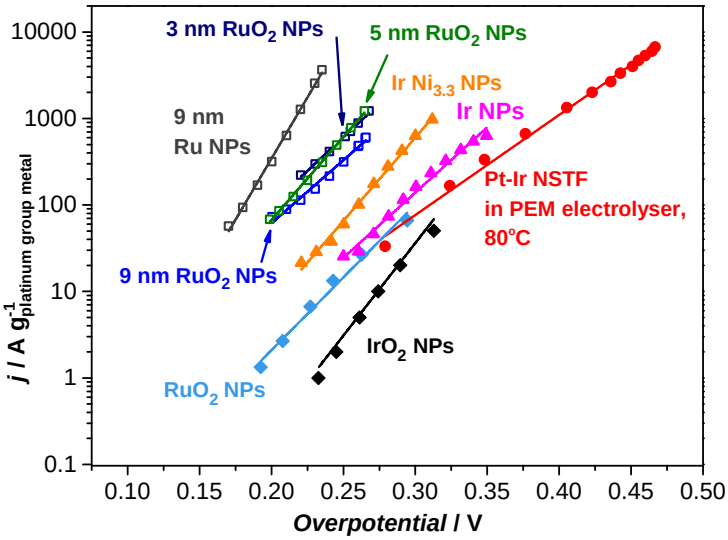

Figure 4.30: State-of-the-art for OER in acid media, expressed in mass activity of precious metal. Data adapted from this work for as deposited 9 nm Ru NPs and for thermally oxidised 3, 5 and 9 nm NPs; data taken from ref. [64] for RuO_2 and IrO_2 NPs; from ref [79] for Ir and $IrNi_{3.3}$ NPs; from ref. [26] for PtIr Nanostructured Thin Film (NSTF).

compared to Pt-Ir NSTF. Hence, the amount of ruthenium required per TW of hydrogen storage capacity would be less than six months.

As mentioned earlier, it is challenging to evaluate the surface area, hence the specific activity. However, by assuming spherical morphology, at least for small particles, it is possible to estimate it and compare it with the state-of-the-art. Figure 4.31 shows the specific activity of thermally oxidized 2, 3 and 5 nm RuO_2 NPs, compared with other works where the catalysts have well-defined surfaces. Also in this case, the mass-selected particles from this work exhibit at least one order of magnitude improvement: at 0.25 V overpotential, 5 nm RuO_2 NPs shows almost 80-fold improvement relative to RuO_2 NPs, prepared by chemical synthesis [64], and 30-fold enhancement compared to epitaxially grown RuO_2 (100) thin film [68].

Furthermore, based on the surface area and the mass activity, it is possible to estimate the turnover frequency (TOF). TOF expresses the number of oxygen molecules evolved per active site. Since it is not possible to evaluate with precision the number of active sites, a lower (TOF_{min}) and an upper (TOF_{max}) boundaries were estimated as follows [190]. TOF_{min} was estimated assuming

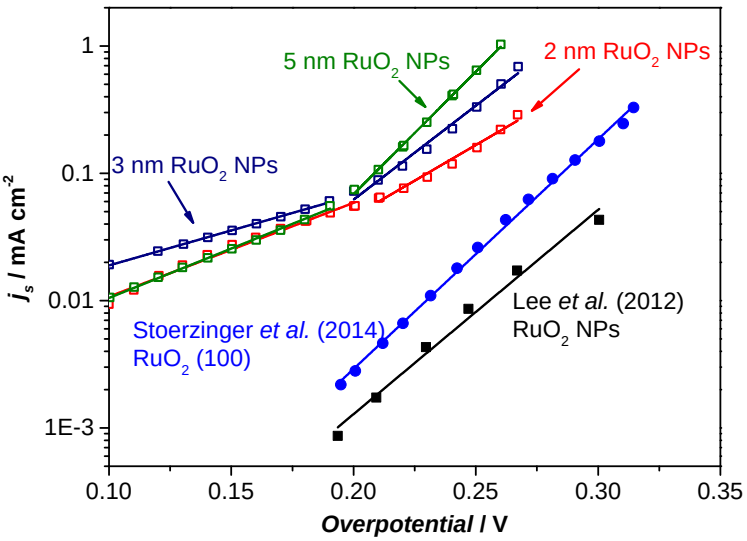

Figure 4.31: Specific activity comparison of RuO_2 OER catalysts with well-defined surfaces. Data from this work for 2, 3 and 5 nm RuO_2 NPs; data taken from [68] for RuO_2 (100) thin film; and from [64] for RuO_2 NPs.

that each Ru atom is active and is involved in the reaction.

$$TOF_{min} = \frac{j\, MW_{RuO_2}}{n_{e^-}\, N_A\, e^-} \tag{4.11}$$

where j is the mass activity in A/g, MW_{RuO_2} is the molecular weight; n_{e^-} is the number of electrons involved in the reaction (4); N_A is the Avogadro's number; and e^- is the electron charge. TOF_{max} was estimated assuming that only the surface is active and involved in the reaction. This is a cautious estimation, since the surface is covered by different sites and the activity is controlled by the most active ones.

$$TOF_{max} = \frac{j\, MW_{RuO_2}}{h_{ML}\, d\, n_{e^-}\, N_A\, e^-} \tag{4.12}$$

where j is the specific activity in $\mathrm{A/cm^2}$; h_{ML} is the height of a monolayer; and d is the density.

Figure 4.32 compares the turnover frequency of 3 nm RuO_2 NPs with the most active and well-defined catalysts in acid media. Again, the catalysts from this work exhibit the highest activity reported, in comparison with nanoparticles prepared by chemical route [64, 79] and oriented thin films [68]. When possible the lower and upper limits for TOF were estimated.

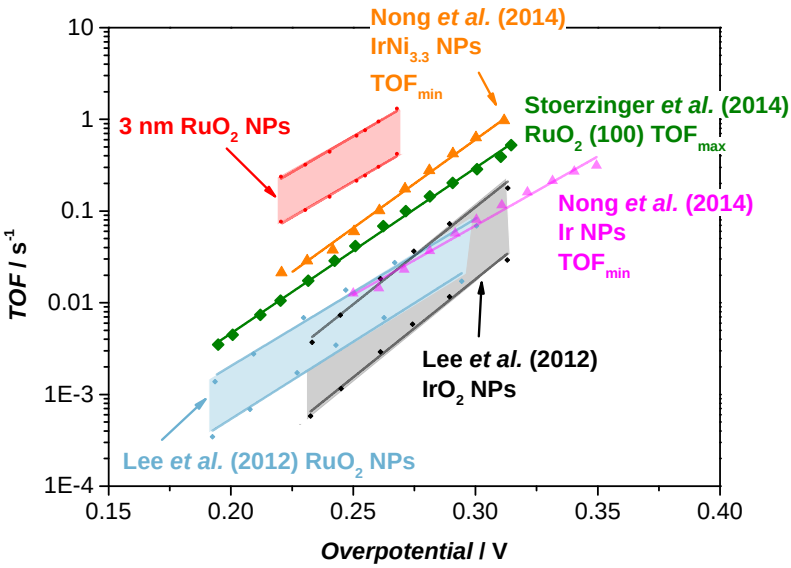

Figure 4.32: Turnover Frequency comparison of RuO_2 with well-defined OER catalysts in acid (except RuO_2 (100)). When possible both TOF_{min} and TOF_{max} were estimated. Data from this work for 3 nm RuO_2 NPs; data taken from [64] for RuO_2 NPs and IrO_2 NPs; from [79] for Ir NPs and $IrNi_{3.3}$; and from [68] for RuO_2 (100) single crystalline film.

Recently, Shao-Horn and coworkers, by investigating epitaxially grown RuO_2 (110) and (100) in alkaline, observed that the more open (100) surface exhibits greater OER performance than the (110) facet. They proposed that the enhancement is due to higher density of cus sites. If we compare the surface density for the 3 nm NPs with RuO_2 (100) single crystalline thin film, we obtain the results summarised in table 4.1. Similarly to the upper limit for the turnover frequency, the estimation of the surface density can be evaluated by considering the entire mass of the particle and by dividing it for the surface area. With this assumption, the NPs exhibit a surface density 5 times higher than the single crystalline thin film. The value is not high enough to explain the improvement in the catalytic activity simply as a higher number of active sites, but presumably there is a different type of site.

We believe that the best performances reported in this work are related to the preparation technique, that allows to high degree of control on the mass and coverage, without introducing impurities. However, the presence of a different site with better catalytic activity is not ruled out and further investigations are needed.

Sample	Surface density
RuO_2 (100)	5.1 $\#_{cus}/nm^2$
3 nm RuO_2	25 atoms/nm^2

Table 4.1: Surface density for RuO_2 (100) single crystalline thin film in alkaline and 2 nm NPs.

4.7 Conclusion

In this chapter, the activity and stability of ruthenium nanoparticles have been illustrated. By preparing mass-selected nanoparticles, this study provides a fundamental investigation of the oxygen evolution reaction on ruthenium and ruthenium dioxide in nanoparticulate form, including the examination of the effect of particle size. In particular, we observed that a proper oxidation treatment drastically improve the stability of ruthenium under the very harsh and oxidizing conditions of OER, affecting its activity.

The extensive characterisation prior and post oxidation, in combination with the management of loading and morphology of the particles, allows an accurate estimation of the mass activity. For small particles it was possible to evaluate the specific activity and upper and lower limits for the turnover frequency. It turned out that the catalysts from this work exhibit the highest OER activity reported so far for precious metals in acidic media. We attribute the activity enhancement to the preparation methods, that allows a controlled deposition of mono-dispersed well-defined nanoparticles, avoiding the use of surfactants or other sources of impurities. Therefore, these data can serve as benchmarks for the oxygen evolution reaction on ruthenium dioxide nanoparticles, in the size range between 3 and 10 nm, which is the highly technologically relevant.

Further investigations should be dedicated to understand more deeply the origin of this improvement, i.e. the presence of a particularly active site [68]. Moreover, a way to replicate such activity in nanoparticles prepared through chemical synthesis is mandatory in order to make their preparation affordable and scalable.

Finally, should strategies for improving the stability be addressed, for instance by addition of iridium or titanium, PEM electrolysers and other technologies limited by the OER could eventually become scalable to the terawatt level.

Chapter 5

Benchmarking the Stability of Water Splitting Catalysts

Although the main requirement for a catalyst is to be highly active, it is essential that it is also stable, and can sustain high activity for several years [57]. This is extremely challenging, especially considering the harsh oxidising conditions to which oxygen evolution catalysts are exposed and the very acidic electrolytes used in PEM electrolysers. As mentioned in chaper 2, only ruthenium and iridium based oxides are active and exhibit moderate stability in acid media.

Regardless extensive studies on OER catalysts, benchmarks and standardized protocols that could allow straightforward comparisons among different laboratories and materials are lacking. Some groups are starting to provide benchmarks, particularly in terms of activity, but not so much in term of stability [91, 100]. When the stability is reported, it is typically evaluated by electrochemical measurements for a few hours, either performing a chronoamperometry test, where the potential is kept constant, or chronopotentiometry, at a fixed current. To determine the long-term stability of a catalyst and its potential applicability in real devices, these techniques may not be exhaustive and may not elucidate the actual corrosion process [142,191,192]. In the case of the oxygen reduction reaction, ORR, the reverse reaction of OER, several accurate tests have been devoted and optimised for reproducing similar conditions to automotive applications [142]. Conversely, such procedures for OER are not well-established in literature and are therefore needed.

As discussed in section 2.1.5, several techniques can be used to monitor catalyst degradation [133]: transmission electron microscopy (TEM) and scanning

tunneling microscopy (STM) can provide insights in changes in the structure and morphology at the nanoscopic level [135, 136, 140, 141, 192, 193]. Alternatively, Rotating Ring Disk Electrode (RRDE) measurement can be used to follow the formation of the corrosion products, e.g. RuO_4 [27, 58, 104]. Furthermore, Electrochemical Quartz Crystal Microbalance (EQCM) and Inductively Coupled Plasma Mass Spectrometry (ICP-MS) can be powerful tools for defining the corrosion rate [57, 111, 134].

In this chapter a procedure to assess the stability of ruthenium dioxide thin films, by a combination of electrochemical measurement with EQCM and ICP-MS analyses, is presented. The example reported here can easily serve as general guidelines to define the corrosion process for other OER catalysts [87].

5.1 Ruthenium

The importance of designing short-term procedures to estimate the corrosion rate of a catalyst is depicted very clearly by ruthenium behaviour (figure 5.1). Ruthenium is known to be very unstable under OER conditions [50, 57, 58, 71].

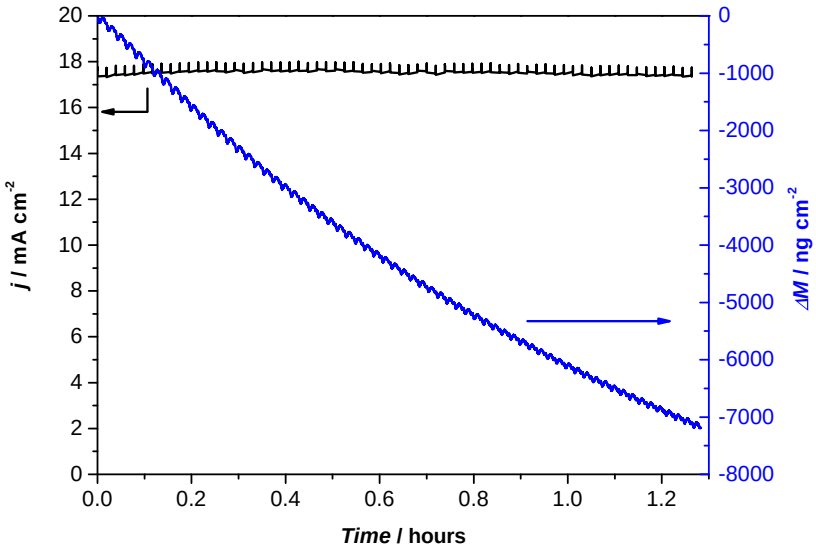

Figure 5.1: Cyclic voltammetry test between 1.0 and 1.7 V (vs.RHE) at 20 mV/s for as deposited Ru thin film in N_2 saturated 0.1 M $HClO_4$ at room temperature in the EQCM set-up. The black line denotes the current density taken at the vertex potential 1.7 V (vs. RHE), while the blue line represents the mass change.

If a thin film is used, in a very short time the complete disappearance of the catalyst can be monitored electrochemically and simply by looking at it, even

though the current remains stable during the whole experiment. Figure 5.1 shows the electrochemical behavior of a ruthenium thin film in acid, which exhibited a lifetime a bit longer than an hour. The electrochemical test consisted of cycling the potential between 1.0 and 1.7 V (vs. RHE) at 20 mV/s. The maximum current, corresponding to the current at 1.7 V (vs. RHE), is represented as a black line in the figure. During electrochemistry the mass loss was monitored with an Electrochemical Quartz Crystal Microbalance (EQCM), denoted in blue. The stable beahviour of the electrochemical current, while the film was clearly corroding, raises questions about the effectiveness of simple electrochemical analyses alone for investigating catalytic stability.

What happens when a catalyst corrodes at a rate that would require several hours, days or months to completely corrode? Performing such long experiments is not feasible at an early stage of the research, even though they will be mandatory in the final steps. Hence, careful design of short-term tests for defining the long-term corrosion is required.

5.2 Ruthenium Dioxide

Ruthenium dioxide thin films were prepared by reactive dc magnetron sputtering from a ruthenium target and deposited either on a gold polycristalline disk for RRDE assembly or on EQCM crystals for stability measuerements. The deposition was carried out at 300^oC with a power of 30 W, in a pressure of 3 mTorr and a flow of 10 sccm of argon and 4 sccm of oxygen. The deposition rate was assessed before the actual deposition using the in-chamber QCM. The QCM was calibrated for ruthenium oxide, by determining the exact thickness of a film ($\sim$ 100 nm) with a profilometer. The film thickness was set to 40 nm.

Before the deposition, the Au disk was mechanically polished with 0.25 μm diamond paste; it was then cleaned by 20 minutes cycles of sonication in isopropanol and milliQ water, with the procedure repeated three times. The EQCM crystals were sonicated in acetone, isopropanol and finally in milliQ water for 20 minutes each.

An essential parameter to estimate the intrinsic activity of a material and fairly compare different catalysts is the specific activity, i.e. the activity normalised with the electrochemically active area. This value is often unknown for oxides and the geometric area is used instead. However, by using thin smooth films, with low roughness factor, it is possible to approximate the electrochemically active surface area (ECSA) with the the geometric area. For this reason the thickness of the film was chosen small enough to avoid the growth of rough structures, but high enough to completely cover the underlying gold electrode. At OER potentials, gold oxidises, giving rise to an increase in the QCM frequency, and at even higher potentials, it can dissolve [57].

5.2.1 Characterisation of the Thin Film

The structure and composition of the films were evaluated by XPS and GA-XRD.

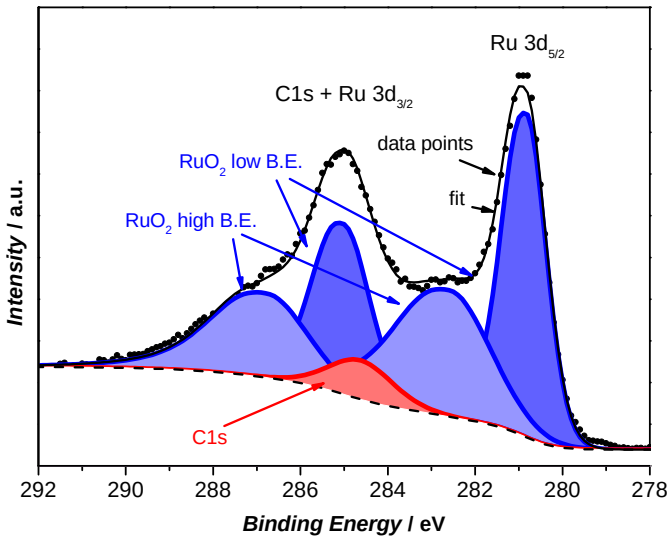

Figure 5.2: XPS spectrum of the Ru3d core level of 40 nm RuO_2 thin film. XPS performed by Paolo Malacrida.

XPS spectrum of the Ru 3d region (figure 5.2) shows the characteristic pair of doublets of the ruthenium dioxide, indicating that the surface is completely oxidised [165].

GA-XRD confirmed the full oxidation of the bulk. The film was deposited on glass, which is amorphous, hence it does not display any peaks that may mask the signal from the film. Figure 5.3 shows the diffractogram of the sputtered film in comparison with the bare substrate, which as expected is completely amorphous, together with a literature reference pattern for rutile RuO_2 [182]. The consistency with the RuO_2 reference pattern indicates that the deposition at 300^oC is sufficient to form the crystalline rutile phase of the film, with the (110) phase as the main orientation [60].

Finally, the morphology of the film was investigated with scanning electron microscopy (SEM). The images in figure 5.4 a) and b) show the microscopic structure of the thin film surface, revealing a low roughness film. Figure 5.4 c) shows a SEM micrograph of ruthenium dioxide prepared by chemical synthesis as reference [194]. Typically, films prepared by chemical synthesis and electrodepostion have high surface roughness with a morphology similar to the one represented in the figure [100, 128]. In comparison with those films, the sput-

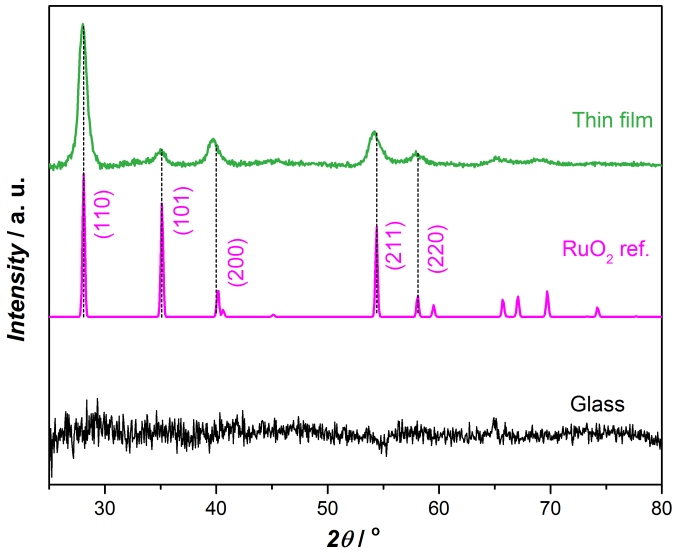

Figure 5.3: GA-XRD of the RuO_2 thin film deposited on a glass substrate. The substrate was measured in the same settings and it is shown for comparison. Rutile RuO_2 reference pattern [182] is also plotted.

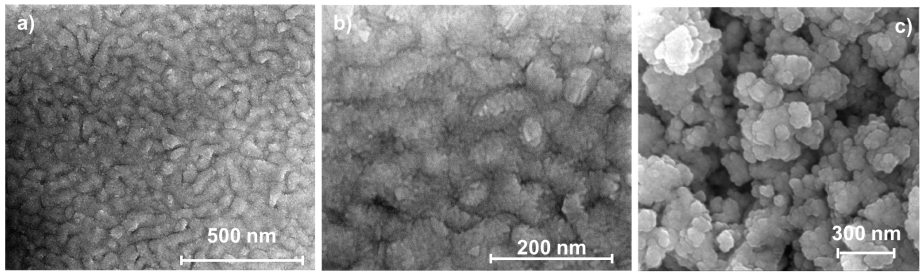

Figure 5.4: SEM micrographs of a RuO_2 thin film using a secondary electron detector and an acceleration voltage of 5.00 kV. a) 100000x magnification; b) 250000x magnification. c) SEM micrograph of ruthenium dioxide prepared by chemical synthesis, taken from [194]; acceleration voltage of 10 kV and 60000x magnification.

tered film looks smoother. Hence, the activity normalised with the geometric area of the sputtered thin film should be close to the real catalytic activity.

5.2.2 Electrochemical measurement and mass loss monitoring

The catalytic activity was measured first. 3 cyclic voltammograms were recorded between 1.0 and 1.7 V (vs. RHE) at 5 mV/s in N_2 saturated 0.05 M H_2SO_4. The electrocatalytic activity was measured both in a RRDE assembly on a gold polycrystalline disk and in the EQCM set-up. Figure 5.5 shows the activity comparison for both configurations. The activity of the film on the EQCM at high

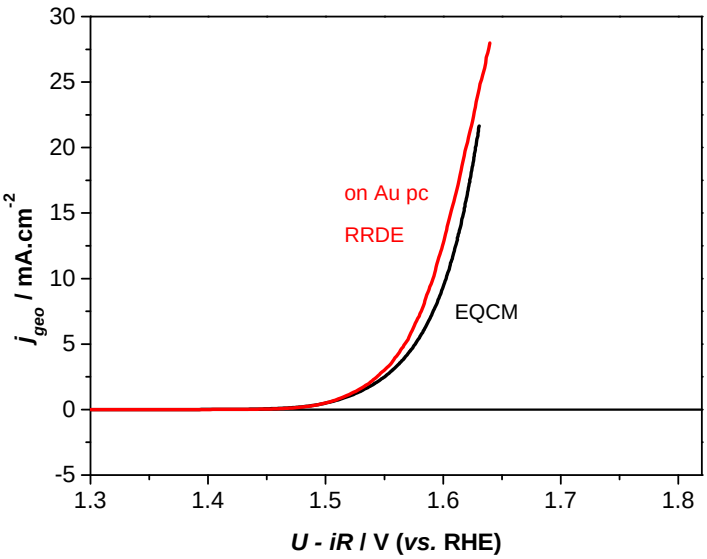

Figure 5.5: Cyclic voltammetry of RuO_2 thin film deposited on Au polycrystalline disk for RRDE measurement and on Au/Ti crystal for EQCM test in N_2 saturated electrolyte at 5 mV/s and at 1600 rpm.

overpotentials is slightly lower than the one obtained with a rotating electrode. However, the onset for the oxygen evolution on the two curves fits very well. The difference is likely due to the static configuration of the EQCM electrode, which does not allow for bubble removal as easy as in the RRDE. Nonetheless, the bubbles did not create interferences for the EQCM at high oxidative potentials as they were not accumulating on the electrode and were moving upwards during the electrochemical test (the EQCM is positioned vertically).

The overpotential, η, needed to sustain a current density of 10 mA/cm^2 is 354 $\pm$ 8 V, based on two independent measurement with the rotating ring disk electrode, which better represents the activity of the films. This value is comparable with literature, even though it is slightly higher, which is likely due to the lower roughness of the samples compared to electrodeposited or chemically

prepared films.

All the stability tests were performed only with the electrochemical quartz crystal microbalance, with which it is possible to monitor the mass variation, while electrochemistry is carried out on the working electrode.

In order to precisely compare the performance of different samples, it is paramount to define the Ohmic drop correctly so that the exact same potential is applied each time. Hence, after cyclic voltammetry, the resistance was measured by Staircase Potentio Electrochemical Impedance Spectroscopy, or Mott Schottky, (SPEIS), and for all the samples it was found to be in the range $10 - 15\,\Omega$.

The QCM was then left to equilibrate, by holding the potential in a region where the oxide is stable, 1.23 V (vs. RHE), until the frequency had reached a constant value. Typically, within $30-45$ minutes and after a small gain in mass, the frequency was stabilised, i.e. the frequency change was less than 1 Hz every 15 minutes. The initial change in frequency is likely connected to temperature equilibration and/or vibration settlement after the assembly.

The stability protocol consists of two following electrochemical tests:

- Chronoamperometry (CA): the electrode was held at a constant potential of 1.8 V (vs. RHE);
- Chronopotentiometry (CP): the electrode was held at a constant current density of 30 mA/cm^2.

Both experiments lasted 2 hours and a 2 mL aliquot of electrolyte was taken at the beginning and at the end of each test to be used in ICP-MS. The potential of 1.8 V (vs. RHE) was chosen to be at a more positive potential than the reversible potential of RuO_4 formation, 1.38 V (vs. RHE) [105, 116], so to observe a pronounced corrosion.

The CA experiments were carried out with a manual iR compensation technique (MIR), to assure that the applied potential was correctly adjusted for the Ohmic drop. Figure 5.6 shows the CA test with the current density represented in black on the left y-axis and the mass change in blue on the right axis. Typically in literature, the current is reported alone, without further investigation. So, by looking solely at the current density, one could argue that, after an initial decay, the catalyst is stable, for at least an hour. However, if the mass is also monitored, it becomes clear that the catalyst is not stable and it loses mass with a constant dissolution rate of 4.4 monolayers (ML) per hour.

The corrosion rate was evaluate in ML equivalent by using the lattice parameters of the RuO_2 (110). Specifically, a monolayer of RuO_2 (110) corresponds to m_{ML} of 216 ng/cm^2, which, for 1 cm^2, is given by:

$$m_{ML} = h_{ML_{RuO_2(110)}}\, d_{RuO_2} \tag{5.1}$$

with $h_{ML_{RuO_2(110)}}$ the height of a monolayer of RuO_2 (110) (3.1 Å, taken from

the inorganic crystal structure database ICSD [182]); and d_{RuO_2} the density of ruthenium dioxide (6.97 g/cm^3).

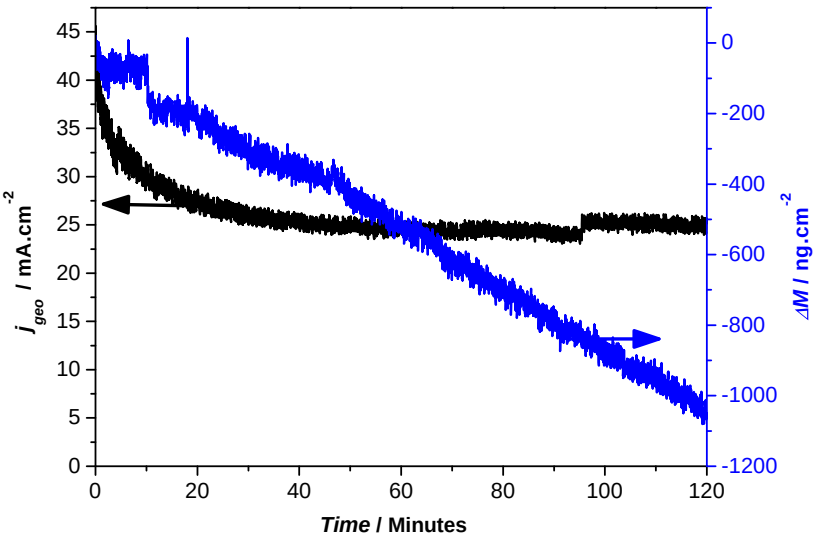

Figure 5.6: Chronoamperometry for a RuO_2 thin film at 1.8 V (vs. RHE) in N_2 saturated 0.05 M H_2SO_4 at room temperature using EQCM set-up. The black line denotes the current density, displayed on the left y-axis, while the blue line represents the mass change, evaluated from the frequency.

The monitoring of the mass is even more important in the chronopotentiometry test, where the deactivation is less noticeable than in the CA, because of the exponential dependence of the current on the potential. Figure 5.7 shows the potential variation together with the mass change. At the beginning, a subtle increase in the potential denotes an energy loss. However, by focusing only on this parameter, the conclusion is again misleading. While the potential suggests that the catalyst is stable over the short-term test, the monitoring of the mass indicates a continuous mass loss with a dissolution rate equivalent to 4.8 ML per hour. The corrosion is very similar to the CA test, since the current density was chosen to be comparable.

The electrolyte was analysed before and after the stability tests by ICP-MS and the results were compared with the EQCM data. Figure 5.8 summarizes the findings for the CA and the CP, where the errors bars are based on four independent measurements. The Ru concentration evaluated with ICP-MS was converted into mass change of oxide per area (ng_{oxide}/cm^2) to make an easier

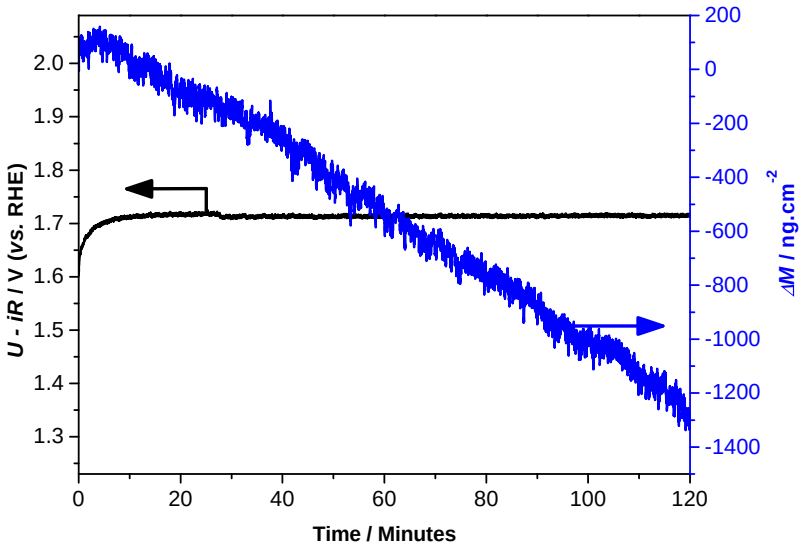

Figure 5.7: Chronopotentiometry for a RuO_2 thin film at 30 mA/cm^2 in N_2 saturated 0.05 M H_2SO_4 at room temperature using EQCM set-up. The black line denotes the potential variation, displayed on the left y-axis, while the blue line represents the mass change, evaluated from the frequency.

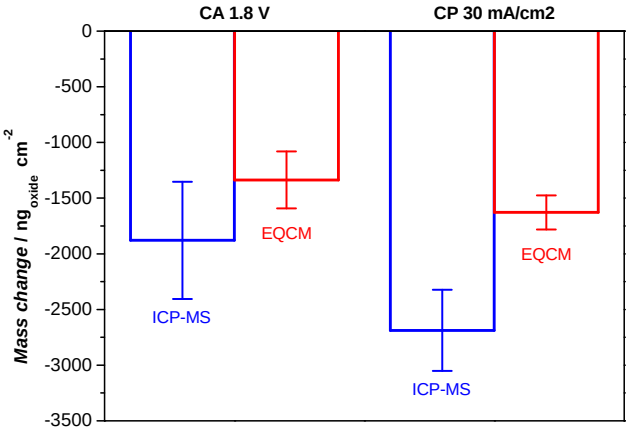

Figure 5.8: Mass dissolution of ruthenium dioxide during 2 h chronoamperometry and chronopotentiometry tests: ICP-MS and EQCM comparison. The error bars are based on four independent experiments.

comparison:

$$Mass\,Change = \frac{(C_{ICP} \cdot V_f)_f - (C_{ICP} \cdot V_i)_i}{A_{geometric}} \cdot \frac{MW_{RuO_2}}{MW_{Ru}} \tag{5.2}$$

where the concentration, C_{ICP}, is given in μg/L. The ICP-MS data show higher losses in both tests. This may be due to the fact that the EQCM is only sensitive to the overlapping area between the quartz crystal and the electrode which corresponds only to the 28% of the electrochemical active area. We believe that the mass loss occurs homogeneously across the surface; however inhomogeneity may affect the analysis and lead to underestimations. Conversely, ICP-MS is sensitive to the whole area, and it is most likely more accurate and representative of the process.

5.3 Static *vs.* Transient Dissolution

In the previous section, the main focus was on potentiostatic measurements of the corrosion. However, depending on the material, potentiodynamic measurements could be preferred or combined with the static ones, in order to enhance the corrosion and/or obtain more insights on the dissolution mechanism. For instance, it has been observed that platinum corrodes much faster when the potential is cycled, since potential changes induce surface reconstruction during which higher dissolution rates occur [195]. Therefore, ruthenium dioxide corrosion under transient conditions was also investigated.

After evaluating the initial activity, by quasi stationary measurements, determining the Ohmic drop and after equilibrating the EQCM as described in the previous section, cyclic voltammetry between 1.0 and 1.8 V (vs. RHE) at 20 mV/s was performed. Figure 5.9 shows the current density and the mass loss over time, corresponding to 350 cycles.

The mass loss after 120 minutes, evaluated from EQCM, is around -350 $ng_{oxide}/\ cm^2$, which is considerably smaller than the corrosion during potentiostatic measurement (-1464 ± 13 from EQCM). This suggests that the dissolution of ruthenium is mainly related to the applied potential and not to surface reconstruction while cycling. These findings correlate closely to the recent observations by Mayrhofer and coworkers on polycrystalline ruthenium [57], as discussed in section 2.1.5.

The conclusions were further confirmed by measurements at a different scan rate. Cyclic voltammetry was performed at 100 mV/s up to 1.8 V (vs. RHE). After 250 cycles, CVs at lower scan rate, 20 mV/s, were also recorded in order to allow enough time to the quartz crystal microbalance to equilibrate and give the right mass change. Figure 5.10 shows the current density and the mass loss during the low scan rate CVs. The gaps in between denote the CVs at high scan rate.

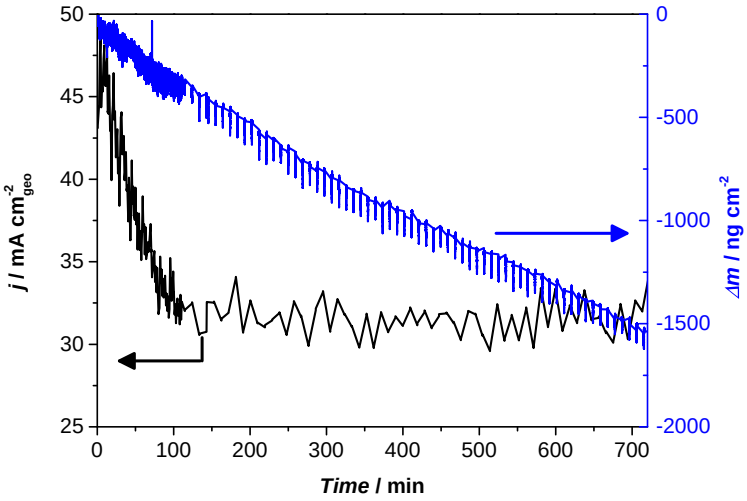

Figure 5.9: Cyclic voltammetry between 1 and 1.8 V (vs. RHE) at 20 mV/s in N_2 saturated 0.05 M H_2SO_4, illustrated over time. The black line represents the current density (at 1.8 V), displayed on the left y-axis; while the blue line represents the mass change evaluated from the frequency, shown on the right y-axis.

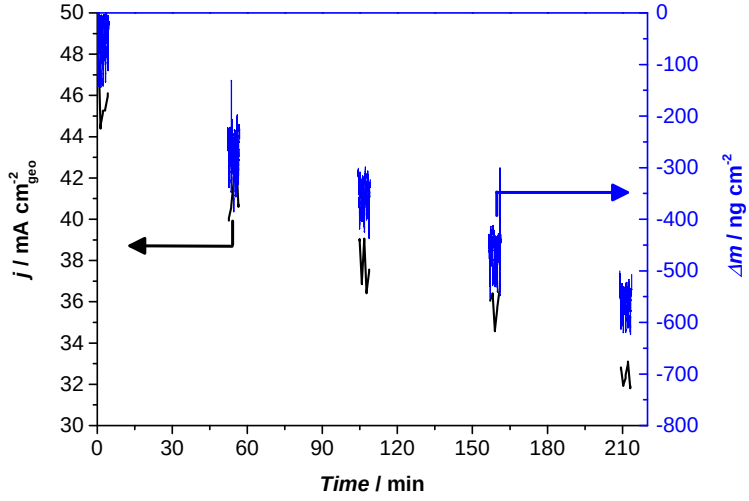

Figure 5.10: Cyclic voltammetry between 1 and 1.8 V (vs. RHE) at 20 mV/s in N_2 saturated 0.05 M H_2SO_4, illustrated over time. 10 cycles at 20 mV/s, were followed by 250 cycles in the same potential range at 100 mV/s (white gaps). The black line represents the current density (at 1.8 V), displayed on the left y-axis and the blue line represents the mass change evaluated from the frequency, shown on the right y-axis.

Table 5.1 compares the mass loss, evaluated with the EQCM, for the potentiodynamic and potentiostatic electrochemical tests. The mass loss after 2 hours potentiostatic tests, CA and CP, is high for both measurements and it is around $-\sim 1500$ ng/cm^2, which corresponds to a total loss of $-\sim 8$ ML. On the other hand, scanning the potential does not induce a comparable mass loss, which is instead around ~ 400 ng/cm^2 (~ 2 ML). Furthermore, the number of cycles does not influence the mass loss and comparable mass is lost after 60 cycles at 20 mV/s and 550 cycles at 100 mV/s. This indicates that what it is important for ruthenium oxide corrosion is not the number of cycles, rather the time the potential is above the dissolution potential for Ru.

Electrochemical Test	Δm 120 min [ng/cm^2]	Δm 250 cycles [ng/cm^2]
CA	-1464 ± 13	
CP	-1566 ± 110	
CVs (20 mV/s)	-350 (60 cycles)	-1100
CVs (100 mV/s)	-400 (550 cycles)	-300

Table 5.1: Ruthenium dioxide mass loss under potentiodynamic and potentiostatic measurements in acidic media.

5.4 Discussion

On account of these results and based on the RuO_2 corrosion rate under potentiostatic conditions, the lifetime of a 40 nm at a potential of 1.8 V (vs. RHE) is 29 hours, which is a very short time for an actual electrolyser.

Furthermore, by assuming that Ru corrosion proceeds according to [104]:

$$RuO_2 + 2H_2O \rightarrow RuO_4 + 4H^+ + 4e^-$$

it is possible to calculate the anodic current that this rate corresponds to, as follow:

$$I_{dissolution} = \frac{(\frac{\Delta m}{MW_{RuO_2}})\, n_{e^-}\, N_A\, e}{t} \tag{5.3}$$

It turns out that the current is equal to 0.6 μA/cm^2, which is more than four orders of magnitude lower than the total current density.

Ideally, the formation of RuO_4 can be followed on the ring in RRDE [58,104] but the required ring current would correspond to high corrosion, as it has been done with mass-selected Ru nanoparticles in chapter 4. Hence, RRDE can hardly be used to determine long-term stability, even though it can be a suitable technique for early stage stability investigations of new catalysts.

On the other hand, the opposite calculation provides useful information, as well. A 40 nm film with a lifetime of 5 years, in the two hour tests illustrated

here, would lose only 0.02 Å. This loss for 1 cm^2 of RuO_2 film in 100 mL electrolyte would correspond to less than 2 ppt. Such a concentration is approaching the limit of detection of Ru with ICP-MS, which is 0.4 ppt. This shows that short-term tests like the ones illustrated in this thesis would need to be combined with long-term testing, in order to confirm the durability of a catalyst in real devices.

5.5 Conclusion

In this chapter guidelines for investigating the electrochemical stability of OER catalysts have been proposed. The focus has been to quantify the corrosion rate of one of the most studied OER catalysts under reaction conditions. Although it is known that ruthenium oxide is only relatively stable at high oxidative potentials, rigorous studies devoted to define its dissolution rate are missing.

It turned out that a ruthenium dioxide thin film of 40 nm loses 4.8 ML per hour at a constant current density of 30 mA/cm^2 and 4.4 ML per hour at a constant potential of 1.8 V (vs. RHE); which, in turn, gives rise to a lifetime of less than 30 hours.

Interestingly, it has been shown that monitoring only the electrochemical parameters, like potential or current density, are not sufficient and can generate misleading conclusions. Indeed the dissolution process can make the film more rough, introducing changes in the microscopic surface area that can lead to higher current density or improved overpotentials. Therefore, it is essential to simultaneously monitor the mass loss. Short-term tests based on a combination of EQCM and ICP-MS analyses can provide a good assessment of the stability of a catalyst. The tests shown here can certainly serve as directions for determining the stability of other catalysts. Furthermore, this approach can generally be applied to other electrocatalytic systems, e.g. oxygen reduction reaction, CO_2 reduction, hydrogen evolution reaction.

Nevertheless, it is important to highlight that the degradation process is material dependent [57], therefore in some cases potentiostatic measurement should be preferred over the potentiodynamic tests. Indeed, from combining potentiostatic with potentiodynamic measurements at different scan rate, it was possible to observe that ruthenium corrosion is a steady state dissolution, related to the time the catalyst is held above the dissolution potential.

Chapter 6

Stabilisation of RuO_2 by Addition of IrO_2

In the previous chapter, the importance of determining the stability of a material under reaction conditions, in particular for long-term applications, was highlighted. In the illustrated experimental conditions, ruthenium dioxide exhibited very poor stability, in close agreement with literature.

However, as discussed in section 2.1.5, ruthenium oxide is commercially used in the chloro-alkali industry, in combination with iridium and titanium, in the so-called dimensionally stable anodes (DSA). Iridium and titanium, which are more stable metal oxides, are used to improve the durability of ruthenium oxide. DFT calcualations performed by Man in Rossmeisl group attempted in explaining this stability enhancement with a termination concept [47]. According to theory, iridium oxide in a ruthenium iridium mixed oxide should migrate to the surface and on the surface to the undercoordinated sites, protecting ruthenium oxide from corrosion [47]. Recent studies by Danilovic *et al.* [122] seem to agree with theory, although experiments were conducted on high iridium surface concentrations. It was observed that the surface of ruthenium iridium mixed oxides was enriched in iridium and that the bulk did not affect the activity and stability of the surface.

In this chapter a strategy, inspired by the theoretical calculations on Ru-Ir oxides and by the DSA, to improve the stability of an active but unstable OER catalyst (ruthenium dioxide) with a more durable material (iridium dioxide), is addressed. In particular, since the bulk seems to not be involved, sub monolayer amounts of iridium oxide are deposited on a ruthenium dioxide surface.

Before that, the stability of a pure iridium dioxide thin film is assessed in more details.

6.1 Iridium Dioxide

Iridium dioxide is often preferred over ruthenium dioxide as catalyst for the oxygen evolution reaction in acid, because of its higher stability and reasonable activity. For instance, it is used in combination with Pt in PEM electrolysers [26]. However, an evaluation of the corrosion rate by monitoring the mass loss is missing. Therefore, by using the guidelines provided in the previous chapter, the dissolution rate for iridium was estimated.

IrO_2 thin films were prepared by reactive sputtering from an iridium target and deposited on EQCM crystals. The deposition was carried out at the same temperature as for the ruthenium dioxide films, 300^oC, with a power of 30 W, a pressure of 5 mTorr, and a flow of 20 sccm of Ar and 5 sccm of O_2, in order to assure the formation of crystalline IrO_2. The film thickness was set to 40 nm.

6.1.1 Characterisation

GA-XRD diffractogram, illustrated in figure 6.1, confirms the formation of bulk rutile IrO_2, with (200) and (110) as preferential orientations.

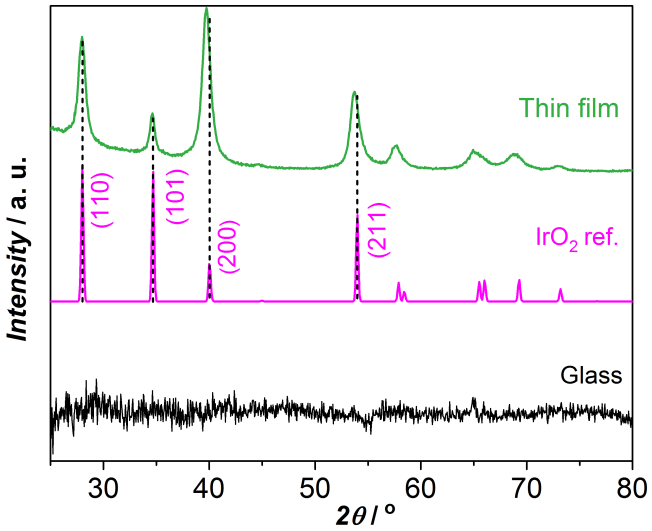

Figure 6.1: GA-XRD of IrO_2 thin film deposited on a glass substrate. The glass substrate was measured in the same settings and it is shown as reference, together with a reference pattern for rutile IrO_2 taken from [196].

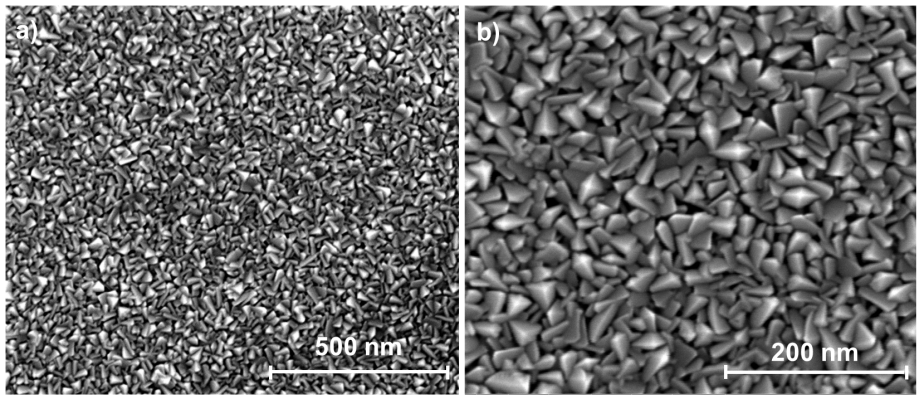

Figure 6.2: SEM micrographs of IrO_2 thin film using a secondary electron detector, an acceleration voltage of 5 kV and dwell time of 50 μs. a) 10000x magnification; b) 250000x magnification.

Figure 6.2 shows SEM images of the microscopic surface of the film. In comparison to RuO_2 SEM pictures (figure 5.4), the IrO_2 film looks more rough, with triangular shape structures protruding in the z direction. This is most likely due to differences in film growth during the deposition, which are material dependent.

Similar findings in terms of different roughness values were observed by Stoerzinger *et al.* on epitaxially grown RuO_2 and IrO_2 films [68]. Strikingly, iridium oxide (100) films exhibited almost 10 times higher roughness than ruthenium oxide (100) films. The difference in roughness among IrO_2 (110) and RuO_2 (110) was instead 4 times. McCrory *et al.* observed much greater roughness for electrodeposited IrO_2 as well, compared to several non noble metal oxides [100].

6.1.2 Activity

The different morphology complicates the comparison of the catalytic activity of ruthenium and iridium oxides, since the geometric area is used to normalise the current. Indeed, IrO_2 thin films seem to exhibit greater activity than ruthenium dioxide, as it is shown in figure 6.3, with an overpotential of 300 ± 5 mV at 5 mA/cm^2. This is contrast to experimental results and theory [48, 57, 58, 68].

Besides having higher surface roughness, the slope of the CV, in particular at high potentials, is lower and not parallel to the ruthenium dioxide CV, suggesting a different mechanism or a contribution from another process. This may be related to the morphology of the film. During OER on IrO_2, problems at high potentials with bubbles and changes in the resistance took place, again indicating the films are more porous than the ruthenium dioxide. High porosity

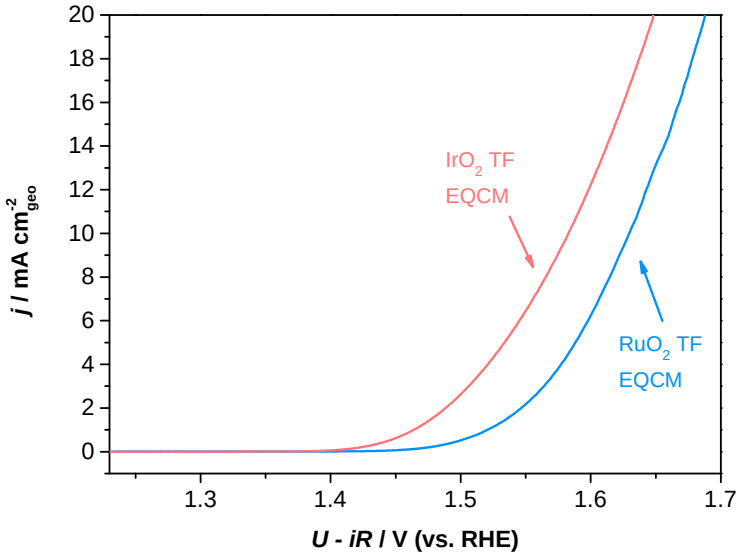

Figure 6.3: Ohmic and capacitance corrected quasi stationary cyclic voltammetry of RuO_2 and IrO_2 thin film, recorded in N_2 saturated 0.05 M H_2SO_4 at 5 mV/s in the EQCM set-up.

of iridium and iridium oxide was observed in previous studies [197, 198].

Another explanation could be related to the recent findings by Shao-Horn and coworkers about orientation dependence of ruthenium and iridium on the OER activity, discussed in section 2.1.4. They observed that in both cases the more open (100) surface was more active than the most studied (110) facet [68]. Our sputtered iridium thin film showed preferential orientation (200), which is parallel to the (100), while ruthenium oxide thin films exhibited the more packed (110) surface. Nevertheless, it seems more plausible to attribute the better activity of iridium to a higher number of active sites due to surface area increase and distinct surface morphology.

Due to the apparent high roughness of the iridium oxide sample in particular, we attempted to obtain smoother surfaces by annealing polished extended polycrystalline (pc) surfaces in an O_2 atmosphere. Similar treatments were performed by Adzic and coworkers on Ru (0001), resulting in a smooth ordered RuO_2 (110) surface [69, 199]. In this case, we set about to do so by annealing polycrystalline Ir and Ru in 1 bar O_2 at 400°C for 2 hours, i.e. similar conditions to the Ru nanoparticles reported in chapter 4, albeit for longer period. XPS data and cyclic voltammetry of as-prepared and thermally annealed pc disks indicate that a surface oxide is formed after annealing.

The electrocatalytic activity measured in a RRDE configuration in sulfu-

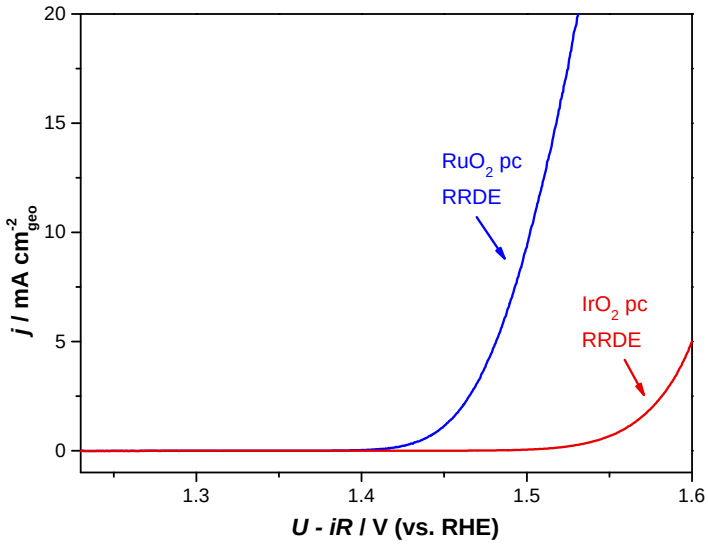

Figure 6.4: Ohmic and capacitance corrected cyclic quasi stationary cyclic voltammetry, recorded in N_2 saturated electrolyte at 5 mV/s and 1600 rpm.

ric acid is shown in figure 6.4. In this case ruthenium oxide possesses higher catalytic activity, in agreement with literature and theoretical calculations [48, 54, 58]. In particular, ruthenium and iridium oxides exhibit an overpotential of 251 ± 1 and 361 ± 11 at 5 mA/cm^2, respectively. The overpotentials for polycrystalline samples and thin films at 5 mA/cm^2 are reported in figure 6.5.

Based on the protocol suggested by McCrory *et al.*, polycrystalline samples have been used to estimate the double layer capacitance, C_{DL}, which is proportional to the electrochemically active surface area, ECSA [100, 200, 201]. Cyclic voltammograms at several scan rates were recorded in a region where no Faradaic process should occur and the charging current can be attributed only to the double layer. An example of a series of CVs for ruthenium dioxide thin film is shown in figure 6.6 a). The potential window was chosen to be 100 mV wide and centered around the open circuit potential, OCP. The potential was held 10 s at each vertex potential before starting the new cycle. The double layer capacitance can then be estimated from the slope of the plot charging current vs. scan rate, as depicted in figure 6.6 b):

$$i_C = \nu \, C_{DL} \tag{6.1}$$

The double layer capacitances, C_{DL}, of the polycrystalline samples and the thin films evaluated from the CVs are shown in figure 6.7. The error bars are based on three independent measurements. The main observation from figure

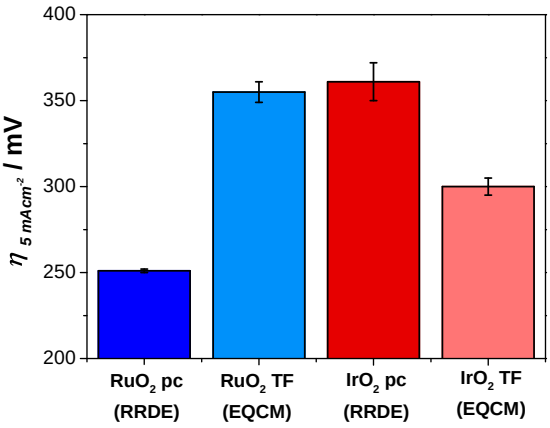

Figure 6.5: Overpotential at 5 mA/cm^2 for RuO_2 and IrO_2 polycrystalline samples (pc) and thin films (TF).

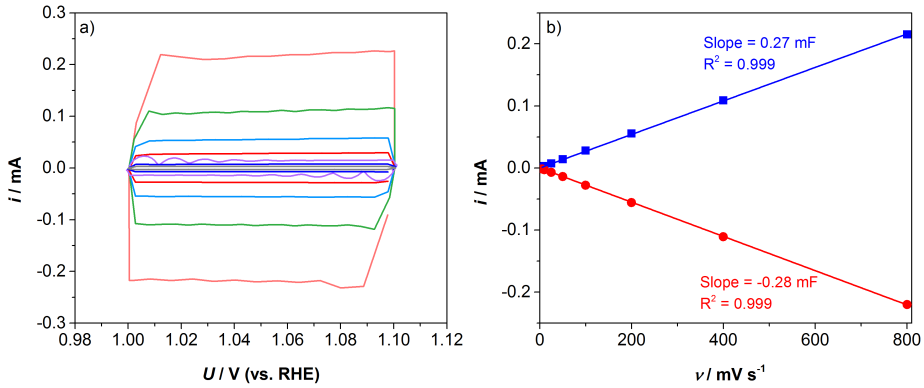

Figure 6.6: a) Cyclic voltammetry of a ruthenium dioxide thin film, recorded at different scan rates ($5 - 10 - 25 - 50 - 100 - 200 - 400 - 800$ mV/s) in N_2 saturated 0.05 M H_2SO_4 solution. The potential was held at the vertex potential for 10 seconds before a new cycle was started. b) Anodic and cathodic charging current measured at 1.05 V (vs. RHE) from the CVs, shown in figure 6.6 a), versus the scan rate.

6.7 is that the IrO_2 thin films have a much higher capacitance than the polycrystalline samples and RuO_2 thin films. By relating the capacitance of TF with pc, it is possible to qualitatively compare the roughness of ruthenium and iridium dioxide thin films. Since the roughness of the polycrystalline samples was not assessed independently, their capacitance was first compared with well-defined flat surfaces from literature [199,202], as reported in table 6.1. The capacitances

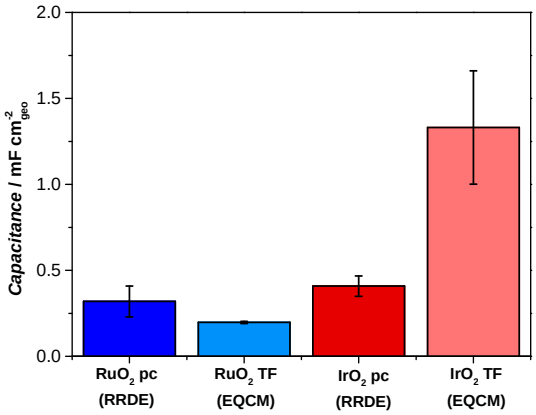

Figure 6.7: Double layer capacitance for ruthenium and iridium dioxide polycrystalline samples and thin films. The error bars are evaluated from three distinct experiments.

Sample	Author	Capacitance (mF/cm^2)
RuO_2 (110) sc	Vukmirovic *et al.*	~ 0.1
RuO_2 (110) sc	Lister *et al.*	~ 0.35
RuO_2 (100) TF	Shao-Horn	~ 0.1
IrO_2 (100) TF	Shao-Horn	~ 0.15
RuO_2 pc	This work	0.32 ± 0.09
RuO_2 TF	This work	0.19 ± 0.01
IrO_2 pc	This work	0.4 ± 0.06
IrO_2 TF	This work	1.33 ± 0.3

Table 6.1: Comparison of the capacitance of pc and TF with well-defined surfaces from literature in acid. RuO_2 (110) single crystals (sc) taken from [199] and [202], RuO_2 and IrO_2 single crystalline TF from private conversation with Shao-Horn.

from [199] and [202] were estimated from a cyclic voltammogram recorded in sulfuric acid at 20 and 100 mV/s, respectively. The capacitance for single crystalline thin films from Shao-Horn were evaluated from cyclic voltammogram performed in 0.1 M $HClO_4$ at 50 mV/s (private conversation). Pc samples from this work exhibited similar capacitances with literature, which allows us to use them for comparing the roughness of the thin films. It turns out that RuO_2 thin film has low roughness, close to the polycrystalline sample, while IrO_2 exhibits a much rougher surface. These results strengthen the hyphotesis that the apparent higher catalytic activity of IrO_2 thin film is due to a surface area effect.

6.1.3 Stability

Figure 6.8 and 6.9 show the stability results of potentiostatic tests for iridium dioxide, following the procedure described in the previous chapter [87].

In the first plot, the current density and the mass loss during a chronoamperometry experiment at 1.8 V (vs. RHE) in the EQCM set-up are shown.

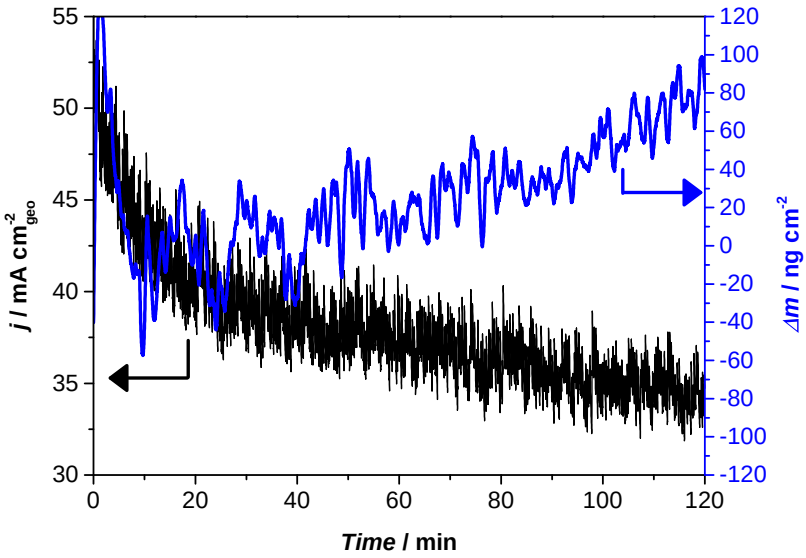

Figure 6.8: Chronoamperometry for IrO_2 thin film at 1.8 V (vs. RHE) in N_2 saturated electrolyte at room temperature. The black line denotes the current density, displayed on the left y-axis; while the blue line denotes the mass variation, displayed on the right y-axis.

The current density decreases over time, in particular at the beginning of the test. However, the mass seem not to change during the 2 hours test; on the contrary, it looks like the mass increases.

Similar behavior is observed during the chronopotentiometry test (figure 6.9), during which a subtle energy loss is accompanied by a small increase in the mass, which is almost zero (around 50 ng/cm^2) and could be correlated to water and oxygen intercalation in the film.

EQCM measurements were combined with ICP-MS analyses of the electrolyte and the results are depicted in figure 6.10. The data shows that during both tests small amount of iridium dissolved in the solution. The metal concentration is considerably lower than what has been found for ruthenium in the same experimental conditions (see section 5.2.2). More specifically, the loss corresponds to a dissolution rate of 0.19 ± 0.07 ML/h and 0.16 ML/h during

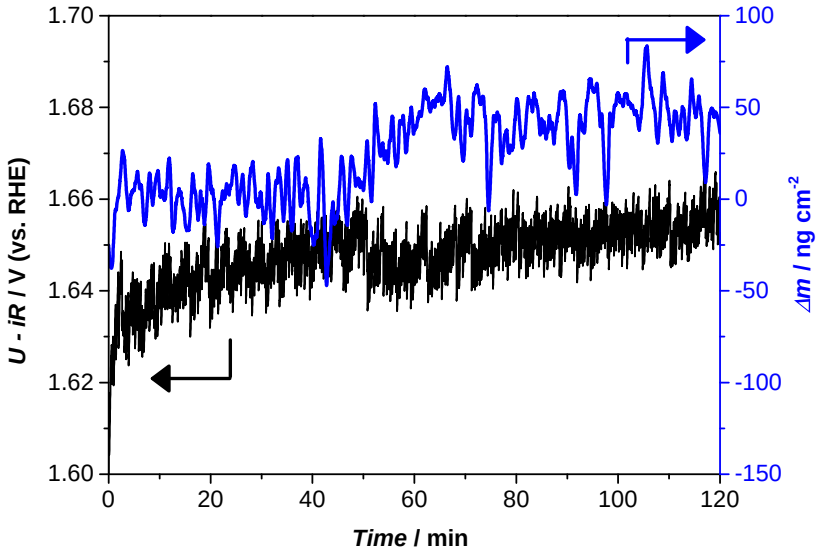

Figure 6.9: Chronopotentiometry for IrO_2 thin film at 30 mA/cm^2 in N_2 saturated electrolyte at room temperature. The black line denotes the potential change, displayed on the left y-axis; while the blue line denotes the mass variation, displayed on the right y-axis.

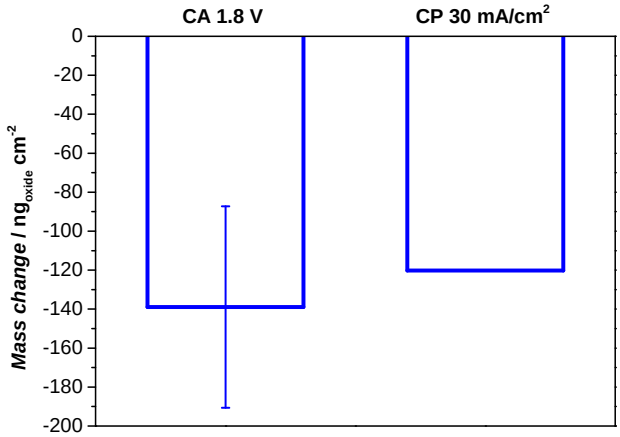

Figure 6.10: Mass dissolution of iridium dioxide during 2 h chronoamperometry at 1.8 V (vs. RHE) and 2 h chronopotentiometry at 30 mA/cm^2 tests. The error bar is based on three independent experiments.

CA and CP test, respectively. In turn, the rate corresponds to a lifetime of 663 hours (less than a month) when the potential is held constant, and 787 hours (∼one month) when the current is kept constant. Based on the ICP-MS results, we can speculate that the apparent increase in mass observed with EQCM may be ascribed to water and oxygen intercalation through the film pores.

In conclusion, IrO_2 thin films exhibits apparent higher catalytic activity, most likely due to higher surface roughness, which makes the comparison with RuO_2 thin film challenging. Furthermore, it shows much better stability than ruthenium dioxide under potentiostatic measurements.

The lower dissolution rate of iridium, in comparison to ruthenium dioxide, is in agreement with the recent findings by Mayrhofer and coworkers on metallic polycrystalline samples [57], discussed in section 2.1.5. They observed that iridium do corrode under OER conditions; however, the corrosion rate is more than an order of magnitude lower than ruthenium.

The comparison of the corrosion rate and the lifetime for 40 nm thick ruthenium and iridium oxide thin films is illustrated in Table 6.2.

Sample	$\left(\frac{dm}{dt}\right)_{1.8V_{RHE}}$ [ML_{oxide}/cm^2h]	$\left(\frac{dm}{dt}\right)_{30mA/cm^2}$ [ML_{oxide}/cm^2h]	$\Delta t_{1.8V_{RHE}}$ [hours]	$\Delta t_{30mA/cm^2}$ [hours]
RuO_2	4.8	4.4	26	26
IrO_2	0.2	0.16	663	787

Table 6.2: Comparison between 40 nm thick RuO_2 and IrO_2 thin film corrosion rate and lifetime under potentiodynamic conditions.

6.2 Ruthenium Dioxide Stabilisation by IrO_2

By using the same approach employed for investigating the corrosion of ruthenium and iridium dioxide thin films, a study of surface modified ruthenium dioxide thin films via addition of small amounts of iridium was performed. Preliminary results are shown herein.

Ruthenium dioxide thin films were prepared by reactive sputter deposition, as described in the previous chapter in section 5.2. When the deposition of ruthenium was concluded, small amounts of iridium oxide were sputtered onto the surface (nominal deposition thickness: 1, 2, 4 and 10 Å). The amount of iridium may look high, considering that a monolayer coverage of iridium dioxide corresponds to 3.2 Å [196]. However, even by considering a low roughness factor for RuO_2, e.g. 2, those amounts should correspond to sub-monolayer additions, except for the highest thickness. The deposition was carried out at 300°C and the sample was held at this temperature for 30 minutes to favor the diffusion of iridium oxide to the undercoordinated sites. It was not possible to use higher

temperature, because above 400°C, in oxygen, the titanium layer underneath the gold film in the EQCM crystals segregates to the surface. However, high temperature may be necessary to favor the diffusion of iridium oxide at the surface.

The samples were first characterised by XPS. The Ru 3d and the Ir 4f core level spectra for a sample with a nominal iridium deposition of 10 Å are shown in figure 6.11 and 6.12, respectively. The XPS spectra for all the samples with variable nominal iridium oxide deposition exhibit very similar peak shapes. In both cases the positions of the peaks attest the presence of the valence state IV (see section 3.2.1). The fitting reveals that the metallic component is zero and only the oxide is present at the surface. Both spectra exhibit the typical features for RuO_2 and IrO_2, with the pair of doublets for the main peak and the satellite [121, 165]. Interestingly, in all cases the Ru 3d and Ir 4f peaks could be fitted with reproducible and fixed positions and similar intensity ratios. This suggests that the chemical phase is not really changing, at least not strongly, among different nominal thickness of iridium. Furthermore, by taking XPS at different angles, we observed that the peaks do not change, indicating that the samples are rather homogeneous.

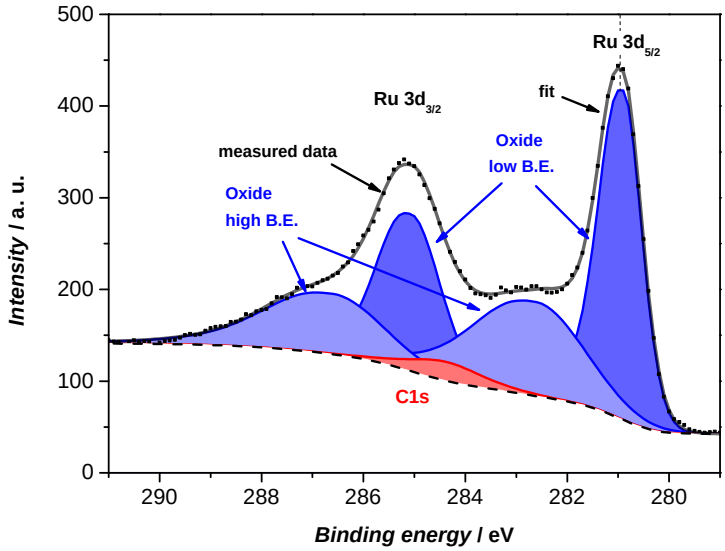

Figure 6.11: XPS spectrum of Ru 3d core level region of a RuO_2 thin film modified with 10 Å IrO_2. XPS taken at 21° emission angle. XPS performed by Paolo Malacrida.

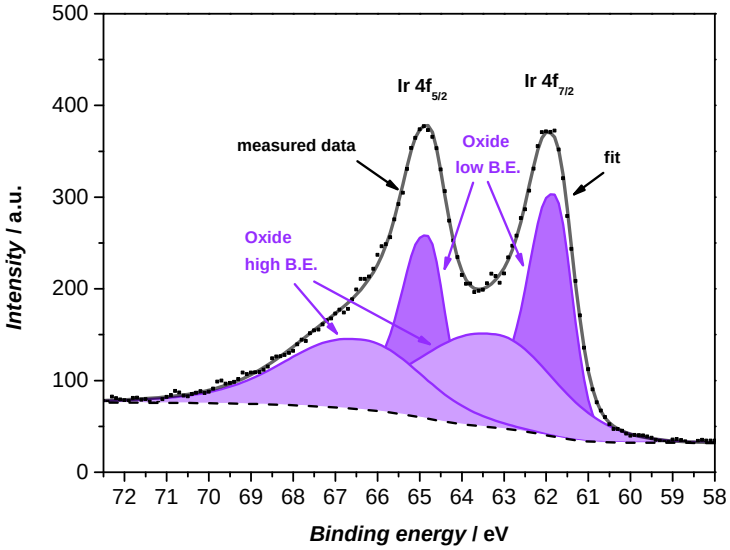

Figure 6.12: XPS spectrum of Ir 4f core level region of a RuO_2 thin film modified with 10 Å IrO_2. XPS taken at 21^o emission angle. XPS performed by Paolo Malacrida.

6.2.1 Activity

The activity was tested by quasi stationary cyclic voltammetry in the EQCM set-up. The CVs are shown in figure 6.13. The difference in activity between pure RuO_2 and IrO_2 films has been explained at the beginning of this chapter and we speculate it is due to microscopic area effect. Small additions of iridium oxide on a film of ruthenium should affect the surface area as well. However, the changes should be low and negligible. As already reported for mixtures of ruthenium and iridium oxides, when iridium is added, the activity goes down [118,120,122,123]. We also observe an activity loss upon deposition of iridium. In particular, we obtained a significant drop of 40 mV at 5 mA/cm^2 for 1 Å IrO_2 surface modified RuO_2, which becomes less pronounced (below 10 mV) as the iridium thickness increases (see insert b) in figure 6.13). The behavior significantly differs from the linear relationship of the overpotential at 0.1 mA/cm^2 on ruthenium iridium mixed oxides, reported by Kötz *et al.* [118].

Angle- resolved XPS on the surface modified films revealed that the 10 Å IrO_2 on RuO_2 shows no ruthenium concentration on the top layers, suggesting that the surface is fully covered with iridium. Hence, the activity of this surface modified film may be close to the intrinsic activity of IrO_2, or at least of a IrO_2 film with a comparable roughness with RuO_2 thin film. The depth profile with the atomic concentration as a function of depth is illustrated in figure 6.14.

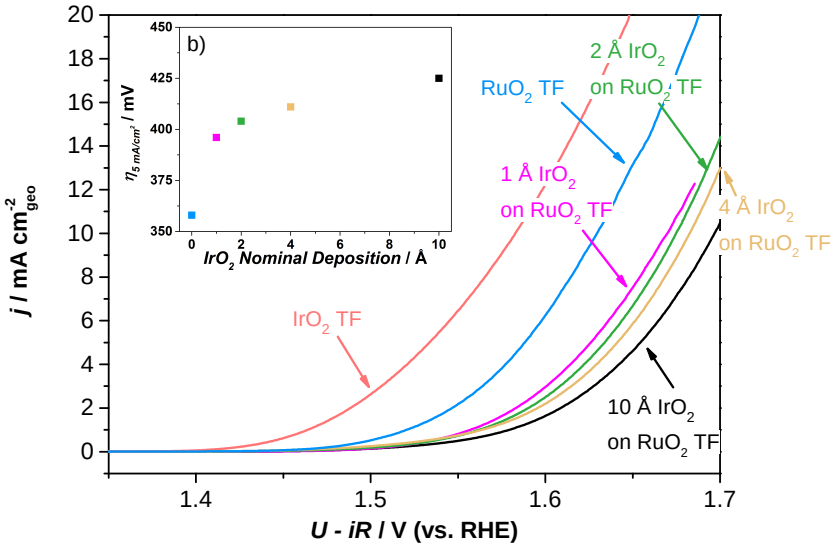

Figure 6.13: a) Quasi stationary CVs in N_2 saturated 0.05 H_2SO_4 at 5 mV/s in the EQCM set-up. Pure RuO_2, pure IrO_2, and surface modified RuO_2 films with 1, 2, 4 and 10 Å of IrO_2 are shown. b) The overpotential at 5 mA/cm^2 versus the iridium nominal deposition (in Å) is plotted as well in the insert b).

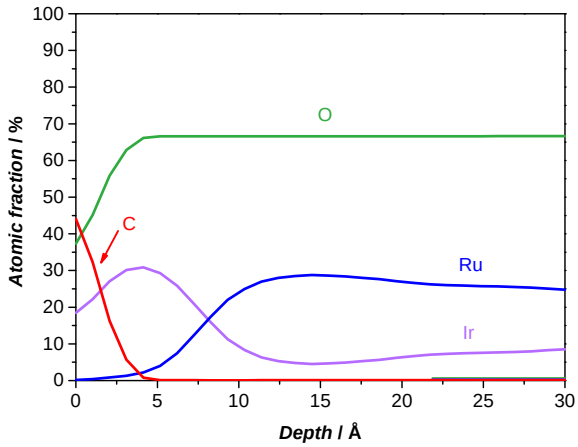

Figure 6.14: Depth profile of the surface modified 10 Å IrO_2 on RuO_2 thin film evaluated using angle resolved - XPS. Measurement performed by Paolo Malacrida.

6.2.2 Stability

To verify any improvement in stability for the surface-modified RuO_2 thin films, the catalysts were tested under potentiostatic conditions, as described in the previous chapter for ruthenium dioxide and in section 6.1.3 for iridium oxide [87]. The results are shown in figure 6.15.

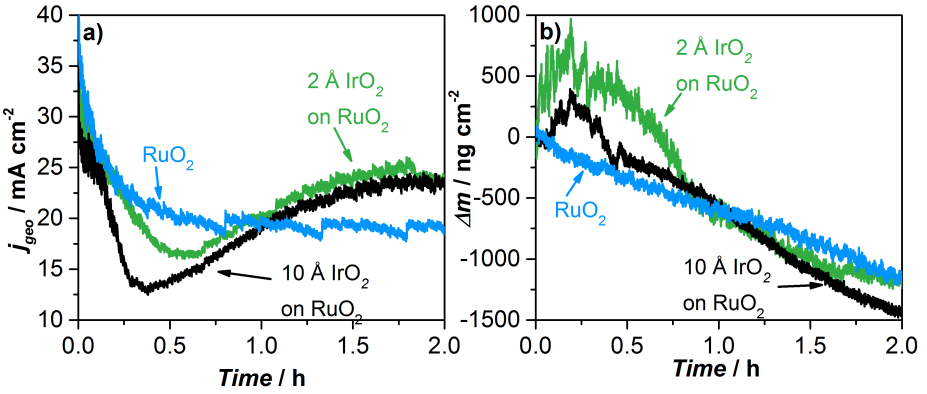

Figure 6.15: 2 hours CA test at 1.8 V (vs. RHE) in N_2 saturated electrolyte at room temperature for pure RuO_2 thin film, 2 Å IrO_2 and 10 Å IrO_2 on RuO_2. a) Current density. b) Mass loss.

Under these operative conditions, no effect on the stability, due to iridium, was observed. At the beginning, both surface-modified films behave differently from pure ruthenium dioxide. They both exhibit lower current density, combined with an increase in the mass. However, this effect is lost in less than an hour, after which they behave like the pure film. ICP-MS analyses of the electrolyte showed that only a fraction of the total amount of deposited iridium dissolved into the solution. On the other hand, if large pieces of film would have detached from the film because of delamination, they would not dissolve into the solution, hence it would be hard to evaluate it with ICP-MS.

We can speculate that the iridium atoms deposited at the surface did not diffuse to the undercoordinated sites when the film was prepared. Therefore, cycling the potential before the chronoamperometry test could help the diffusion towards undercoordinated sites. Hence, CVs were performed before the potentiostatic test. The results are shown in figure 6.16.

As in the previous case, an effect of the iridium seems to occur at the beginning of the chronoamperometry test (lower activity, increase in mass). However, again the effect vanishes within the first hour.

Although no or little stabilising effect was observed during the potentiostatic experiments, improvements were documented during the initial potentio-

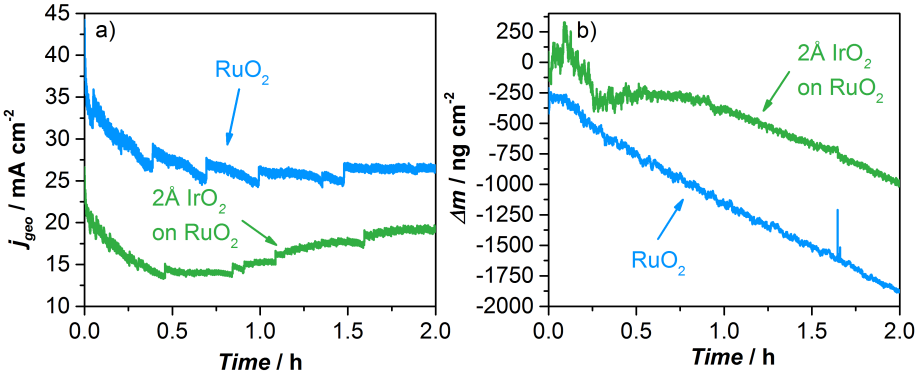

Figure 6.16: 2 h CA test at 1.8 V (vs. RHE) in N_2 saturated electrolyte at room temperature for pure RuO_2 thin film and 2 Å IrO_2 on RuO_2, after 60 cycles ($\sim$ 2 hours) between 1.23 and 1.8 V (vs. RHE) at 20 mV/s. a) Current density. b) Mass loss.

dynamic test. This could indicate that cyclicing the potential can indeed help the diffusion of iridium on the surface.

The stability tests with dynamic operations are reported in figure 6.17. An

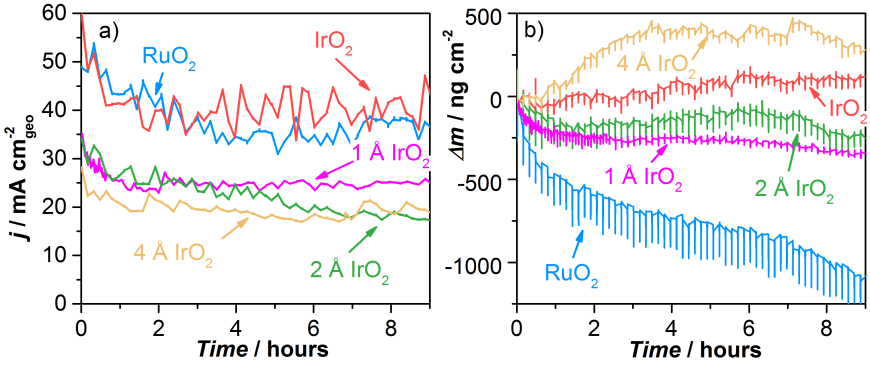

Figure 6.17: Cyclic voltammetry between 1.23 and 1.8 V (vs. RHE) at 20 mV/s in N_2 saturated electrolyte at room temperature for pure RuO_2 and IrO_2 thin film, and 2 and 4 Å IrO_2 on RuO_2. a) Current density at 1.8 V vs. time. b) Mass loss evaluated from the EQCM.

effect due to additions of iridium is now visible and an improvement in stability seems to occur over the 9 hours test, measured by EQCM (figure 6.17 b), with a parallel loss in activity (figure 6.17 a). The samples with 1 Å of IrO_2 exhibits

a drastic improvement in stability, in comparison to pure RuO_2, while further addition of iridium oxide, such as 2 Å, induce slight extra improvements. The sample with 4 Å of IrO_2 behaves differently from the other surface-modified samples. It exhibits a mass gain over time. A similar but less pronounced behavior was observed for the pure IrO_2 film. This behaviour may be related to the ability of the EQCM to adapt its properties, while the potential is cycled. In particular, if the capacitance of the oscillator circuit, C_0, is not compensated correctly, the measured frequency may be wrong. By observing C_0 during the experiments, it was found that over long time test, the compensation tends to be slightly off. Therefore, long term tests with EQCM are not very reproducible.

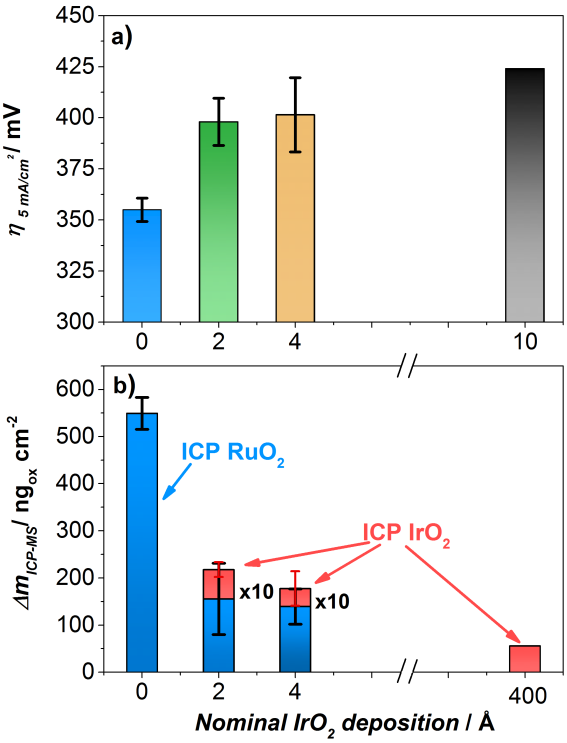

Figure 6.18: a) Overpotential at 5 mA/cm^2, from the first quasi stationary CV, recorded at 5 mV/s between 1.23 and 1.8 V (vs. RHE), as a function of the nominal IrO_2 deposition. b) ICP-MS mass loss for RuO_2 (in blue) and IrO_2 (in red) evaluated after 150 cycles. The error bars are evaluated from at least four distinct experiments.

Nevertheless, EQCM measurements were combined with analyses of the electrolyte by ICP-MS. An aliquot from the electrolyte was taken after 150 cylcles, corresponding to $\sim$ 2 h and 22 min. The ICP-MS results are shown in figure

6.18 b), in combination with the initial activity (figure 6.18 a). It is important to highlight that, as discussed at the beginning of the chapter, 40 nm IrO_2 thin film has a much higher roughness than 40 nm RuO_2 and the apparent overpotential is only 300 mV at 5 mA/cm^2. For this reason, the overpotential for a thin film of IrO_2 is not shown in figure 6.18 a). However, the loss in activity as the amount of iridium increases is illustrated by showing the overpotential for 10 Å IrO_2 surface modified RuO_2, which, from AR-XPS, seem to fully cover the RuO_2 film and may have an activity closer to the instrinsic catalytic activity of IrO_2.

The ICP-MS results show that a stability improvement occurs, although not as drastic as hoped. Most strikingly, the stability after addition of 2 Å IrO_2 was improved with $\sim 72\%$. Further addition of iridium, 4 Å IrO_2, did not produce any significant change: both activity and stability are similar to the results for 2 Å IrO_2 sample.

6.2.3 Discussion

The termination concept with iridium dioxide diffusing to the undercoordinated sites and protecting ruthenium dioxide from dissolution could be a possible interpretation of the experimental results. The fact that ruthenium dioxide dissolution does not go to zero when the surface is modified could indicate that not all the undercoordinated sites are covered, hence protected. However, it is difficult to confirm it, especially because iridium dioxide is an active OER catalyst as well. It is challenging to distinguish between iridium dioxide acting as a more stable overlayer or as a stabiliser towards RuO_2.

To better understand the mechanism further investigations are needed, in particular attempts should be addressed to follow in situ the corrosion mechanism. A possible way could be the use of a scanning tunneling microscopy (STM) or an EC-STM on well-defined and flat surfaces. By performing STM on Pt modified Ru(0001) single crystal before and after electrochemistry, Behm and coworkers observed surface reconstruction and dissolution occurring at the steps [203]. Combining STM with electrochemistry or using EC-STM is very challenging, but it could lead to a better understanding of the ruthenium dioxide corrosion mechanism and the stabilising effect of iridium dioxide.

A simpler but very interesting experiment would be to produce the samples at higher temperatures to verify any temperature effect. That might help the diffusion of iridium oxide and support the theoretical interpretation.

Addionally, X-ray Absorption Spectroscopy could be used to determine the electronic and structural properties of ruthenium iridium mixed oxides, e.g. X-ray Absorption Near Edge Spectroscopy (XANES) and Extended X-Ray Absorption Fine Structure (EXAFS) [122, 125]. Although XANES gives information about the oxidation state of the bulk, investigations of the Ru K-edge on very thin film could provide the average value for the near surface region. RuO_2 corrosion occurs when Ru is in a higher oxidation state than VI [58, 112].

Observing that, in mixed ruthenium iridium oxides, ruthenium oxidation state does not go above VI could indicate that iridium dioxide has a stabilising effect on it [125]. On the other hand, by using EXAFS, which provides information such as interatomic distances, coordination numbers and elemental identities of the neighboring atoms, it may be possible to understand if iridium dioxide coordinates with ruthenium dioxide or if it forms islands and agglomerates.

Finally, substituting iridium with another stable material, which is not active for OER, could help understanding if the observed effect is only due to the performance of iridium as a more stable skeleton and not as a stabiliser of ruthenium dioxide. Possible alternatives are titanium oxide and tantalum oxide. Both are cheap and abundant materials [7] and are extremely stable at high oxidative potentials [105]. Furtermore, they already proved to have a positive effect on the stability when mixed with ruthenium and with ruthenium iridium mixed oxides [127,128].

6.3 Conclusion

In this chapter a new approach for improving the stability of an active OER catalyst under acidic conditions by a termination concept has been reported. The case of ruthenium dioxide, active but unstable OER catalyst, stabilised by iridium oxide, which is less active but more stable, has been shown. Preliminary results on surface modified ruthenium dioxide thin films suggests an improvement in stability with a lower activity loss.

This approach is hoped to be applicable to other oxides. The first step would be substituting the guest material with a cheaper and as stable element, e.g. titanium, tantalum, etc.. Finally, the ultimate goal would be to use the same approach with a cheaper host material. Indeed, in parallel to the present investigation, experiments at our laboratory on titanium modified manganese oxide films in acid have shown promising results [109].

Chapter 7

Overall conclusion and outlook

7.1 Conclusion

The core of this project was to investigate the intrinsic catalytic activity of ruthenium oxide, its stability under reaction conditions and how to improve its durability.

Initially, we have pointed out the importance of studying well-defined surfaces, where electronic properties can be distinguished from surface area effects. Commercial ruthenium nanoparticles showed poor reproducibility and difficulties related to conductivity and inhomogeneities of the samples. On the other hand, mass-selected nanoparticles, prepared by a physical method, provided a model investigation of the oxygen evolution reaction. Thanks to extensive characterisation, by a combination of physical surface sensitive techniques and electrochemistry, it was found that OER activity and stability are highly sensitive to the surface pre-treatment. In well agreement with literature, we observed that a proper oxidation treatment can improve the stability of nanoparticulate catalysts, although affecting the activity [58, 65, 71, 107]. Thermally annealed RuO_2 nanoparticles exhibited significantly better activity than the current state-of-the-art, with a 30-fold improvement in mass activity compared to Pt-Ir nano whiskers used in real PEM electrolysers at 80^oC [26].

The well-defined shape of small particles allowed to evaluate the specific activity and the turnover frequency, which showed the highest values reported so far for precious metal oxides in acidic media. Furthermore, the effect of particle size was investigated and a tentative maximum at around $3-5$ nm was

identified.

To approach the stability issues, we reported a combinatorial investigation with EQCM measurements and ICP-MS analyses on ruthenium dioxide thin films. We showed that the solely electrochemical measurements are not enough to evaluate the long-term stability of a catalyst and other complementary techniques are required. We also reported that the stability procedure (potentiodynamic and potentiostatic operations) needs to be adapted depending on the investigated material and its corrosion mechanism. In particular, ruthenium dioxide corrosion is a static process that is controlled by the applied potential and not by potential cycling.

A way to improve the stability of ruthenium, which in turn could be applied to the mass-selected nanoparticles, is by mixing it with iridium or another stable oxide, e.g. titanium, tantalum. This has been done in the past and it lead to the development of the dimensionally stable anodes, DSA® [28, 119]. DFT calculations on Ru-Ir mixed oxides suggested that the improved stability of the DSA® may be due to a termination process [47]. Iridium should preferably segregate to the undercoordinated sites, which are the most prone to corrosion [108], and impede the ruthenium dissolution. Preliminary results on surface modified ruthenium dioxide thin films with a variety of iridium thicknesses showed a little improvement in the stability with a slight effect on the activity, achievable only under potentiodynamic operations.

7.2 Outlook

To achieve a better understanding of the critical parameters that control the oxygen evolution reaction and the nature of the improved activity on the mass-selected ruthenium oxide nanoparticles reported in this study, further investigations are required. In particular, it would be interesting to correlate the electrochemical properties of the nanoparticles with extensively charcterised single crystalline oxide surfaces. Similarly to what has been done with Pt mass-selected nanoparticles for the oxygen reduction reaction, the use of temperature programmed desorption (TPD) technique on RuO_2 could help identify the density of active sites on distinct surfaces [204]. On the other hand, ambient pressure XPS on as-deposited and thermally oxidised nanoparticles could help elucidating the reasons behind the differences in stability and activity [113].

At the same time, it is essential to develop a proper chemical synthesis which allows the preparation of large surface area catalysts with similar activity as the mass-selected nanoparticles.

Although the stability of the nanoparticles was drastically improved by preoxidation of the catalysts, the durability reported here is not sufficient for real devices. Further improvements will be needed.

In this perspective, it is important to elucidate the mechanism by which iridium (or titanium) stabilises ruthenium dioxide. Addition of sub monolayer

or tiny amounts of a stable oxide may be a good way to verify the hyphotesis suggested by theory, i.e. iridium oxide diffuses to the undercoordinated sites protecting ruthenium [47]. However, the use of sputtered thin films showed some complications related to the roughness of the iridium dioxide film and to the fact that it is problematic to distinguish between iridium oxide acting as a stable overlayer or as a stabiliser. Furthermore, it is not possible to directly observe where the iridium is exactly located. An interesting, but challenging, approach would be the use of RuO_2 single crystals and electrochemical scanning tunneling microscopy to observe the corrosion mechanism. Titanium and tantalum oxide should be preferred over iridium, because they are inactive towards OER. A RuO_2 surface fully covered with either Ti or Ta will exhibit great stability but it will be inactive. By tuning the amount of Ti and Ta, a stable catalyst retaining the activity of RuO_2 should be obtained.

Finally, similarly to what has been done for ORR [133, 142, 191, 192], more standardized protocols to assess the durability of OER catalysts for short-term and in particular long term-test should be provided.

Bibliography

[1] U. S. census bureau, "U.s. and world population clock, http://www.census.gov/popclock/," November 2014.

[2] "United nations population fund. population trends. linking population, poverty and development, http://www.unfpa.org/pds/trends.htm," November 2014.

[3] D. W. Thompson, *On Growth and Form*. 1942 ed., 1917.

[4] R. E. Smalley, "Future Global Energy Prosperity: The Terawatt Challenge," *Materials Matters*, vol. 30, pp. 412–417, 2004.

[5] N. S. Lewis and D. G. Nocera, "Powering the Planet: Chemical Challenges in Solar Energy Utilization.," *Proceedings of the National Academy of Sciences of the United States of America*, vol. 103, no. 43, pp. 15729–35, 2006.

[6] N. Armaroli and V. Balzani, "The Future of Energy Supply: Challenges and Opportunities.," *Angewandte Chemie (International ed. in English)*, vol. 46, no. 1-2, pp. 52–66, 2007.

[7] P. C. K. Vesborg and T. F. Jaramillo, "Addressing the terawatt challenge: scalability in the supply of chemical elements for renewable energy," *RSC Advances*, vol. 2, no. 21, pp. 7933–7947, 2012.

[8] BP, "BP Statistical Review of World Energy," tech. rep., 2014.

[9] C. A. S. Hall and J. W. Day, "Revisiting the limits to growth after peak oil," *American Scientist*, vol. 97, no. 3, pp. 230–237, 2009.

[10] N. Armaroli and V. Balzani, "The Legacy of Fossil Fuels.," *Chemistry, an Asian journal*, vol. 6, no. 3, pp. 768–784, 2011.

[11] R. F. Service, "Solar energy - is it time to shoot for the sun?," *Science*, vol. 309, no. 5734, pp. 548–551, 2005.

[12] J. Tamanini, A. Bassi, C. Hoffman, and J. Valenciano, "The Global Green Economy Index," tech. rep., Dual Citizen LLC, 2014.

[13] "The Danish Climate Policy Plan Towards a Low Carbon Society," Tech. Rep. August, Danish Energy Agency, Copenhagen, 2013.

[14] "EMD International. http://www.emd.dk/el/."

[15] U. Eberle and R. von Helmolt, "Sustainable Transportation Based on Electric Vehicle Concepts: a Brief Overview," *Energy & Environmental Science*, vol. 3, no. 6, pp. 689–699, 2010.

[16] FuelCellToday, "Water Electrolysis & Renewable Energy Systems," tech. rep., 2013.

[17] M. Gattrell, N. Gupta, and A. Co, "Electrochemical reduction of co_2 to hydrocarbons to store renewable electrical energy and upgrade biogas," *Energy Conversion and Management*, vol. 48, no. 4, pp. 1255–1265, 2007.

[18] J. R. Varcoe, P. Atanassov, D. R. Dekel, A. M. Herring, M. A. Hickner, P. A. Kohl, R. Kucernak, W. E. Mustain, K. Nijmeijer, K. Scott, T. Xu, and L. Zhuang, "Anion-exchange Membranes in Electrochemical Energy Systems," *Energy & Environmental Science*, 2014.

[19] W. Sheng, H. A. Gasteiger, and Y. Shao-Horn, "Hydrogen Oxidation and Evolution Reaction Kinetics on Platinum: Acid vs Alkaline Electrolytes," *Journal of The Electrochemical Society*, vol. 157, no. 11, pp. B1529–B1536, 2010.

[20] P. Sanchis, L. M. Gandia, and P. Sanchis, "Water Electrolysis: Current Status and Future Trends," *Proceeding of the IEEE*, vol. 100, no. 2, pp. 410–427, 2012.

[21] I. E. Agency, "Hydrogen Implementing Agreement. Alkaline Electrolysis," tech. rep., 2012.

[22] S. Kotrel and S. Bräuninger, "Industrial Electrocatalysis," in *Handbook of Heterogeneous Catalysis* (G. Ertl, H. Knôzinger, F. Schuth, and J. Weitkamp, eds.), ch. 8.1, pp. 1936–1958, Wiley-CPH, 2nd ed., 2008.

[23] S. Grigoriev, V. Porembsky, and V. Fateev, "Pure hydrogen production by PEM electrolysis for hydrogen energy," *International Journal of Hydrogen Energy*, vol. 31, no. 2, pp. 171–175, 2006.

[24] K. E. Ayers, E. B. Anderson, C. Capuano, B. Carter, L. Dalton, G. Hanlon, J. Manco, and M. Niedzwiecki, "Research Advances towards Low Cost, High Efficiency PEM Electrolysis," *ECS Transactions*, vol. 33, no. 1, pp. 3–15, 2010.

[25] K. C. Neyerlin, W. Gu, J. Jorne, and H. A. Gasteiger, "Study of the Exchange Current Density for the Hydrogen Oxidation and Evolution Reactions," *Journal of The Electrochemical Society*, vol. 154, no. 7, pp. B631–B365, 2007.

[26] M. K. Debe, S. M. Hendricks, G. D. Vernstrom, M. Meyers, M. Brostrom, M. Stephens, Q. Chan, J. Willey, M. Hamden, C. K. Mittelsteadt, C. B. Capuano, K. E. Ayers, and E. B. Anderson, "Initial Performance and Durability of Ultra-Low Loaded NSTF Electrodes for PEM Electrolyzers," *Journal of The Electrochemical Society*, vol. 159, no. 6, pp. K165–K176, 2012.

[27] E. Fabbri, A. Habereder, K. Waltar, R. Kotz, and T. Schmidt, "Developments and perspectives of oxide-based catalysts for the oxygen evolution reaction," *Catalysis Science & Technology*, 2014.

[28] S. Trasatti, "Electrocatalysis: understanding the success of DSA®," *Electrochimica Acta*, vol. 45, no. 15-16, pp. 2377–2385, 2000.

[29] S. Trasatti, "Surface Chemistry of Oxides and Electrocatalysis," *Croatia Chemica Acta*, vol. 63, no. 3, pp. 313–329, 1990.

[30] S. Trasatti, "Electrochemistry and Environment: The role of Electrocatalysis," *International Journal of Hydrogen Energy*, vol. 20, no. 10, pp. 835–844, 1995.

[31] H. Dau, C. Limberg, T. Reier, M. Risch, S. Roggan, and P. Strasser, "The Mechanism of Water Oxidation: From Electrolysis via Homogeneous to Biological Catalysis," *ChemCatChem*, vol. 2, no. 7, pp. 724–761, 2010.

[32] M. T. Koper, "Thermodynamic Theory of Multi-Electron Transfer Reactions: Implications for Electrocatalysis," *Journal of Electroanalytical Chemistry*, vol. 660, no. 2, pp. 254–260, 2011.

[33] T. Erdey-Gruz and M. Volmer, "The theory of hydrogen high tension.," *Zeitschrift Fur Physikalische Chemie*, vol. 150, pp. 203–213, 1930.

[34] J. Tafel, "The polarisation of cathodic hydrogen development.," *Zeitschrift Fur Physikalische Chemie - Stochiometrie und Verwandtschaftslehre*, vol. 50, no. 6, pp. 641–712, 1905.

[35] J. Heyrovsky, "A theory of overpotential," *Recueil Des Travaux Chimiques Des Pays - Bas*, vol. 46, pp. 582–585, 1927.

[36] L. Chen, D. Guay, and A. Lasia, "Kinetics of the Hydrogen Evolution Reaction on RuO_2 and IrO_2 Oxide Electrodes in H_2SO_4 Solution: An AC Impedance Study," *Journal of electrochemical Society*, vol. 143, no. 11, pp. 3576–3584, 1996.

[37] N. Pentland, J. O. Bockris, and E. Sheldon, "Hydrogen Evolution Reaction on Copper, Gold, Molybdenum, Palladium, Rhodium, and Iron," *Journal of The Electrochemical Society*, vol. 104, no. 3, p. 182, 1957.

[38] J. Kibsgaard, T. F. Jaramillo, and F. Besenbacher, "Building an Appropriate Active-Site Motif into a Hydrogen-Evolution Catalyst with Thiomolybdate $[Mo_3S_{13}]^{2-}$ Clusters.," *Nature chemistry*, vol. 6, no. 3, pp. 248–53, 2014.

[39] Z. Chen, D. Cummins, B. N. Reinecke, E. Clark, M. K. Sunkara, and T. F. Jaramillo, "Core-Shell MoO_3-MoS_2 Nanowires for Hydrogen Evolution: A functional Design for Electrocatalytic Materials," *Nano Letters*, vol. 11, pp. 4168–4175, 2011.

[40] A. K. M. S. Huq and A. J. Rosenberg, "Electrochemical Behavior of Nickel Compounds - The Hydrogen Evolution Reaction on NiSi, NiAs, NiSb, NiS, $NiTe_2$, and thier Constituent Elements," *Journal of electrochemical Society*, vol. 111, no. 3, pp. 270–277, 1964.

[41] A. Bélanger and A. K. Vijh, "Hydrogen Evolution Reaction on Vanadium, Chromium, Manganese, Cobalt," *Journal of electrochemical Society*, vol. 121, no. 2, pp. 225–230, 1971.

[42] A. K. Vijh, "Electrolytic Hydrogen Evolution Reaction on Aluminum in Acid Solutions," *The Journal of Physical Chemistry*, vol. 72, no. 4, pp. 1148–1156, 1968.

[43] W. Sheng, M. Myint, J. G. Chen, and Y. Yan, "Correlating the Hydrogen Evolution Reaction Activity in Alkaline Electrolytes with the Hydrogen Binding Energy on Monometallic Surfaces," *Energy & Environmental Science*, vol. 6, no. 5, pp. 1509–1512, 2013.

[44] C. Chen, Y. Kang, Z. Huo, Z. Zhu, W. Huang, H. L. Xin, J. D. Snyder, D. Li, J. a. Herron, M. Mavrikakis, M. Chi, K. L. More, Y. Li, N. M. Markovic, G. a. Somorjai, P. Yang, and V. R. Stamenkovic, "Highly Crystalline Multimetallic Nanoframes with three-Dimensional Electrocatalytic Surfaces.," *Science*, vol. 343, no. 6177, pp. 1339–1343, 2014.

[45] J. R. McKone, B. F. Sadtler, C. A. Werlang, N. S. Lewis, and H. B. Gray, "NiMo Nanopowders for Efficient Electrochemical Hydrogen Evolution," *ACS Catalysis*, vol. 3, pp. 166–169, 2013.

[46] W. Sheng, A. P. Bivens, M. Myint, Z. Zhuang, R. V. Forest, Q. Fang, J. G. Chen, and Y. Yan, "Non-Precious Metal Electrocatalysts with High Activity for Hydrogen Oxidation Reaction in Alkaline Electrolytes," *Energy & Environmental Science*, vol. 7, no. 5, pp. 1719–1724, 2014.

[47] I. C. Man, *Theoretical study of electro-catalysts for oxygen evolution.* Phd thesis, Technical University of Denmark, February 2011.

[48] J. Rossmeisl, Z.-W. Qu, H. Zhu, G.-J. Kroes, and J. Nø rskov, "Electrolysis of water on oxide surfaces," *Journal of Electroanalytical Chemistry*, vol. 607, no. 1-2, pp. 83–89, 2007.

[49] S. Trasatti, "Electrocatalysis in the Anodic Evolution of Oxygen and Chlorine," *Electrochimica Acta*, vol. 29, pp. 1503–1512, 1984.

[50] Y. Matsumoto and E. Sato, "Electrocatalytic Properties of Transition Metal Oxides for Oxygen Evolution Reaction," *Materials Chemistry and Physics*, vol. 14, pp. 397–426, 1986.

[51] J. Rossmeisl, A. Logadottir, and J. Nø rskov, "Electrolysis of water on (oxidized) metal surfaces," *Chemical Physics*, vol. 319, no. 1-3, pp. 178–184, 2005.

[52] T. Bligaard, J. K. Nø rskov, S. Dahl, J. Matthiesen, C. Christensen, and J. Sehested, "The Brønsted–Evans–Polanyi relation and the volcano curve in heterogeneous catalysis," *Journal of Catalysis*, vol. 224, no. 1, pp. 206–217, 2004.

[53] A. Vojvodic, F. Calle-Vallejo, W. Guo, S. Wang, A. Toftelund, F. Studt, J. I. Martínez, J. Shen, I. C. Man, J. Rossmeisl, T. Bligaard, J. K. Nø rskov, and F. Abild-Pedersen, "On the behavior of Brønsted-Evans-Polanyi relations for transition metal oxides.," *The Journal of chemical physics*, vol. 134, no. 24, p. 244509, 2011.

[54] I. C. Man, H.-Y. Su, F. Calle-Vallejo, H. a. Hansen, J. I. Martínez, N. G. Inoglu, J. Kitchin, T. F. Jaramillo, J. K. Nø rskov, and J. Rossmeisl, "Universality in Oxygen Evolution Electrocatalysis on Oxide Surfaces," *ChemCatChem*, vol. 3, no. 7, pp. 1159–1165, 2011.

[55] P. Sabatier, "Announcement. hydrogenation and dehydrogenation for catalysis.," *Berichte Der Deutschen Chemischen Gesellschaft*, vol. 44, pp. 1984–2001, 1911.

[56] M. H. Miles and M. A. Thomason, "Periodic Variations of Overvoltages for Water Electrolysis in Acid Solutions from Cyclic Voltammetric Studies," *Journal of electrochemical Society*, vol. 123, no. 10, pp. 1459–1461, 1976.

[57] S. Cherevko, A. R. Zeradjanin, A. A. Topalov, N. Kulyk, and J. J. Mayrhofer, "Dissolution of noble metals during oxygen evolution in acidic media," *ChemCatChem*, vol. 6, pp. 2219–2223, 2014.

[58] N. Danilovic, R. Subbaraman, K.-C. Chang, S. H. Chang, Y. Kang, J. D. Snyder, A. P. Paulikas, D. Strmcnik, Y.-T. Kim, D. J. Myers, V. R. Stamenkovic, and N. M. Markovic, "Activity-Stability Trends for the Oxygen Evolution Reaction on Monometallic Oxides in Acidic Environments," *The Journal of Physical Chemistry Letters*, vol. 5, no. 14, pp. 2474–2478, 2014.

[59] S. Ardizzone, M. Falciola, and S. Trasatti, "Effect of the Nature of the Precursor on the Electrocatalytic Properties of Thermally Prepared Ruthenium Oxide," *J. Electrochem. Soc.*, vol. 136, no. 5, pp. 3–8, 1989.

[60] E. Tsuji, A. Imanishi, K. Fukui, and Y. Nakato, "Electrocatalytic Activity of Amorphous RuO_2 Electrode for Oxygen Evolution in an Aqueous Solution," *Electrochimica Acta*, vol. 56, no. 5, pp. 2009–2016, 2011.

[61] G. Lodi, E. Sivieri, A. De Battisti, and S. Trasatti, "Ruthenium Dioxide-Based Film Electrodes. III. Effect of Chemical Composition and Surface Morphology on Oxygen Evolution in Acid Solutions," *Journal of Applied Electrochemistry*, vol. 8, pp. 135–143, 1978.

[62] D. Galizzioli, F. Tantardini, and S. Trasatti, "Ruthenium dioxide: a new electrode material. I. Behaviour in acid solutions of inert electrolytes," *Journal of Applied Electrochemistry*, vol. 4, pp. 57–67, 1974.

[63] C. Iwakura, K. Hirao, and H. Tamura, "Preparation of Ruthenium Dioxide Characteristics in Acid Solutions," *Electrochimica Acta*, vol. 22, pp. 335–340, 1977.

[64] Y. Lee, J. Suntivich, K. J. May, E. E. Perry, and Y. Shao-Horn, "Synthesis and Activities of Rutile IrO_2 and RuO_2 Nanoparticles for Oxygen Evolution in Acid and Alkaline Solutions," *The Journal of Physical Chemistry Letters*, vol. 3, pp. 399–404, 2012.

[65] M. Vukovic, "Oxygen Evolution on an Electrodeposited Ruthenium Electrode in Acid Solution - The Effect of Thermal Treatment," *Electrochimica Acta*, vol. 34, pp. 287–291, 1989.

[66] I. Katsounaros, S. Cherevko, A. R. Zeradjanin, and K. J. J. Mayrhofer, "Oxygen Electrochemistry as a Cornerstone for Sustainable Energy Conversion," *Angewandte Chemie International Edition*, vol. 52, pp. 2–22, 2013.

[67] P. Castelli, S. Trasatti, F. H. Pollak, and W. E. O'Grady, "Single Crystal as Model Electrocatalysts Oxygen Evolution on RuO_2 (110)," *Journal of Electroanalytical Chemistry*, vol. 210, pp. 189–194, 1986.

[68] K. A. Stoerzinger, L. Qiao, M. D. Biegalski, and Y. Shao-Horn, "Orientation-Dependent Oxygen Evolution Activities of Rutile IrO_2 and RuO_2," *The Journal of Physical Chemistry Letters*, vol. 5, no. 110, pp. 1636–1641, 2014.

[69] M. Vukmirovic, R. Sabatini, and R. Adzic, "Growth of RuO_2 by electrochemical and gas-phase oxidation of an Ru(0001) surface," *Surface Science*, vol. 572, no. 2-3, pp. 269–276, 2004.

[70] R. Kötz, H. J. Lewerenz, and S. Stucki, "XPS Studies of Oxygen Evolution on Ru and $Ru0_2$ Anodes," *Journal of electrochemical Society*, vol. 130, no. 4, pp. 825–828, 1983.

[71] S. Stucki and A. Menth, "Physikalisch-chemische Probleme bei der Erzeugung und Speicherung chemischer sekundarer Energietrager," *Ber. Bunsenges. Phys. Chem.*, vol. 84, pp. 1008–1013, 1980.

[72] F. J. Perez-Alonso, D. N. McCarthy, A. Nierhoff, P. Hernandez-Fernandez, C. Strebel, I. E. L. Stephens, J. H. Nielsen, and I. Chorkendorff, "The effect of size on the oxygen electroreduction activity of mass-selected platinum nanoparticles.," *Angewandte Chemie (International ed. in English)*, vol. 51, no. 19, pp. 4641–3, 2012.

[73] M. Nesselberger, M. Roefzaad, R. F. Hamou, P. U. Biedermann, F. F. Schweinberger, S. Kunz, K. Schloegl, G. K. H. Wiberg, S. Ashton, U. Heiz, K. J. J. Mayrhofer, and M. Arenz, "The Effect of Particle Proximity on the Oxygen Reduction Rate of Size-Selected Platinum clusters.," *Nature materials*, vol. 12, no. 10, pp. 919–24, 2013.

[74] P. Hernandez-Fernandez, F. Masini, D. N. McCarthy, C. E. Strebel, D. Friebel, D. Deiana, P. Malacrida, A. Nierhoff, A. Bodin, A. M. Wise, J. H. Nielsen, T. W. Hansen, A. Nilsson, I. E. L. Stephens, and I. Chorkendorff, "Mass-selected nanoparticles of Pt_xY as model catalysts for oxygen electroreduction," *Nature Chemistry*, vol. 6, no. 8, pp. 732–738, 2014.

[75] J. Jirkovský, M. Makarova, and P. Krtil, "Particle Size Dependence of Oxygen Evolution Reaction on Nanocrystalline RuO_2 and $Ru_{0.8}Co_{0.2}O_{1-x}$," *Electrochemistry Communications*, vol. 8, no. 9, pp. 1417–1422, 2006.

[76] K. Macounová, J. Jirkovský, M. V. Makarova, J. Franc, and P. Krtil, "Oxygen evolution on $Ru_{1-x}Ni_xO_{2-y}$ nanocrystalline electrodes," *Journal of Solid State Electrochemistry*, vol. 13, no. 6, pp. 959–965, 2009.

[77] B. R. Cuenya, S.-H. Baeck, T. F. Jaramillo, and E. W. McFarland, "Size- and support-dependent electronic and catalytic properties of Au^0/Au^{3+} nanoparticles synthesized from block copolymer micelles.," *Journal of the American Chemical Society*, vol. 125, pp. 12928–34, Oct. 2003.

[78] G. A. Tritsaris, J. Greeley, J. Rossmeisl, and J. K. Nø rskov, "Atomic-Scale Modeling of Particle Size Effects for the Oxygen Reduction Reaction on Pt," *Catalysis Letters*, vol. 141, no. 7, pp. 909–913, 2011.

[79] H. N. Nong, L. Gan, E. Willinger, D. Teschner, and P. Strasser, "IrO_x core-shell nanocatalysts for cost- and energy-efficient electrochemical water splitting," *Chemical Science*, vol. 5, pp. 2955–2963, 2014.

[80] J. Greeley, I. E. L. Stephens, A. S. Bondarenko, T. P. Johansson, H. a. Hansen, T. F. Jaramillo, J. Rossmeisl, I. Chorkendorff, and J. K. Nø rskov, "Alloys of Platinum and Early Transition Metals as Oxygen Reduction Electrocatalysts.," *Nature chemistry*, vol. 1, no. 7, pp. 552–6, 2009.

[81] R. Forgie, G. Bugosh, K. C. Neyerlin, Z. Liu, and P. Strasser, "Bimetallic Ru Electrocatalysts for the OER and Electrolytic Water Splitting in Acidic Media," *Electrochemical and Solid-State Letters*, vol. 13, no. 4, pp. B36–B39, 2010.

[82] V. Petrykin, Z. Bastl, J. Franc, K. Macounova, M. Makarova, S. Mukerjee, N. Ramaswamy, I. Spirovova, and P. Krtil, "Local Structure of Nanocrystalline $Ru_{1-x}Ni_xO_{2-\delta}$ Dioxide and Its Implications for Electrocatalytic Behavior - An XPS and XAS Study," *Journal of Physical Chemistry C*, vol. 113, pp. 21657–21666, 2009.

[83] V. Petrykin, K. Macounová, M. Okube, S. Mukerjee, and P. Krtil, "Local structure of Co doped RuO_2 nanocrystalline electrocatalytic materials for chlorine and oxygen evolution," *Catalysis Today*, vol. 202, pp. 63–69, 2013.

[84] N. B. Halck, V. Petrykin, P. Krtil, and J. Rossmeisl, "Beyond the volcano limitations in electrocatalysis - oxygen evolution reaction," *Physical chemistry chemical physics: PCCP*, vol. 16, no. 27, pp. 13682–13688, 2014.

[85] T. Reier, M. Oezaslan, and P. Strasser, "Electrocatalytic Oxygen Evolution Reaction (OER) on Ru, Ir, and Pt Catalysts: A Comparative Study of Nanoparticles and Bulk Materials," *ACS Catalysis*, vol. 2, no. 8, pp. 1765–1772, 2012.

[86] M. Vukovic, "Oxygen evolution reaction on thermally treated iridium oxide films," *Journal of Applied Electrochemistry*, vol. 17, pp. 737–745, 1987.

[87] R. Frydendal, E. A. Paoli, B. P. Knudsen, B. Wickman, P. Malacrida, E. L. Ifan, and I. Chorkendorff, "Benchmarking stability for oxygen evolution reaction catalysts: the importance of monitoring mass losses," *ChemElectroChem*, 2014.

[88] L. Trotochaud, J. K. Ranney, K. N. Williams, and S. W. Boettcher, "Solution-Cast Metal Oxide Thin Film Electrocatalysts for Oxygen Evolution.," *Journal of the American Chemical Society*, vol. 134, no. 41, pp. 17253–17261, 2012.

[89] L. Trotochaud, S. L. Young, J. K. Ranney, and S. W. Boettcher, "Nickel-Iron Oxyhydroxide Oxygen-Evolution Electrocatalysts: the Role of Intentional and Incidental Iron Incorporation," *Journal of the American Chemical Society*, vol. 136, no. 18, pp. 6744–53, 2014.

[90] R. D. L. Smith, M. S. Prevot, R. D. Fagan, Z. Zhang, P. a. Sedach, M. K. J. Siu, S. Trudel, and C. P. Berlinguette, "Photochemical Route for Accessing Amorphous Metal Oxide Materials for Water Oxidation Catalysis," *Science*, vol. 340, no. 6, pp. 60–63, 2013.

[91] J. Suntivich, K. J. May, H. A. Gasteiger, J. B. Goodenough, and Y. Shao-Horn, "A perovskite oxide optimized for oxygen evolution catalysis from molecular orbital principles.," *Science (New York, N.Y.)*, vol. 334, no. 6061, pp. 1383–1385, 2011.

[92] A. Grimaud, K. J. May, C. E. Carlton, Y. L. Lee, M. Risch, W. T. Hong, J. Zhou, and Y. Shao-Horn, "Double perovskites as a family of highly active catalysts for oxygen evolution in alkaline solution.," *Nature communications*, vol. 4, pp. 1–7, 2013.

[93] Y. Gorlin and T. F. Jaramillo, "A Bifunctional Nonprecious Metal Catalyst for Oxygen Reduction and Water Oxidation.," *Journal of the American Chemical Society*, vol. 132, no. 39, pp. 13612–4, 2010.

[94] J. D. Blakemore, H. B. Gray, J. R. Winkler, and A. M. Mu, "Co_3O_4 Nanoparticle Water-Oxidation Catalysts Made by Pulsed-Laser Ablation in Liquids," *ACS Catalysis*, vol. 3, pp. 2497–2500, 2013.

[95] K. Juodkazis, J. Juodkazyte, R. Vilkauskaite, and B. Šebeka, "Oxygen Evolution on Composite Ruthenium and Nickel Oxides Electrode," *Chemija*, vol. 19, no. 1, pp. 1–6, 2008.

[96] Y. Gorlin, C.-J. Chung, J. D. Benck, D. Nordlund, L. Seitz, T.-C. Weng, D. Sokaras, B. M. Clemens, and T. F. Jaramillo, "Understanding Interactions between Manganese Oxide and Gold That Lead to Enhanced Activity for Electrocatalytic Water Oxidation.," *Journal of the American Chemical Society*, vol. 136, no. 13, pp. 4920–6, 2014.

[97] R. Frydendal, M. Busch, N. B. Halck, E. A. Paoli, and P. Krtil, "Enhancing Activity for the Oxygen Evolution Reaction: The Beneficial Interaction of Gold with Manganese and Cobalt Oxides," *ChemCatChem*, 2014.

[98] I. E. L. Stephens, A. S. Bondarenko, U. Grø nbjerg, J. Rossmeisl, and I. Chorkendorff, "Understanding the Electrocatalysis of Oxygen Reduction on Platinum and its Alloys," *Energy & Environmental Science*, vol. 5, no. 5, p. 6744, 2012.

[99] U. A. Paulus, T. J. Schmidt, H. A. Gasteiger, and R. J. Behm, "Oxygen Reduction on a High-Surface Area Pt / Vulcan Carbon Catalyst: a Thin-Film Rotating Ring-Disk Electrode Study," *Journal of Electroanalytical Chemistry*, vol. 495, pp. 134–145, 2001.

[100] C. C. L. McCrory, S. Jung, J. C. Peters, and T. F. Jaramillo, "Benchmarking heterogeneous electrocatalysts for the oxygen evolution reaction.," *Journal of the American Chemical Society*, vol. 135, no. 45, pp. 16977–87, 2013.

[101] P. Millet, R. Ngameni, S. Grigoriev, and V. Fateev, "Scientific and Engineering Issues Related to PEM Technology: Water Electrolysers, Fuel Cells and Unitized Regenerative Systems," *International Journal of Hydrogen Energy*, vol. 36, no. 6, pp. 4156–4163, 2011.

[102] K. E. Ayers, L. T. Dalton, and E. B. Anderson, "(Invited) Efficient Generation of High Energy Density Fuel from Water," *ECS Transactions*, vol. 41, no. 33, pp. 27–38, 2012.

[103] R. Kötz, S. Stucki, D. Scherson, and D. M. Kolb, "In-Situ Identification of RuO_4 as the Corrosion Product during Oxygen Evolution on Ruthenium in Acid Media," *Journal of Electroanalytical Chemistry*, vol. 172, pp. 211–219, 1984.

[104] M. Vukovic, "Rotating Ring-Disc Electrode Study of the Enhanced Oxygen Evolution on an Activated Ruthenium Electrode," *Journal of Chemical Society Faraday Transactions*, vol. 86, no. 22, pp. 3743–3746, 1990.

[105] M. Pourbaix, *Atlas of Electrochemical Equilibria in Aqueous Solutions.* 1974.

[106] H. J. Lewerenz, S. Stucki, and R. Kôtz, "Oxygen Evolution and Corrosion: XPS Investigations on Ru and RuO_2 Electrodes," *Surface Science*, vol. 126, pp. 463–468, 1983.

[107] S. Trasatti, "Electrochemical Theory. Oxygen Evolution," in *Encyclopedia of electrochemical power sources, Volume II*, pp. 49–55, Elsevier B.V, 2009.

[108] J. Greeley, "Structural Effects on Trends in the Deposition and Dissolution of Metal-Supported Metal Adstructures," *Electrochimica Acta*, vol. 55, no. 20, pp. 5545–5550, 2010.

[109] R. Frydendal, "Stability and Activity of New Mixed Oxide Catalysts for the Oxygen Evolution Reaction under Acidic Conditions," Master's thesis, Technical University of Denmark.

[110] S. H. Chang, N. Danilovic, K.-C. Chang, R. Subbaraman, A. P. Paulikas, D. D. Fong, M. J. Highland, P. M. Baldo, V. R. Stamenkovic, J. W. Freeland, J. A. Eastman, and N. M. Markovic, "Functional links between stability and reactivity of strontium ruthenate single crystals during oxygen evolution.," *Nature communications*, vol. 5, p. 4191, 2014.

[111] S. Cherevko, A. A. Topalov, A. R. Zeradjanin, I. Katsounaros, and K. J. J. Mayrhofer, "Gold dissolution: towards understanding of noble metal corrosion," *RSC Advances*, vol. 3, no. 37, p. 16516, 2013.

[112] R. Kötz, H. Neff, and S. Stucki, "Anodic Iridium Oxide Films: XPS - Studies of Oxidation State Changes and O_2 - Evolution," *Journal of The Electrochemical Society*, vol. 131, no. 1, p. 72, 1984.

[113] H. G. Sanchez Casalongue, M. L. Ng, S. Kaya, D. Friebel, H. Ogasawara, and A. Nilsson, "In Situ Observation of Surface Species on Iridium Oxide Nanoparticles during the Oxygen Evolution Reaction," *Angewandte Chemie (International ed. in English)*, vol. 126, no. 28, pp. 7297–7300, 2014.

[114] J. Willsau, O. Wolter, and J. Heitbaum, "Does the Oxide Layer Take Part in the Oxygen Evolution Reaction on Platinum? A DEMS Study," *Journal of Electroanalytical Chemistry*, vol. 195, pp. 299–306, 1985.

[115] O. Diaz-Morales, F. Calle-Vallejo, C. de Munck, and M. T. Koper, "Electrochemical water splitting by gold: evidence for an oxide decomposition mechanism," *Chemical Science*, vol. 4, pp. 2334–2343, 2013.

[116] M. Wohlfahrt-Mehrens and J. Heitbaum, "Oxygen Evolution on Ru and RuO_2 electrodes studied using Isotope Labelling and On-line Mass Spectrometry," *Journal of Electroanalytical Chemistry*, vol. 237, pp. 251–260, 1987.

[117] S. Fierro, T. Nagel, H. Baltruschat, and C. Comninellis, "Investigation of the Oxygen Evolution Reaction on Ti/IrO_2 Electrodes Using Isotope Labelling and On-line Mass Spectrometry," *Electrochemistry Communications*, vol. 9, no. 8, pp. 1969–1974, 2007.

[118] R. Kötz and S. Stucki, "Stabilization of RuO_2 by IrO_2 for Anodic Oxygen Evolution in Acid Media," *Electrochimica Acta*, vol. 31, no. 10, pp. 1311–1316, 1986.

[119] H. B. Beer, "The Invention and Industrial Development of Metal Anodes," *Journal of The Electrochemical Society*, vol. 127, no. 8, p. 303C, 1980.

[120] C. Angelinetta, S. Trasastti, L. D. Atanasoska, and R. T. Atanasoski, "Surface Properties of RuO_2 + IrO_2 Mixed Oxide Electrodes," *Journal of Electroanalytical Chemistry*, vol. 214, pp. 535–546, 1986.

[121] C. Angelinetta, S. Trasatti, L. D. Atanasoska, Z. S. Minevski, and R. T. Atanasoski, "Effect of Preparation on the Surface and Electrocatalytic Properties of $RuO_2 + IrO_2$ Mixed Oxide Electrodes," *Materials Chemistry adn Physics*, vol. 22, pp. 231–247, 1989.

[122] N. Danilovic, R. Subbaraman, K. C. Chang, S. H. Chang, Y. Kang, J. Snyder, A. P. Paulikas, D. Strmcnik, Y. T. Kim, D. Myers, V. R. Stamenkovic, and N. M. Markovic, "Using Surface Segregation To Design Stable Ru-Ir Oxides for the Oxygen Evolution Reaction in Acidic Environments," *Angewandte Chemie*, 2014.

[123] M. E. G. Lyons and S. Floquet, "Mechanism of Oxygen Reactions at Porous Oxide Electrodes. Part 2–Oxygen Evolution at RuO_2, IrO_2 and $Ir_xRu_{1-x}O_2$ Electrodes in Aqueous Acid and Alkaline Solution.," *Physical chemistry chemical physics*, vol. 13, no. 12, pp. 5314–35, 2011.

[124] L. E. Owe, M. Tsypkin, K. S. Wallwork, R. G. Haverkamp, and S. Sunde, "Iridium – Ruthenium Single Phase Mixed Oxides for Oxygen Evolution : Composition Dependence of Electrocatalytic Activity," *Electrochimica Acta*, vol. 70, pp. 158–164, 2012.

[125] K. Sardar, E. Petrucco, C. I. Hiley, J. D. B. Sharman, P. P. Wells, A. E. Russell, R. J. Kashtiban, J. Sloan, and R. I. Walton, "Water- Splitting Electrocatalysis in Acid Conditions Using Ruthenate- Iridate Pyrochlores," *Angewandte Chemie (International ed. in English)*, vol. 53, no. 41, pp. 10960–4, 2014.

[126] M. Vukovic, D. Cukman, M. Milun, L. D. Atanasoska, and R. T. Atanasoski, "Anodic Stability and Electrochromism of Electrodeposited Coatings on Titanium," *Journal of Electroanalytical Chemistry*, vol. 330, pp. 663–673, 1992.

[127] V. M. Jovanovic, A. Dekanski, P. Despotov, B. Nikolic, and R. T. Atanasoski, "The roles of the Ruthenium Concentration Profile, the Stabilizing Component and the Substrate on the Stability of Oxide Coatings," *Journal of Electroanalytical Chemistry*, vol. 339, pp. 147–165, 1992.

[128] R. S. Yeo, J. Orehotsky, W. Visscher, and S. Srinivasan, "Ruthenium-Based Mixed Oxides as Electrocatalysts for Oxygen Evolution in Acid Electrolytes," *Journal of Electrochemical Society*, vol. 128, no. 9, pp. 1900–1904, 1981.

[129] R. Hutchings, K. Müller, R. Kötz, and S. Stucki, "A structural investigation of stabilized oxygen evolution catalysts," *Journal of Material Science*, vol. 19, pp. 3987–3994, 1984.

[130] J. Boodts and S. Trasatti, "Effect of Composition on the Electrocatalytic Activity of the Ternary Oxide $Ru_{0.3}Ti_{0.7-x}Sn_xO_2$. I. Oxygen Evolution from $HClO_4$ Solutions," *Journal of Electrochemical Society*, vol. 137, no. 12, pp. 3784–3789, 1990.

[131] C. P. De Pauli and S. Trasatti, "Composite Materials for Electrocatalysis of O_2 Evolution: IrO_2 + SnO_2 in Acid Solution," *Journal of Electroanalytical Chemistry*, vol. 539, pp. 145–151, 2002.

[132] A. Marshall, B. Bø rresen, G. Hagen, M. Tsypkin, and R. Tunold, "Electrochemical Characterisation of $Ir_xSn_{1-x}O_2$ Powders as Oxygen Evolution Electrocatalysts," *Electrochimica Acta*, vol. 51, no. 15, pp. 3161–3167, 2006.

[133] A. S. Bandarenka, E. Ventosa, A. Maljusch, J. Masa, and W. Schuhmann, "Techniques and methodologies in modern electrocatalysis: evaluation of activity, selectivity and stability of catalytic materials.," *Analyst*, vol. 139, no. 6, pp. 1274–91, 2014.

[134] B. Wickman, H. Grönbeck, P. Hanarp, and B. Kasemo, "Corrosion Induced Degradation of Pt/C Model Electrodes Measured with Electrochemical Quartz Crystal Microbalance," *Journal of The Electrochemical Society*, vol. 157, no. 4, p. B592, 2010.

[135] M. Wakisaka, S. Asizawa, H. Uchida, and M. Watanabe, "In situ STM observation of morphological changes of the Pt(111) electrode surface during potential cycling in 10 mM HF solution.," *Physical chemistry chemical physics : PCCP*, vol. 12, no. 16, pp. 4184–90, 2010.

[136] L. Tang, B. Han, K. Persson, C. Friesen, and T. He, "Electrochemical Stability of Nanometer-Scale Pt Particles in," *Journal of American Society*, no. 14, pp. 596–600, 2010.

[137] E. Kuznetsova, *Structure, Selectivity and Electrocatalytic Activity of Iridium-Based Oxides for Oxygen Evolution*. Phd thesis, Norwegian University of Science and Technology, 2014.

[138] E. Kuznetsova, A. Cuesta, M. Thomassen, and S. Sunde, "Identification of the Byproducts of the Oxygen Evolution Reaction on Rutile- Type Oxides Under Dynamic Conditions," *Journal of Electroanalytical Chemistry*, vol. 728, pp. 102–111, 2014.

[139] K. A. Stoerzinger, W. T. Hong, E. J. Crumlin, H. Bluhm, M. D. Biegalski, and Y. Shao-Horn, "Water Reactivity on the $LaCoO_3$ (001) Surface: An Ambient Pressure X-ray Photoelectron Spectroscopy Study," *Journal of Physical Chemistry C*, vol. 118, pp. 19733–19741, 2014.

[140] K. J. May, C. E. Carlton, K. A. Stoerzinger, M. Risch, J. Suntivich, Y. L. Lee, A. Grimaud, and Y. Shao-Horn, "Influence of Oxygen Evolution during Water Oxidation on the Surface of Perovskite Oxide Catalysts," *The Journal of Physical Chemistry Letters*, vol. 3, no. 22, pp. 3264–3270, 2012.

[141] F. J. Perez-Alonso, C. F. Elkjæ r, S. S. Shim, B. L. Abrams, I. E. Stephens, and I. Chorkendorff, "Identical locations transmission electron microscopy study of Pt/C electrocatalyst degradation during oxygen reduction reaction," *Journal of Power Sources*, vol. 196, no. 15, pp. 6085–6091, 2011.

[142] A. Ohma, K. Shinohara, A. Iiyama, T. Yoshida, and A. Daimaru, "Membrane and Catalyst Performance Targetsfor Automotive Fuel Cells by FCCJ Membrane, Catalyst, MEA WG," *ECS Transactions*, vol. 41, pp. 775–784, 2011.

[143] H. Haberland, M. Karrais, M. Mall, and Y. Thurner, "Thin films from energetic cluster impact: A feasibility study," *Journal of Vacuum Science & Technology A: Vacuum, Surfaces, and Films*, vol. 10, no. 5, p. 3266, 1992.

[144] T. Hihara and K. Sumiyama, "Formation and Size Control of a Ni Cluster by Plasma Gas Condensation," *Journal of Applied Physics*, vol. 84, no. 9, pp. 5270–5726, 1998.

[145] R. M. Nielsen, S. Murphy, C. Strebel, M. Johansson, I. Chorkendorff, and J. H. Nielsen, "The morphology of mass selected ruthenium nanoparticles from a magnetron-sputter gas-aggregation source," *Journal of Nanoparticle Research*, vol. 12, no. 4, pp. 1249–1262, 2009.

[146] R. Nielsen, S. Murphy, C. Strebel, M. Johansson, J. Nielsen, and I. Chorkendorff, "A Comparative STM Study of Ru Nanoparticles Deposited on HOPG by Mass-Selected Gas Aggregation Versus Thermal Evaporation," *Surface Science*, vol. 603, no. 24, pp. 3420–3430, 2009.

[147] C. E. Strebel, *Structure and Reactivity of Nanoparticles*. Phd thesis, Technical Uniersity of Denmark, October 2012.

[148] F. Masini, C. E. Strebel, D. N. McCarthy, A. U. F. Nierhoff, J. Kehres, E. M. Fiordaliso, J. H. k. Nielsen, and I. Chorkendorff, "Methanation on mass-selected Ru nanoparticles on a planar SiO_2 model support: The importance of under-coordinated sites," *Journal of Catalysis*, vol. 308, pp. 282–290, 2013.

[149] B. Von Issendorff and R. E. Palmer, "A new high transmission infinite range mass selector for cluster and nanoparticle beams," *Review of Scientific Instruments*, vol. 70, no. 12, pp. 4497–4501, 1999.

[150] G. Sauerbrey, "Verwendung von Schwingquarzen zur Wägung dünner Schichten und zur Mikrowägung," *Zeitschrift für Physik*, vol. 155, pp. 206–222, 1959.

[151] M. Moseler, H. Häkkinen, and U. Landman, "Supported Magnetic Nanoclusters: Soft Landing of Pd Clusters on a MgO Surface," *Physical Review Letters*, vol. 89, no. 17, p. 176103, 2002.

[152] S. J. Carroll, S. G. Hall, R. E. Palmer, and R. Smith, "Energetic Impact of Size-Selected Metal Cluster Ions on Graphite," *Physical Review Letters*, pp. 3715–3718, 1998.

[153] F. Masini, P. Hernández-Fernández, D. Deiana, C. E. Strebel, D. N. McCarthy, A. Bodin, P. Malacrida, I. Stephens, and I. Chorkendorff, "Exploring the phase space of time of flight mass selected Pt x Y nanoparticles," *Physical Chemistry Chemical Physics*, 2014.

[154] D. Depla, S. Mahieu, and J. E. Green, "Handbook of Deposition Technologies for Films and Coatings," in *Handbook of Deposition Technologies for Films and Coatings*, ch. 5, pp. 253–296, Elsevier, third ed., 2010.

[155] J. Green, "Thin film deposition at the nanoscale.." Annual International Course in Telecommunications Demiconductor Technology Nanotechnology, 2013.

[156] S. Berg and T. Nyberg, "Fundamental understanding and modeling of reactive sputtering processes," *Thin Solid Films*, vol. 476, no. 2, pp. 215–230, 2005.

[157] D. Carter, B. Sproul, and D. Christie, "Effective Control for Reactive Sputtering Processes," *Vacuum Technology & Coating*, vol. 7, no. 4, pp. 60–67, 2006.

[158] A. S. Varela, *The Catalysis of CO_2 Electro- Reduction and Related Processes*. PhD thesis, Technical University of Denmark, 2014.

[159] G. A. Somorjai, *Chemistry in Two Dimensions: surfaces*. Ithaca: Cornell University Press, 1981.

[160] D. R. Dreyer, S. Park, C. W. Bielawski, and R. S. Ruoff, "The chemistry of graphene oxide.," *Chemical Society reviews*, vol. 39, no. 1, pp. 228–40, 2010.

[161] E. Seddon and K. Seddon, *The chemistry of ruthenium : Topics in inorganic and general chemistry* 19. Elsevier,1984, 1984.

[162] H. Over, "Surface Chemistry of Ruthenium Dioxide in Heterogeneous Catalysis and Electrocatalysis: From Fundamental to Applied Research.," *Chemical reviews*, vol. 112, no. 6, pp. 3356–426, 2012.

[163] P. Cox, J. Goodenough, P. Tavener, D. Telles, and R. Egdell, "The electronic-structure of $bi_{2-x}gd_xru_2o_7$ and ruo_2 - a study by electron-spectroscopy," *Journal of Solid State chemistry*, vol. 62, no. 3, pp. 360–370, 1986.

[164] K. Reuter and M. Scheffler, "Surface Core-Level Shifts at an Oxygen-Rich Ru Surface: O/Ru(0001) vs. RuO_2 (110)," *Surface Science*, vol. 490, pp. 20–28, 2001.

[165] H. Over, A. P. Seitsonen, E. Lundgren, M. Smedh, and J. N. Andersen, "On the Origin of the $Ru3d_{5/2}$ Satellite Feature from RuO_2 (110)," *Surface Science*, vol. 504, pp. L196–L200, 2002.

[166] B. A. van Brussel and J. T. M. De Hosson, "Glancing Angle X-Ray Diffraction: A Different Approach," *Applied Physics Letters*, vol. 64, no. 12, pp. 1585–1587, 1994.

[167] M. Birkholz, *Thin Film Analysis by X-Ray Scattering*. Wiley-VCH, 2006.

[168] F. Cavalca, *Illuminating Electron Microscopy of Photocatalysts*. PhD thesis, 2013.

[169] T. Pajkossy, L. Kibler, and D. Kolb, "Voltammetry and Impedance Measurements of Ir(100) Electrodes in Aqueous Solutions," *Journal of Electroanalytical Chemistry*, vol. 600, pp. 113–118, 2007.

[170] P. Kaghazchi, F. Simeone, K. A. Soliman, L. A. Kibler, and T. Jacob, "Bridging the Gap between Nanoparticles and Single Crystal Surfaces," *Faraday Discussions*, vol. 140, pp. 69–80, 2008.

[171] M. S. Cruz, M. J. G. Tejera, and M. C. Villamanan, "Reduction Electroquimique de l'Ion ClO_4^- sur l'Electrode d'Iridium," *Electrochimica Acta*, vol. 30, no. 11, pp. 1563–1569, 1985.

[172] N. Markovic, M. Hanson, G. Mcdougall, and E. Yeager, "The Effects of Anions of Hydrogen Electrosorption on Platinum Single-Crystal Electrodes," *Journal of Electroanalytical Chemistry*, vol. 214, pp. 555–566, 1986.

[173] A. Lam, H. Li, S. Zhang, H. Wang, D. P. Wilkinson, S. Wessel, and T. T. Cheng, "Ex situ Study of Chloride Contamination on Carbon Supported Pt Catalyst," *Journal of Power Sources*, vol. 205, pp. 235–238, 2012.

[174] S. Hadzi-Jordanov, H. Angerstein-Kozlowska, and B. Conway, "Surface oxidation and H deposition at ruthenium electrodes : Resolution of component processes in potential-sweep experiments," *Electroanalytical Chemistry and Interfacial Electrochemistry*, vol. 60, pp. 359–362, 1975.

[175] D. A. Buttry and M. D. Ward, "Measurement of interfacial processes at electrode surfaces with the electrochemical quartz crystal microbalance," *Chemical Reviews*, vol. 92, pp. 1355–1379, Sept. 1992.

[176] K. K. Kazanawa and J. G. Gordon, "The Oscillation Frequency of a Quartz Resonator in Contact with a Liquid," *Analytica Chimica Acta*, vol. 175, pp. 99–105, 1985.

[177] R. Scumacher, G. Borges, and K. K. Kanazawa, "The Quartz Microbalance: A Sensitive Tool to Probe Surface Reconstruction on Gold Electrodes in Liquid," *Surface Science*, vol. 163, pp. L–621–L626, 1985.

[178] C. Gabrielli, M. Keddam, and R. Torresi, "Calibration of the Electrochemical Quartz Crystal Microbalance," *Journal of electrochemical Society*, vol. 138, no. 9, pp. 2657–2660, 1991.

[179] P. Elmer, "The 30- Minute Guide to ICP-MS," tech. rep., 2011.

[180] M. Wilms, M. Kruft, G. Bermes, and K. Wandelt, "A New and Sophisticated Electrochemical Scanning Tunneling Microscope Design for the Investigation of Potentiodynamic Processes," *Review of Scientific Instruments*, vol. 70, no. 9, pp. 3641–3650, 1999.

[181] O. M. Magnussen, "Ordered Anion Adlayers on Metal Electrode Surfaces.," *Chemical reviews*, vol. 102, no. 3, pp. 679–725, 2002.

[182] C. E. Boman, "Refinement of the Crystal Structure of Ruthenium Dioxide," *Acta Chemica Scandinavica*, vol. 24, pp. 116–122, 1970.

[183] A. Patterson, "The Scherrer Formula for X-Ray Particle Size Determination," *Physical Review*, vol. 56, pp. 978–982, 1939.

[184] S. Siahrostami, A. Verdaguer-Casadevall, M. Karamad, D. Deiana, P. Malacrida, B. Wickman, M. Escudero-Escribano, E. a. Paoli, R. Frydendal, T. W. Hansen, I. Chorkendorff, I. E. L. S. Stephens, I. E. Stephens, and J. Rossmeisl, "Enabling direct H_2O_2 production through rational electrocatalyst design.," *Nature materials*, vol. 12, no. 12, pp. 1137–43, 2013.

[185] X. S. Yan, P. Lin, X. Qi, and L. Yang, "Finnis–Sinclair potentials for fcc Au–Pd and Ag–Pt alloys," *International Journal of Materials Research*, vol. 102, no. 4, pp. 381–388, 2011.

[186] E. O. Hall and J. Crangle, "An X-ray investigation of the reported high-temperature allotropy of ruthenium," *Acta Crystallographica*, vol. 10, no. 3, pp. 240–241, 1957.

[187] B. S. Yeo and A. T. Bell, "Enhanced Activity of Gold-Supported Cobalt Oxide for the Electrochemical Evolution of Oxygen.," *Journal of the American Chemical Society*, vol. 133, no. 14, pp. 5587–93, 2011.

[188] J. Greeley, R. J., A. Hellman, and J. K. Nø rskov, "Theoretical trends in particle size effects for the oxygen reduction reaction," *Zeitschrift Fur Physikalische Chemie-International Journal of Research in Physical Chemistry & Chemical Physics*, vol. 221, pp. 1209–1220, 2007.

[189] K. Hartl, M. Nesselberger, K. J. Mayrhofer, S. Kunz, F. F. Schweinberger, G. Kwon, M. Hanzlik, U. Heiz, and M. Arenz, "Electrochemically induced nanocluster migration," *Electrochimica Acta*, vol. 56, no. 2, pp. 810–816, 2010.

[190] M. W. Louie and A. T. Bell, "An Investigation of Thin Film Ni Fe Oxide Catalysts for the Electrochemical Evolution of Oxygen," *Journal of the American Chemical Society*, vol. 135, pp. 12329–12337, 2013.

[191] H. A. Gasteiger, S. S. Kocha, B. Sompalli, and F. T. Wagner, "Activity Benchmarks and Requirements for Pt, Pt-alloy, and non-Pt Oxygen Reduction Catalysts for PEMFCs," *Applied Catalysis B: Environmental*, vol. 56, pp. 9–35, Mar. 2005.

[192] K. J. Mayrhofer, J. C. Meier, S. J. Ashton, G. K. Wiberg, F. Kraus, M. Hanzlik, and M. Arenz, "Fuel cell catalyst degradation on the nanoscale," *Electrochemistry Communications*, vol. 10, no. 8, pp. 1144–1147, 2008.

[193] J. C. Meier, I. Katsounaros, C. Galeano, H. J. Bongard, A. A. Topalov, A. Kostka, A. Karschin, F. Schüth, and K. J. J. Mayrhofer, "Stability investigations of electrocatalysts on the nanoscale," *Energy & Environmental Science*, vol. 5, no. 11, p. 9319, 2012.

[194] F. Cui, H. Chen, X. Cui, J. Shi, L. Li, J. Zhao, and Q. He, "Enhancement in electrochemical catalytic activity of mesoporous $\mathrm{ruo}_x\mathrm{h}_y$ and $\mathrm{pt/ruo}_x\mathrm{h}_y$ by gas treatment," *Dalton Transactions*, no. 18, pp. 3395–3402, 2009.

[195] A. A. Topalov, I. Katsounaros, M. Auinger, S. Cherevko, J. C. Meier, S. O. Klemm, and K. J. J. Mayrhofer, "Dissolution of platinum: limits for the deployment of electrochemical energy conversion?," *Angewandte Chemie (International ed. in English)*, vol. 51, no. 50, pp. 12613–5, 2012.

[196] A. A. Bolzan, C. Fong, B. J. Kennedy, and C. J. Howard, "Structural Studies of Rutile-Type Metal Dioxides," *Acta Crystallographica Section B Structural Science*, vol. 53, no. 3, pp. 373–380, 1997.

[197] J. Mozota and B. E. Conway, "Surface and Bulk Processes at Oxidized Iridium Electrodes. I. Monolayer Stage and Transition to Reversible Multilayer Oxide Film Behavior," *Electrochimica Acta*, vol. 28, no. 1, pp. 1–8, 1983.

[198] L. D. Burke and D. P. Whelan, "A Voltammetric Investigation of the Charge Storage Reactions of Hydrous Iridum Oxide Layers," *Journal of Electroanalytical Chemistry*, vol. 162, pp. 121–141, 1984.

[199] M. B. Vukmirovic, P. Liu, J. T. Muckerman, and R. R. Adzic, "Electrodeposition of Pt Onto RuO_2 (110) Single- Crystal Surface," *Journal of Physical Chemistry C*, vol. 2, no. 110, pp. 15306–15311, 2007.

[200] S. Trasatti and O. A. Petrii, "Real Surface Area Measurements," *Journal of Electroanalytical Chemistry*, vol. 327, pp. 353–376, 1992.

[201] L. D. Burke and O. J. Murphy, "Cycling Voltammetry As a Technique for Determining the Surface Area of RuO_2 Electrodes," *Journal of Electroanalytical Chemistry*, vol. 96, pp. 19–27, 1979.

[202] T. Lister, Y. Tolmachev, Y. Chu, W. Cullen, H. You, R. Yonco, and Z. Nagy, "Cathodic Activation of RuO_2 Single Crystal Surfaces For Hydrogen-Evolution Eeaction," *Journal of Electroanalytical Chemistry*, vol. 554-555, pp. 71–76, 2003.

[203] A. Engstfeld, J. Klein, S. Brimaud, and R. Behm, "Electrochemical Stability and Restructuring and its Impact on the Electro-Oxidation of CO: Pt Modified Ru(0001) Electrodes," *Surface Science*, pp. 1–10, 2014.

[204] J. Wang, C. Y. Fan, K. Jacobi, and G. Ertl, "Adsorption and Reaction of CO on RuO_2(110) Surfaces," *Surface Science*, vol. 481, pp. 113–118, 2001.

Paper I

Oxygen Evolution on Well-defined Mass-Selected Ru and RuO_2 Nanoparticles

Elisa A. Paoli, Federico Masini, Rasmus Frydendal, Davide Deiana, Christian Schlaup, Thomas W. Hansen, Sebastian Horch, Ifan E.L. Stephens, Ib Chorkendorff

Chemical Science, 2014, *DOI* : 10.1039/*C*4*SC*02685*C*

Chemical Science

EDGE ARTICLE

View Article Online
View Journal

Cite this: DOI: 10.1039/c4sc02685c

Oxygen evolution on well-characterized mass-selected Ru and RuO_2 nanoparticles†

Elisa A. Paoli,[a] Federico Masini,[a] Rasmus Frydendal,[a] Davide Deiana,[b] Christian Schlaup,[a] Mauro Malizia,[a] Thomas W. Hansen,[b] Sebastian Horch,[a] Ifan E. L. Stephens*[a] and Ib Chorkendorff*[a]

Received 2nd September 2014
Accepted 15th September 2014

DOI: 10.1039/c4sc02685c

www.rsc.org/chemicalscience

Oxygen evolution was investigated on model, mass-selected RuO_2 nanoparticles in acid, prepared by magnetron sputtering. Our investigations include electrochemical measurements, electron microscopy, scanning tunneling microscopy and X-ray photoelectron spectroscopy. We show that the stability and activity of nanoparticulate RuO_2 is highly sensitive to its surface pretreatment. At 0.25 V overpotential, the catalysts show a mass activity of up to 0.6 A mg^{-1} and a turnover frequency of 0.65 s^{-1}, one order of magnitude higher than the current state-of-the-art.

Introduction

Renewable sources of energy, such as wind or solar, are inherently intermittent. As they contribute an increasing amount to overall energy usage, more effective and sustainable methods are required to store the energy harvested. For instance, renewable energy could be used to split water electrochemically or photoelectrochemically to form hydrogen, as an energy carrier.[1–5] Nonetheless, the efficiency of water splitting devices is largely defined by the sluggish kinetics of the oxygen evolution reaction (OER). As such, a judicious choice of the electrocatalyst material is imperative. The catalyst needs to be active, stable, and minimize the use of any scarce elements, so that it is scalable. Indeed, no water splitting device will make an impact to the global energy landscape, unless it can be scaled to the Terawatt (TW) level.[6,7] This is a set of stringent requirements for the catalyst material. Indeed, there is a general call for more model studies of the catalysis of oxygen evolution, with the aim of improving the electrocatalysis of this reaction.[2,8–13]

Of the different water splitting technologies, proton exchange membrane (PEM) electrolysers are arguably the most amenable towards small-scale delocalized storage of renewable electricity.[4] Whereas traditional electrolysers operate in base, proton exchange membrane (PEM) electrolysers operate in acid. They hold some distinct advantages over traditional alkaline electrolysers, namely:[14] (a) high efficiency at high current density, (b) the ability to manage fluctuating power inputs, (c) a solid electrolyte, and (d) a fast start up time. PEM electrolysers typically employ anode catalysts based on oxides of Ir, which are not only expensive, but also extremely scarce.[6,15,16] Debe *et al.* showed that by employing an OER catalyst consisting of nanostructured whiskers of $PtIrO_x$, they could achieve unprecedented low precious metal loadings of 0.3 mg cm^{-2} at the anode.[17,18] We estimate that scaling up this device to a TW level of hydrogen storage capacity would require half a year of the annual global production of Pt and 10 years' Ir production (as described in the ESI†). Clearly, despite significant recent advances, current PEM electrolysis technology is not scalable to the TW level.[1] One solution to this problem could be to replace the precious metals with more abundant elements. However, the harsh acidic and oxidizing conditions at the anode render most catalysts inactive or unstable, except for oxides of Ir or Ru,[19] the latter also being subject to severe supply limitations.[6]

Consequently, a prerequisite for TW-scale PEM electrolyser technology is the development of a catalyst that has an appreciably higher mass activity (in A g^{-1} precious metal) than the current state-of-the-art. It turns out that RuO_2 is more active than IrO_2,[11,20–22] but it is somewhat unstable towards dissolution towards RuO_4.[23–26] According to the theoretical "volcano" model developed by Rossmeisl, Nørskov and coworkers, RuO_2 is the most active pure metal oxide catalyst for OER, because it exhibits the closest to optimal binding to the reaction intermediates.[11] Further improvements can be achieved by combining ruthenium with nickel and cobalt;[27–31] however, these bimetallic materials are highly unstable under acidic conditions.

Most studies of the OER on RuO_2, simply report the catalytic activity, but neglect corrosion; when the corrosion rate has been monitored, it has been significant, at around 10–40% of the total anodic current.[13,24,26,32–35] Nonetheless, it turns out that RuO_2 can be stabilized, both by mixing with other oxides such as Ir or Ti,[23,36–39] or by providing it with appropriate oxidation

[a]Center for Individual Nanoparticle Functionality (CINF), Department of Physics, Kgs. Lyngby DK-2800, Denmark. E-mail: ib.chorkendorff@fysik.dtu.dk

[b]Center for Electron Nanoscopy (CEN), Kgs. Lyngby DK-2800, Denmark

† Electronic supplementary information (ESI) available. See DOI: 10.1039/c4sc02685c

treatment.[34,40,41] Oxides grown anodically under ambient conditions from metallic precursors tend to be highly active, but also unstable.[34,40] Moreover, according to a recent report by Strasser and coworkers, nanoparticles of 4–6 nm in diameter, with anodically-grown surface oxides, will show much lower stability than extended surfaces with the same pre-treatment.[24,41] On the other hand, should extended surfaces of RuO_2 be formed under thermal oxidation conditions, by pre-treating in O_2 at temperatures above 350 °C, they will show much higher stability than the anodic oxides, but somewhat lower activity.[34,40,41] Thus far, no studies have provided a comprehensive examination of the activity and stability of nanoparticulate RuO_2 under well-defined conditions. As highlighted by Mayrhofer and coworkers in a recent review,[8] systematic studies on the effect of particle size for the oxygen evolution reaction are missing, unlike the oxygen reduction reaction. Although size effects are reported on chemically synthesized RuO_2 particles greater than 15 nm in diameter,[30] it is of greater technological relevance to examine smaller particles, where the surface area is maximised.[42,43] Moreover, size effects are typically likely to be more pronounced for particles smaller than 10 nm in diameter.[43,44]

Herein, we focus on the evaluation of oxygen evolution activity and corrosion of well-defined, mass-selected Ru nanoparticles, as a function of size. In particular, we aim to establish the extent to which the mass activity of nanoparticulate RuO_2 can be maximized and at the same time monitor the catalyst stability. We adapt a methodology previously used in our laboratory to investigate the oxygen reduction reaction.[43,45,46] The mass selected electrocatalysts are prepared in a magnetron sputter source, using an ultra-high-vacuum (UHV) compatible technique.[47,48] This allows a high degree of control over critical parameters such as particle size, electrode coverage and density,[49] and it avoids the inherent artefacts introduced by chemical synthesis from precursors and surfactants.[50]

Results and discussions

The catalysts were formed by vacuum deposition of mass-selected nanoparticles from a ruthenium target,[51] deposited directly onto glassy carbon or Au electrodes. The mass ranged from 0.035×10^6 u to 2.9×10^6 u, which would correspond to a range in size of 2–9 nm, assuming perfectly spherical particles. We tested both (a) as-deposited particles (Ru NPs) which were not subjected to any further treatment before exposure to the electrochemical environment and (b) thermally oxidized particles (RuO_2 NPs), which, prior to electrochemical measurements, were treated in a tube furnace at 400 °C under 1 bar oxygen for 1 minute. The loading was determined directly from the deposition current. The structure and composition were tested using X-ray Photoelectron Spectroscopy (XPS), Glancing Angle – X-Ray Diffraction (GA-XRD), High Angle Annular Dark Field – Scanning Transmission Electron Microscopy (HAADF-STEM) and Scanning Electron Microscopy (SEM). The electrocatalysts were tested in a Rotating Ring Disk Electrode set-up. Furthermore, Electrochemical Scanning Tunneling Microscopy (EC-STM) was used to directly observe the catalyst dissolution under reaction conditions.[52] Inductively Coupled Plasma – Mass Spectrometry (ICP-MS) was used to analyze the electrolyte post-OER.

The catalyst composition and crystallographic structure were probed using XPS and GA-XRD. The as-deposited particles (Fig. 1a) exhibit two pairs of doublets for the Ru 3d core level, with a separation of ~1 eV; this indicates the presence of both metallic and oxidized Ru in the near-surface region. On other hand, the thermally oxidized particles (Fig. 1b) could only be fitted to a single doublet, confirming that a RuO_2 layer of at least 1.5 nm has formed.

GA-XRD measurements confirm the full oxidation of the particles (Fig. 2). The most intense peak from the reference pattern for metallic ruthenium can be identified in the as-deposited ruthenium catalyst. However, the peaks of the thermally oxidized ruthenium correspond closely to the RuO_2 rutile phase. The remaining peaks correspond to the Au(111) substrate.

The projected particle area distribution for four different thermally oxidized samples, together with the corresponding HAADF-STEM images, are shown in Fig. 3a–d. Smaller particles show a more regular, spherical shape, whereas the larger particles are rough and form tetrahedrons. These observations correspond well with earlier studies from our laboratory on metallic Ru.[49–51]

The OER activity of glassy carbon supported thermally oxidized RuO_2 nanoparticles was measured voltammetrically in N_2-saturated 0.05 M H_2SO_4. The OER mass activity of the thermally oxidized RuO_2 particles is plotted in Fig. 4a as a function of particle mass. There is some scatter in the data, which we attribute to uncertainties in the total mass deposited. This is despite significant endeavours to minimize the error in the measurement, by carefully choosing deposition parameters and monitoring the coverage of particles using XPS, as described in the ESI.† Incidentally, we obtained a similar catalytic activity on a polycrystalline gold electrode, indicating no influence from the substrate. We can tentatively identify a maximum in activity for the particles with a diameter of 3–5 nm. This could suggest the terrace is the active site for oxygen evolution, analogous to similar reports for the oxygen reduction reaction.[43,44,56] Smaller particles will have a decreased number of terraces sites, and hence will exhibit a lower specific activity.

It is challenging to assess the specific activity of the catalyst as a function of particle size, as we do not have an accurate measure of the surface area for all particle sizes, in particular the larger nanoparticles, which have a non-spherical morphology. Nevertheless, since the smaller particles do in fact exhibit a spherical morphology, we can estimate the surface area and hence the specific activity. It turns out that the specific activity of the 0.1×10^6 u RuO_2 nanoparticles at 1.48 V (*vs.* RHE) is 0.32 mA cm_{Ru}^{-2} which is over an order of magnitude more active than both films and nanoparticles reported in the literature.[22,57] (For further details see the ESI†). Moreover, based on the specific activity and mass activity, we can also estimate the turnover frequency (TOF), a fundamental parameter which represents the number of oxygen molecules produced per second. We can estimate the lower bound, *i.e.*

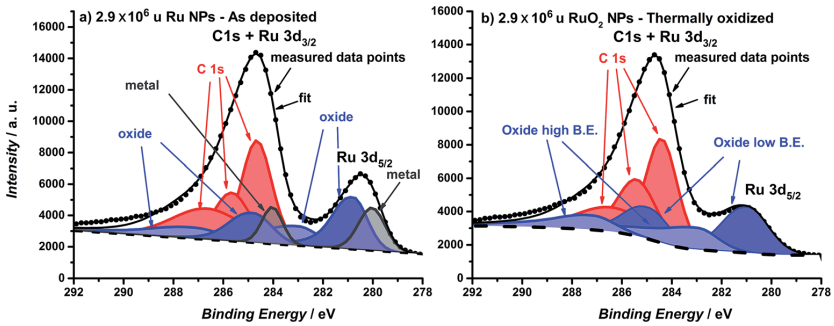

Fig. 1 XPS spectra of the Ru 3d core level region of (a) as-deposited 2.9×10^6 u Ru nanoparticles and (b) thermally oxidized 2.9×10^6 u RuO_2 nanoparticles. Ruthenium oxide is fitted with two species and carbon is fitted with three species. For further details about the fitting see the ESI.†

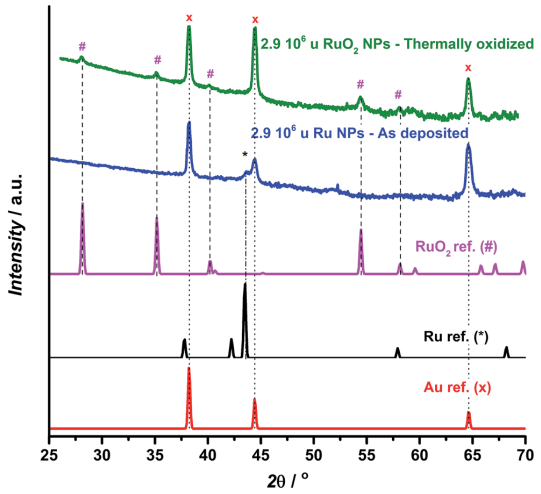

Fig. 2 GA-XRD for as deposited (blue) and thermally oxidized (green) 2.9×10^6 u ruthenium nanoparticles deposited on a Au(111) single crystalline substrate, together with reference patterns for Au,[53] Ru[54] and RuO_2.[55]

TOF_{min}, by assuming that each Ru atom is active for the OER. On the other hand, we can estimate the upper bound, TOF_{max}, by assuming only the surface atoms are active (in reality, we view this TOF_{max} as a conservative estimate; the surface will be covered with a range of different catalytic sites, whereas the activity will be dominated by the most active). In Fig. 4b we show the estimated TOF of the 0.1×10^6 u RuO_2 nanoparticles from this work, in comparison with the most active catalysts in the literature (we have only included catalysts with a well-defined mass or surface area). For further details on how the TOF was estimated, see the ESI.† There is a factor of three difference between TOF_{min} and TOF_{max}; although this is significant, it is lower than that reported for other similar systems.[58] The figure demonstrates that the TOF frequency of the particles reported herein is the highest in the literature for the OER under acidic conditions. We speculate that this might be related to the preparation technique, which allowed us to obtain well-defined and monodisperse nanoparticles, without the inherent impurities that could be introduced from a chemical synthesis method.

Although it is a prerequisite for efficient catalysts to have high activity, it is also essential that the catalyst stability is tested, particularly due to the corrosive conditions under which OER catalysts operate.[26,60] The cyclic voltammogram of the largest nanoparticles, 2.9×10^6 u, is plotted in Fig. 5a. The as-deposited Ru particles possess a higher activity than the thermally oxidized RuO_2 particles, in agreement with earlier reports on extended surfaces.[61] Even so, the as-deposited nanoparticles corrode immediately to form RuO_4. According to ring current measurements,[32,35] the anodic dissolution on our Ru nanoparticles constituted 15% of the total current, a similar degree of stability to commercial Ru/C catalysts[24] or polycrystalline Ru.[13] On the other hand, the thermally oxidized RuO_2 nanoparticles showed a negligible ring current, suggesting that the activity should be solely due to the OER. This notion was confirmed by both ICP-MS and the direct measurement of oxygen using gas chromatography, as described in the ESI.†

In order to directly observe the catalyst dissolution, we employed electrochemical scanning tunnelling microscopy (EC-STM). The STM images, shown in Fig. 5b and c, of Ru dissolution were taken in Ar-saturated 0.05 M H_2SO_4. The potential was scanned from 1.3 V to 1.5 V *vs.* RHE. The as-deposited and thermally oxidized nanoparticles show distinct behaviour from each other, under OER conditions. The as-deposited Ru (Fig. 5b) disappeared from view, as the potential was raised, due to dissolution, while RuO_2 (Fig. 5c) exhibited no evidence of corrosion in the same potential range. These microscopic data correlate closely with the data from RRDE experiments and ICP-MS, described in the ESI.†

Most strikingly, the particles tested here show a mass activity of at least one order of magnitude higher than the state-of-the-art for precious metal based OER catalysts in acid, as shown in Fig. 6.[17,57] The thermally oxidized 0.5 and 0.1×10^6 u RuO_2 particles exhibit a 45-fold increase, relative to RuO_2

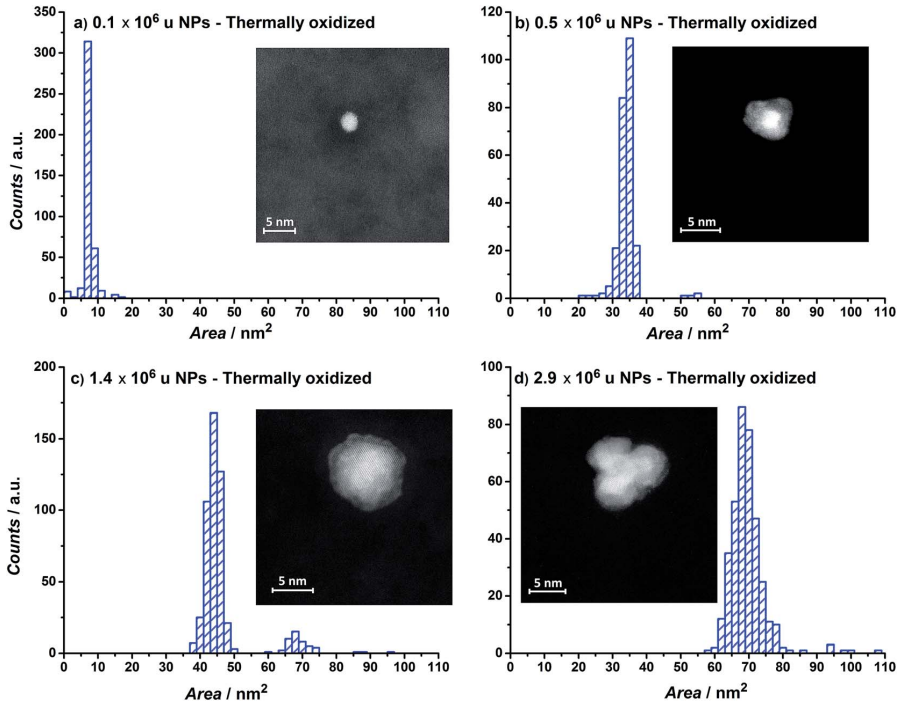

Fig. 3 Nanoparticle area distributions and HAADF-Scanning Transmission Electron Microscopy images of thermally annealed RuO_2/Si_3N_4 samples for particle mass of (a) 0.1×10^6, (b) 0.5×10^6, (c) 1.4×10^6 and (d) 2.9×10^6 u.

nanoparticles prepared by a chemical route,[57] a 30-fold improvement compared to the $PtIrO_x$ in an electrolyser at 80 °C,[17] and a 9-fold enhancement relative to Ir $Ni_{3.3}$ core–shell nanoparticles.[59] Assuming that the activity enhancement persists to higher overpotentials, we demonstrate that the precious metal oxide loading in a PEM electrolyser and in other technologies using oxygen evolution could be decreased by an order of magnitude. Our data provides an impetus for synthetic chemists to produce such active catalysts, using a more scalable method.

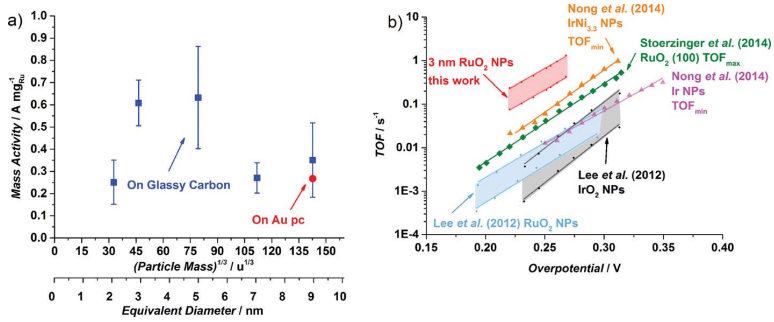

Fig. 4 (a) OER mass activities at 1.48 V (*vs.* RHE) of different thermal oxidized RuO_2 particle masses (0.035×10^6 u, 0.1×10^6 u, 0.5×10^6 u, 1.4×10^6 u and 2.9×10^6 u) on a Glassy Carbon (GC) disk, from the first ohmic and capacitance corrected CV. The Ru mass was evaluated from the deposition current. The error bars are based on four independent measurements. The activity for 2.9×10^6 u nanoparticles on a Au polycrystalline disk is also shown. The particle size is shown as both the $(\text{particle mass})^{1/3}$ and the equivalent diameter that the particles would be, should they be perfectly spherical. (b) Turnover frequency comparison of different catalysts in acid. When possible, both minimum and maximum TOF were estimated. Data adapted from this work for thermally oxidized 0.1×10^6 u NPs; adapted from ref. 57 for RuO_2 and IrO_2 NPs; from ref. 22 for RuO_2 (100); and from ref. 59 for Ir NPs and Ir $Ni_{3.3}$ NPs.

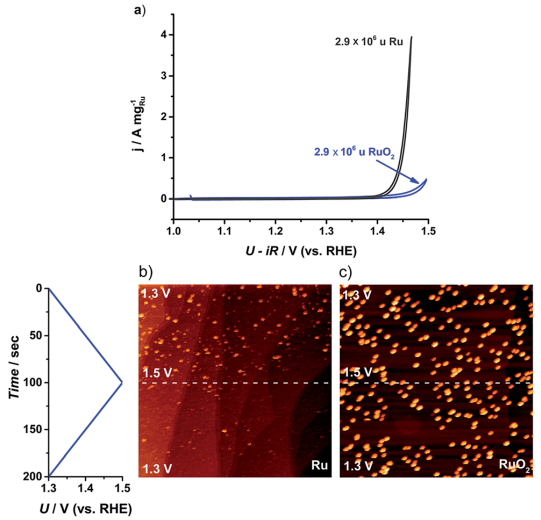

Fig. 5 (a) Cyclic voltammogram (CV) for the first cycle of the as-deposited Ru and thermally oxidized RuO_2 2.9×10^6 u nanoparticles on GC. CV recorded in N_2 saturated 0.05 M H_2SO_4 between 1.0 and 1.5 V (*vs.* RHE) at 20 mV s^{-1} and 1600 rpm. (b) and (c) Potentiodynamic STM images of Ru dissolution in Ar-saturated 0.05 M H_2SO_4 solution. The potential was scanned between 1.3 and 1.5 V (*vs.* RHE) at 2 mV s^{-1}: (b) 0.001 monolayer of as-deposited 0.1×10^6 u Ru nanoparticles, (520 nm),[2] $U_B = -299$ mV, $I_T = 1$ nA; (c) 0.001 monolayer of thermally treated 0.1×10^6 u RuO_2 nanoparticles, (516 nm),[2] $U_B = -245$ mV, $I_T = 1$ nA.

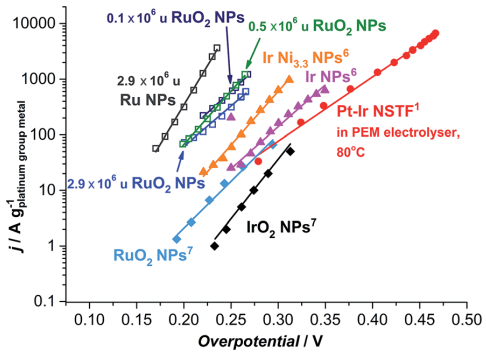

Fig. 6 State-of-the-art for the oxygen evolution reaction in acidic media. Data adapted from this work for as-deposited and thermally oxidized 2.9×10^6 u nanoparticles (NPs) and thermally oxidized 0.1 and 0.5×10^6 u NPs; adapted from ref. 57 for RuO_2 and IrO_2 NPs; from ref. 59 for Ir NPs and Ir $Ni_{3.3}$ NPs; and ref. 17 for Pt–Ir nanostructured thin films (NSTF) at 80 °C. The solid lines serve to guide the eye.

Conclusion

In summary, we have investigated the activity and stability of as-deposited and thermally oxidized Ru nanoparticles. By using mass selected nanoparticles, our work provides a model investigation of the OER on RuO_2 and the effect of particle size. The particles reported here exhibit a one order of magnitude improvement in activity relative to the state-of-the-art and a tentative maximum at around 3–5 nm. An appropriate oxidation treatment can provide moderate stability to RuO_2, and only slightly compromise on its high activity. Moreover, the well-defined shape and small size of the nanoparticles reported herein allow us to make an accurate estimate of the turnover frequency; it turns out it is appreciably higher than previous reports from the literature for oxygen evolution on any catalyst in acid. Should further improvements be made to the stability of RuO_2 nanoparticles (for instance through the addition of Ir or Ti[23,36–39]), PEM electrolysis, as well as other technologies which are limited by oxygen evolution, could eventually become scalable to the TW level.

Author contributions

E.A.P. performed the measurements of the electrocatalytic activity and stability, the GA-XRD experiments, and wrote the first draft and designed the figures; R.F. co-performed the electrochemical measurements and GA-XRD; F.M. prepared the nanoparticles, performed XPS and SEM; D.D performed STEM; C.S. performed EC-STM; M.M performed the gas chromatography experiments; T.W.H. supervised the STEM; S.H. supervised the EC-STM experiments; I.E.L.S supervised the electrochemical measurements and co-wrote the first draft; I.C. supervised the vacuum experiments and conceived the idea. All authors discussed and analysed the data and commented on the manuscript.

Acknowledgements

The authors gratefully acknowledge financial support from the Danish Ministry of Science's UNIK initiative, Catalysis for Sustainable Energy and the Danish Council for Strategic Research's project MEDLYS (10-093906). The Center for Individual Nanoparticle Functionality is supported by the Danish National Research Foundation (DNRF54).

References

1 E. Fabbri, A. Habereder, K. Waltar, R. Kotz and T. Schmidt, *Catal. Sci. Technol.*, 2014, DOI: 10.1039/C4CY00669K, accepted.
2 H. Dau, C. Limberg, T. Reier, M. Risch, S. Roggan and P. Strasser, *ChemCatChem*, 2010, **2**, 724–761.
3 M. G. Walter, E. L. Warren, J. R. McKone, S. W. Boettcher, Q. Mi, E. a. Santori and N. S. Lewis, *Chem. Rev.*, 2010, **110**, 6446–6473.
4 S. Kotrel and S. Bräuninger, in *Handbook of Heterogeneous Catalysis*, ed. G. Ert, Wiley-CPH, 2008, pp. 1936–1958.
5 K. Maeda and K. Domen, *J. Phys. Chem. Lett.*, 2010, **1**, 2655–2661.
6 P. C. K. Vesborg and T. F. Jaramillo, *RSC Adv.*, 2012, **2**, 7933–7947.
7 R. E. Smalley, *Mater. Matters*, 2004, **30**, 412–417.

8 I. Katsounaros, S. Cherevko, A. R. Zeradjanin and K. J. J. Mayrhofer, *Angew. Chem., Int. Ed.*, 2013, **52**, 2–22.
9 O. Diaz-Morales, F. Calle-Vallejo, C. de Munck and M. T. M. Koper, *Chem. Sci.*, 2013, **4**, 2334–2343.
10 J. Suntivich, K. J. May, H. A. Gasteiger, J. B. Goodenough and Y. Shao-Horn, *Science*, 2011, **334**, 1383–1385.
11 I. C. Man, H.-Y. Su, F. Calle-Vallejo, H. A. Hansen, J. I. Martínez, N. G. Inoglu, J. Kitchin, T. F. Jaramillo, J. K. Nørskov and J. Rossmeisl, *ChemCatChem*, 2011, **3**, 1159–1165.
12 J. Rossmeisl, A. Logadottir and J. K. Nørskov, *Chem. Phys.*, 2005, **319**, 178–184.
13 N. Danilovic, R. Subbaraman, K.-C. Chang, S. H. Chang, Y. J. Kang, J. D. Snyder, A. P. Paulikas, D. Strmcnik, Y.-T. Kim, D. J. Myers, V. R. Stamenkovic and N. M. Markovic, *J. Phys. Chem. Lett.*, 2014, **5**, 2474–2478.
14 K. E. Ayers, E. B. Anderson, C. Capuano, B. Carter, L. Dalton, G. Hanlon, J. Manco and M. Niedzwiecki, *ECS Trans.*, 2010, **33**, 3–15.
15 A. Marshall, B. Børresen, G. Hagen, M. Tsypkin and R. Tunold, *Energy*, 2007, **32**, 431–436.
16 a. S. Aricò, S. Siracusano, N. Briguglio, V. Baglio, a. Blasi and V. Antonucci, *J. Appl. Electrochem.*, 2012, **43**, 107–118.
17 M. K. Debe, S. M. Hendricks, G. D. Vernstrom, M. Meyers, M. Brostrom, M. Stephens, Q. Chan, J. Willey, M. Hamden, C. K. Mittelsteadt, C. B. Capuano, K. E. Ayers and E. B. Anderson, *J. Electrochem. Soc.*, 2012, **159**, K165–K176.
18 S. Grigoriev, V. Porembsky and V. Fateev, *Int. J. Hydrogen Energy*, 2006, **31**, 171–175.
19 M. Pourbaix, *Atlas of Electrochemical Equilibria in Aqueous Solutions*, Houston, TX, 1974.
20 J. Rossmeisl, Z.-W. Qu, H. Zhu, G.-J. Kroes and J. K. Nørskov, *J. Electroanal. Chem.*, 2007, **607**, 83–89.
21 S. Trasatti, *Electrochim. Acta*, 1984, **29**, 1503–1512.
22 K. A. Stoerzinger, L. Qiao, M. D. Biegalski and Y. Shao-horn, *J. Phys. Chem. Lett.*, 2014, **5**, 1636–1641.
23 R. Kötz and S. Stucki, *Electrochim. Acta*, 1986, **31**, 1311–1316.
24 T. Reier, M. Oezaslan and P. Strasser, *ACS Catal.*, 2012, **2**, 1765–1772.
25 K. E. Ayers, L. T. Dalton and E. B. Anderson, *ECS Trans.*, 2012, **41**, 27–38.
26 S. Cherevko, A. R. Zeradjanin, A. A. Topalov, N. Kulyk and J. J. Mayrhofer, *ChemCatChem*, 2014, **6**, 2219–2223.
27 N. B. Halck, V. Petrykin, P. Krtil and J. Rossmeisl, *Phys. Chem. Chem. Phys.*, 2014, **16**, 13682–13688.
28 R. Forgie, G. Bugosh, K. C. Neyerlin, Z. Liu and P. Strasser, *Electrochem. Solid-State Lett.*, 2010, **13**, B36–B39.
29 K. C. Neyerlin, G. Bugosh, R. Forgie, Z. Liu and P. Strasser, *J. Electrochem. Soc.*, 2009, **156**, B363–B369.
30 K. Macounová, J. Jirkovský, M. V. Makarova, J. Franc and P. Krtil, *J. Solid State Electrochem.*, 2009, **13**, 959–965.
31 V. Petrykin, K. Macounová, M. Okube, S. Mukerjee and P. Krtil, *Catal. Today*, 2013, **202**, 63–69.
32 M. Vukovic, *J. Chem. Soc., Faraday Trans.*, 1990, **86**, 3743–3746.
33 S. H. Chang, N. Danilovic, K.-C. Chang, R. Subbaraman, A. P. Paulikas, D. D. Fong, M. J. Highland, P. M. Baldo, V. R. Stamenkovic, J. W. Freeland, J. A. Eastman and N. M. Markovic, *Nat. Commun.*, 2014, **5**, 4191.
34 C. Iwakura, K. Hirao and H. Tamura, *Electrochim. Acta*, 1977, **22**, 335–340.
35 R. Kötz, S. Stucki, D. Scherson and D. M. Kolb, *J. Electroanal. Chem.*, 1984, **172**, 211–219.
36 H. B. Beer, *J. Electrochem. Soc.*, 1980, **127**, 303C.
37 S. Trasatti, *Electrochim. Acta*, 2000, **45**, 2377–2385.
38 C. Comninellis and G. P. Vercesi, *J. Appl. Electrochem.*, 1991, **21**, 136–142.
39 C. Comninellis and G. P. Vercesi, *J. Appl. Electrochem.*, 1991, **21**, 335–345.
40 D. Galizzioli, F. Tantardini and S. Trasatti, *J. Appl. Electrochem.*, 1974, **4**, 57–67.
41 M. B. Vukmirovic, R. L. Sabatini and R. R. Adzic, *Surf. Sci.*, 2004, **572**, 269–276.
42 B. R. Cuenya, S.-H. Baeck, T. F. Jaramillo and E. W. McFarland, *J. Am. Chem. Soc.*, 2003, **125**, 12928–12934.
43 F. J. Perez-Alonso, D. N. McCarthy, A. Nierhoff, P. Hernandez-Fernandez, C. Strebel, I. E. L. Stephens, J. H. Nielsen and I. Chorkendorff, *Angew. Chem., Int. Ed.*, 2012, **51**, 4641–4643.
44 G. a. Tritsaris, J. Greeley, J. Rossmeisl and J. K. Nørskov, *Catal. Lett.*, 2011, **141**, 909–913.
45 P. Hernandez-Fernandez, F. Masini, D. N. McCarthy, C. E. Strebel, D. Friebel, D. Deiana, P. Malacrida, A. Nierhoff, A. Bodin, A. M. Wise, J. H. Nielsen, T. W. Hansen, A. Nilsson, I. E. L. Stephens and I. Chorkendorff, *Nat. Chem.*, 2014, **6**, 732–738.
46 F. Masini, P. Hernández-Fernández, D. Deiana, C. E. Strebel, D. N. McCarthy, A. Bodin, P. Malacrida, I. Stephens and I. Chorkendorff, *Phys. Chem. Chem. Phys.*, 2014, DOI: 10.1039/C4CP02144D, accepted.
47 H. Haberland, M. Karrais, M. Mall and Y. Thurner, *J. Vac. Sci. Technol., A*, 1992, **10**, 3266.
48 B. Von Issendorff and R. E. Palmer, *Rev. Sci. Instrum.*, 1999, **70**, 4497–4501.
49 R. M. Nielsen, S. Murphy, C. Strebel, M. Johansson, I. Chorkendorff and J. H. Nielsen, *J. Nanopart. Res.*, 2009, **12**, 1249–1262.
50 S. Ardizzone, M. Falciola and S. Trasatti, *J. Electrochem. Soc.*, 1989, **136**, 3–8.
51 F. Masini, C. E. Strebel, D. N. McCarthy, A. U. F. Nierhoff, J. Kehres, E. M. Fiordaliso, J. H. Nielsen and I. Chorkendorff, *J. Catal.*, 2013, **308**, 282–290.
52 L. Tang, B. Han, K. Persson, C. Friesen and T. He, *J. Am. Chem. Soc.*, 2010, 596–600.
53 X. Yan, P. Lin, X. Qi and L. Yang, *Int. J. Mater. Res.*, 2011, **102**, 381–388.
54 E. O. Hall and J. Crangle, *Acta Crystallogr.*, 1957, **10**, 240–241.
55 C. E. Boman, *Acta Chem. Scand.*, 1970, **24**, 116–122.
56 J. Greeley, R. J. A. Hellman and J. K. Nørskov, *Z. Phys. Chem.*, 2007, **221**, 1209–1220.
57 Y. Lee, J. Suntivich, K. J. May, E. E. Perry and Y. Shao-horn, *J. Phys. Chem. Lett.*, 2012, **3**, 399–404.

58 M. W. Louie and A. T. Bell, *J. Am. Chem. Soc.*, 2013, **135**, 12329–12337.
59 H. N. Nong, L. Gan, E. Willinger, D. Teschner and P. Strasser, *Chem. Sci.*, 2014, **5**, 2955–2963.
60 R. Frydendal, E. A. Paoli, B. P. Knudsen, B. Wickman, P. Malacrida and E. L. Ifan, *ChemElectroChem*, 2014, DOI: 10.1002/celc.201402262R1, accepted.
61 S. Stucki and A. Menth, *Ber. Bunsen-Ges.*, 1980, **84**, 1008–1013.

Supporting Information

Oxygen Evolution on Well-Characterized Mass-Selected Ru and RuO_2 Nanoparticles

Elisa A. Paoli[a], Federico Masini[a], Rasmus Frydendal[a], Davide Deiana[b], Christian Schlaup[a], Mauro Malizia[a], Thomas W. Hansen[b], Sebastian Horch[a], Ifan E.L Stephens[a], Ib Chorkendorff[a]

[a] Center for Individual Nanoparticle Functionality (CINF), Department of Physics, Kgs. Lyngby DK-2800, Denmark

[b] Center for Electron Nanoscopy (CEN), Kgs. Lyngby DK-2800, Denmark

Preparation of mass-selected Ru nanoparticles.

The nanoparticles were prepared using a magnetron sputter gas aggregation source (Birmingham Instruments Inc.), combined with time-of-flight mass filtering[1], and deposited onto either electrodes (glassy carbon or Au(111)) for electrochemical measurement or Si_3N_4 grid for TEM analysis. The substrates were mounted in a multi-chamber ultrahigh vacuum (UHV) system (Omicron, Multiscan Lab) with a base pressure in the low 10^{-10} mbar region. The gas aggregation technique involves Ar^+ sputtering of a metallic target (in this study a Ru target from Kurt J. Lesker Inc.), to produce an atomic vapor that is condensed into nanoparticles through collisions with cooled Ar and He gas. Many of the nanoparticles produced via Ar^+ sputtering are ionized; thus the particles can be filtered based on their mass-to-charge ratio, which in turn allows the deposition of particles with a narrow size distribution.

Following the particle production and filtering stages, the ionized nanoparticles are directed using Einzel lenses onto the support mounted in the vacuum chamber. The Einzel lenses can be used to control the breadth and position of the particle beam, which gives control of the total number of particles that are deposited on the surface, as well as the density of the nanoparticles. The combination of particle counting and mass selection allow us to accurately estimate the amount of catalyst deposited onto the glassy carbon. The total deposited mass was calculated with the formula:

$$M_{dep} = m_p I_{dep} t$$

Where m_p is the single particle mass, set using the mass filter, assuming singly charged particles, I_{dep} is the deposition current and t is the deposition time.

X-Ray Photoelectron Spectroscopy (XPS) Characterization.

Elemental characterization of the supported Ru nanoparticles was performed in-situ for each deposition, i.e. without breaking the vacuum, using X-ray Photoemission Spectroscopy (XPS).

Post-oxidation and post-electrochemistry (EC) XPS measurements were performed with the same apparatus after re-introducing the sample in the UHV system.

The XPS measurements of the as-prepared nanoparticles were directly taken under UHV after each deposition. The analysis chamber base pressure was 2 x 10^{-11} mbar. The X-ray source XR-50 was a non-monochromatized Al Kα (1486.7 eV), manufactured by SPECS GmbH. The employed pass energy was 25 eV. The atomic concentrations were quantified by integration of the Ru 3d, C 1s peaks after background removal. A Shirley-type background was chosen for this purpose. The intensities were corrected for the relative sensitivity factors.

Fitting of the XPS spectra was performed with Gaussian-Lorentzian functions mixed with exponential tail, using CASA XPS software. Carbon was fitted using three different features, which we attribute to carbon and to its surface oxides. Ruthenium was fitted using two peaks for metallic ruthenium, two peaks for ruthenium dioxide (oxide at low B.E.) and another couple of peaks for the satellite features at higher binding energy (oxide at high B.E. in figure 1 and in figure S1). [2–5]

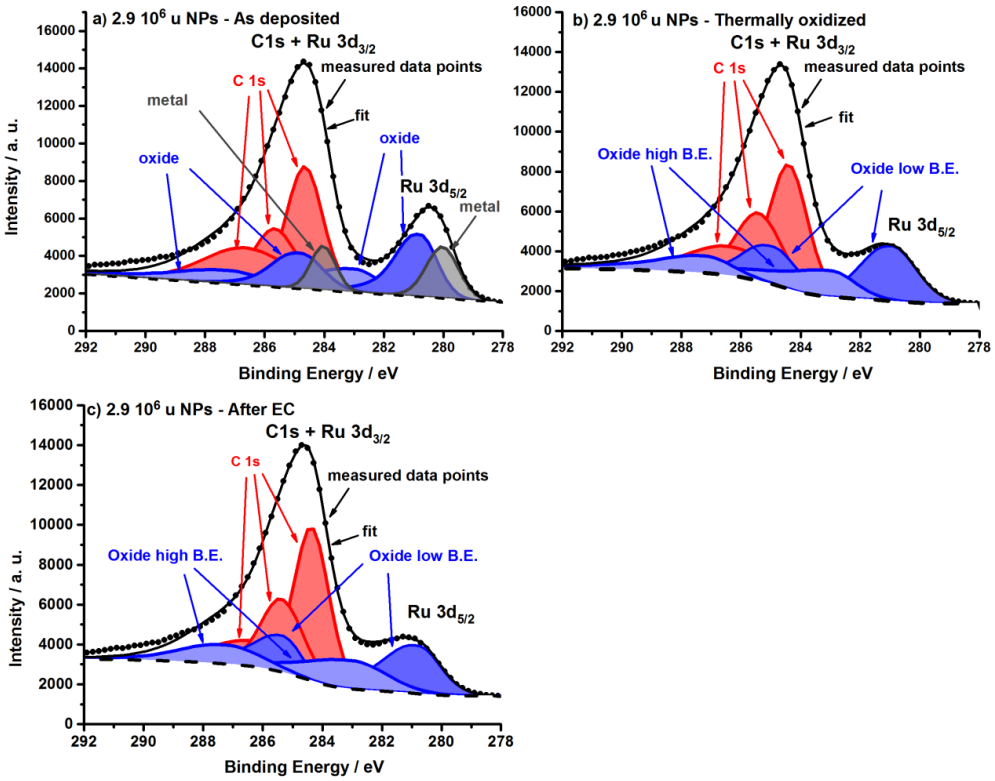

Figure S1. XPS spectra of the Ru 3d core level region for 2.9 10^6 u (a) *as-deposited* Ru, (b) thermally oxidized RuO_2 and (c) RuO_2 after electrochemistry (EC) nanoparticles on Glassy Carbon disk.

In order to independently estimate the total mass deposited, XPS measurements were used. To do this, we calculated the XPS Ru3d-to-C1s ratio, which is an estimate of the Ru nanoparticle projected coverage.

$$X_{Ru} = \frac{I_{Ru3d}}{I_{Ru3d} + I_{C1s}}$$

Where Ru3d represents the total ruthenium contribution normalized with the sensitivity factor and C1s the total corrected contribution from the carbon

$$I_{Ru3d} = \frac{I_{Ru3d\ 3/2} + I_{Ru3d\ 5/2}}{S_{Ru}}$$

Where $Ru3d_{3/2}$ and $Ru3d_{5/2}$ represent the integration of the Ru 3d peaks and S_{Ru} is the Scofield cross section factor for Ru α is the angle between the detector and the normal to the surface of the sample.

$$I_{Corrected\ C1s} = I_{C1s}\left(1 - \left(\frac{\pi\left(r_{electrode}^2 - r_{dep}^2\right)}{\pi\, r_{electrode}^2}\right)\right) - I_{Ru3d}\left(exp\left(-\frac{d}{\lambda cos(\alpha_{detector})}\right)\right)$$

Where C1s is the integration of C1s XPS peak, $r_{electrode}$ is the radius of the electrode, and r_{dep} is the radius of the deposited area and λ is the mean free path.

We then computed the total mass (M_{XPS}) and surface area (A_{XPS}) by assuming Ru spherical particles, using the following formulas:

$$M_{XPS} = \left(\frac{A_{XPS}}{4\pi\left(\frac{d}{2}\right)^2}\right) m_p 1.66 \times 10^{-18} \times 10^{12}$$

$$A_{XPS} = 4\pi X_{Ru} r^2{}_{dep}$$

Where X_{Ru} is the Ru signal fraction, d is the diameter of the nanoparticle, r_{dep} is the radius of the area where the particles are deposited on.

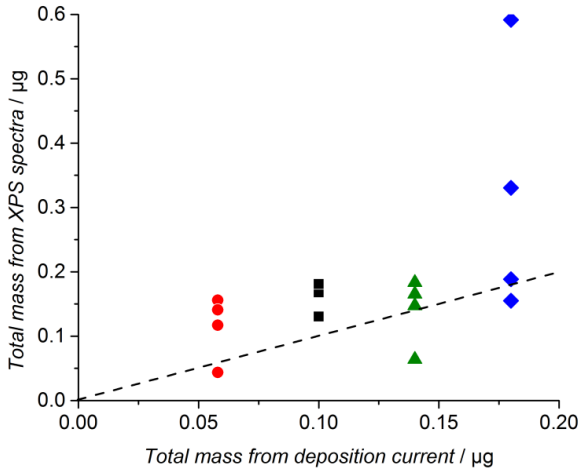

Figure S2. Comparison between the total deposited mass of ruthenium estimated from the XPS spectra assuming spherical particles vs. the total mass measured from the deposition current. The dashed line shows the theoretical correlation, if there were a 1:1 correspondence between the two measures of the deposited mass. Each color represents a different mass: 0.1 10^6 u (red circle), 0.5 10^6 u (black square), 1.4 10^6 u (green triangle) and 2.9 10^6 u (blue rhombus).

Figure S2 shows a good correlation between the mass from XPS and the mass from the deposition current for the particles with a mass up to 1.4 10^6 u. The data from XPS are based on the assumption of spherical particles, which is not the case for big particles. The STEM images shown in Figure 1(c-f,) clearly show that, the largest particles have a very rough shape, which might explain the scatter for these particles in Figure S2. Consequently, for the plot of the mass activity, Figure 4 in the main text, the mass activity was calculated on the basis of the mass from the deposition current.

Glancing Angle – X-Ray Diffraction (XRD)

To identify the structure of the nanoparticles before and after thermal oxidation, Glancing Angle XRD was performed on 2.9 10^6 u nanoparticles deposited on a Au(111) disk. The glancing angle XRD technique limits the signal from the substrate making it easier to single out information from the particles. To further enhance the signal from the nanoparticles, the loading was increased up to ~20 μg/cm^2. The measurements were conducted on PAN analytical X'pert Pro XRD equipment with X-ray wavelength at 1.54 Å for the CuKα line. Alignment of the sample was performed with reflectometry and the incident angle set to $\omega = 0.5^o$. The scan range used was $2\theta = [35\,;\,70]$. Reference patterns for gold, metallic ruthenium and rutile RuO_2 were found in ref [6] ref. [7] and ref. [8], respectively. In Figure 2 the measured pattern before and after oxidation can be seen together with the reference patterns. After thermal treatment, rutile RuO_2 peaks appear clearly, while the metallic peak at 43.5^o disappears, indicating that the bulk of the particles are fully oxidized.

Scanning Transmission Electron Microscopy (STEM) and Scanning Electron Microscopy (SEM) characterisation.

TEM analysis was performed on mass-selected RuO_2 nanoparticles deposited on Si_3N_4 TEM-windows. The projected area distributions were obtained from high angle annular dark field (HAADF) STEM micrographs acquired in a FEI Titan Analytical 80-300 electron microscope equipped with a CEOS Cescor probe spherical aberration corrector and operated at 300 kV accelerating voltage. Within each specimen, the analysis was carried out with the same microscope condition, constant acquisition dwell time as well as the HAADF detector settings.

SEM images were obtained using a Helios EBS3 microscope, with an accelerating voltage of 5kV and using a secondary electron detector. In Figure S3 SEM images are shown. Identical Location (IL) SEM was not used and the difference in local particle distribution may be due to imaging of different areas of the electrode where the particles are randomly distributes. However, after thermal oxidation neither sintering nor aggregation was observed while, after electrochemistry, particles migrate forming agglomerates.[9]

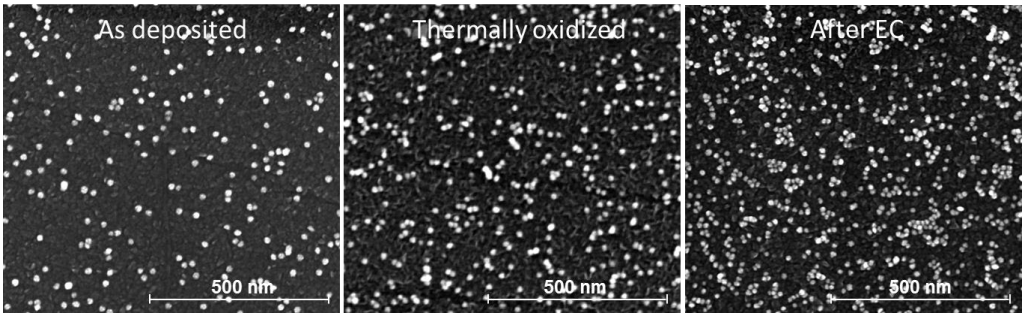

Figure S3. SEM micrographs of the same sample 2.9 10^6 u (a) as deposited Ru Nps, (b) thermally oxidized RuO_2 Nps and (c) RuO_2 after electrochemical Nps (2 Cycles between 1.00 and 1.23 V at 20 mV/s and 4 hours at 1.5V). Magnification 125000x; accelerating voltage 5.00 kV.

Electrochemical characterisation

All the electrochemical measurements were performed in a Rotating Ring Disk Electrode (RRDE) assembly, provided by Pine Instruments Corporation, using a Bio-Logic Instruments VMP2 multichannel potentiostat/galvanostat with EIS analyzer, controlled by a computer. Data was acquired using the Bio-Logic EC-Lab software. The electrochemical cell was a standard three-compartment glass cell, equipped with a Luggin capillary. The auxiliary electrode was a carbon rod and the reference was a $Hg/HgSO_4$ electrode. All the potentials are expressed with respect to the reversible hydrogen electrode (RHE) and the reference electrode was calibrated against an actual hydrogen electrode for each measurement at room temperature in the same electrolyte. All the experiments were performed in a nitrogen saturated 0.05M sulfuric acid at 1600 rpm and at room temperature. The acid electrolyte was prepared from 98% sulfuric acid (Merck Suprapur) and diluted with Millipore water (18 MΩ cm).

All the CVs were corrected for Ohmic losses (~50 Ω on Glassy Carbon and ~40 Ω on Au(111)). The Ohmic compensated current is then capacitance-corrected by taking the average between the forward (positive) and the backward (negative) scans[10] (fig S4).

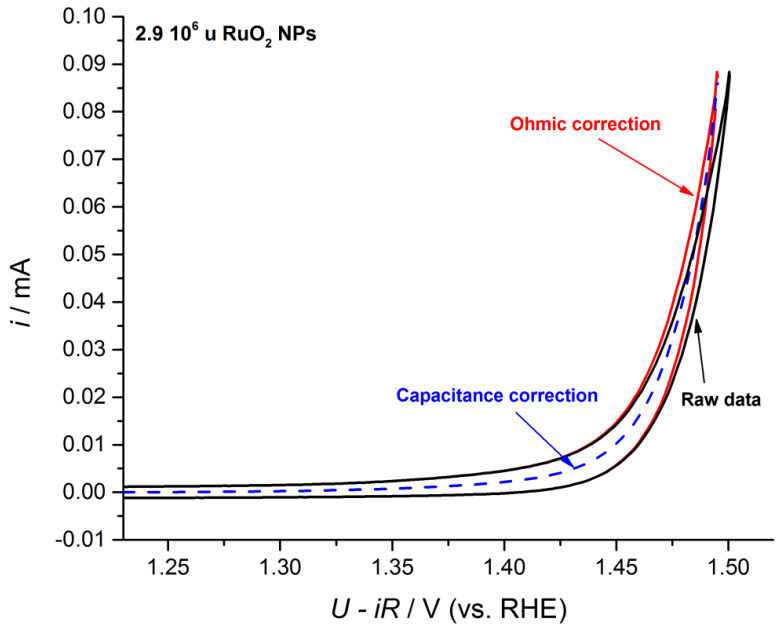

Figure S4. Ohmic and capacitance corrected cyclic voltammetry of 2.9 10^6 u thermally oxidized RuO_2 nanoparticles on Glassy carbon. The data were first compensated for the Ohmic resistance and then for the capacitance, by taking the average between the anodic and cathodic sweeps.

The rotating ring disk electrode (Pine) with a Platinum ring was calibrated using the same configuration with a ferricyanide redox couple in a 0.1M KOH solution (Merck)[11]. The collection efficiency was estimated to be 0.20 ± 0.01, evaluated from three different measurements. The ring was held either at 1.1 V vs. RHE to reduce the RuO_4 produced during OER[12] or at 0.4 V vs. RHE to collect the generated oxygen[11].

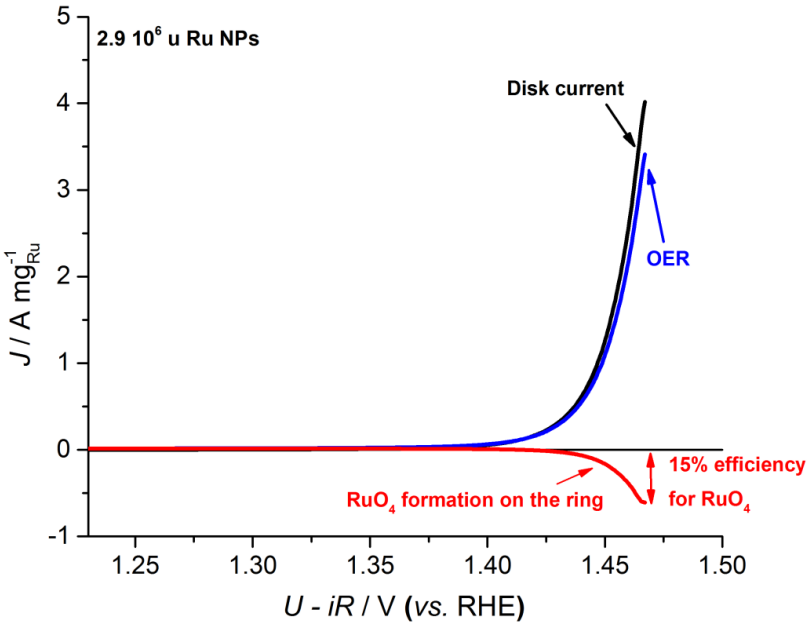

Figure S5. RRDE voltammogram of as deposited 2.9 10^6 u Ru nanoparticles at 1600 rpm in N_2 saturated electrolyte with the disk current (black), the ring current (red) and the current corresponding to Oxygen Evolution (blue). While cycling the potential on the disk, the generated RuO_4 is collected and reduced at the ring, which is held at 1.1 V (vs. RHE).

By integrating the charge due to the reduction of RuO_4, it is possible to evaluate the mass loss of Ru during Oxygen Evolution, as follows:[12]

Initial mass from deposition current = 0.18 µg

Integration of the ring peak, Q_{ring} = 0.063 mC

Number of electrons per RuO_4 reduced, n_{e^-} = 1

Number of Ru atoms, n_{atoms}:

$$\frac{Q_{ring}}{n_{e^-}\, e^- \times 1000} = 3.93 \text{ x } 1014$$

Mass of dissolved Ru, m:

$$\frac{n_{atoms} \times Molecular\ weight_{Ru}}{N_A} = 6.6 \text{ x } 10\text{-}8 \text{ g}$$

Mass loss:

$$\frac{m_{dissolved,Ru}}{m_{initial}} = \frac{6.6 \times 10^{-8} \times 10^{6}}{0.18} \times 100 = 37\ \%$$

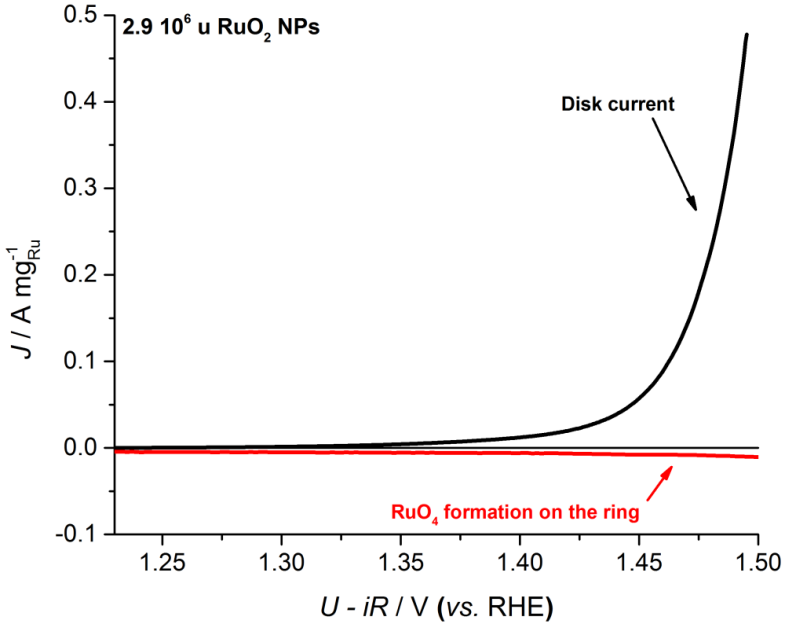

Figure S6. RRDE voltammogram of thermally annealed 2.9 10^6 u RuO_2 nanoparticles at 1600 rpm in N_2 saturated electrolyte with the disk current (black) and the ring current (red).

In the case of thermally annealed 2.9 10^6 u nanoparticles, shown in Figure S6, the ring current can be neglected, since it does not significantly exceed the noise level. This suggests that the oxygen evolution can account for the entire disk current. This is confirmed by direct measurement of O_2 with a Gas Chromatograph.

Mass Activity

The mass activity was evaluated by taking the value of the current, after Ohmic drop compensation and capacitance correction (as shown in Figure S4) at 1.48 V vs. RHE (η = 0.25 V) and then normalizing the value with the mass of ruthenium. The mass was estimated from the neutralization current during the cluster deposition.

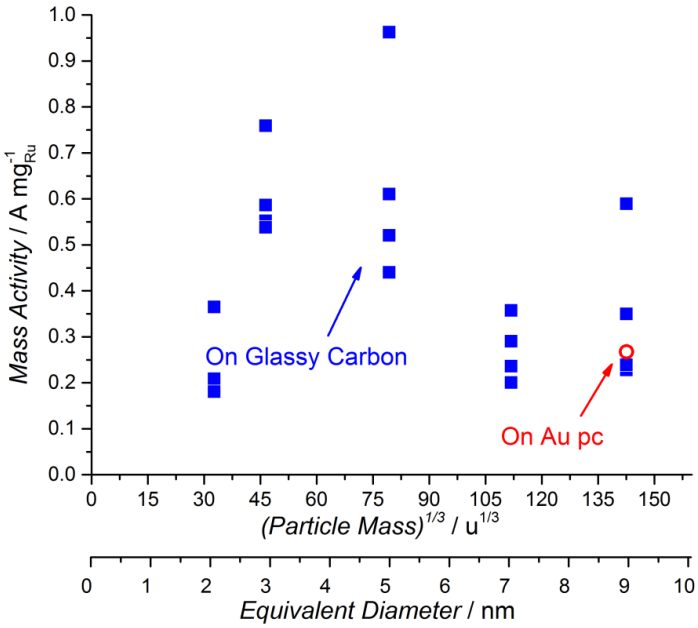

Figure S7. OER mass activities at 1.48 V (vs. RHE) of different single particle mass (0.035, 0.1, 0.5, 1.4, 2.9 10^6 u) of thermally oxidized RuO_2, from cyclic voltammogram in N_2 saturated 0.05M H_2SO_4 at 1600 rpm with a sweep rate of 20 mV/s. All the data points are shown. Activity on Au polycrystalline disk for 2.9 10^6 u nanoparticles is also shown.

Figure S7 shows that similar activities can be obtained both on glassy carbon disk and on gold polycrystalline disk.

Calculation of how many years of precious metal annual production would be required to install 1 TW of hydrogen storage capacity

Pt-Ir PEM electrolysers[13]

Pt at the cathode: 0.05 mg/cm^2

Pt at the anode: 0.15 mg/cm^2

Ir at the anode: 0.15 mg/cm^2

Equilbrium potential at 80°C: 1.18 V

Calculate at 1.4 A/cm^2 (65% efficiency)

Annual Pt production = 2 x 10^8 g[14]

Annual Ir production =9 x 10^6 g[14]

Power stored: $P_{stored} = 1.18 \times 1.4 = 1.65\ Wcm^{-2}$

Total Precious metal: $Pt_{cathode} + Pt_{anode} + Ir_{anode} = 0.35\ mg\ cm^{-2}$

Total Precious metal requirement: $0.35/1.65 = 0.21\ g\ kW^{-1}$

Total precious metal / TW of hydrogen storage capacity: 2.1×10^8 g

Total Pt / TW = $2.1 \times 10^8 \times \frac{0.2}{0.35} = 1 \times 10^8$ g, which corresponds to 0.5 year of Pt annual production

Total Ir/ TW $= 2.1 \times 10^8 \times \frac{0.15}{0.35} = 9 \times 10^7$ g, which corresponds to 10 years of Ir annual production

The RuO_2 nanoparticles presented in this work shows a 30-fold improvement in mass activity compared to PtIr. If we could reproduce such an improvement in a real electrolyzer, we could decrease the precious metal loading of at least one order of magnitude. By doing a similar

calculation as above and considering that the annual Ru production is higher than Ir ($2.5\ 10^7$ g)[14] we find that the amount of Ru required per TW of hydrogen storage capacity would constitute less than half a year of the annual production.

Specific activity

The specific activity was evaluated for 0.1 10^6 u RuO_2 nanoparticles, which shows spherical shape, by normalizing the current with the surface area of ruthenium. The surface area was calculated form the deposition cluster current as follows:

$$\boldsymbol{A_{dep} = A_p I_{dep} t_{dep} n_p}$$

Where A_p is the projected area of the single particle, $\boldsymbol{I_{dep}}$ is the the deposition current, $\boldsymbol{t_{dep}}$, is the deposition time and $\boldsymbol{n_p}$ is the number of particles per Coulomb. In Figure S8 the specific activity of 0.1 10^6 u RuO_2 is compared with the work by Shao-Horn and co-workers. In their investigations, they evaluated the specific activity of RuO_2 nanoparticles and RuO_2 thin films, estimating the surface area of the catalysts.

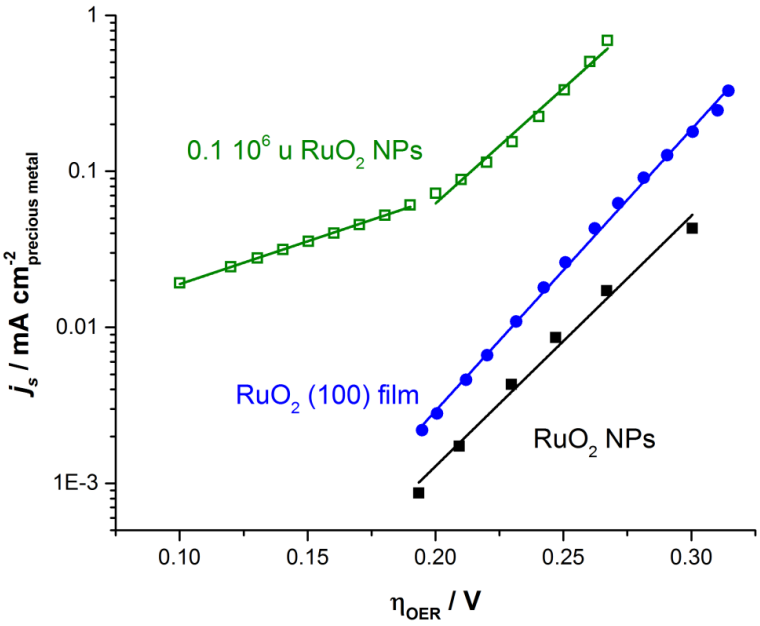

Figure S8. Comparison of the specific activity of 0.1 10^6 u RuO_2 NPs from this work with RuO_2 (100) film from ref [15] and RuO_2 NPs from ref [16].

Turnover Frequency (TOF)

Turnover frequency (TOF) was calculated in two ways:

1) TOF_{min} represents the lower bound and it was estimated from the mass activity, using the following formula:

$$TOF_{min} = \frac{J\ MW_{RuO_2}}{n_{e-}\ N_A\ e^-}$$

Where J is the mass activity in A/g, MW_{RuO_2} is the molecular weight, n_{e-} is the numbers of electrons involved in the reaction (4 electrons), N_A is the Avogadro´s number and e^- is the charge of the electron.

2) TOF_{max} represents the upper bound and it was estimated from the specific activity, using the following formula:

$$TOF_{max} = \frac{J\ MW_{RuO_2}}{h_{ML}\ d\ n_{e-}\ N_A\ e^-}$$

Where J is the specific activity in A/cm^2, MW_{RuO_2} is the molecular weight, h_{ML} is the height of a monolayer, d is the density, n_{e-} is the numbers of electrons involved in the reaction (4 electrons), N_A is the Avogadro´s number and e^- is the charge of the electron.

Coverage on Au(111) electrode

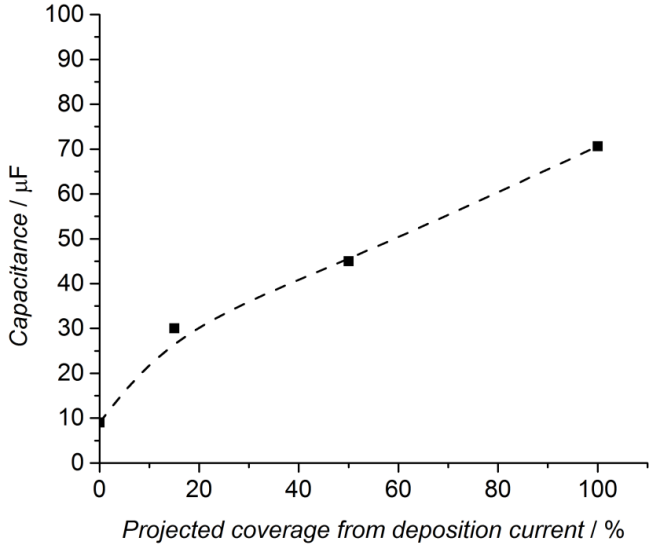

Figure S9. Comparison of 2.9 10^6 u thermally oxidized RuO_2 coverage on Au(111) disk, calculated with the neutralization cluster current and using the capacitance measured with electrochemical impedance spectroscopy.

Stability measurements

Chronoamperometry and Inductively Coupled Plasma – Mass Spectrometer

The ruthenium dissolved into the electrolyte was measured ex-situ by ICP-MS at the end of the chronoamperometrical test. A performance check and calibration were performed prior to each experiment.

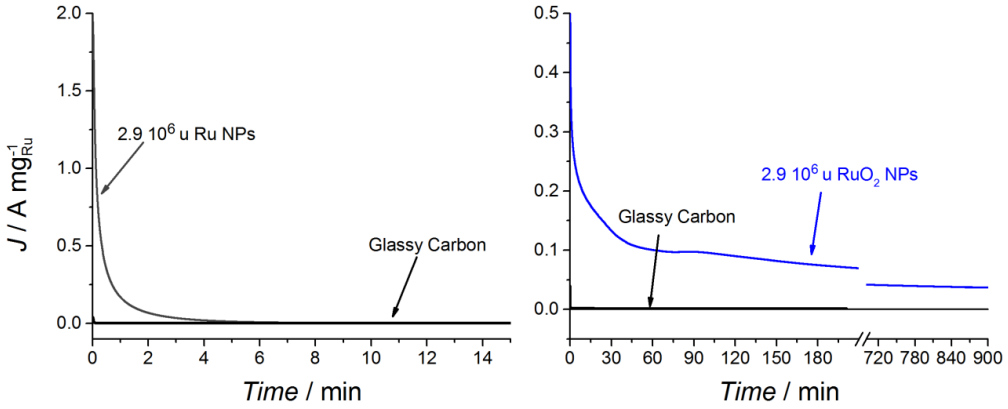

Figure S10. Chronoamperometry at 1.5 V (vs. RHE) in N_2 saturated electrolyte at 1600 rpm for 2.9 10^6 u (a) as-deposited Ru and (b) thermally oxidized RuO_2 nanoparticles.

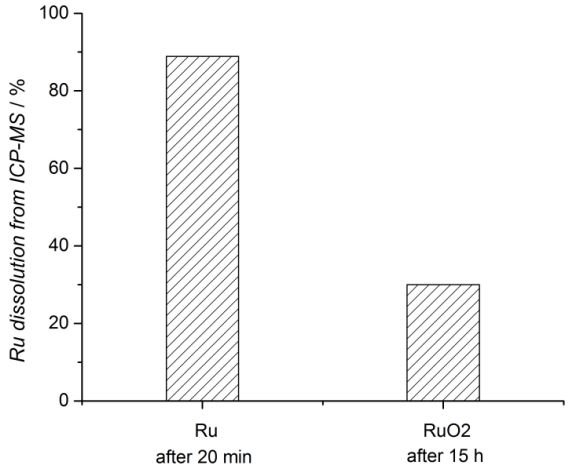

Figure S11. Ruthenium dissolution percentage relative to the initial mass loading, evaluated from the deposition cluster current, after 20 minutes of chronoamperometry for the metallic nanoparticles and 15 hours for the oxide.

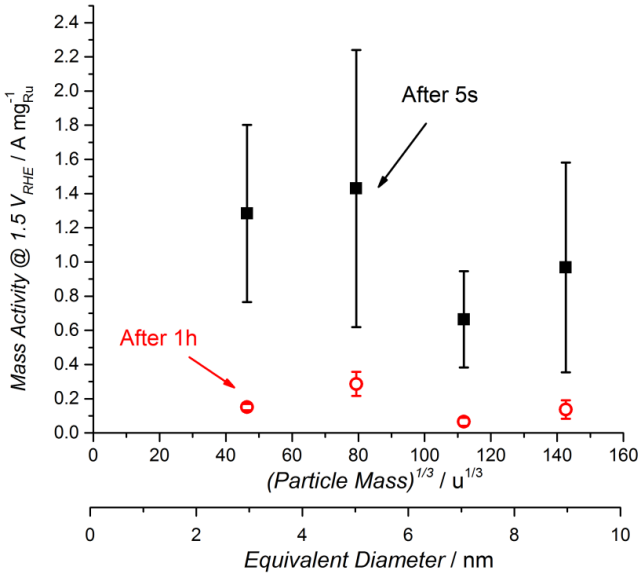

Figure S12. Comparison of OER mass activities extrapolated from Chronoamperometry at 1.5 V (vs. RHE) after 5 seconds (to avoid the initial charging current) and after 1 hour for 0.1, 0.5, 1.4 and 2.9 10^6 u thermally oxidized RuO_2 nanoparticles

Electrochemical Scanning Tunneling Microscope characterisation

The EC-STM images were acquired using a custom-build EC-STM setup, which is described in detail elsewhere[17]. Tunneling tips were prepared by electrochemical etching of a 0.25 mm Pr/Ir (90/10) wire and subsequently coated with commercial hot-glue. All STM images were recorded in constant current mode and under a protective gas atmosphere of argon (scientific quality, 6.0). A Pt wire served as a Pt/PtO pseudo reference electrode, for calibration against RHE the potential of the well-known "butterfly"-peaks of the order/disorder transition of sulfate on Au(111) was used[18]. The potential stability and accuracy of this pseudo reference electrode

amounts to ±25 mV. A 0.05 M H_2SO_4 solution was used as electrolyte, which was deaerated prior to measurements with argon (scientific quality, 6.0).

Potentiodynamic STM images were obtained by sweeping the working electrode's potential with a linear ramp of 2 mV s^{-1} while acquiring a STM image. Before and after acquisition of each potentiodynamic image, STM images under constant potential conditions were recorded at the same place (Fig. S13), allowing to distinguish between a local inhomogeneity of the particle distribution and the corrosion reaction.

The appearance of the particles in STM images is heavily influenced by the shape of the tunneling tip and does not reflect their actual shape. However, this tip-convolution effect does not affect the qualitatively observed stability of the Ru and RuO_2 particles under certain potential conditions; consequently we choose to neglect it in the discussion.

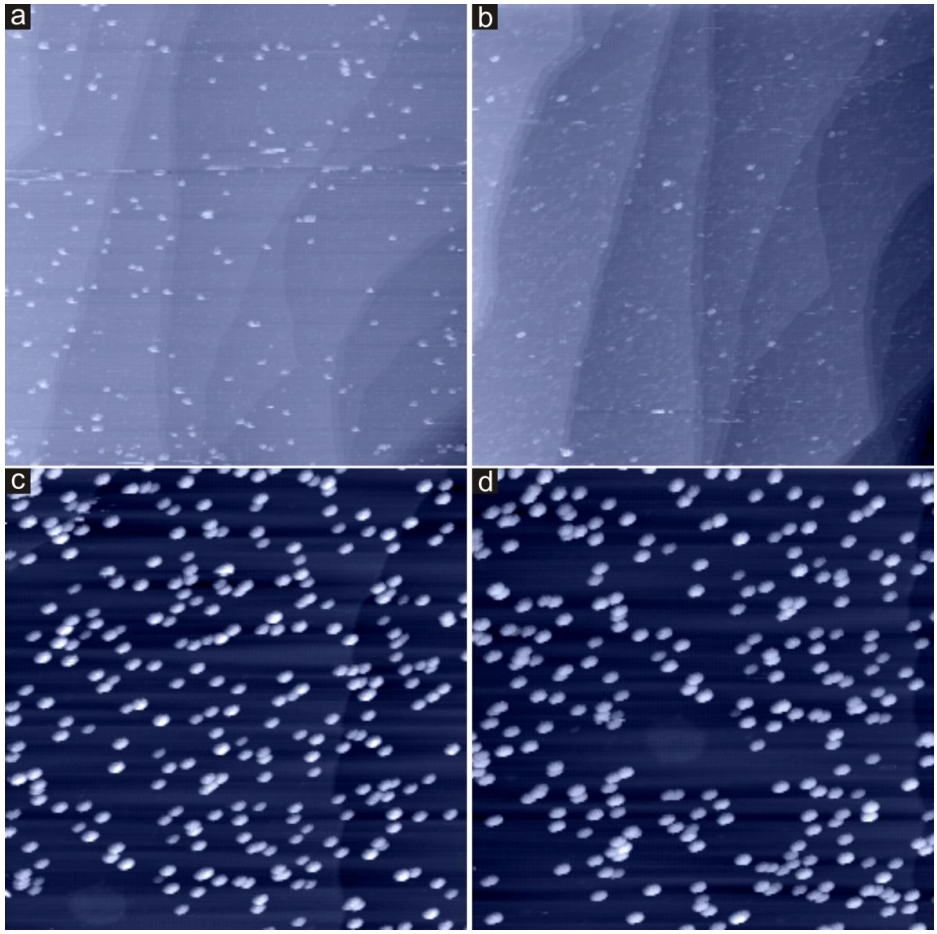

Figure S13. STM images recorded before (a,c) and after (b,d) the potentiodynamic STM images in the manuscript. a), b) 0.001 ML Ru particles (3 nm): (520 nm)2, E = 1277 mV, UB=-299 mV, IT=1 nA; c), d) 0.001 ML RuO_2 particles (3 nm): (516 nm)2, E = 1277 mV, UB=-245 mV, IT=1 nA.

Determination of Oxygen concentration and Faradaic efficiency

The Faradaic efficiency of RuO_2 nanoparticles was measured using gas chromatography in an H-type electrochemical cell. The cell was purged using He to remove air from the electrolyte and headspace before the beginning of the experiment. The complete removal of air was verified using the gas chromatograph. The system was subsequently kept under closed circulation loop condition by using a pump. The gas present in the headspace was sampled during the experiment every 10 minutes using an automated injection valve for determination of the gas composition.

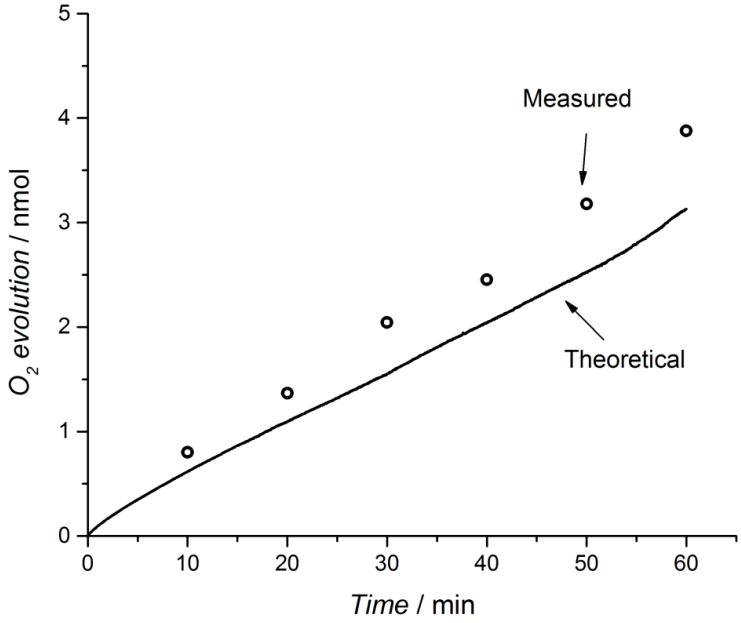

Figure S14. Oxygen evolution directly measured with a Gas Chromatograph in a He saturated H-cell and compared with the oxygen evaluated from the charge.

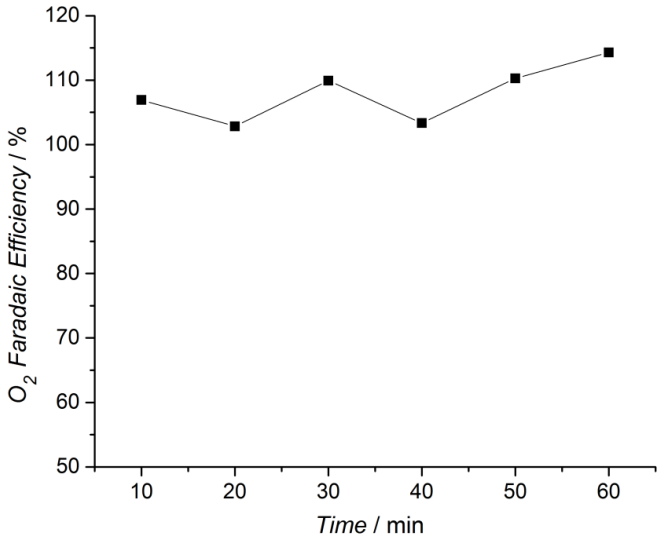

Figure S15. Faradaic efficiency as a function of time.

REFERENCES

1. B. Von Issendorff and R. E. Palmer, *Rev. Sci. Instrum.*, 1999, **70**, 4497–4501.

2. H. Over, A. P. Seitsonen, E. Lundgren, M. Smedh, and J. N. Andersen, *Surf. Sci.*, 2002, **504**, L196–L200.

3. W. Chen, M. Zhang, D. W. Zhang, S.-J. Ding, J.-J. Tan, M. Xu, X.-P. Qu, and L.-K. Wang, *Appl. Surf. Sci.*, 2007, **253**, 4045–4050.

4. S. Bhaskar, P. S. Dobal, S. B. Majumder, and R. S. Katiyar, *J. Appl. Phys.*, 2001, **89**, 2987–2992.

5. D. Rochefort, P. Dabo, D. Guay, and P. M. a. Sherwood, *Electrochim. Acta*, 2003, **48**, 4245–4252.

6. X. Yan, P. Lin, X. Qi, and L. Yang, *Int. J. Mater. Res.*, 2011, **102**, 381–388.

7. E. O. Hall and J. Crangle, *Acta Crystallogr.*, 1957, **10**, 240–241.

8. C. E. Boman, *Acta Chem. Scand.*, 1970, **24**, 116–122.

9. K. Hartl, M. Nesselberger, K. J. J. Mayrhofer, S. Kunz, F. F. Schweinberger, G. Kwon, M. Hanzlik, U. Heiz, and M. Arenz, *Electrochim. Acta*, 2010, **56**, 810–816.

10. J. Suntivich, K. J. May, H. A. Gasteiger, J. B. Goodenough, and Y. Shao-Horn, *Science*, 2011, **334**, 1383–1385.

11. U. A. Paulus, T. J. Schmidt, H. A. Gasteiger, and R. J. Behm, 2001, **495**, 134–145.

12. M. Vukovic, *J. Chem. Soc. Faraday Trans.*, 1990, **86**, 3743–3746.

13. M. K. Debe, S. M. Hendricks, G. D. Vernstrom, M. Meyers, M. Brostrom, M. Stephens, Q. Chan, J. Willey, M. Hamden, C. K. Mittelsteadt, C. B. Capuano, K. E. Ayers, and E. B. Anderson, *J. Electrochem. Soc.*, 2012, **159**, K165–K176.

14. P. C. K. Vesborg and T. F. Jaramillo, *RSC Adv.*, 2012, **2**, 7933–7947.

15. K. A. Stoerzinger, L. Qiao, M. D. Biegalski, and Y. Shao-horn, *J. Phys. Chem. Lett.*, 2014, **5**, 1636–1641.

16. Y. Lee, J. Suntivich, K. J. May, E. E. Perry, and Y. Shao-horn, *J. Phys. Chem. Lett.*, 2012, **3**, 399–404.

Paper II

Benchmarking the Stability of Oxygen Evolution Reaction Catalysts: The Importance of Monitoring Mass Losses
Rasmus Frydendal, Elisa A. Paoli, Brian P. Knudsen, Björn Wickman, Paolo Malacrida, Ifan E.L. Stephens, Ib Chorkendorff
ChemElectroChem, 2014, *DOI* : 10.1002/*celc*.201402262

ChemPubSoc Europe

DOI: 10.1002/celc.201402262

Benchmarking the Stability of Oxygen Evolution Reaction Catalysts: The Importance of Monitoring Mass Losses

Rasmus Frydendal,[a] Elisa A. Paoli,[a] Brian P. Knudsen,[a] Björn Wickman,[a, b] Paolo Malacrida,[a] Ifan E. L. Stephens,*[a] and Ib Chorkendorff*[a]

Because of the rising need for energy storage, potentially facilitated by electrolyzers, improvements to the catalysis of the oxygen evolution reaction (OER) become increasingly relevant. Standardized protocols have been developed for determining critical figures of merit, such as the electrochemical surface area, mass activity and specific activity. Even so, when new and more active catalysts are reported, the catalyst stability tends to play a minor role. In this work, we monitor corrosion on RuO_2 and MnO_x by combining the electrochemical quartz crystal microbalance (EQCM) with inductively coupled plasma mass spectrometry (ICP–MS). We show that a meaningful estimation of the stability cannot be achieved based on purely electrochemical tests. On the catalysts tested, the anodic dissolution current was four orders of magnitude lower than the total current. We propose that even if long-term testing cannot be replaced, a useful evaluation of the stability can be achieved with short-term tests by using EQCM or ICP–MS.

1. Introduction

Water electrolysis is set to play a key role in the provision of solar fuels, as a sustainable substitute for fossil fuels.[1] Polymer electrolyte membrane (PEM) electrolysers are particularly well-suited towards the localised storage of renewables such as wind or solar, which are inherently intermittent. It turns out that the majority of the efficiency losses on these devices can be traced back to the oxygen evolution reaction (OER).[2,3] Consequently, it is critical that the OER catalyst has a sufficiently high activity, to minimise these losses, and that this activity is stable over the whole lifetime of the catalyst. This is particularly challenging, not only because the anode operates at inherently oxidising potentials, but also as a result of the acidic electrolyte of PEM electrolysers. At present, only IrO_x and RuO_x based materials show reasonable activity and stability under such conditions.[4,5] The best-performing catalysts in acidic media are shown in the Tafel plot in Figure 1 a, which provides an overview of the current state of the art, clearly dominated by oxide catalysts based on the scarce elements Ru and Ir. However, should PEM electrolysis make a true impact to the global energy landscape, it will need to be scaled up to the terawatt level;[6] consequently, the loading of the precious metals required to catalyse the OER should be decreased drastically or eliminated altogether.[7,8] In principle, the proton-con-

[a] R. Frydendal, E. A. Paoli, B. P. Knudsen, Dr. B. Wickman, Dr. P. Malacrida, Prof. I. E. L. Stephens, Prof. I. Chorkendorff
Center for Individual Nanoparticle Functionality
Department of Physics, Technical Univ. of Denmark
DK-2800 Kongens Lyngby (Denmark)
E-mail: ifan.stephens@fysik.dtu.dk
ibchork@fysik.dtu.dk

[b] Dr. B. Wickman
Department of Applied Physics
Chalmers University of Technology
SE-41296 Göteborg (Sweden)

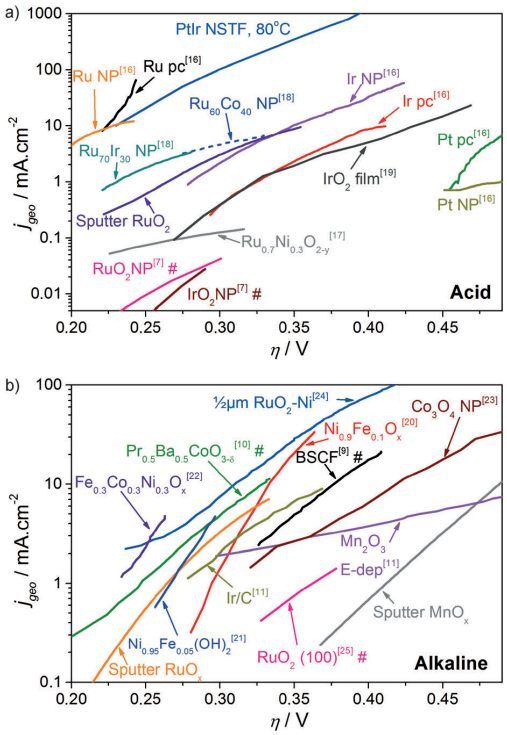

Figure 1. Overview of the state of the art for the oxygen evolution reaction: a) In acid media. Data adapted from: Present work for sputtered RuO_2,[16] for Ru, Ir and Pt polycrystalline (pc) and nanoparticles (NP),[17] for $Ru_{0.7}Ni_{0.3}O_{2-y}$ nanocrystals,[18] for RuCo and RuIr NP,[19] for IrO_2 film and[7] for RuO_2 and IrO_2 NP (# normalised to oxide area). b) In alkaline media. Data adapted from: Present work for sputtered MnO_x, from this group for sputtered RuO_x,[20] for $Ni_{0.9}Fe_{0.1}O_x$,[21] For $Ni_{0.95}Fe_{0.05}(OH)_2$,[22] for $Fe_{0.3}Co_{0.3}Ni_{0.3}O_x$,[9] for $Ba_{0.5}Sr_{0.5}Co_{0.8}Fe_{0.2}$ (# normalised to oxide area),[10] for $Pr_{0.5}Ba_{0.5}CoO_{3-\delta}$ (# normalised to oxide area),[11] for Ir/C and Mn_2O_3 E-dep,[23] for Co_3O_4 NP,[24] for RuO_2-Ni and[25] for RuO_2 (100) (normalised to oxide area).

ducting polymers used in PEM electrolysers could be replaced by hydroxide-conducting membranes; indeed, several materials have recently been discovered in alkaline electrolytes with a catalytic activity at least as high as that of RuO_x and IrO_x.[9–12] In Figure 1b, the best-performing OER catalysts in alkaline media are shown in a unified Tafel plot (it should be noted that in this plot the activity of some of the catalysts has been reported as a current density normalised according to the microscopic surface area, denoted by the symbol # in the plot, whereas other catalysts have been normalised according to the geometric surface area). It is clear from the plot that the most active catalysts are primarily based on Ni or Co. Even so, the use of alkaline polymeric membranes comes at the cost of increased overpotential for hydrogen evolution, and lower membrane conductivity and stability.[13–15]

Regardless of the pH of the electrolyte, robust OER catalyst benchmarks are required that allow a straightforward comparison of catalyst performance between different experimental groups.[4,7] Critical parameters include: 1) the geometric activity, that is, the current normalised according to the geometric or projected area, 2) the mass activity, that is, the current per unit mass precious metals, 3) the specific activity, the current normalised according to the microscopic area, and 4) the stability of the catalyst.

In a commercial device, it is essential that the geometric activity is maximised, to minimise overpotentials. Moreover, should precious metal oxides be employed, a high geometric activity should not be reliant on significant loadings of scarce elements, that is, the mass activity should also be maximised. Both the geometric activity and mass activity can be maximised by employing materials with a high specific activity and a high surface area. However, to judge whether a material is intrinsically active for a reaction, knowledge of the specific activity becomes important. This metric, in turn, is dependent on an accurate knowledge of the electrochemically active surface area, which is challenging to measure on oxides. Alternatively, the catalyst activity can be assessed using smooth thin films, where the microscopic surface area is as close as possible to the geometric surface area.[20,26,27]

The procedures for assessing the stability of OER catalysts are not well established in the literature; this is in contrast to the reverse of the OER, the oxygen reduction reaction (ORR), where detailed tests for assessing the catalyst stability have been developed to simulate the conditions required for automotive applications[28]. Thus far, most researchers have assessed the stability under OER conditions for a limited number of hours, by performing chronopotentiometry at a constant current density or chronoamperometry at a constant potential. However, it remains questionable whether such measurements can provide the basis upon which one could judge the long-term performance of a catalyst in a real device over the required lifetime, that is, a number of years.

A number of methods exist to monitor catalyst corrosion.[29] Microscopic techniques, such as scanning tunneling microscopy[30,31] and transmission electron microscopy,[32–35] can monitor changes in the electrode morphology and structure. On the other hand, macroscopic techniques can be applied to determine the corrosion rates; these include the rotating ring disk electrode (RRDE; for example, for monitoring the anodic dissolution of RuO_2[36,37]), the quartz crystal microbalance,[38] and inductively coupled plasma mass spectrometry (ICP–MS).[39–41] Nonetheless, as of yet, no standardized protocols for assessing the stability under OER conditions have emerged.

Herein, we present guidelines for establishing the stability of OER electrocatalysts. By combining standard RDE tests with electrochemical quartz crystal microbalance[42] (EQCM) measurements and inductively coupled plasma mass spectrometry (ICP–MS), we provide a detailed description of corrosion processes that take place in parallel to the OER. The catalysts investigated are RuO_2 and MnO_x. RuO_2 is an extensively studied material with a high activity in acidic electrolyte.[16,43–45] However, the stability of RuO_2 is limited at high overpotentials. MnO_x has been proposed as a more abundant and inexpensive alternative to RuO_2;[46–49] not only is it active for the OER, but also for the ORR, opening up possibilities for its use in regenerative fuel cells.[50] Manganese can form numerous oxides and many of these have been reported active for OER in alkaline and neutral electrolytes.[51] However, as for ruthenium dioxide, the stability can be an issue at high overpotentials.

Experimental Section

Preparation of Thin Films

Thin MnO_x and RuO_2 films were prepared by reactive sputter deposition on Au polycrystals and EQCM crystals. The deposition rates were calibrated with an in-chamber QCM. Prior to deposition, the samples were sonicated in acetone, isopropanol, and then Millipore water (18.2 MΩ). RuO_2 films were deposited at 300 °C and 3 mTorr with a power of 50 W using an argon and oxygen flow at a ratio of 5:2, with a metallic Ru target. MnO_x films were deposited at 200 °C, 5 mTorr, and 140 W with an argon and oxygen flow at a ratio of 5:1, and a metallic Mn target. The EQCM crystals were purchased from Stanford Research Systems (QCM200) and consist of a gold film deposited onto AT-cut quartz with a titanium layer in between for improved adhesion. The top electrode, functioning as working electrode for the electrochemical measurements, has a geometrical surface area of 1.37 cm^2. The bottom electrode is smaller, 0.38 cm^2, and the QCM is sensitive only in the overlapping region of the top and bottom electrodes. This means that approximately 28% of the electrochemically active layer is sensitive to the QCM measurement. The frequency change is converted to mass change using the Sauerbrey equation, as explained below. In this equation, a homogeneous mass change across the electrode is assumed. Because of the semiconducting nature of manganese oxides, we used a mask to confine the MnO_x area to where the QCM is sensitive (the central 0.38 cm^2 of the top electrode). This was done to diminish effects of local potential differences, for example, caused by gradients in film thickness. The remaining part of the gold film was covered with TiO_2, which introduced negligible currents and no frequency change during the stability tests. As RuO_2 is expected to be a metallic conductor, all of the gold film was covered with RuO_2. The Au polycrystalline electrodes (0.196 cm^2) used in RDE tests were polished prior to deposition with 0.25 μm diamond paste, then plasma cleaned in argon and annealed to 700 °C in two consecutive cycles. The targets for sputtering had a 99.95% purity and were purchased from AJA International.

Electrochemical Tests

The electrochemical tests on RuO_2 were performed in a glass cell with 0.05 M N_2-saturated H_2SO_4 (Merck Suprapur 96%, diluted with 18.2 MΩ Millipore water) at room temperature. The tests on MnO_x were performed in a two-compartment Teflon cell with 1 M N_2-saturated KOH (Merck Suprapur 99.995, diluted with 18.2 MΩ Millipore water) at room temperature. For the tests in sulfuric acid, a Hg/$HgSO_4$ reference electrode was used, whereas for the tests in KOH, a Hg/HgO in 20 wt% KOH reference electrode was used. The reference-electrode potentials were measured with respect to a reversible hydrogen electrode (RHE) by bubbling 1 bar hydrogen over a clean Pt surface in the same electrolyte. In both electrolytes, graphite rods were used as counter electrodes. All the data is presented using the RHE scale and corrected for Ohmic losses, found from the fitted high-frequency intercept measured using electrochemical impedance spectroscopy over the range of 1–200 000 Hz at a DC potential of 10 mV. The Ohmic drop for tests in 0.05 M H_2SO_4 was in the range of 15–18 Ω, whereas the tests in 1 M KOH comprised an Ohmic drop in the range of 3–5 Ω. For chronoamperometry measurements, the Ohmic drop was compensated at 85% using the Bio-Logic software EC-lab method MIR. Mass changes from EQCM measurements were calculated using the Sauerbrey equation with $C_f = (56.6 \pm 2.8)$ Hz cm^2 μg^{-1};[52] this value was calibrated by the electrodeposition of silver onto the Au-coated quartz crystal, repeated six times.[53] Each stability test performed by both EQCM and ICP–MS was repeated four times.

Since gold is not expected to be stable at high oxidative potentials,[40] we did not perform reference measurements with the bare EQCM crystals. Instead, the gold was coated by the catalyst thin film, as described above, and we measured the amount of gold in the electrolyte after OER tests. Based on two-hour tests at 1.9 V_{RHE} for three MnO_x samples, the increase of gold was less than 9 ng cm^{-2} or equivalent to less than 0.6 Hz. We therefore assumed that Au is sufficiently masked from the electrolyte.

At high current densities, gas formation on the electrode affects the frequency measurement; however, since the electrode was oriented vertically, the bubbles moved upwards and did not accumulate on the active area. While the bubble formation could cause some noise in the measurement, it would not have an effect on the trends observed over two-hour experiments.

Characterisation Methods

ICP–MS experiments were performed with equipment from Thermo Fisher Scientific, model iCAP-QC ICP-MS. Samples were taken out of the electrolyte before and after each measurement using a pipette. For tests in 0.05 M H_2SO_4, the samples were analysed without further dilution, whereas for 1 M KOH, the samples were diluted to 0.1 M to protect the ICP–MS components. For the quantitative analysis, calibration tests were performed using diluted solutions of Mn or Ru, made from standards with 1000 μg_{metal} mL^{-1} purchased from SCP Science. Calibrations were made with at least three concentrations. These were prepared in the range of 0.1 to 10 μg L^{-1} since the concentrations of Mn and Ru in the investigated electrolytes are all within that range. The calibration curves obtained could all be fitted to a linear curve with an R^2 of 0.99 or better. To calculate the total mass loss with ICP–MS, the volume of the electrolyte was measured for each experiment. For measurements with the two-compartment Teflon cell, only the volume of the compartment containing the working electrode was used. It was confirmed with a separate ICP–MS test that the amount of metal in the reference-electrode compartment was negligible. The thin films were evaluated by X-ray photoelectron spectroscopy using a Theta Probe instrument (Thermo Scientific) where the base pressure was 5×10^{-10} mbar. The X-ray source was monochromatized $Al_{K\alpha}$ (1486.7 eV). Furthermore, the thin films were analysed by X-ray diffraction (XRD) using a PANanalytical X'pert PRO equipment with an X-ray wavelength of 1.54 Å for the $Cu_{K\alpha}$ line.

2. Results and Discussion

To determine the structure of the two oxides, we performed glancing-angle XRD measurements. In Figure 2a, the diffractograms for RuO_2 and MnO_x are shown, together with literature references and a measurement for the glass substrate. For the RuO_2 film, the diffractogram obtained was consistent with a rutile RuO_2 structure,[54] whereas for MnO_x, no significant peaks were found, indicating that the film is amorphous. To

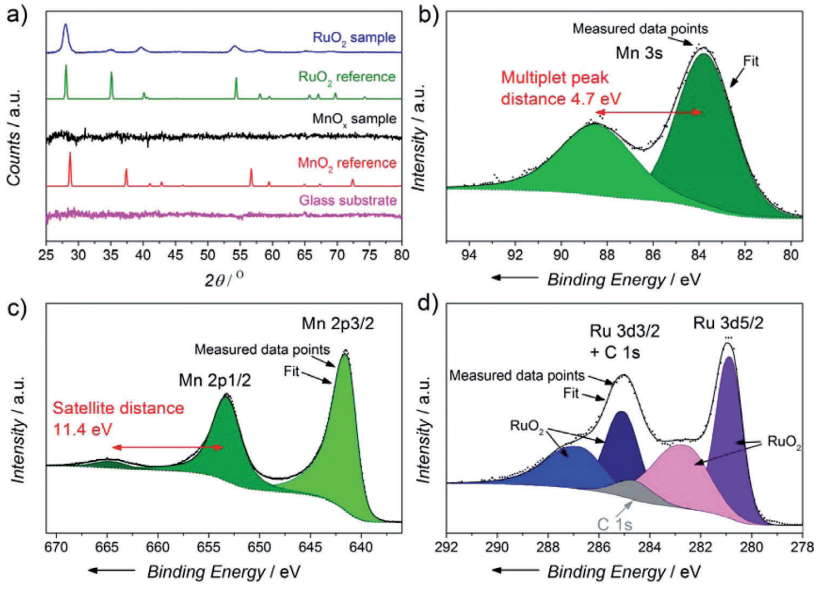

Figure 2. a) XRD diffractograms for RuO_2, MnO_x and the substrate, together with literature references. The literature data for RuO_2 is from Ref. [54] and that for MnO_2 from Ref. [59]. b) XPS spectra of the Mn 3s region for a 40 nm MnOx on EQCM sample. The red arrow indicates the difference in binding energy for the Mn 3s multiplet splitting. c) XPS spectra of the Mn 2p region for a 40 nm MnO_x on EQCM sample. The red arrow indicates the distance from the Mn 2p1/2 peak to its corresponding satellite. d) XPS spectra of the Ru 3d core level region for a 40 nm RuO_2 on EQCM sample.

further characterise the composition, XPS analyses were carried out. The results can be seen in Figure 2b–d for MnO_x and RuO_2, respectively. The MnO_x film was evaluated using the Mn 3 s multiplet splitting and Mn $2p_{1/2}$ distance between the main peak and its satellite.[55,56] The former was found to be 4.7 eV and the latter 11.4 eV, suggesting that the stoichiometry is consistent with MnO_2, which is also the most stable surface for Mn under OER conditions.[57] The RuO_2 film was evaluated based on the position and area of the Ru 3d lines, which matched with RuO_2 literature references.[58]

The electrochemical results are described in experimental order to ensure ease of reproducibility. As a first step, the activity of each sample was evaluated by using standard cyclic voltammetry at 5 mV s^{-1}. Representative results can be seen in Figure 3 for both RDE and EQCM setups. A useful figure of merit is the overpotential needed to sustain 10 mA cm^{-2}.[3] For RuO_2 in 0.05 M H_2SO_4 it is (354 ± 8) mV whereas for MnO_x it is (494 ± 6) mV, using the results from the RDE setup, based on two independent measurements for each oxide. These overpotentials are comparable to earlier reports in the literature, even though the films are only 40 nm thick and deposited onto smooth substrates, likely resulting in lower surface areas compared to samples made by electrodeposition or thermally prepared oxides. The activity obtained in the EQCM setup is slightly lower at high overpotentials for both samples; this discrepancy could result from a less facile bubble removal, compared to the rotating disk. However, the onsets of OER are the same in the two setups. Next, the Ohmic loss was evaluated by using impedance spectroscopy, followed by a stabilisation period during which the measured resonance frequency for the EQCM settled at a constant level. We observed that the frequency reading became stable after approximately 30 to 60 min, presumably due to temperature equilibration or equipment vibrations from cell assembly. Our criterion for establishing the stability was that the frequency would change less than 1 Hz over 15 min, which corresponds to a lower change than for any subsequent OER test. In the case of the RuO_2, the films were stabilised at 1.23 V_{RHE} whereas the MnO_x films were

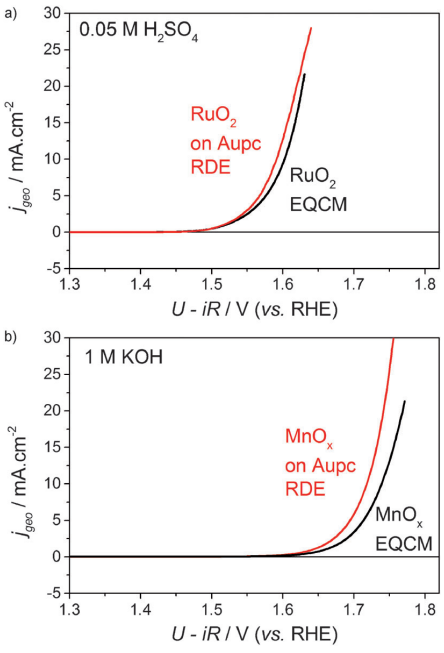

Figure 3. Cyclic voltammetry curves at room temperature for: a) 40 nm RuO_2 in 0.05 M N_2-saturated H_2SO_4. b) 40 nm MnO_x in 1 M N_2-saturated KOH. The scan rate was 5 mV s^{-1} and 1600 RPM (revolutions per minute) were used in the RDE tests. The current was normalised to the geometric area. The first anodic sweeps are shown.

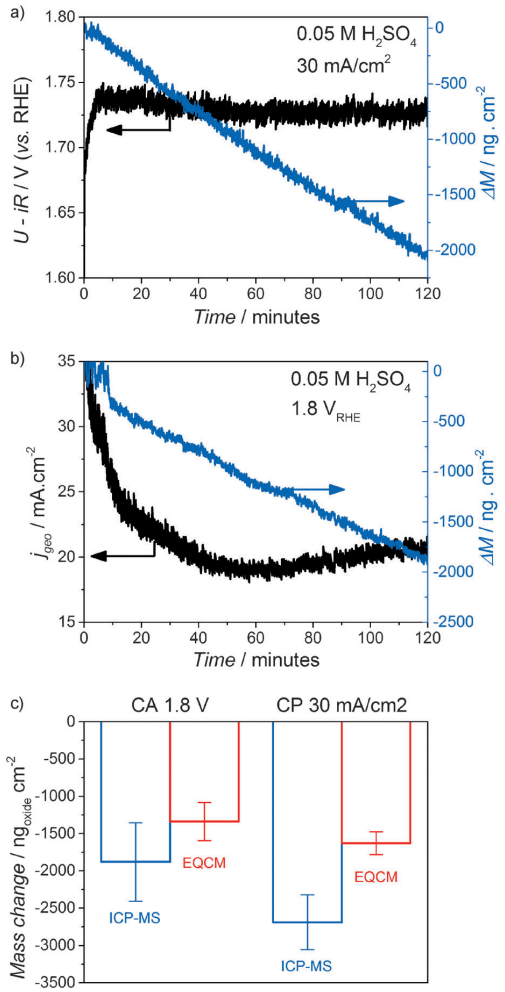

Figure 4. a) Chronopotentiometry at 30 mA cm^{-2} for 40 nm RuO_2 by using EQCM in 0.05 M N_2-saturated H_2SO_4 at room temperature. The black line indicates the measured potential and the blue line indicates the change in mass based on in situ resonance frequency measurements. b) Chronoamperometry at 1.8 V_{RHE} for 40 nm RuO_2 by using EQCM in 0.05 M N_2-saturated H_2SO_4 at room temperature. c) Comparison of the mass change found from EQCM and ICP–MS based on four separate experiments. The mass loss from the ICP–MS measurements was adjusted to the equivalent RuO_2 mass (rather than the Ru mass) for more direct comparison to EQCM measurements.

stabilised at 1.4 V_{RHE}; in both cases these potentials were chosen on the basis that the dioxide phases would be stable.[59] After the initial period of cycling, impedance measurement and stabilisation, samples for ICP–MS analysis were taken. From four measurements on each catalyst we found an average of (123 ± 60) $ng_{oxide}\,cm^{-2}$ RuO_2 and (472 ± 240) $ng_{oxide}\,cm^{-2}$ MnO_2 present in the solution prior to further testing. These results indicate that the initial cyclic voltammetry induces mass losses for both materials, these losses being more significant for MnO_x. During subsequent corrosion measurements, to assess the amount of Ru or Mn dissolved during the test, the initial amount of dissolved Ru or Mn at the start of the measurement was subtracted from the final amount.

Once the frequency had stabilised, first chronoamperometry, CA, and then chronopotentiometry, CP, measurements were started. For RuO_2, we measured CA at 1.8 V_{RHE} and CP at 30 $mA\,cm^{-2}$. These parameters were chosen to ensure that the potential was positive of the reversible potential for RuO_4 formation, 1.39 V_{RHE},[60] under standard conditions. For MnO_x, potentials at 1.8 and 1.9 V_{RHE} and a current density of 20 $mA\,cm^{-2}$ were chosen to be positive of the potential for MnO_4^- formation.[60] All stability tests were carried out for 2 h. We have observed that longer term tests tend to yield a poorer reproducibility; this could be a result of thickness gradients giving rise to local conductivity issues, exposed substrate, redeposition of dissolved species or precipitation. It should also be noted that corrosion mechanisms are highly dependent on the material.[39] The degradation of some materials may actually be accelerated by potential cycling (as shown by Mayrhofer and co-workers to be the case for Pt, by combining cyclic voltammetry with online ICP measurements[61]). Consequently, to study the resistance to corrosion of such materials, potentiodynamic—rather than potentiostatic—tests would be necessary.

2.1. Stability of RuO_2

In the case of RuO_2, the results from chronopotentiometry and chronoamperometry can be seen in Figure 4 a,b. Chronopotentiometry, as a technique, should correspond to the performance for a constant hydrogen production load on an electrolyser. The extra overpotential needed to sustain the hydrogen production is directly correlated to energy loss. In Figure 4 a, it can be seen that RuO_2 can maintain a stable performance, which changes only slightly during 2 h. However, looking at the mass change associated with the test, it is clear that there is a constant mass loss. This mass loss is equivalent to 4.8 monolayers (ML) per hour assuming the density and lattice parameters of (110) RuO_2 layers.[54] Figure 4 b shows the results of the chronoamperometry measurement. The potential is held constant throughout the measurement; since the current depends exponentially on the potential, any deactivation shows up more clearly than in a chronopotentiometry measurement. A constant potential at 1.8 V_{RHE} yields a mass loss equivalent of 4.4 ML per hour. With this rate, it would take approximately 29 h to corrode all of the 40 nm film. Assuming that the corrosion proceeds in accordance to $RuO_2 + 2H_2O \rightarrow RuO_{4(aq)} + 4H^+ + 4e^-$,[36] a dissolution rate of 4 ML per hour would be equivalent to 0.6 $\mu A\,cm^{-2}$, that is, more than four orders of magnitude lower than the oxygen evolution current density. In principle, the transient formation of RuO_4[36] could be detected with a rotating ring disk electrode setup; however, the necessary current sensitivity would be unrealistic. We also analysed the solution by ICP–MS after the electrochemical tests; Figure 4 c compares the EQCM and ICP–MS results. The mass losses found from the ICP–MS measurements shown in Figure 4 c are converted to RuO_2 equivalent since ICP–MS is only sensitive towards single elements and not the initial oxides. Comparing the two methods, there are differences for

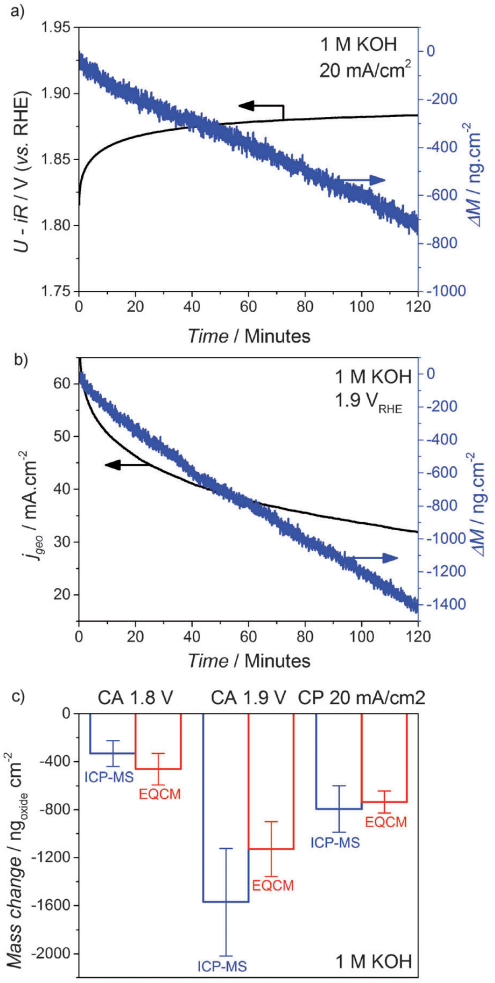

Figure 5. a) Chronopotentiometry at 20 $mA\,cm^{-2}$ for 40 nm MnO_x by using EQCM in 1 M N_2-saturated KOH at room temperature. The black line indicates the measured potential and the blue line indicates the change in mass based on in situ resonance frequency measurements. b) Chronoamperometry at 1.9 V_{RHE} for 40 nm MnO_x by using EQCM in 1 M N_2-saturated KOH at room temperature. c) Comparison of the mass change found from EQCM and ICP–MS based on four separate experiments. The mass loss from the ICP–MS measurements was adjusted to the equivalent MnO_2 mass (rather than the Mn mass), for more direct comparison to EQCM measurements.

both tests. The losses evaluated by ICP–MS are higher than what is seen from the EQCM method. This could be due to the fact that EQCM is only sensitive to about 28% of the catalytically active area, as descibed in the experimental section. We assume a homogeneous mass loss across the electrode but an inhomogenous current distribution could result in a wrong estimation. On the other hand, ICP–MS is sensitive to losses from the entire electrode area, which is likely to give a more accurate evaluation.

2.2. Stability of MnO_x

Chronopotentiometry and chronoamperometry tests were also carried out for MnO_x in alkaline solution, 1 M KOH, as shown on Figure 5 a,b. Compared to the results for RuO_2, the chronopotentiometry test results in a larger increase of potential during the two hours. The graph in Figure 5 a also shows the importance of choosing an axis length spanning only the relevant data range so the change is easily spotted. However, on the basis of the chronoamperometry measurement in Figure 5 b, the deactivation is even clearer because of the exponential behaviour of the current density as a function of the overpotential. However, in both measurements, a constant mass loss takes place in parallel with the oxygen evolution current. At 1.9 V_{RHE}, the loss of 1128 ng cm^{-2} is equivalent to about 3.9 ML per hour, assuming the density and lattice parameters of rutile (110) MnO_2 layers,[59] while a constant current at 20 mA cm^{-2} leads to a loss of about 2.6 ML per hour.[1] Assuming that the losses are due to anodic dissolution, that is, $MnO_2 + 2H_2O \rightarrow MnO_4^-{}_{(aq)} + 4H^+ + 3e^-$,[60] this rate would be equivalent to a current density of 0.35 μA cm^{-2}, more than four orders of magnitude lower than the total current.[2] The mass losses were also evaluated by ICP–MS after each measurement, as shown in Figure 5 c. We note that the error bars are rather large. Nonetheless, the two methods show an overall agreement. Extrapolating the data here, the time required to completely corrode a 40 nm-thick MnO_x film would be approximately 36 h at a constant potential of 1.9 V_{RHE}. From another perspective, a confirmation of stability for a given catalyst would require that a specific lifetime can be ensured. As an example, a lifetime of five years for a 40 nm film corresponds to a maximum of 0.02 Å dissolved material in a two-hour test. This rate for a RuO_2 catalyst on a 1 cm^2 electrode in 100 mL of electrolyte results in a less than 2 ppt concentration in the ICP–MS analysis. Such concentrations approach the limit of detection, that is, 0.4 ppt for Ru,[62] which complicates meaningful extrapolation. Therefore, a comprehensive lifetime evaluation should be accompanied by a long-term test. In Table 1, the relevant stability metrics and standard deviations are listed together with the OER activity of the thin films.

Table 1. Stability metrics from EQCM and ICP–MS.

Sample[a]	$\eta_{10\ mA\ cm^{-2}}$ [mV] from RDE		$\Delta M_{1.8\ V(RHE)}$ 2 h [$ng_{oxide}\ cm^{-2}$]	$\Delta M_{1.9\ V(RHE)}$ 2 h [$ng_{oxide}\ cm^{-2}$]	$\Delta M_{30\ mA\ cm^{-2}}$ 2 h [$ng_{oxide}\ cm^{-2}$]	$\Delta M_{20\ mA\ cm^{-2}}$ 2 h [$ng_{oxide}\ cm^{-2}$]
RuO_2	360 ± 8	EQCM	−1464 ± 13/	–	−1566 ± 110/	–
		ICP-MS	−1915 ± 69		−2624 ± 346	
MnO_x	490 ± 6	EQCM	−462 ± 131/	−1128 ± 229/	–	−735 ± 93/
		ICP-MS	−332 ± 108	−1570 ± 447		−793 ± 194

[a] For both oxides the measured mass losses are shown with corresponding standard deviation from four independent measurements. The overpotentials listed here are from RDE tests based on two independent measurements. Mass losses from EQCM are calculated from the frequency change using the Sauerbrey equation. Values for ICP–MS are corrected to the corresponding dioxide masses.

From these measurements, it is clear that solely examining current or potential changes for a small number of hours is insufficient to establish the long-term performance of an OER catalyst in an electrolyser. On the contrary, the anodic dissolution of a catalyst may actually manifest itself over a short-term measurement as an improvement in current density or decreased overpotential, due to an increased surface area.[34] OER conditions may lead to an increase in the microscopic surface area, a decrease in the catalyst surface area and a structural change to a more stable phase; without prior knowledge, it is not possible to determine which of these processes would predominate. Therefore, we emphasise that explicit analyses of mass changes are needed to quantify the stability of these catalysts.

3. Conclusions

In conclusion, we have shown that the stability of catalysts for the oxygen evolution reaction can be assessed by means of short-term tests based on a combination of EQCM and ICP–MS. It is clear that it is not possible to even roughly estimate the long-term performance of a catalyst on the basis of short-term chronopotentiometry or chronoamperometry measurements alone. Benchmarking and standardising research efforts are still at an early stage for this reaction. Nonetheless, when a new catalyst is discovered, rigorous and transparent criteria should be applied to establish whether or not the material is stable. While the end goal should be to test catalysts over the long term in actual devices, the quantification of mass losses using well-defined electrodes combined with EQCM and ICP–MS provides a less-time-consuming, albeit meaningful, alternative. Finally, although we have focused on the oxygen evolu-

[1] *We assumed a MnO_2 composition on the basis of our XPS analysis. Although the XRD experiments suggested that the films are amorphous, we take the view that the rutile (110) plane provides a reasonable approximation of the surface termination. Should we have chosen a different structure, the interplanar distance would always be between 2–4 Å, varying the loss in monolayers by less than a factor of two. The exact surface termination will not change our overall conclusions.*

[2] *It is conceivable that MnO_2 dissolves via a two-electron process to MnO_4^{2-},[60] which would lead to a corrosion current density of 0.26 μA cm^{-2}, rather than 0.35 μA cm^{-2}. Regardless, this will not change the picture presented herein, as the anodic current would still be negligible in comparison to the overall dissolution current.*

tion reaction, the findings of this report are general and could be applied to many other electrochemical reactions, including hydrogen evolution, oxygen reduction and CO_2 reduction.

Acknowledgements

The authors gratefully acknowledge financial support from the Danish Ministry of Science's UNIK initiative, Catalysis for Sustainable Energy. The Center for Individual Nanoparticle Functionality is supported by the Danish National Research Foundation (DNRF54). B.W. thanks Formas (project number 219-2011-959) for financial support.

Keywords: corrosion · electrochemistry · heterogeneous catalysis · thin films · water splitting

[1] J. Greeley, N. M. Markovic, *Energy Environ. Sci.* **2012**, *5*, 9246.
[2] A. Marshall, B. Børresen, G. Hagen, M. Tsypkin, R. Tunold, *Energy* **2007**, *32*, 431 – 436.
[3] M. G. Walter, E. L. Warren, J. R. McKone, S. W. Boettcher, Q. Mi, E. A. Santori, N. S. Lewis, *Chem. Rev.* **2010**, *110*, 6446 – 6473.
[4] C. C. L. McCrory, S. Jung, J. C. Peters, T. F. Jaramillo, *J. Am. Chem. Soc.* **2013**, *135*, 16977 – 16987.
[5] S. Trasatti, *J. Electroanal. Chem.* **1980**, *111*, 125 – 131.
[6] R. Smalley, *MRS Bull.* **2005**, *30*, 00.
[7] Y. Lee, J. Suntivich, K. May, E. E. Perry, Y. Shao-Horn, *J. Phys. Chem. Lett.* **2012**, *3*, 399 – 404.
[8] P. C. K. Vesborg, T. F. Jaramillo, *RSC Adv.* **2012**, *2*, 7933.
[9] J. Suntivich, K. J. May, H. A. Gasteiger, J. B. Goodenough, Y. Shao-Horn, *Science* **2011**, *334*, 1383 – 1385.
[10] A. Grimaud, K. J. May, C. E. Carlton, Y.-L. Lee, M. Risch, W. T. Hong, J. Zhou, Y. Shao-Horn, *Nat. Commun.* **2013**, *4*, 2439.
[11] Y. Gorlin, T. F. Jaramillo, *J. Am. Chem. Soc.* **2010**, *132*, 13612 – 13614.
[12] M. Gong, Y. Li, H. Wang, Y. Liang, J. Z. Wu, J. Zhou, J. Wang, T. Regier, F. Wei, H. Dai, *J. Am. Chem. Soc.* **2013**, *135*, 8452 – 8455.
[13] W. Sheng, H. A. Gasteiger, Y. Shao-Horn, J. E. Soc, P. B-b, *J. Electrochem. Soc.* **2010**, *157*, B1529.
[14] K. Ayers, L. Dalton, E. Anderson, *ECS Trans.* **2012**, *41*, 27 – 38.
[15] M. Piana, M. Boccia, A. Filpi, E. Flammia, H. A. Miller, M. Orsini, F. Salusti, S. Santiccioli, F. Ciardelli, A. Pucci, *J. Power Sources* **2010**, *195*, 5875 – 5881.
[16] T. Reier, M. Oezaslan, P. Strasser, *ACS Catal.* **2012**, *2*, 1765 – 1772.
[17] K. Macounová, J. Jirkovský, M. V. Makarova, J. Franc, P. Krtil, *J. Solid State Electrochem.* **2009**, *13*, 959 – 965.
[18] R. Forgie, G. Bugosh, K. C. Neyerlin, Z. Liu, P. Strasser, *Electrochem. Solid-State Lett.* **2010**, *13*, B36.
[19] M. Vuković, *J. Appl. Electrochem.* **1987**, *17*, 737 – 745.
[20] L. Trotochaud, J. K. Ranney, K. N. Williams, S. W. Boettcher, *J. Am. Chem. Soc.* **2012**, *134*, 17253 – 17261.
[21] L. Trotochaud, S. L. Young, J. K. Ranney, S. W. Boettcher, *J. Am. Chem. Soc.* **2014**, *136*, 6744 – 6753.
[22] R. D. L. Smith, M. S. Prévot, R. D. Fagan, Z. Zhang, P. A. Sedach, M. K. J. Siu, S. Trudel, C. P. Berlinguette, *Science* **2013**, *340*, 60 – 63.
[23] J. Blakemore, H. Gray, J. Winkler, A. Müller, *ACS Catal.* **2013**, *3*, 2497 – 2500.
[24] K. Juodkazis, J. Juodkazytė, R. Vilkauskaitė, B. Šebeka, V. Jasulaitienė, *CHEMIJA* **2008**, *19*, 1 – 6.
[25] K. Stoerzinger, L. Qiao, M. D. Biegalski, Y. Shao-Horn, *J. Phys. Chem. Lett.* **2014**, *5*, 1636 – 1641.
[26] R. Subbaraman, D. Tripkovic, K.-C. Chang, D. Strmcnik, A. P. Paulikas, P. Hirunsit, M. Chan, J. Greeley, V. Stamenkovic, N. M. Markovic, *Nat. Mater.* **2012**, *11*, 550 – 557.
[27] M. Risch, K. A. Stoerzinger, S. Maruyama, W. T. Hong, I. Takeuchi, Y. Shao-Horn, *J. Am. Chem. Soc.* **2014**, *136*, 5229 – 5232.
[28] A. Ohma, K. Shinohara, A. Iiyama, T. Yoshida, A. Daimaru, *ECS Trans.* **2011**, *41*, 775 – 784.
[29] A. S. Bandarenka, E. Ventosa, A. Maljusch, J. Masa, W. Schuhmann, *Analyst* **2014**, *139*, 1274 – 1291.
[30] L. Tang, B. Han, K. Persson, C. Friesen, T. He, K. Sieradzki, G. Ceder, *J. Am. Chem. Soc.* **2009**, *132*, 596 – 600.
[31] M. Wakisaka, S. Asizawa, H. Uchida, M. Watanabe, *Phys. Chem. Chem. Phys.* **2010**, *12*, 4184 – 4190.
[32] K. J. J. Mayrhofer, J. C. Meier, S. J. Ashton, G. K. H. Wiberg, F. Kraus, M. Hanzlik, M. Arenz, *Electrochem. Commun.* **2008**, *10*, 1144 – 1147.
[33] F. J. Perez-Alonso, C. F. Elkjær, S. S. Shim, B. L. Abrams, I. E. L. L. Stephens, I. Chorkendorff, *J. Power Sources* **2011**, *196*, 6085 – 6091.
[34] K. J. May, C. E. Carlton, K. A. Stoerzinger, M. Risch, J. Suntivich, Y.-L. Lee, A. Grimaud, Y. Shao-Horn, *J. Phys. Chem. Lett.* **2012**, *3*, 3264 – 3270.
[35] J. C. Meier, I. Katsounaros, C. Galeano, H. J. Bongard, A. A. Topalov, A. Kostka, A. Karschin, F. Schüth, K. J. J. Mayrhofer, *Energy Environ. Sci.* **2012**, *5*, 9319.
[36] M. Vuković, *J. Chem. Soc. Faraday Trans.* **1990**, *86*, 3743 – 3746.
[37] N. Danilovic, R. Subbaraman, K.-C. Chang, S. H. Chang, Y. Kang, J. D. Snyder, A. P. Paulikas, D. Strmcnik, Y.-T. Kim, D. J. Myers, V. R. Stamenkovic, N. M. Markovic, *J. Phys. Chem. Lett.* **2014**, *5*, 2427 – 2478.
[38] B. Wickman, H. Grönbeck, P. Hanarp, B. Kasemo, *J. Electrochem. Soc.* **2010**, *157*, B592 – B598.
[39] S. Cherevko, A. R. Zeradjanin, A. A. Topalov, N. Kulyk, J. J. Mayrhofer, *ChemCatChem* **2014**, DOI: 10.1002/cctc.201.
[40] S. Cherevko, A. a. Topalov, A. R. Zeradjanin, I. Katsounaros, K. J. J. Mayrhofer, *RSC Adv.* **2013**, *3*, 16516 – 16527.
[41] L. Xing, M. A. Hossain, M. Tian, D. Beauchemin, K. T. Adjemian, G. Jerkiewicz, *Electrocatalysis* **2014**, *5*, 96 – 112.
[42] D. A. Buttry, M. D. Ward, *Chem. Rev.* **1992**, *92*, 1355 – 1379.
[43] G. Lodi, E. Sivieri, A. De Battisti, S. Trasatti, *J. Appl. Electrochem.* **1978**, *8*, 135 – 143.
[44] H. Over, *Chem. Rev.* **2012**, *112*, 3356 – 3426.
[45] E. A. Paoli, F. Masini, R. Frydendal, D. Deiana, C. Schlaup, M. Malizia, T. W. Hansen, S. Horch, I. E. L Stephens, I. Chorkendorff, *Chem. Sci.* **2014**, DOI: 10.1039/C4SC02685C.
[46] H. Dau, C. Limberg, T. Reier, M. Risch, S. Roggan, P. Strasser, *ChemCatChem* **2010**, *2*, 724 – 761.
[47] Y. Gorlin, T. F. Jaramillo, *J. Electrochem. Soc.* **2012**, *159*, H782 – H786.
[48] K. L. Pickrahn, S. W. Park, Y. Gorlin, H.-B.-R. Lee, T. F. Jaramillo, S. F. Bent, *Adv. Energy Mater.* **2012**, *2*, 1269 – 1277.
[49] K. Mette, A. Bergmann, J.-P. Tessonnier, M. Hävecker, L. Yao, T. Ressler, R. Schlögl, P. Strasser, M. Behrens, *ChemCatChem* **2012**, *4*, 851 – 862.
[50] J. W. Desmond Ng, Y. Gorlin, T. Hatsukade, T. F. Jaramillo, *Adv. Energy Mater.* **2013**, *3*, 1545 – 1550.
[51] D. M. Robinson, Y. B. Go, M. Mui, G. Gardner, Z. Zhang, D. Mastrogiovanni, E. Garfunkel, J. Li, M. Greenblatt, G. C. Dismukes, *J. Am. Chem. Soc.* **2013**, *135*, 3494 – 3501.
[52] G. Sauerbrey, *Z. Phys.* **1959**, *155*, 206 – 222.
[53] C. Gabrielli, M. Keddam, R. Torresi, *J. Electrochem. Soc.* **1991**, *138*, 2657 – 2660.
[54] C. Boman, *Acta Chem. Scand.* **1970**, *24*, 116 – 122.
[55] Y. Gorlin, B. Lassalle-Kaiser, J. D. Benck, S. Gul, S. M. Webb, V. K. Yachandra, J. Yano, T. F. Jaramillo, *J. Am. Chem. Soc.* **2013**, *135*, 8525 – 8534.
[56] V. Di Castro, G. Polzonetti, *J. Electron Spectrosc. Relat. Phenom.* **1989**, *48*, 117 – 123.
[57] H.-Y. Su, Y. Gorlin, I. C. Man, F. Calle-Vallejo, J. K. Nørskov, T. F. Jaramillo, J. Rossmeisl, F. Jaramillo, *Phys. Chem. Chem. Phys.* **2012**, *14*, 14010 – 14022.
[58] R. Kötz, H. J. Lewerenz, S. Stucki, *J. Electrochem. Soc.* **1983**, *130*, 825 – 829.
[59] W. H. Baur, *Acta Crystallogr. Sect. B* **1976**, *32*, 2200 – 2204.
[60] M. Pourbaix, *Atlas of Electrochemical Equilibria in Aqueous Solutions*, Pergamon Press, Oxford, **1966**.
[61] A. Topalov, I. Katsounaros, M. Auinger, S. Cherevko, J. C. Meier, S. O. Klemm, K. J. J. Mayrhofer, *Angew. Chem. Int. Ed.* **2012**, *51*, 12613 – 12615; *Angew. Chem.* **2012**, *124*, 12782 – 12784.
[62] *ICP Application Note for iCAP-QC*, Thermo Fisher Scientific, **2012**.

Received: July 31, 2014
Published online on ■■ ■■, 2014

ARTICLES

R. Frydendal, E. A. Paoli, B. P. Knudsen, B. Wickman, P. Malacrida, I. E. L. Stephens, I. Chorkendorff**

■■ – ■■

Benchmarking the Stability of Oxygen Evolution Reaction Catalysts: The Importance of Monitoring Mass Losses

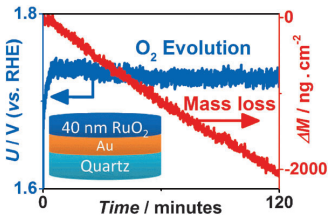

Quantifying stability: It is shown that short-term electrochemical measurements are inadequate to establish oxygen evolution catalyst stability. Independent measurements of mass losses are essential.